UiO : University of Oslo

Robert Hagala

Astrophysical Simulations for Uncovering Signatures of Gravity

Thesis submitted for the degree of Philosophiae Doctor

Institute of Theoretical Astrophysics
Faculty of Mathematics and Natural Sciences

2019

Preface

For millennia, mankind has looked up to the night sky in amazement and wonder. From the ancient astronomers of Mesopotamia and until today, we have uncovered a lot about how the Universe works. We can measure and model the tiniest subatomic processes, as well as the largest cosmic structures. Still, it is evident that we do not fully understand everything. Just like a child keeps asking "but why?" when given an answer, a scientist will also ask "but why?" when finding a new model that seems to describe the physical world. My own curiosity for astrophysics was sparked at a young age, when looking at artist impressions of planets, galaxies and black holes in a science book for children. This fascination and fear of the unknown, is what inspired my thesis to be about the nature of gravity and how it might be analysed. Finally, more than twenty years later, I am finishing a thesis for the degree of *Philosophiae Doctor* in astrophysics.

My thesis is an advance in the science of describing gravity through non-linear astrophysical simulations. The research is conducted under the supervision of professor David F. Mota (UiO) and Claudio Llinares (Portsmouth). The purpose of the three introductory chapters and the conclusions of this thesis is to make my research better understandable and to set my publications in a broader perspective.

In chapter 1, I will present the definition and history of cosmology and astrophysics, as well as an introduction to the theory of general relativity. Furthermore, to motivate my work related to extensions of general relativity, I will point to problems with the currently accepted theory.

I will introduce modified gravity and concepts related to it in chapter 2, including some example models. A big part of studying modified gravity on a theoretical basis is to determine whether some specific modification to gravity can actually be detected with astronomical observations. Hence, I will also describe some possible probes that can be used to distinguish the vast amount of different models for gravity.

My work has relied heavily on numerical calculations, specifically computer simulations. I will explain the history and application of such simulations in the context of both general relativity and modified gravity in chapter 3. Most of my time during this doctorate was spent on simulating models with a disformally coupled scalar field. Many new phenomena found in these simulations will be discussed in detail in chapter 3.

Following chapter 3, I will include the main work of this thesis and of my doctorate: three scientific papers presented in chronological order. The common theme to them is numerical simulations and understanding gravity. All three papers were written in collaboration with David F. Mota and Claudio Llinares,

with me being first author on two of them.

In chapter 4, after the papers, I will conclude my work by summarising the results of the three main papers and exploring the implications of these results.

Acknowledgements

Thanks to the Universe in general for aligning in a way that allowed me to write this thesis!

There are many people I want to thank; without you, this thesis would never be a reality. First I should thank my supervisors, David Mota and Claudio Llinares. They have allowed me a lot of freedom, and found a good combination of friendly guidance and dropping me into the unknown for me to learn science by doing science. Thanks a lot to the administration at ITA, especially Brenda, for helping me do all the paperwork and helping me structure my work-flow the last couple of months. Furthermore I would like to thank some other scientists and collaborators, who all have inspired my work with stimulating conversations and ideas: Jack, Carsten, Purnendu, Antonio, Shinji, Leonardo, Hans Arnold, Mattia, and Marta.

Many important and wonderful people have entered my life during these few years, through the university or otherwise. I am sorry if I am forgetting someone, but here is the list in no particular order: Lluis, Ainar, Bridget, Robert (the other one), Marie, Monica, Ragnhild, Ata, Ada, Ranajoy, Eivor, Hanne, Nina, Pål, Odd, Dabao, Cecilie, Helén, Magna Karina, Anna, Veera, Anja, Georgina, Angie and Villő. I am looking forward to spending more time with all of you.

Then we have all my long-time friends. These are too many to mention, but the ones standing out lately include: Sigrid, Alexander, Christian, Kristian, Ingvild, Jørn, Khoa, Eigil, Silje, Roar, Trygve, Sigurd, Mathias, Tommy, and Solveig. Of course I want to thank my family (hi mom and dad!) for supporting me throughout my work and in life in general. A special thanks to my sister Lillian for helping me develop the perfect title for my thesis.

Finally, thank you so much to Jørn, Lillian and Yngvar, for reading and helping me with spotting errors and inconsistencies in the text of this thesis. I will pay the good deed forward.

In memory of the two wonderful cats Arcus and Ella, you are deeply missed.

Robert Hagala
Oslo, October 2019

List of Papers

Paper I

Robert Hagala, Claudio Llinares, and David F. Mota 'Cosmic Tsunamis in Modified Gravity: Scalar waves disrupting screening mechanisms'. In: *Physical Review Letters* (2017).
DOI: 10.1103/PhysRevLett.118.101301.
arXiv: 1607.02600.

Paper II

Claudio Llinares, Robert Hagala, and David F. Mota 'Non-linear Phenomenology of Disformally Coupled Quintessence'. Accepted for publication in *Monthly Notices of the Royal Astronomical Society.* (2019).
arXiv: 1902.02125.

Paper III

Robert Hagala, Claudio Llinares, and David F. Mota 'The Slingshot Effect as a Probe of Transverse Motions of Galaxies'. In: *Astronomy & Astrophysics* (2019).
DOI: 10.1051/0004-6361/201935261.
arXiv: 1907.01429.

Contents

List of Figures

List of Tables

List of Symbols and Abbrevations

Symbol	Meaning	Notes
a	Scale factor	Current scale of the Universe. Normalised to $a = 1$ today, with $a = 0$ at Big Bang.
c	Speed of light in vacuum	Taken to be a universal constant. In this thesis I use units where $c = 1$.
G		Newton's gravitational constant
H	Hubble factor	The rate of expansion of the Universe. $H \equiv \dot{a}/a$.
H_0	Hubble constant	The Hubble factor today, $H_0 = H(z = 0)$. The factor tells how fast one Mpc of space is expanding.
h	Dim.less Hubble parameter	The dimensionless re-scaling of H_0, defined as $h = H_0/(100\,\mathrm{km/s/Mpc})$.
$g_{\mu\nu}$	Metric tensor	Describes distances in space-time. The line element is $\mathrm{d}s^2 = g_{\mu\nu}\mathrm{d}x^\mu \mathrm{d}x^\nu$.
M_{Pl}	Planck Mass	A mass scale. In natural units $M_{\mathrm{Pl}}^{-2} = 8\pi G$.
p	Pressure	
$R^\alpha_{\beta\mu\nu}$	Riemann curvature tensor	Tensor fully describing the curvature of space-time.
$R_{\mu\nu}$	Ricci tensor	Contraction of the Riemann Tensor. $R_{\mu\nu} = R^\alpha_{\mu\alpha\nu}$.
R	Ricci scalar	Invariant scalar describing the local curvature. $R = g^{\mu\nu}R_{\mu\nu} = R^\nu_\nu$.
$T_{\mu\nu}$	Stress–energy tensor	Describes the contents of the Universe. The diagonal contains the density ρ and pressure p.
t	Time coordinate	Cosmic time, usually since the Big Bang (can be measured in seconds, years or megayears).

Symbol	Meaning	Notes
z	Redshift	A measure of the cosmic redshift of an object. Also used as a measure for time, such that $z = 0$ today, and higher redshift is further into the past. Cosmic redshift relates to the scale factor as $a = 1/(1 + z)$.
δ	Overdensity	The density contrast with respect to the background density $\bar{\rho}$. Defined as $\delta \equiv (\rho/\bar{\rho}) - 1$.
γ_{PPN}	PPN gamma	A post-Newtonian parameter relating the metric perturbations Ψ and Φ. Can be used to distinguish GR from some other theories of gravity.
γ^2	Disformal kinetic fraction	Defined in equation (2.10) on page 25.
σ	Standard deviation	A measure used when presenting a value with uncertainities, or to express the significance of a deviation from predictions. A deviation of more than 2σ from the expected value is considered significant.
ρ	Matter density	When written without subscript, it is the total matter density $\rho = \rho_{DM} + \rho_{\text{baryons}}$
Ψ	Newtonian potential	Gravitational potential, can be used to calculate the gravitational force in Newtonian gravity.
ϕ	Scalar field	A propagating degree of freedom in scalar–tensor theories.
Λ	Cosmological constant	A constant representing the energy density of the vacuum in the framework of GR.
AMR	Adaptive mesh refinement	A method to locally increase the resolution of numerical simulations.
CDM	Cold dark matter	Invisible pressureless matter that only interacts through gravity.

Symbol	Meaning	Notes
ΛCDM		Read "Lambda CDM". The concordance model of cosmology, where the two main components are Λ and cold dark matter.
CMB	Cosmic microwave background	The oldest observable photons, originating at the time of last scattering, when the universe first became transparent.
EOM	Equation of motion	A (typically second order) differential equation describing the dynamics of a scalar field.
GR	General Relativity	Discovered/invented by Einstein in 1915. Describes gravity through the geometry of spacetime.
pc	Parsec	Unit of length used in astronomy, approximately 3.3 light years.

Chapter 1

Introduction

The nature of gravity is a disputed topic within astrophysics. The concept of gravity has been around for a long time, yet we do not understand it completely. A way to interpret gravity is through one of the most influential scientific theories: the theory of *general relativity*. Since the nature of gravity in the Universe outside of the solar system is difficult to measure directly, astrophysicists need to run astrophysical simulations in the pursuit of understanding its nature. Non-linear simulations aim at resolving phenomena in regions of space that are not possible to probe through simpler computational methods. In this dissertation, I will explore the question of how the nature of gravity can be better understood through non-linear astrophysical simulations. To probe alternatives to general relativity, I will conduct simulations with theories of modified gravity and investigate some of their signatures. Before looking at alternatives to general relativity, I will discuss what general relativity is and how it applies to cosmology. In this chapter, I will introduce the basic concepts which are necessary to appreciate the rest of the thesis.

For this chapter only, I will assume that conventional general relativity fully describe gravity and space-time.

1.1 Astronomy, Astrophysics, and Cosmology

The terms astronomy, astrophysics, and cosmology are interconnected; All of them are research fields related to the Universe beyond the Earth.

Astronomy concerns observations and measurements of phenomena outside of Earth. Objects studied and mapped in astronomy include our own Sun, the planets in our solar system, the stars in our galaxy, distant galaxies, and even exotic phenomena like supernovae and the surroundings of black holes. The keyword here is that astronomy, in the strictest sense, only covers *observations*.

The common definition of *astrophysics* is the combination of physical laws with astronomical observations to model and explain the underlying workings of the Universe and objects within it. Hence, astrophysics is the more theoretical counterpart to astronomy. Most of the mathematical models (physical laws) used in astrophysics are discovered and tested in laboratories on Earth, or tested with space probes in our solar system. These laws are then extrapolated out of our solar system, assuming that they also work on the scales of galaxies and larger.

Cosmology concerns the origin and evolution of the Cosmos as a whole, including its early evolution, the expansion rate of space, the clustering of matter to form large scale structures, and the evolution of the average ratios between the components of the Universe. In the context of this thesis, I will use the

term “cosmology” when referring to the science of large scale properties of the Universe. There is no strict definition of “large scales”, but any structures larger than the size of a cluster of galaxies will, in general, be considered large scales. Although astrophysics is a more general term than cosmology, I will often use the term “astrophysics” to refer to phenomena on galaxy scales and smaller, where the electromagnetic force starts to play a part.

1.2 History of Cosmology

Before the modern scientific method was established, most attempts at explaining or describing the workings of the Universe were based on myths, stories, or religion. With the lack of precise observations of objects beyond the Earth, and no direct information about objects beyond the Solar System, the early concepts regarding cosmology were developed by natural philosophers.

An example of a historical cosmology is old Norse cosmology, wherein there are nine realms connected by the cosmic tree Yggdrasil. According to old Norse mythology, in the beginning, there was a place of extreme cold called Niflheim and a place of extreme heat, called Muspelheim. These two polarities were separated by the gaping primordial void Ginnungagap. As these two extremes started to come in contact, objects, creatures, and the nine realms emerged from the resulting dynamic.

Different historical cosmologies from around the world have suggested both finite and infinite universes in size, as well as finite and infinite in time. Many of the concepts—for instance the idea of a cyclic universe—appear in several different cultures. The idea of Yggdrasil, or a central tree of life, has appeared in the ancient Indian and Babylonian cosmologies as well as in the old Norse cosmology [Lum16]

In the 16th century, Copernicus suggested that the Earth and other planets circle the Sun, which sparked the Copernican revolution. Soon other scholars (most notably Galileo Galilei), influenced by the ideas of Copernicus, started to do observations and spread ideas about this heliocentric world view. This led to an increasing amount of people asking critical questions about the teachings of the established cosmologies [Lev11].

The Copernican principle—the realisation that the physical laws on Earth are not special—opened up for the possibility to apply the laws of nature on objects on the celestial sky. Newton’s law of universal gravitation, which opened up for discoveries by among others Einstein, allowed scientists to build testable and increasingly precise models to understand the observed phenomena of the night sky.

1.3 Modern Concordance Cosmology

The *concordance model of cosmology* is the currently accepted model for the physics governing the evolution of the Universe. The common name for the

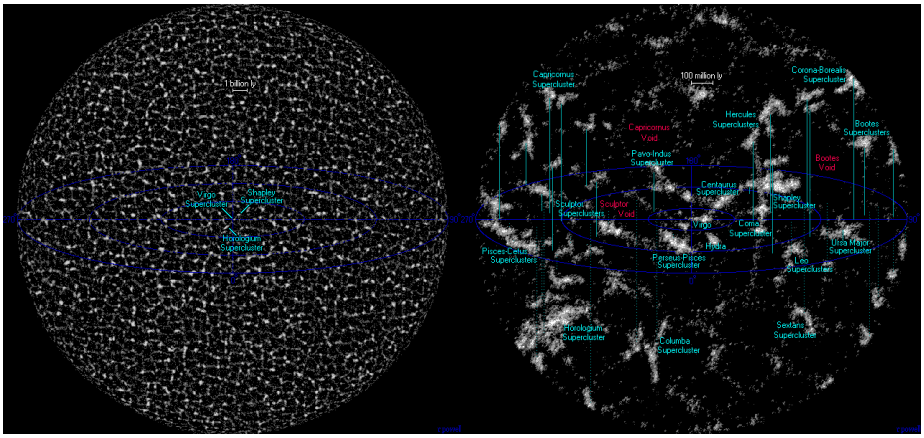

Figure 1.1: Large scale homogeneity of the observable universe. The left map shows an artist's impression of the distribution of galaxies on the scales of the observable universe, several gigaparsecs across. The right map is zoomed in to show the nearby super-clusters of galaxies within 300 megaparsecs (1 billion light-years). Each white dot represents a single galaxy.
Figures belong to Richard Powell, licensed under a Creative Commons Attribution-ShareAlike 2.5 Licence. They can be found online at http://www.atlasoftheuniverse.com/universe.html

concordance model of today is ΛCDM[1]. Theories that go beyond the concordance model can include modifications to gravity, exotic models for dark matter, modifications to the Standard Model of particle physics, different neutrino masses, and even new details in the implementation of known physics on galaxy scales. In this section, I will describe the origin and reasoning behind dark matter and dark energy, as well as explaining briefly how cosmologists work to refine the cosmological model.

At the base of the physical cosmology of today lies an extension of the Copernican principle, namely the cosmological principle: Our location in space is not considered special, and when viewed at large enough scales, the Universe is homogeneous and isotropic. In other words, the properties of the Universe are smooth and do not depend on direction; If we draw a large enough sphere somewhere in space, it should contain approximately the same amount and distribution of matter and energy as if you draw it at another point in space. The left panel of figure 1.1 shows a distribution of galaxies similar to the distribution in the observable universe. The left-hand side resembles the largest known scales of the Universe, where galaxies are relatively smoothly distributed. Surveys mapping out the large scale structure of the local universe support such homogeneity at scales larger than about 100 Mpc [Nte+17].

[1] "Lambda-CDM"

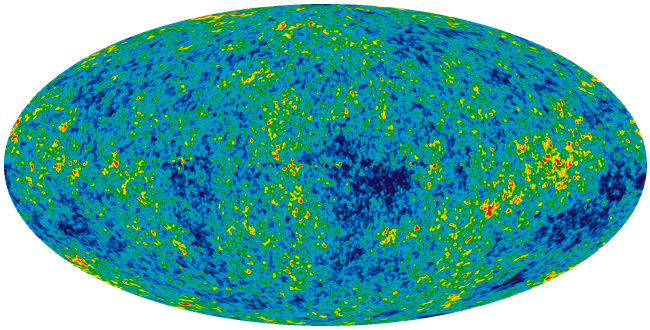

Figure 1.2: Temperature fluctuations of the CMB sky, after subtracting the dipole (which is due to the motion with respect to the CMB rest frame). The CMB sky has a mean value of 2.7 K, and the colors represent temperature fluctuations in the range of $\pm 200\,\mu$K.
Image credit: NASA/WMAP Science Team. Image is freely available online at https://map.gsfc.nasa.gov/media/121238/index.html

Another important part of the foundation of modern cosmology is the theory of *general relativity* (GR). Gravitational interactions and the dynamics of space-time itself can be described in the framework of GR. The geometry of space-time is affected by matter and energy content of the Universe, while the resulting curvature of space-time gives rise to what is perceived as a gravitational force. GR can also be used to calculate the expansion of space, the overall evolution of space-time itself.

In the 1920s, just a few years after Einstein introduced general relativity, Edwin Hubble discovered that distant galaxies seem to have a velocity directed radially out from us. The velocities of the receding galaxies increases with distance, which is widely believed to be due to a cosmic expansion of space. A universe dominated by matter is allowed to expand at any given point in time, but will expand slower and slower, and may collapse in the future[2]. In the late 1990s, two separate groups discovered evidence that the Universe expands at an accelerated rate [Pa99; Ra98]. No known form of matter or energy could explain an accelerated expansion, which prompted the introduction of the concept of *dark energy*. One way to model this dark energy is with a constant vacuum energy of empty space, represented with a cosmological constant Λ in Einstein's equations. Such a cosmological constant supplies a negative pressure, sufficient to drive an accelerated expansion.

Dark matter is a proposed matter component which only interacts through gravity. With the law for gravity described by GR, we need five to ten times more matter inside of any given galaxy than the sum of all visible matter in

[2] A future collapse would happen if the global topology of the Universe was closed, i.e. like the surface of a sphere. I do not consider curvature in this thesis because the current Universe is measured to be topologically flat within the errors of the measurements [Pla+18].

that galaxy. Without this dark matter, the stars rotating around the disc of the galaxy would not be bound to the galaxy gravitationally; Their measured velocities are so large that most of the stars would be expected to fly away and escape their host galaxy. It turns out that the observed orbital velocities can be described if we assume the existence of a diffuse dark matter halo in addition to the normal, or *baryonic*, matter. The case is similar when considering individual galaxies in a galaxy cluster; The velocity dispersion of the galaxies is so high that without several times extra matter in the cluster, the galaxies would not stay clustered together.

In modern cosmology, charting the evolution of the Universe is often done by applying physics in reverse. Cosmologists apply the known laws of nature on the observed universe, but backwards in time, to infer how it was at an earlier point. An example of this is the currently observed expansion of the Universe. If we reverse the observed expansion, we can infer that the content of the Universe was hotter and denser in the past. If we go 13.8 billion years back [Pla+18], the Universe should be infinitely hot and dense, a singularity commonly known as the Big Bang. During the first couple of thousand years of the Universe, it was too hot to form any kinds of normal matter, all the contents of the Universe was in the form of hot plasma. As the Universe expanded, the energy was spread over a larger volume and hence the average temperature decreased. This continuous expansion and cooling is still ongoing today.

The finite speed of light implies that observing photons that originated far away from us also means observing far into the past. The oldest light reliably measured are photons from the *cosmic microwave background radiation* (CMB), commonly shown as a map of temperature fluctuations as seen in figure 1.2. CMB photons originate from the time of last scattering, when the hot plasma-filled Universe became cold enough to be transparent, about 380 thousand years after the Big Bang. The temperature map (after subtracting the Doppler shift dipole) has an average of about 2.7 K and inhomogeneities smaller than a factor of 10^{-4}. The temperature fluctuations are related to the matter fluctuations at the time of last scattering, supporting the claim that the universe was highly homogeneous at this time. We can use known theories to infer physically what happened even further back in time than the time of last scattering, but our predictions break down at the Planck epoch, about 10^{-43} seconds after the Big Bang. This is because there does not exist an accepted theory for quantum gravity, which is needed to describe the behaviour of the Universe at the densities and temperatures in the Planck epoch [Pen91].

When considering cosmological scales, the movement of matter is mainly affected only by gravity. The reason why other forces can be neglected is that they have an extremely short range compared to gravity. Gravity does not have any charge, and to our knowledge, there does not exist negative mass. This means that gravity is always attractive between two massive objects, and the strength of gravity increases when the masses grow. On the other hand, it is very difficult to increase any of the other forces of nature beyond a certain point,

since the physical structures that are needed would grow increasingly unstable[3]. The gas component of galaxies and galaxy clusters have a close to neutral electric charge on average, and the main component of these structures is dark matter, which does not interact with electromagnetism. Even if electromagnetic forces can have an impact on the gas interaction within a single galaxy cluster or when two clusters collide [Kie+17], it will not measurably affect the formation of structures on cosmological scales, which is dominated by the dark matter. This claim is supported by the statistical similarity between the observed large scale structure and dark matter-only simulations [KVA12]. See also section 3.2 for a brief discussion of implementations that include baryon physics on considerably smaller scales than galaxy clusters, where electromagnetic effects cannot be ignored.

To reiterate: the observed properties of the Universe on large scales can be explained fairly well with only dark matter, dark energy, and the principles of GR. This phenomenological model has become known as ΛCDM, after the two main energy components: a cosmological constant Λ, and cold dark matter (CDM). Normal matter, which I will from now on call baryons, only constitutes about 5 % of the total energy-matter content of the Universe, but their contribution to the overall evolution of the Universe since the Big Bang is not negligible. The resulting concordance model, ΛCDM, has had great success in explaining the Universe on cosmological scales. In section 1.6 I will discuss issues with this model.

In parts of this thesis and the included papers, I might use the terms GR and ΛCDM interchangeably. Both of these terms will refer to the concordance model with standard gravity, as opposed to alternative theories for gravity. Throughout the thesis, I will not modify any of the other components of the concordance model, like baryons and dark matter.

1.4 Conventions

Throughout this thesis, I will use the conventions described in this section. I work in natural units of space and time, such that the speed of light is unity, $c = 1$. The metric signature used is $(-,+,+,+)$. I will mostly work in a Friedmann–Lemaître–Robertson–Walker (FLRW) metric, or a perturbed version of it, often called the *Newtonian gauge*. The line element in the Newtonian gauge is

$$\mathrm{d}s^2 = -(1+2\Psi)\,\mathrm{d}t^2 + a^2(t)\,(1-2\Phi)\,\mathrm{d}x^i\mathrm{d}x^i. \tag{1.1}$$

In the absence of anisotropic stress in GR, the two metric perturbations are equal, $\Psi = \Phi$. In the non-relativistic limit, the metric perturbation Ψ is equivalent to the Newtonian gravitational potential, and this is what I will call Ψ throughout this thesis.

[3]For instance, to increase electrostatic force, you would need an increasing amount of similar electric charge in a small volume. Similar electric charges repel each other, so beyond a given charge density the energy needed to add another charged particle would be enough to destroy the structure.

I employ the Einstein summation convention, where repeated indices in tensor equations are implicitly summed over all components. Latin indices are spatial and go from 1 to 3, while Greek indices are space-time and go from 0 to 3, 0 being the time component. Specifically $x^i y^i = x^1 y^1 + x^2 y^2 + x^3 y^3$, and furthermore $x^\mu y_\mu = x^0 y_0 + x^1 y_1 + x^2 y_2 + x^3 y_3$, where the raising or lowering of indices with the metric $g_{\mu,\nu}$ often introduces an opposite sign for the zeroth component with respect to the spatial components.

I use comma notation for partial derivatives, (i.e. $A_{,\phi} = \partial A / \partial \phi$ for the scalar ϕ). Comma notation with a greek index signifies partial derivatives with respect to the corresponding space-time coordinate, and can be combined with Einstein summation notation. A dot over a quantity means a partial derivative with respect to cosmic time t.

1.5 Modelling a Universe

In many branches of physics, an action is considered the most fundamental equation from which the dynamics of the system can be derived. When studying the interaction between matter and gravity, the starting point is the *Einstein–Hilbert action*, which is given by

$$S = \int \left[\frac{1}{16\pi G} (R - 2\Lambda) + \mathcal{L}_M \right] \sqrt{-g} \mathrm{d}^4 x. \tag{1.2}$$

Here, Λ is the cosmological constant, G is Newton's gravitational constant, g is the determinant of the metric ($g = \det(g_{\mu\nu})$), and R is the Ricci scalar, which describes the local curvature at each point in space-time. All matter fields are encoded in the total matter Lagrangian $\mathcal{L}_M$, which includes both dark matter $\mathcal{L}_{DM}$ and the standard model particles $\mathcal{L}_{SM}$.

With the technique of variation of action, the Einstein–Hilbert action yields the *Einstein field equations*,

$$R_{\mu\nu} - \frac{1}{2} g_{\mu\nu} R + \Lambda g_{\mu\nu} = 8\pi G T_{\mu\nu}, \tag{1.3}$$

where $R_{\mu\nu}$ is the Ricci curvature tensor and $T_{\mu\nu}$ is the stress–energy tensor. Equation (1.3) is a tensor equation with 10 independent components, together constituting the Einstein field equations. These equations fully describe the gravitational interaction; The left-hand side can be interpreted as the geometry of space-time, and the right-hand side can be interpreted as the matter and energy contents of the Universe. Simply put, the equation says that matter tells space-time how to curve, and the curved space-time tells matter how to move.

1.5.1 Expansion History

The observable universe is considered to be very homogeneous on scales larger than about 100 Mpc [Nte+17], which is illustrated in the left map of figure 1.1. At the time of the CMB, the observable universe was highly homogeneous, with

perturbations smaller than a factor 10^{-4}, as seen in figure 1.2. When assuming perfect homogeneity—using only average quantities—one can solve the Einstein field equations analytically[4]. This yields the *Friedmann equations*, which can be used to calculate the expansion rate, as well as the relative densities of matter and dark energy. In a spatially flat universe ($k = 0$), the Friedmann equations are

$$\left(\frac{\dot{a}}{a}\right)^2 = \frac{8\pi G\rho + \Lambda}{3}, \tag{1.4}$$

$$\frac{\ddot{a}}{a} = -\frac{4\pi G}{3}(\rho + 3p) + \frac{\Lambda}{3}. \tag{1.5}$$

Where a is the scale factor. $\dot{a}$ is then the expansion rate of the Universe[5], and $\ddot{a}$ is the acceleration of the expansion. Here, p is the pressure and ρ is the density of the total matter and radiation content of the Universe. The equations can be expanded to include several components (hot gas, dark matter, radiation).

Notice that without the cosmological constant Λ, the acceleration of a flat universe can only be negative. Given that the content of the Cosmos has positive pressure and density, the expansion rate of an expanding universe will eventually slow down. Another thing to note is how the cosmological constant is equivalent to a fluid with negative pressure in equation (1.5). At late times, the pressure of matter and radiation can be considered negligible, but at early times, when the Universe was hotter and contained more radiation, the pressure p is important.

With the Friedmann equations (1.4) and (1.5), the past and future expansion history can be found, as well as the relative ratios of baryonic matter, dark matter, and dark energy. Inserting the right numbers for the total amount of matter and a cosmological constant, one gets an expansion history matching the current observations very closely. When playing around with the different possibilities for the components, one can have a universe ending in a Big Rip, Big Crunch, Big Void, and so on [NJP15].

1.5.2 Structure Formation

The Universe is not completely homogeneous. When studying scales smaller than a gigaparsec, structures called the *cosmic web* appear, as seen in the maps of figure 1.1. Through the study of simple models for spherical collapse, or through simulations (see chapter 3), one can predict properties of these structures from first principles and a set of simplifying assumptions. A simple, yet powerful technique to calculate the growth of structures on large scales is *linear perturbation theory*. This technique is not part of my doctoral work, but it

[4] Averaging and then evolving is not equivalent to evolving and then averaging, due to the nonlinear nature of the Einstein field equations. This backreaction effect is often considered small, but scientists disagree if it is completely negligible [Buc+15]. Nevertheless, evolving the averaged Universe is a useful exercise for developing an intuition for cosmology.

[5] The expansion rate is related to the Hubble factor such that $H = \dot{a}/a$.

is nevertheless useful for understanding structure growth, hence I briefly describe the approach in Appendix C.

From precise measurements of the CMB, one can infer the tiny fluctuations of the matter/energy density over 13 billion years ago. The Universe was not completely homogeneous at this point, and it is believed that these minuscule inhomogeneities were sourced by quantum fluctuations that froze into real structures during the period of inflation [Rio02]. When these fluctuations manifested, over-densities of dark matter started to grow and form gravitational wells, long before the Universe became transparent. After the time of last scattering, when the Universe became transparent to photons and the CMB was released, baryonic matter was allowed to fall into the gravitational wells set up by dark matter. Matter continued to cluster due to gravity while the Universe expanded, and the large scale collapse is still happening today. This results in an increasingly complex fractal-like structure called the cosmic web. The cosmic web can be seen when looking closely at the seemingly homogeneous large scale galaxy distribution of figure 1.1, and also appears very clearly in N-body simulations of the Universe on large scales.

1.5.3 Parameter Prediction from CMB

By assuming the ΛCDM concordance model, combined with numerical methods to evolve the background expansion and linear structure formation, it is possible to infer statistical properties of the CMB temperature map. Cosmologists that study the CMB use Monte Carlo Markov chain methods to sample the parameter space of the ΛCDM model, and by comparing the observed CMB sky with the simulated CMB from linear perturbation theory, they are able to find the best-fit parameters of the ΛCDM model. It is also possible to combine the constraints from the CMB temperature map with other data sources, resulting in even stricter constraints.

Under the assumption of a ΛCDM cosmology, the Planck collaboration has inferred the cosmological parameters given in table 1.1, from CMB TT,TE,EE+lowE+lensing [Pla+18]. I will use these parameters throughout this thesis unless stated otherwise. This is not a full list of independent model parameters used in their fitting process, but rather derived quantities that are useful for modelling and simulations.

1.6 Open Questions

Even if the concordance model works remarkably well for many purposes, there are still many questions left unanswered if we accept it as it is today. In this section, I will discuss several of these questions, and argue why each of them is considered a potential problem in the framework of ΛCDM.

Table 1.1: Selected Cosmological Parameters, from Planck 2018 (TT,TE,EE+lowE+lensing) [Pla+18]

Parameter	Value	Notes
H_0	67.39 ± 0.54 km/s/Mpc	Expansion rate of the Universe today.
Ω_Λ	0.6897 ± 0.0074	Fraction of dark energy density.
Ω_m	0.3142 ± 0.0074	Fraction of total matter density, the sum of dark and baryonic.
σ_8	0.8110 ± 0.0089	Amplitude of mass fluctuations of the scale of $8\,\mathrm{Mpc}/h$.
n_s	0.9638 ± 0.0058	Spectral index. The tilt of the primordial power spectrum. $n_s < 1$ suggests more fluctuations on large scales than on small scales.
z_{re}	$7.49^{+0.83}_{-0.75}$	The redshift of re-ionisation, the time when the first stars/galaxies ionised neutral hydrogen.

1.6.1 Quantum Gravity

Quantum gravity is an effort to merge the macroscopic theory of general relativity with the microscopic theory of quantum mechanics. The naive method to create a model for quantum gravity, is to apply the same prescription as when quantising the other fundamental forces. However, this does not give a healthy theory, because GR is not renormalisable (see e.g. [Sho07]). It seems that there is an incompatibility between GR and quantum mechanics that cannot be resolved within the current framework. Quantum gravity is needed to have a precise model that describes the force of gravity on systems where quantum effects are important, like inside of black holes and during the first fraction of a second after the Big Bang [Pen91]. Another reason for developing a working theory for quantum gravity is because this can allow us to unify all the fundamental forces into one framework, referred to as the *theory of everything*.

1.6.2 The Fine-Tuning Problem and the Cosmological Constant Problem

The inferred value of Λ from cosmological data has a very specific value, $\Lambda = 1.1056 \times 10^{-52}\,\mathrm{m}^{-2}$, which is derived from the value of $\rho_\Lambda = \Omega_\Lambda \rho_c$ found by the Planck collaboration [Pla+18]. The conversion can be found in the 00-component of Einstein's field equations (1.3), where the cosmological constant Λ on the left-hand side is equivalent to a term $8\pi G\rho_\Lambda$ on the right-hand side. Although Λ is allowed in Einstein's field equations, there is no known mechanism for giving it this specific value. Nothing is preventing Λ from being an independent

constant of nature, but philosophically it would be more tractable if the value appears naturally from a more fundamental mechanism.

The expected vacuum energy scale from particle physics varies depending on the assumptions and your chosen cutoff scale. An illustrative example is the Higgs condensate, which is expected to contribute with a vacuum energy density of $\rho_{\text{vac}} \sim -(250\,\text{GeV})^4$, resulting in $\Lambda = -1.7 \times 10^4\,\text{m}^{-2}$ [Bas15]. Compared to this, the measured dark energy scale of Λ is minuscule (and also has the opposite sign). A cancellation of this many orders of magnitude, which still leaves the measured value, is a fine-tuning which is difficult to explain without physics beyond GR or beyond the Standard Model of particle physics. Furthermore, the cosmological constant problem is not necessarily that the observed value is not equal to the predicted value, but rather that we run into radiative instabilities (the repeated need for fine-tuning) when trying to normalise the value of the vacuum energy [Pad15].

1.6.3 Coincidence Problem

The coincidence problem comes from questioning why we live in a time where the amount of dark matter and dark energy is of the same order of magnitude. The concordance model, and many alternative models have the unlikely coincidence that these two energy densities are very similar at the current time, even if the energy scales of these two components are vastly different. If we were to check the energy densities 10 billion years ago or 10 billion years in the future, the values would not coincide. The probability of this coincidence in itself is hard to gauge, but it is still worth looking into, because an alternative model that answers this problem could be considered a more natural choice than one that does not [AT10].

1.6.4 Small Scale Problems

When performing pure ΛCDM simulations, without including baryonic matter, the behaviour and structure of the Universe on galaxy scales does not match current measurements of galaxies. For instance, dark matter haloes in simulations are significantly more dense (cuspy) in the centre than what can be inferred from observations. With advances in the implementations of baryonic physics during the last decade or so, it is believed that baryons can, at least partially, solve the small scale problems. This is still an area of debate, and many alternative theories for dark matter are still motivated by attempts to solve the small scale problems [DL17].

1.6.5 Inflation

The period of *inflation* is a rapid expansion proposed to have happened shortly after the Big Bang. Inflation lasted approximately 10^{-33} seconds, and during this period the Universe is thought to have expanded by a factor of 10^{26}. The inflation paradigm explains many puzzling things about the Universe, for instance

why very distant areas of the Universe seem to have been in thermal contact at the time of recombination. Inflation also helps explain the set-up of the initial conditions needed in ΛCDM to evolve into the Universe we see today [Rio02]. There are no measured physical mechanisms that can give rise to inflation. Usually a theoretic *inflaton field* is suggested, but no traces of this field have been observed to this date.

1.6.6 Asymmetry Between Matter and Anti-Matter

The observable universe contains almost exclusively matter, and very little anti-matter. The current model of particle physics allows pairs of particles and anti-particles to emerge from vacuum fluctuations. No known process explains why there are not equal amounts of matter and anti-matter in the observable universe. In the current framework, we need a process occurring out of equilibrium, and breaking many known symmetries of the standard model of particle physics. Such a process has not been observed. An alternative framework, specifically beyond the standard model of particle physics, could introduce mechanisms to explain this asymmetry. An example of a framework that is claimed to allow such mechanisms is loop quantum gravity [LS03].

1.6.7 The Hubble Tension

One way to measure the expansion rate of the Universe (or the local Hubble parameter H_0), is to map the velocities of objects with a known distance, among others type Ia supernovae [Rie+16]. This data set can be used to estimate the amount of expansion at a given distance, but is usually limited by low redshifts of the objects, as well as possible systematics in deriving the distances to the measured objects. Another way to infer the expansion rate is to use the mathematical framework of the concordance model, and tune the model parameters to match the observed CMB [Pla+18]. The recovered expansion rate from the best fit ΛCDM parameters is significantly lower than the value measured with supernovae, with $H_0 = 68 \pm 1\,\mathrm{km/s/Mpc}$ and $H_0 = 73 \pm 2\,\mathrm{km/s/Mpc}$ respectively [Fre17]. The difference can be due to systematic errors in the measurements of either the supernovae or the CMB, but if it turns out that this tension is real, it is a strong suggestion of new physics; Either the assumptions behind the supernova calculations are wrong, or the concordance model must be updated.

1.6.8 The Nature of Dark Energy and Dark Matter

For me personally, the most convincing argument to study alternatives to ΛCDM is a more philosophical one. Although the two main components of the model—dark energy and cold dark matter—help explain observations nicely, they have never been directly detected. All the evidence for these components that were mentioned in section 1.3 is indirect evidence, and many of the effects can individually be described without Λ or CDM.

Even if the dark components of the Universe exist, the question about their nature remains. Dark energy can be due to a cosmological constant, the vacuum energy of quantum foam, a hitherto unknown field rolling down a potential, or a modification of gravity. Suggested candidates for dark matter include particles, either weakly interacting massive particles or tiny non-interacting particles that we will never measure directly. Another suggestion to explain dark matter is through primordial black holes spread evenly around the Cosmos [Gar17].

1.6.9 The Fate of the Universe

Dark energy described with a cosmological constant is believed to result in an accelerated expansion which continues until the heat death of the Universe, where entropy approaches an asymptotic limit and any remaining physical processes will occur increasingly slowly. During the expansion, galaxies themselves will not expand, but distant groups of galaxies will expand out of each others causal horizon. Stars will eventually die, and matter will gather into black holes, which after a very long time will evaporate through Hawking radiation [Fra82].

If dark energy and gravity is described better with another model, the prediction will be different. Although the inevitable heat death of the Universe is not a problem with the ΛCDM model itself, a better understanding of the nature of gravity and dark energy can help us model and understand the ultimate fate of the Universe.

Chapter 2

Modified Gravity

Modified gravity is one of the proposed solutions to the shortcomings of ΛCDM that I discussed in section 1.6. A modification to gravity is any model that extends or challenges the current theory of how gravitation works. Ideally, such modifications to gravity should still be able to explain observed phenomena at least as well as the currently accepted theory. Such modifications have been suggested several times throughout history, both as gradual extensions to the accepted theory, or as a complete paradigm shift in the way to think about gravity. In this chapter, I will present a short history of gravitational theory, before discussing modern modifications to gravity, including the disformal model. Towards the end of the chapter, I will shift my focus to possible methods of probing the nature of gravity, which can be used for distinguishing between different gravitational theories.

2.1 History of Gravity

In ancient Greece the Aristotelian view of gravity was that massive bodies would move towards the "centre of the Universe", while the Ether (heavens) moves circularly around the centre. Aristotle concluded that a heavy object falls faster than a light object [Rov13]. During the 17th century, Galileo discovered that all objects accelerate equally when falling in a vacuum. This indicated that Aristotle's laws of motion were just approximations to a "deeper theory". The Aristotelian laws are good approximations to gravity in combination with the effect of air resistance, given that the object reaches its terminal velocity.

On the surface of the Earth, the gravitational acceleration seems uniform as a function of the vertical direction, unless measured with extreme precision. Upon further investigation, the force of gravity is weaker with increased distance from the source. For instance, considering the Huascarán region in Peru, the gravitational acceleration is $9.764\,\mathrm{m/s^2}$ at altitudes of 7 km above sea level and $9.775\,\mathrm{m/s^2}$ in a nearby valley at 1 km above sea level, a difference of 0.1 % [Hir+13]. It was discovered that the force of gravity seemed to decrease according to an inverse square law, $F \propto 1/r^2$. Robert Hooke and Isaac Newton extended this theory to other objects in the Solar System, resulting in a theory for universal gravity. This theory is commonly called *Newtonian gravity*.

The Newtonian model for gravity was successful in predicting the position of the (then unknown) planet Neptune from the irregular motion of Uranus. Neptune was discovered at the predicted position in 1846 [Ada46]. Mercury has a perihelion precession[1] which at that time was not explainable by gravitational

[1] In Newtonian gravity, a planet orbiting a star is expected to follow an elliptic orbit, where the axes of the ellipse do not move. The perihelion is the point of the ellipse closest to the

effects from the known planets, tidal forces, or other known physics. An extra planet (Vulcan) was proposed to explain it, but never found.

Einstein introduced his special and general theories of Relativity, which allowed the speed of light in vacuum to be universally constant and independent of frame. The theory of *general relativity* (GR) introduces an equivalence between acceleration and gravitation, where motions of objects can be explained through the curvature of space-time around massive bodies. GR gives different predictions compared to Newtonian gravity in some regimes (e.g. close to massive bodies). The theory of GR is a very successful one; it neatly reduces to Newtonian gravity in environments where Newtonian gravity gives correct answers, like what we encounter on Earth and in most of our Solar System. With GR corrections, Mercury's precession is explained well without the need of an additional planet.

Contrary to in the Newtonian model, light waves in GR are expected to follow the warped space-time and hence curve around massive bodies[2]. Einstein's prediction of this effect was confirmed exactly 100 years ago this year, through observing how the path of light from stars was bent when passing close to the Sun during a solar eclipse [Ken19].

The physics of gravity saw a paradigm shift 330 years ago with Newtonian gravity, and another paradigm shift 100 years ago with the introduction of GR. When will we see the next paradigm shift in our knowledge of gravity? Modifications to GR appeared shortly after Einstein published his theory, but these were mostly considered curiosities. Some important names associated to the ground-breaking work that paved the road for modern modified gravity are Eddington, Weyl, and the collaborative works of Kaluza–Klein and Brans–Dicke. See [Cli+12] for details on further theories, including the theories I will mention later in this chapter.

2.2 Why Modify Gravity?

The short answer to why we want to look for alternative theories is that the theory we currently have is not completely perfect. In section 1.6 I showed several problems with the concordance model, and in this section I briefly explain how some of these problems can be solved by modifying gravity.

The next step in achieving a grand unified theory in quantum physics is quantum gravity, but because GR is not renormalisable, we need to go beyond GR to achieve this. Different theories have been proposed that are expected to be renormalisable, for instance Hořava–Lifshitz gravity [Ho 09]. Due to the difficulties in testing these theories and distinguishing them from GR, there is still no accepted conclusion.

Modifications to gravity have been proposed to solve the coincidence problem and the fine-tuning problem. A dark energy component which is coupled to the

Sun, and perihelion precession refers to the movement of this axis.

[2]If assuming that light is a particle, and applying the universality of free fall, Newtonian gravity also predicts a deflection of light around massive bodies, but only half of the value seen in GR.

density of matter can exhibit a *tracking behaviour*, where the energy density of dark energy converges to a value similar to the energy density of matter. This happens even if the initial value of the dark energy is not fine-tuned [AT10].

Even if GR has been successful in predicting a wide range of observations, we still have the metaphysical problems with the concordance model; it predicts known observations well, but the nature of the dark matter and dark energy are unknown, and the specific value of Λ seems arbitrary. I think that many scientists will have a problem with accepting "this is just how it is" as an answer to the question "but why?".

There are myriads models of modified gravity, all with their pros and cons [AT10; Bra12; Cli+12]. The consensus is that none of the current known models answer all of the problems with the concordance model. Furthermore, in the cases when the modification to gravity replaces the cosmological constant, we still need a mechanism or symmetry to prevent vacuum energy to be as large as the predicted value from particle physics.

Even if a specific model studied is not realistic, understanding the specific phenomena that arise in a model opens up for new ideas, new probes, and unknown phenomenology. Mapping out these could be part of the bigger puzzle in order to find a good model in the future.

2.3 How to Modify Gravity

As already mentioned, there are many theories of modified gravity [Cli+12; Joy+15]. We can introduce extra degrees of freedom through additional scalar fields, vector fields, tensor fields, or any combination of those. Furthermore, other phenomenological models arise from extra dimensions and braneworlds, Lorentz violation, and a non-zero graviton mass. My work mostly focuses on adding a single scalar field coupled to matter. However, I will introduce a modification to gravity called $f(R)$ first.

Any viable theory must reduce to something indistinguishable from GR on Solar System scales, and mimic the phenomenology of ΛCDM on the largest scales. Intermediate scales around a few Mpc have more freedom because we do not have as high precision in our current measurements. If the modification to gravity is approximately the strength of gravity, we need what is called a *screening mechanism* to recover GR in our Solar System. I will introduce the theory for screening mechanisms in section 2.5.

An active field of research is new probes that can distinguish the theoretical models from each other and from GR. I will mention some of these and explain how they can be used to distinguish different theories in section 2.7.

2.3.1 $f(R)$-gravity

In the Einstein–Hilbert action, we can allow the Ricci scalar R to become a function of R. $R \to f(R)$.

$$S = \int \left[\frac{1}{16\pi G} f\left(R\right) + \mathcal{L}_M \right] \sqrt{-g} \mathrm{d}^4 x. \tag{2.1}$$

Einstein tried $f(R) = R$, which is the simplest combination of the Ricci scalar that gives equations of motion which recover Newtonian gravity in the weak-field regime, what we experience on Earth. There is freedom to construct the function $f(R)$ with additional terms and still recover both GR and Newton predictions in the Solar System. The extra freedom allows parts of the function $f(R)$ to mimic a cosmological constant in the Einstein–Hilbert action at late times. The ideas of $f(R)$ have also been successfully applied in some theories for inflation, most notably the Starobinsky model [Sta80].

Variation of the action (2.1) yields an equation of motion for $\psi_{\mathrm{f(R)}} \equiv \partial f / \partial R$. The so-called scalaron $\psi_{\mathrm{f(R)}}$ acts as a propagating scalar degree of freedom, which indicates that there is a mapping between $f(R)$ and scalar–tensor theories [Afo+19]. This means that through studying theories with a scalar field we can also study and understand the corresponding $f(R)$ theories.

2.3.2 Scalar Fields

I will now consider *scalar–tensor* theories, where gravity is described by a combination of the usual GR tensor and an additional scalar. This is a common way to modify gravity, and can range from simple to very complicated, depending on the mathematical form of the couplings of the field. The rest of this thesis considers scalar–tensor theories.

In single field scalar–tensor models, there is one extra propagating degree of freedom, also known as a scalar field, which is denoted ϕ. The potential energy of the field $V(\phi)$ can act as dark energy; Specifically, the field can supply a negative pressure similar to a cosmological constant in the slow roll limit, where the potential dominates the energy of the field, $V(\phi) \gg \dot{\phi}^2$.

A free (uncoupled) scalar field, which can give rise to dark energy when rolling along a potential, is called *quintessence*[3]. The first study of a rolling scalar field in the cosmological context is given in [RP88], and later (but before the discovery of dark energy) by among others [FJ97]. The potential can always be fixed to mimic ΛCDM within observational limits. Unless we observe a significantly varying equation of state—which there is no evidence for at this point—this model is indistinguishable from ΛCDM and can not be considered a better choice [AT10]. If the field does not couple to any other component of the universe, there is no way to interact with it or detect it. Even if quintessence is not directly ruled out, ΛCDM is preferred because it contains fewer degrees of

[3]Strictly speaking, the uncoupled quintessence is not a modification to gravity, and usually not considered a scalar–tensor model, because it does not change the gravitational interactions.

freedom. This philosophy is similar to the principle of Occam's Razor; if two descriptions work equally well, we choose the simplest one (in this case, the cosmological constant).

In scalar–tensor models, the scalar field is in some way coupled to other components of the universe. I will mainly consider scalar field couplings to non-relativistic matter, even though couplings to other species, like neutrinos, are also possible [Bro+06]. The coupling between the matter component and the scalar field is a two-way coupling. This means that the evolution of matter is affected through a scalar field *fifth force*, and that the evolution of the scalar field is influenced by the local matter density. Instead of a uniform roll, as expected from uncoupled quintessence, the field now has perturbations that to some extent correlate with the matter distribution.

2.3.3 Horndeski Lagrangian, and the Choice of Frame

The *Horndeski Lagrangian* [Hor74] is believed to be the most general structure a scalar–tensor theory can have which allows second-order equations of motion without introducing *Ostrogradsky instabilities*, or unphysical states called ghosts. I will not state the general Horndeski Lagrangian here as it is beyond the scope of this thesis. Theories beyond Horndeski are also possible by allowing higher-order equations of motion, which will not always lead to instabilities [Gle+15].

The *Einstein frame* has gravity described by Einstein space-time with an additional fifth force. The *Jordan frame* has all motions explained by the curvature of space-time without a fifth force, but the curvature is affected in a modified way. Generally, the physics described in the Einstein and Jordan frames are thought to be equivalent; The resulting measurable quantities are independent of the frame chosen when doing the calculations (in section 2.6.2 I discuss this further for the disformal case). Throughout this thesis, I will use the Einstein frame, where the scalar field adds a fifth force in addition to GR.

2.4 Equation of Motion and the Fifth Force

In this section I will give a more technical description of scalar–tensor theories, mentioned in the previous sections. In these theories, the modified Einstein–Hilbert action can be written

$$S = \int \sqrt{-g}\left[\frac{R}{16\pi G} + \mathcal{L}_\phi\right] + \sqrt{-\tilde{g}}\tilde{\mathcal{L}}_M \mathrm{d}^4x, \tag{2.2}$$

where $\mathcal{L}_\phi$ is the Lagrangian of the scalar field. For the case of a *canonical* scalar field, the Lagrangian is given by the difference in kinetic and potential energy, $\mathcal{L}_\phi = X - V(\phi)$, where the kinetic energy is given by $X \equiv -\frac{1}{2}\phi^{,\mu}\phi_{,\mu}$. Here we can see how a small kinetic term and an approximately constant potential with value $V(\phi) \approx \Lambda/(8\pi G)$ can mimic the cosmological constant in (1.2).

The modification to gravity is introduced through a transformation of the metric in the matter section (the last term of equation 2.2), which results in

matter following modified geodesics. The modified gravity metric $\tilde{g}$ is related to the gravitational metric g through a transformation. A typical *conformal* transformation is given by

$$\tilde{g}_{\mu\nu} = A(\phi)\, g_{\mu\nu}. \tag{2.3}$$

The scalar function A in conformal transformations rescale the metric in all space-time dimensions with the same factor.

Variation of the action (2.2) with respect to the metric—just like in the GR case—yields a modified set of Einstein's field equations, which can be used to calculate the modified geodesic equations. The difference between the modified geodesics and the GR geodesics defines the extra fifth force, which a test particle is subjected to in addition to GR gravity. For conformal theories, the fifth force is expected to be proportional to the gradient of the scalar field, specifically

$$\mathbf{F}_\phi \propto -\frac{A_{,\phi}}{A}\nabla\phi. \tag{2.4}$$

For more detailed mathematical descriptions of the variation of the action in scalar–tensor theories, see for instance [Wat06; ZKM13]. A simple conformal theory defined by $A = 1 + a_1\phi$ (where a_1 is a constant model parameter) has a fifth force on the form $\mathbf{F}_\phi \propto -\nabla\phi$ when assuming $a_1\phi \ll 1$.

A point worth noting here is that when applying scalar–tensor theories to explain dark energy, it is not the intention that the fifth force should be responsible for the accelerated cosmic expansion. For a canonical scalar field, the potential energy V is typically the source of dark energy in the Einstein–Hilbert action (2.2). However, the fifth forces can in some case mimic the extra force commonly associated with dark matter [Bur+19].

Varying the action with respect to ϕ gives the scalar field *equation of motion* (EOM), also called the Klein–Gordon equation, which can be used to calculate the behaviour of the scalar field. The conformal EOM in an expanding FLRW metric is given by

$$\ddot{\phi} + 3H\dot{\phi} - \frac{1}{a^2}\nabla^2\phi = -\frac{\partial V_{\text{eff}}}{\partial\phi}, \tag{2.5}$$

where the *effective potential*, V_{eff}, typically is a function of the scalar field ϕ and the local matter density ρ. V_{eff} can also include the gravitational potential Ψ and derivatives of both ϕ and Ψ.

For all scalar–tensor theories, the EOM (2.5) is a wave equation with an additional—and often non-trivial—source term. The field stretches when it is perturbed, and restores towards the equilibrium value as waves spread out from the source of the perturbation, similar to ripples on the surface of water. Compared to gravitational waves in the tensor sector, which can only arise from quadrupole perturbations, waves in the scalar can be monopole. This means that a spherically symmetric but pulsating mass distribution can generate scalar field waves. In section 3.5.3 and in Paper I, I study these waves in more detail.

Fifth forces arising from a scalar field are expected to be attractive. Results from field theory state that a scalar boson with a standard kinetic term mediates an attractive force, like the force of gravity. Paper II explores, among other

things, the possibility for a disformally coupled scalar field mediating a repulsive fifth force. A fifth force acting opposite of gravity, even for a short period of time, is not expected from a field with a canonical kinetic term in the Lagrangian. I will discuss the kinetic term of the disformal model in section 2.6.2.

2.5 Screening Mechanisms

A problem we encounter when trying to modify gravity by introducing a coupled scalar field is that the fifth force, which works in addition to GR, affects normal matter too much. We need to recover GR in systems where it has been tested rigorously, like on earth, in the Solar System, for pulsars timings, and for merging black holes that generate gravitational waves [Fer19]. This does mostly mean that we need to recover GR on small scales or in regions of high density (the average density in the Solar System is many orders of magnitude higher than the average of the known Universe). Modifications to gravity are allowed in low-density regions and at large scales. See section 2.7 for a description of some common tests of gravity.

We could hypothetically tune the coupling between the field and matter to be arbitrarily small, such that the modifications become negligible. However, this fine-tuning is not any better than the fine-tuning problem of ΛCDM. A preferred solution is a coupling of similar strength to gravity, but which is hidden through what is called a *screening mechanism*.

There are many available mechanisms that screen the fifth forces through different means (see e.g. [Bra12] for an introduction or [Joy+15] for a thorough review). Examples of screening mechanisms are the symmetry restoration in the symmetron model, the chameleon mechanism, k-mouflage, and Vainshtein screening. I will introduce them briefly here.

2.5.1 The Chameleon Model

The screening mechanism in the *chameleon model* relies on the field acquiring a deep effective potential in high densities [KW04]. Such a deep potential is equivalent to a very high effective mass for the field, which means that the fifth force becomes short range, and is effectively turned off.

For a $n = 1$ chameleon, the effective potential is given by

$$V_{\text{eff}} = \rho \left(1 + \frac{\beta}{M_{\text{Pl}}}\phi\right) + \frac{M^5}{\phi}, \tag{2.6}$$

where M and β are parameters of the model. M_{Pl} is the Planck mass. See figure 2.1 for a sketch of the shape of the effective potential in high and low densities. The slope of the potential becomes very steep in high-density environments, or close to a massive body. In low-density environments, however, the field is approximately free and allowed to mediate a long-range fifth force.

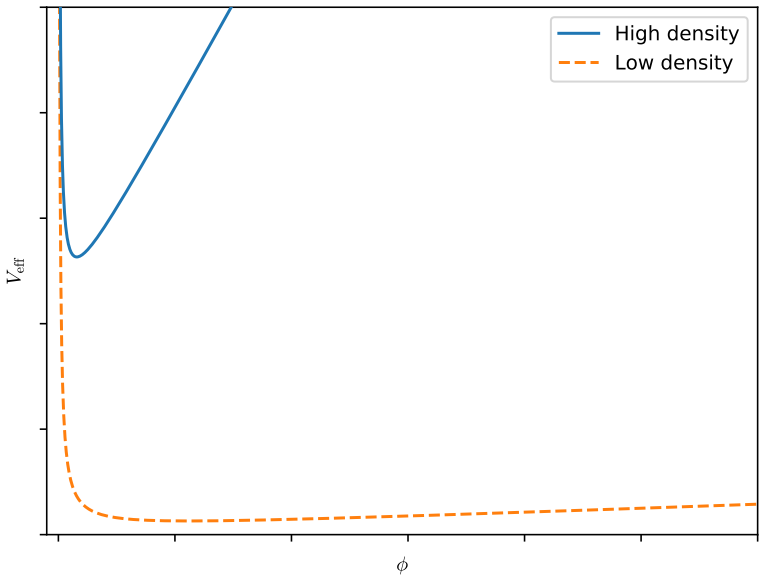

Figure 2.1: Sketch of the effective potential in the chameleon model. The two lines represent the effective potential in high densities (blue solid) and in low densities (orange dashed).

2.5.2 The Symmetron Model

The *symmetron model* also has an effective potential that changes shape in higher densities. Unlike the chameleon, the fifth force is not screened by increasing the effective mass. The symmetron screening relies on restoring a $\phi \to -\phi$ symmetry in high densities [HK10]. This symmetry restoration forces the expectation value of ϕ to be close to zero, effectively reducing the coupling of the field to zero.

In the case of the symmetron model, the effective potential is

$$V_{\text{eff}} = \frac{1}{2}\left(\frac{\rho}{M^2} - \mu^2\right)\phi^2 + \frac{1}{4}\lambda\phi^4, \tag{2.7}$$

where M, μ, and λ are (positive valued) parameters of the model. The effective potential is illustrated in figure 2.2. In high densities and in the early universe, the symmetron effective potential has a single minimum at $\phi = 0$. When the density goes down, there is a spontaneous symmetry breaking which results in the effective potential acquiring two non-zero minima. The coupling is defined through a conformal transformation of the metric, $\tilde{g}_{\mu\nu} = A(\phi)\, g_{\mu\nu}$, with $A(\phi) = 1 + (\phi/M)^2$. In high-density areas, $\phi \approx 0$, which in turn moves the value

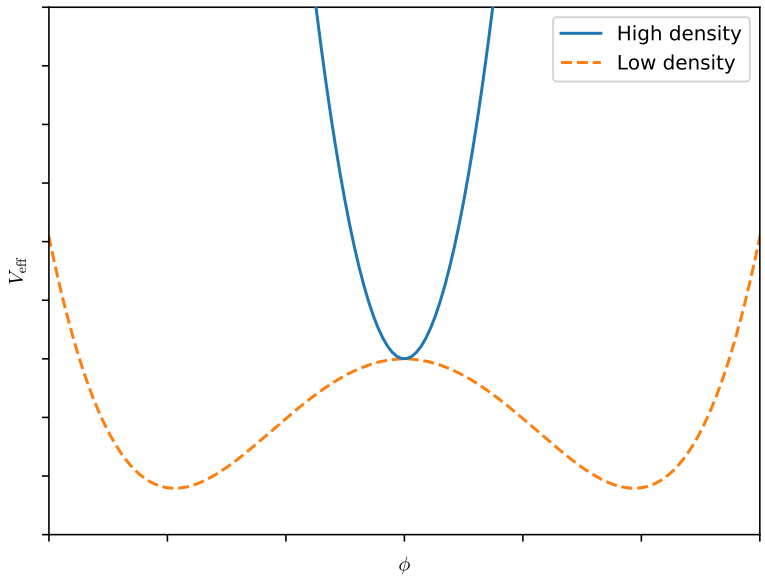

Figure 2.2: Sketch of the effective potential in the symmetron model. The two lines represent the effective potential in high densities (blue solid) and in low densities (orange dashed).

of the conformal factor A close to unity. This essentially hides the modifications to gravity by recovering $\tilde{g}_{\mu\nu} = g_{\mu\nu}$.

Special topological defects called *domain walls* can arise in the Symmetron model due to the two-minima shape of the effective potential. This happens after the spontaneous symmetry breaking if one region of space falls to one minimum, and another region falls to the other minimum. As the two regions with opposite sign for the scalar field grow to touch each other, the wall between them contains significant amounts of stored energy in the gradient of the scalar field. If the domain walls collapse, the gradient energy is released in the form of waves in the scalar field.

2.5.3 Screening Through Field Derivatives

In these theories, the Lagrangian includes derivatives of the scalar field. Common among these theories is that the fifth force is allowed to be of gravity strength far from a massive body, while it is suppressed at short distances from the massive body. The fifth force is proportional to the field gradient $F_\phi \propto \nabla\phi$, and the derivative terms suppress the field gradient in the proximity of a massive body.

The k-mouflage model includes first-order derivatives of the field, $\partial\phi$, in the Lagrangian. The fifth force in these first-order derivative theories reduces to zero (because the field gradient becomes small) when the gravitational acceleration increases near a massive body [BDZ09].

The *galileon model* includes higher-order derivatives, like $\partial^2\phi$, in the Lagrangian. The terms are tuned to avoid higher-order ghost instabilities in the equation of motion [NRT09]. This is an example of a theory with a *Vainshtein screening*. At long distances from a massive source, the non-linear derivative terms are negligible and the equation of motion is similar to a conformal scalar field. In this linear regime, the field is allowed to mediate a gravity strength force with a gradient approximately following $\partial\phi/\partial r \propto 1/r^2$. Within the Vainshtein radius, the non-linear derivative terms start dominating and the field perturbation is suppressed. Hence, the field profile achieves a weaker gradient, $\partial\phi/\partial r \propto 1/\sqrt{r}$. The weaker field slope means that as we approach the massive object, the strength of normal $1/r^2$ gravity will increase faster than the fifth forces, rendering the fifth forces negligible [BD13].

2.5.4 Coupling in the Dark Sector

A possible alternative to screening is a coupling in the *dark sector* only. In this paradigm, the extra degree of freedom—the scalar field—only couples to dark matter, and not to Standard Model particles [Bol+13]. In this way, photons and visible matter both follow the GR geodesics precisely. Other experiments we do in the Solar System or in a laboratory, which measure normal matter, will also give the same prediction as GR.

With a pure N-body simulation, we assume that all matter behaves like pressureless dust. In practice, such a simulation is a dark matter-only simulation—without baryons. Because we do not include baryons, we expect our density distribution to accurately represent a theory with a coupling only in the dark sector, at least on scales larger than galaxies. I will describe the technicalities of N-body simulations further in section 3.2.

2.6 The Disformal Model

Disformal couplings were introduced by Bekenstein in 1993, who was motivated by the idea of finding the most general physically allowed relation between the Einstein and Jordan frame metrics [Bek93]. In typical conformal theories without a disformal coupling, the stress–energy tensor is coupled to the scalar field in such a way that the density of matter directly influences the value of the scalar, and vice versa. In theories with a *disformal* coupling, the stress–energy tensor is coupled to the spatial and temporal derivatives of the field, which allows for more complex dynamics.

2.6.1 Equations

The relation between the two metrics in the Einstein–Hilbert action (2.2) is in the disformal case given by

$$\tilde{g}_{\mu\nu} = A(\phi)\, g_{\mu\nu} + B(\phi)\, \phi_{,\mu}\phi_{,\nu}. \tag{2.8}$$

Here we still allow a conformal coupling $A(\phi)$, as well as a new disformal coupling $B(\phi)$. In the most general case, both of these couplings can also depend on the kinetic energy of the field X, but I do not consider this case in my work. What I will call a *pure disformal* coupling is when $A = 1$. The conformal factor A cannot be zero because it is needed to recover GR (i.e. $\tilde{g}_{\mu\nu} = g_{\mu\nu}$). In Appendix A, I present the derivation of the equation of motion as well as the fifth forces in the pure disformal model.

The equation of motion for a pure disformally coupled scalar field, in an expanding FLRW metric is

$$\left(1+\gamma^2\rho\right)\ddot{\phi} + 3H\dot{\phi} - \frac{1}{a^2}\nabla^2\phi = -\gamma^2\rho\left(\frac{B_{,\phi}}{2B}\dot{\phi}^2\right) - V_{,\phi}, \tag{2.9}$$

where the comma subscript $_{,\phi}$ denotes a partial derivative with respect to ϕ, the combination γ^2 is given by

$$\gamma^2 \equiv \frac{B}{1-2BX}, \tag{2.10}$$

and the kinetic energy of the field is

$$X \equiv -\frac{1}{2}\phi^{,\mu}\phi_{,\mu}. \tag{2.11}$$

The acceleration due to the fifth force in the pure disformal case is

$$\mathbf{F}_\phi = -\frac{\left(B\ddot{\phi} + \frac{1}{2}B_{,\phi}\dot{\phi}^2\right)}{1-2BX}\nabla\phi, \tag{2.12}$$

which, in the low kinetic energy X and constant B limit, can be approximated as $\mathbf{F}_\phi \propto -\ddot{\phi}\nabla\phi$. In other words, the disformal fifth force is dominated by a term proportional to the acceleration of the field ($\ddot{\phi}$). In the conformal fifth force, given in equation (2.4), no time derivatives are possible[4].

2.6.2 Canonical or Not?

The disformal field Lagrangian in the Einstein-Hilbert action (2.2) only contains a canonical kinetic term, $\mathcal{L}_\phi = X - V(\phi)$, when written in the Einstein frame. However, the coupling in the matter sector is written in a way that hides several terms involving the derivatives of the field. When performing the transformation $\tilde{g}_{\mu\nu} = A(\phi)\, g_{\mu\nu} + B(\phi)\, \phi_{,\mu}\phi_{,\nu}$ in the matter sector of the Einstein-Hilbert action, higher-order terms and kinetic mixing terms can appear. Specifically, when

[4]When assuming that the conformal factor $A(\phi)$ is a function of ϕ only.

transforming this theory to the Jordan frame, the field Lagrangian does not have the canonical form [SV15]. For a more technical discussion on disformal transformations and the resulting kinetic term, see for instance [Tsu15]. There is currently no consensus on which (if any) of the two frames is the physical one, although they both are thought to describe the same physics. In the conformal case, the physics described by the Jordan and Einstein frames are equivalent [PV14], and in the disformal case, they seem to be equivalent as long as the time coordinate is chosen carefully [DNS15]. One special case where the frames do not necessarily describe the same physics, is when the disformal transformation is singular and hence not invertible [Dom+15]. Such (possibly unhealthy) theories based on singular disformal transformations are often dubbed mimetic gravity.

2.6.3 Expected Phenomena and Screening

The main disformal effects can be predicted intuitively from the EOM (equation 2.9), even with a constant disformal coupling B. After isolating the field acceleration on the left-hand side of the EOM, assuming that the kinetic energy X is small, and ignoring the term with the derivative of B, we find

$$\ddot{\phi} \approx \frac{1}{(1+B\rho)}\left[\frac{1}{a^2}\nabla^2\phi - 3H\dot{\phi} - V_{,\phi}\right]. \tag{2.13}$$

The biggest difference from the conformal equation of motion is the pre-factor $1/(1+B\rho)$, which effectively suppresses the field acceleration in areas with high density ρ. This means that the disformal field is frozen in the dense early universe, as well as in over-dense matter haloes. Another difference is that there are no explicit terms including the matter density ρ inside the bracket on the right-hand side, which in the conformal case gives density dependent effective potentials. The naive approach for calculating the field perturbations is to solve the quasi-static equation of motion (see section 3.5.1), which corresponds to neglecting the time derivative terms and solving the resulting Poisson's equation,

$$\nabla^2\phi = a^2 V_{,\phi}. \tag{2.14}$$

Because the bare potential does not depend on density or position, the naive solution to this equation is that the field value is uniform in space and at the bottom of the potential. We find in Paper II that this is not the case, and that the density dependent acceleration induced by the pre-factor $1/(1+B\rho)$ is responsible for field perturbations associated with over-dense regions. This behaviour will be discussed further in section 3.6.3.3.

The fifth force is proportional to the field acceleration $\ddot{\phi}$ (in addition to the field gradient $\nabla\phi$), as seen from equation (2.12). This indicates that in areas where the field is frozen, the fifth force is also suppressed. This gives rise to a disformal screening mechanism, which hides the pure disformal fifth force in the early universe and in the Solar System [KMZ12]. In mixed models, with both a conformal and disformal coupling, the disformal coupling contributes to screening the conformal fifth force in the early universe, because the field gradients will not evolve due to the suppressing factor $1/(1+B\rho)$.

If there is a spatial gradient in ϕ, the transformation $g \to \tilde{g}$ will stretch space more along the direction of the gradient. This means that the disformal model can generate anisotropies in the matter distribution if the large scale gradients of the field are significant.

2.7 Probes for Modified Gravity

In this section I describe some methods that have been proposed to distinguish gravitational theories from each other. A significant deviation from the predictions of the concordance model in any of these probes could challenge GR and imply new physics, like modified gravity.

2.7.1 Parametrized Post-Newtonian Formalism

The parametrized Post-Newtonian (PPN) framework aims to quantify possible gravitational effects beyond Newtonian gravity, including effects related to a preferred frame, a preferred location, and the possible violation of conservation of momentum. The full Will–Nordtvedt PPN formalism has 10 post-Newtonian parameters entering the line element. The two most common of these parameters in the context of testing gravity are $\gamma_{\rm PPN}$ and $\beta_{\rm PPN}$, also known as the Eddington–Robertson–Schiff parameters. Both of these are exactly 1 in GR [Wil06]. In a redshift-zero system with Newtonian potential Ψ, the line element when including the post-Newtonian $\gamma_{\rm PPN}$ and $\beta_{\rm PPN}$ is given by

$$\mathrm{d}s^2 = -\left(1 + 2\Psi + 2\beta_{\rm PPN}\Psi^2\right)\mathrm{d}t^2 + (t)\left(1 - 2\gamma_{\rm PPN}\Psi\right)\mathrm{d}x^i\mathrm{d}x^i. \tag{2.15}$$

The PPN parameter $\gamma_{\rm PPN}$ is interpreted as the amount of spatial curvature produced by a mass at rest. It can be written as the ratio of the lensing and gravitational potentials, $\gamma_{\rm PPN} = \Phi/\Psi$, when assuming $\Psi^2 \approx 0$. In GR it is expected that $\gamma_{\rm PPN} = 1$, while in theories of modified gravity, the deviation from 1 is closely related to the amplitude of the fifth force. Experimentally measuring the values of $|\gamma_{\rm PPN} - 1|$ and $|\beta_{\rm PPN} - 1|$ are ways of quantifying the difference between modified gravity and GR. The parameter $\gamma_{\rm PPN}$ can be measured through the gravitational time delay or the deflection of light, while $\beta_{\rm PPN}$ can for instance be measured through the perihelion shift of Mercury.

2.7.2 Solar System Tests

The Cassini probe is part of an experiment to determine the $\gamma_{\rm PPN}$ parameter with high accuracy by measuring the amount of delay and deflection of photons passing close to the Sun [BIT03]. I explain how this constraint applies to some conformal theories in section 2.7.2.1. The perihelion shift of Mercury can be used to constrain the $\beta_{\rm PPN}$ parameter, as described in [Sha90]. Lunar laser ranging also help constraining gravity by placing limits on the forces between the Earth and the Moon, as well as on Lorentz symmetry [Bou+17]. See [ZNZ19] for a study that combines the Cassini constraints with lunar laser ranging as well as

pulsar timing for constraining parameters of the Brans–Dicke and chameleon models.

2.7.2.1 Cassini Bounds on Conformal Theories

The Cassini radio link experiment achieved a one-σ constraint [BIT03]

$$|\gamma_{\mathrm{PPN}} - 1| \lesssim 10^{-5}. \tag{2.16}$$

Conformally coupled theories predict $|\gamma_{\mathrm{PPN}} - 1| \propto A(\phi) - 1$. The chameleon and symmetron models have conformal factors approximated as $A(\phi) = 1 + (\phi/M)^n$ for $n = 1$ and $n = 2$ respectively, where M is a mass scale. These theories therefore predict $|\gamma_{\mathrm{PPN}} - 1| \propto \phi^n$, which requires a certain strength of the screening mechanism to keep the field expectation value sufficiently close to zero in the Solar System [Zha+16].

Using the cameleon model as an example, the amplitude of the deviation of γ_{PPN} is given by

$$|\gamma_{\mathrm{PPN}} - 1| = \frac{2\beta\phi}{M_{\mathrm{Pl}}\Psi}, \tag{2.17}$$

where Ψ is the Newtonian potential. At the surface of the Sun, $\Psi \approx 2 \times 10^{-6}$ in natural units where $c = \hbar = 1$. From the effective potential in equation (2.6), one can find that the expectation value (minimum of V_{eff}) for the field is

$$\phi_0(\rho) = \sqrt{\frac{M^5 M_{\mathrm{Pl}}}{\beta\rho}}. \tag{2.18}$$

A lower estimate for the density ρ, is the local dark matter density in the Milky Way halo, $\rho_{\mathrm{gal}} \approx 10^{-118} M_{\mathrm{Pl}}^4$. Inserting these estimates into equation (2.17) gives

$$|\gamma_{\mathrm{PPN}} - 1| = \frac{2\beta\sqrt{\frac{M^5 M_{\mathrm{Pl}}}{\beta \times 10^{-118} M_{\mathrm{Pl}}^4}}}{2 \times 10^{-6} M_{\mathrm{Pl}}}. \tag{2.19}$$

Simplifying this equation, and applying the constraint (2.16), gives

$$10^{65}\sqrt{\beta\frac{M^5}{M_{\mathrm{Pl}}^5}} \lesssim 10^{-5}, \tag{2.20}$$

which reduces to the following parameter combination constraint,

$$\beta\left(\frac{M}{M_{\mathrm{Pl}}}\right)^5 \lesssim 10^{-140}. \tag{2.21}$$

The coupling β is expected to be $\mathcal{O}(1)$ for a gravitational strength force in the unscreened region. When assuming $\beta \approx 1$, the resulting constraint on the mass scale M is

$$M \lesssim 10^{-28} M_{\mathrm{Pl}} \approx 1\mathrm{eV}. \tag{2.22}$$

2.7.3 Laboratory Tests

Atom interferometry can test models with a density sensitive fifth force. In this experiment, a beam of neutral particles—typically atoms or neutrons—are sent falling through a vacuum chamber close to a massive source mass. A laser pulse can be used to split and manipulate the beam of the particles, such that the wave function travels along two different paths before it is recombined. The fifth force in screened theories (like the chameleon model) is expected to be more screened close to the source mass, so a particle accelerates towards Earth with a different rate depending on the distance from the source mass. The interference pattern when combining the wave function can be used to constrain the difference in the fifth force along the two paths [BCH15; Ham+15a]. Other laboratory experiments, such as a torsion pendulum, can also be used to constrain some specific models [Upa13]. Furthermore, there are studies on how to detect alternative models of dark matter in particle colliders like the LHC [Har+15], as well as studies on which signatures can be expected from scalar field dark energy in particle colliders [BBE15; Bra+16].

2.7.4 Pulsar Timing and Stellar Properties

Pulsars have a very stable rotation rate, and can thus be used as precisely ticking clocks. The strong equivalence principle of GR can be tested to very high precision through pulsar timing of binary and triple systems [Ren19]. Stars situated in unscreened regions can evolve differently than in GR. Modifications that enhance gravity—like the chameleon model—are expected to increase the temperature and brightness of affected stars, and hence reduce their life-span [SJV14].

2.7.5 Background Evolution and CMB

On the largest scales, measurements of the expansion history of the Universe can reveal details about the underlying theory of gravity. The dark energy component of ΛCDM is expected to have a constant equation of state $w \equiv p/\rho = -1$. Some theories of modified gravity predict deviations from $w = -1$. A time-varying equation of state is considered a smoking gun of quintessence and of many scalar–tensor theories [AT10].

With linear perturbation theory and numerical methods, it is possible to do parameter fitting with modified gravity. In Appendix C, I compare the linearised Einstein equations in GR to a conformally coupled scalar–tensor theory. In conformal scalar–tensor theories, the growth of perturbations is in general enhanced when compared to GR, which can be seen from the fact that the scalar field perturbation $\delta\phi$ appears in a term similar to the gravitational potential Ψ in the Euler equation for velocity divergence. In other words: the fifth force enhances gravity. See section C.2.1 of Appendix C for more details.

The Planck collaboration did extensive work in constraining some extensions to ΛCDM which modify the CMB [Pla+16]. They worked in the effective field

theory framework, which allows to probe a wider, but less specific, set of modified gravity theories. The CMB, in combination with late time probes, can be used to very precisely estimate the allowed deviations from ΛCDM over a large span of time and scales. In the following subsection, I briefly introduce the most important measurable effects on the CMB from modified gravity. I then proceed to introduce the Integrated Sachs–Wolfe effect and the slingshot effect in detail, because they are important for the understanding of my work in Paper III.

2.7.5.1 Modified Gravity Effects on the CMB

In most theories of modified gravity, dark energy is not exactly a cosmological constant. The varying equation of state and the varying ratio of dark energy to matter, can all modify the expansion history. This results in a potentially measurable change in the distance to the surface of last scattering.

Changes in the gravitational potentials, and enhanced growth of structure, can be measured through a change in the *integrated Sachs–Wolfe* (ISW) effect compared to the GR case. The ISW effect is a result of CMB photons changing energy when passing through an evolving gravitational potential; I will explain the ISW in more detail in section 2.7.5.2. An increased growth of structure can also lead to a measured amplitude of perturbations σ_8 at late times which disagrees with the σ_8 predicted from evolving ΛCDM with the parameters inferred from the CMB.

Modified gravity can change the effect of gravitational lensing. This changes the lensing potential, and can also modify the lensing of B-mode polarisation. Detection of B-modes is one of the primary science goals of future CMB missions, with the aim of identifying primordial gravitational waves within the GR framework.

Especially in the inferred values of H_0 and σ_8, there is some tension between the data from CMB and local observations. However, the alternative models that the Planck collaboration tested do not significantly improve these tensions [Pla+16]. Similar conclusions have been reached by other groups that apply different models [DSA19]. There is still a possibility that specific modified gravity theories which have not yet been compared to the data in this way (or models that have not yet been developed) might be a better fit than ΛCDM.

2.7.5.2 The Integrated Sachs–Wolfe Effect

In GR and most of its modifications, photons change their trajectories and energies when moving through the curved space-time. The change in trajectories can be seen in the effect of gravitational lensing, where the curvature around a massive body will bend and concentrate light rays like a convex lens. Such gravitational deflection has been observed around our Sun [Ken19], and also around more massive objects like galaxies and clusters. The first discovery of a strongly lensed quasar was done in 1979 [WCW79], where a galaxy in the line of sight bends the light of the quasar such that two separate images of the single quasar can be observed.

A photon moving through a gravitational potential will lose or gain energy as the level of the potential changes. This can for instance be seen in the red-shifting of light leaving a massive star, where the photon spends energy when climbing out of the potential well. The ISW effect is the change of photon energy as a photon passes through a gravitational potential which is evolving in time; If an over-density is stretching due to the cosmic expansion, its gravitational potential becomes shallower, and a photon which gained energy while falling into the potential well will lose a smaller amount of energy when climbing out of the shallower potential. The result on the CMB field is that CMB photons have a higher inferred temperature in regions where they have passed through a supercluster that expands due to cosmic expansion, or have a lower inferred temperature if they have passed through a supercluster that is increasing its density through accretion. The ISW effect can also be seen in under-dense regions, where an expanding void will leave a cold spot in the CMB.

Mathematically, the change in temperature ΔT of a photon due to the ISW effect is given as a time integral of the change in total potential over the life of the photon [Dod03]:

$$\frac{\Delta T}{T_0} = \int_{t_e}^{t_o} \left(\dot{\Psi} + \dot{\Phi}\right) \mathrm{d}t. \tag{2.23}$$

Here, T_0 is the initial (background) temperature, t_e is the time of emission, t_o is the time of observation, and $\dot{\Psi}, \dot{\Phi}$ are the time derivatives of the metric perturbations (potentials). Under the assumption of no anisotropic stress, $\Psi = \Phi$ in the GR case, and we can write the ISW as

$$\frac{\Delta T}{T_0} = 2 \int_{t_e}^{t_o} \left(\dot{\Psi}\right) \mathrm{d}t. \tag{2.24}$$

Any physical process that changes the metric perturbations Ψ or Φ over time will give an imprint on the CMB through the ISW effect. This includes an increased growth of structure, or modifications to gravity that introduce a different relation between matter and the metric perturbations. Both of these effects can come from a coupled scalar field, affecting either the clustering through a fifth force or affecting the lensing potential through the coupling between matter and the metric.

2.7.5.3 The Slingshot Effect

A special case of the ISW effect is the slingshot effect. If a non-evolving massive body (e.g. a galaxy) has a velocity component perpendicular to the line of sight relative to the observer, CMB photons that pass close to this mass are exposed to a time-evolving potential well. On their way to the observer, the CMB photons pass through a potential well that becomes deeper in front of the moving mass and shallower behind the moving mass; There is a net increase in ΔT behind the object and a net decrease in ΔT in front of the object, resulting

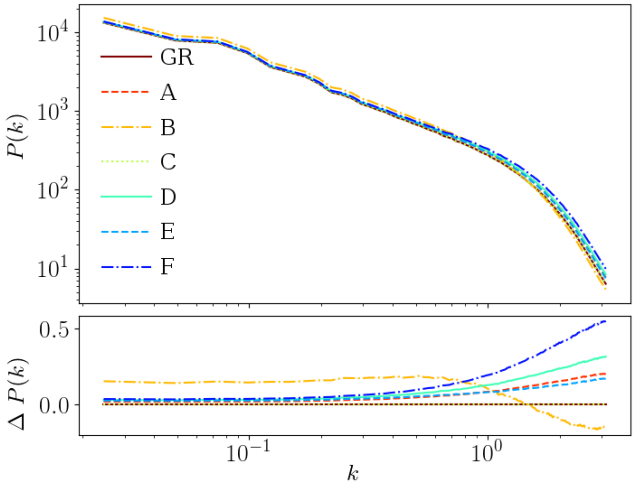

Figure 2.3: Example of the dark matter power spectrum of the redshift zero universe for some different models. The units of k along the horizontal axis are in h/Mpc. The lower panel shows the relative difference with respect to ΛCDM. Figure is compiled from my own N-body simulations of toy models of gravity.

in a characteristic dipole pattern. More details on these calculations can be found in Appendix B.

The slingshot dipole of a single moving galaxy or galaxy cluster has a ΔT that is subdominant to the CMB perturbations and the current instrument noise, and thus has not been measured yet. In Paper III we propose a stacking scheme to measure the slingshot effect and infer the average transverse infall velocity of galaxies into a supercluster. This method is sensitive to the concentration $m/r_{\rm vir}$ of the infalling galaxies, as well as their average infall velocity v_r. In typical scalar–tensor theories, the fifth force is attractive and enhances gravitational collapse, therefore we expect both $m/r_{\rm vir}$ and v_r to increase the measured slingshot effect for these theories.

2.7.6 Matter Power Spectrum

The redshift zero fluctuations in the density of the Universe are often displayed by plotting the *power spectrum*, abbreviated $P(k)$. The power spectrum visualises the amount of clustering, or correlations, on a given scale. An example of the matter power spectra from a set of simulations with several different models for gravity are shown in figure 2.3. The brown line is the power spectrum of ΛCDM, while the other lines are toy models for modified gravity with a variety of parameters. The horizontal axis of the graph represents the scale of structure, with increasing wave-number k corresponding to smaller scales. The largest

scales are on the left-hand side of the horizontal axis and the smallest scales are to the right. The vertical axis, or the power, represents the amount of clustering on that given scale.

To be more specific, the power spectrum is a Fourier transform of the two-point correlation function of the matter over-density field in 3D space. The over-density is defined as

$$\delta(\mathbf{x}) = \frac{\rho(\mathbf{x}) - \bar{\rho}}{\bar{\rho}}, \tag{2.25}$$

where $\bar{\rho}$ is the average (background) matter density. The two point correlation function in real space is given by

$$\xi(\mathbf{r}) = \langle \delta(\mathbf{x})\, \delta(\mathbf{x}+\mathbf{r}) \rangle . \tag{2.26}$$

Under the assumption of isotropy, we can average the two-point function over all directions without losing information. Then, $\xi(r) = \xi(\mathbf{r})_{|\mathbf{r}|=r}$ describes the amount of self correlation in the density field at distances of r. The power spectrum $P(k)$ is defined by the Fourier transform

$$P(k) = \int \xi(\mathbf{x})\, e^{-i\mathbf{k}\cdot\mathbf{x}}\, \mathrm{d}^3x \Big|_{|\mathbf{k}|=k} . \tag{2.27}$$

The spatial Fourier transform of the over-density $\delta(\mathbf{x})$ is $\tilde{\delta}(\mathbf{k})$. From Fourier quantities, the power spectrum can also be written as [Dod03]

$$\left\langle \tilde{\delta}(\mathbf{k})\, \tilde{\delta}(\mathbf{k}') \right\rangle = (2\pi)^3 P(k)\, \delta^3(\mathbf{k}-\mathbf{k}') . \tag{2.28}$$

The angular bracket on the left-hand side is the average of the product, over the whole distribution, and δ^3 denotes the 3D Dirac delta function. The scalar value k is the magnitude of the vector $\mathbf{k}$. Repeated over- or under-densities on a certain scale k, will increase the product on the left-hand side, and hence lead to a higher power $P(k)$ on that scale.

By extracting the galaxy two-point function from observational galaxy catalogues, it is possible to build a precise galaxy power spectrum up to distances of some hundred Mpc [Coo04]. There is introduced a bias when comparing the theoretical dark matter power spectrum—typically generated from simulations—with the observed galaxy power spectrum from galaxy surveys [DJS18]. We do not have access to observe the dark matter distribution directly[5], hence a common alternative is to assume that the galaxies trace the dark matter distribution to a given extent. The highest density peaks of the dark matter distribution form galaxies, and these galaxies are typically highly clustered compared to the dark matter. This bias can be modelled as a linear galaxy bias b, which appears as a factor enhancing the galaxy over-density

$$\delta_g = b\delta_{\mathrm{DM}}. \tag{2.29}$$

[5] Although, the dark matter distribution can be inferred indirectly through e.g. gravitational lensing.

The power spectrum—or rather the change in power with relation to GR—can be used to differentiate different models of gravity. The lower panel of figure 2.3 shows the relative difference in power with respect to the ΛCDM model (GR).

$$\Delta P\left(k\right) = \frac{P\left(k\right)}{P\left(k\right)_{\mathrm{GR}}} - 1. \tag{2.30}$$

An increase in the force of gravity on a given length scale is expected to increase correlations, and therefore power, on that scale. Most scalar–tensor theories for modified gravity have a fifth force that is attractive, which enhances gravity on the smallest scales. This effect is seen in most of the example models in the plot: model A, D, E, and F all show a significant increase of 5 to 50 % in power on scales smaller than $k = 1h/\mathrm{Mpc}$. Model C has a very weak coupling, so the fifth forces have not affected the matter distribution significantly; The $P(k)$ of model C is indistinguishable from that of GR.

Model B shows behaviour which is not typically expected from scalar–tensor theories. Here the power on the largest scales is significantly higher than in the GR case, while it is lower than GR on the smallest scales. One interpretation of this could be that gravity is effectively enhanced on the largest scales, while there is an effect suppressing gravity or otherwise smoothing out the matter distribution on small scales.

The largest scales of the power spectrum can be compared to linear theory, while on the smallest scales (below a few megaparsecs) we need non-linear approaches like N-body simulations to model the power spectrum precisely. On these scales, there is currently some freedom to modify gravity because the power is not well constrained with current surveys. Upcoming surveys (like Euclid and SKA) will be able to more precisely discern modifications to gravity on Mpc scales.

2.7.7 Beyond the Power Spectrum

For a Gaussian density distribution, the power spectrum contains enough information to reconstruct the underlying density field. However, the power spectrum does not retain all information about other density distributions. One way to extract more information from a non-Gaussian density field is by going to higher-order statistics. The bi-spectrum is for instance based on the three-point correlation function (whereas the power spectrum is based on the two-point correlation function).

Linear perturbation theory predicts that a matter distribution in an expanding universe evolves as a log-normal distribution, under the assumption of GR and a Gaussian velocity field [CJ91]. Hence, the logarithm of the matter density field, $\log\left(\rho\right)$, is expected to be close to Gaussian. Taking the power spectrum of the logarithmic density field retains more information about the original density distribution [GE15]. When taking the power spectrum of a realistic density distribution, the small and highly over-dense areas containing galaxies and clusters are weighted the most and contribute more to the power spectrum

than other areas. These over-dense regions are expected to be screened in most theories of modified gravity. Hence, the traditional power spectrum mostly probes regions where we know that gravity is similar to GR. Other transformation functions for the density field can yield a power spectrum that is more sensitive to differences induced by modified gravity [LM17].

2.7.8 Void Statistics

Most of the currently viable theories of modified gravity apply some kind of screening mechanism, which effectively hides the differences from GR in high-density environments like in galaxy clusters. For this reason, we expect modifications of gravity to be stronger in environments of lower density, like filaments and voids [Fal+18]. One simple statistical tool is to look at the abundance of voids within a certain under-density or size range. With better measurements, it is possible to map the density field around voids to find the void profiles, which can be compared to the ones from simulations. Other statistical methods include finding the power spectrum of voids [Per+19].

2.7.9 Velocity Statistics

When an external force acts on a test particle, the particle will first change its velocity before it significantly changes its position. This means that velocities of galaxies are sensitive to changes in the fifth force affecting that galaxy. The velocities of objects relative to the Earth can be measured with the Doppler effect, which gives a red-shift or a blue-shift of spectral lines depending on if the object moves away from or towards the Earth. The Doppler shift only measures the radial velocity component, and furthermore it is not trivial to disentangle the peculiar radial velocity from the radial velocity due to expansion of space between the object and the observer.

From the radial velocity field of galaxies, it is possible to extract an estimator for the velocity power spectrum [How+17], as well as the pairwise velocity dispersion [Iva+16]. Both of these statistics can be used to constrain theories of gravity.

Knowledge of the *transverse velocity* component would add more information to galaxy catalogues, allowing us to disentangle the cosmic expansion from peculiar velocities and giving better statistics when comparing models to observations. In Paper III we present a method to use the *slingshot effect* to measure the transverse motions of galaxies falling into a galaxy cluster. The slingshot effect results in an increase in energy for photons passing behind a moving massive object, and a decrease in energy for photons passing in front of the moving object. This effect is very small, but by combining the images around many infalling galaxies, we expect that the average infall velocity can be detected with this effect in the near future.

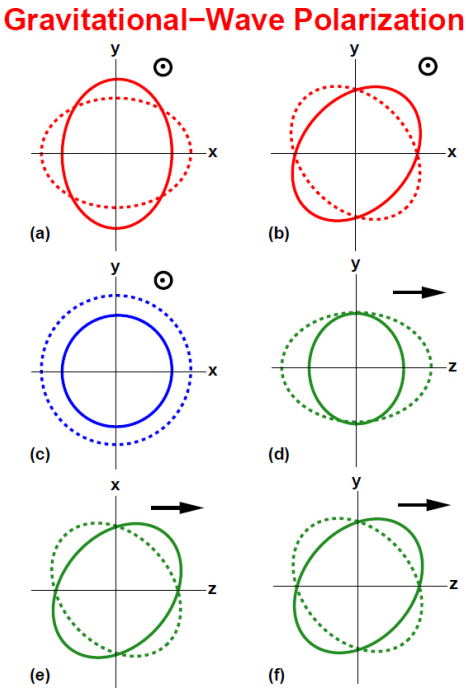

Figure 2.4: A schematic of possible gravitational wave polarisations. Only modes (a) and (b) are allowed to propagate in GR. The figure is re-used from [Wil06], with permission from Clifford Will. The original figure was accessed at https://link.springer.com/article/10.12942%2Flrr-2006-3

2.7.10 Gravitational Waves

The most stringent constraints on modified gravity from gravitational waves are from the binary neutron star merger GW170817, where there was an associated gamma-ray burst detected directly after the gravitational waves. This constrains the speed of gravitational waves to be very close to the speed of light, which rules out theories where the coupling is expected to change the speed of gravitational waves [EZ18].

With more detectors, it will be possible to measure the polarisation of gravitational waves precisely. See figure 2.4 for illustrations of the deformations of space when a gravitational wave with a given polarisation passes Earth. Pure GR only allows propagating tensor waves, resulting in deformations of type (a) and (b). Scalar field theories in general allow monopole deformations (c), and some theories predict the propagation of the other modes (d), (e), or (f) as well [ACD08]. The detection of a monopole gravitational wave (or other exotic polarisations) will be a strong sign of gravity beyond GR [GSO16].

Chapter 3

Numerical Simulations

The computation power available for scientists is continuously growing. This is due to an increase in the number of transistors per processor core, but also due to more processor cores being assembled in each super-computer. Combined with the effort of programmers to find more efficient solutions to numerical problems, this allows us to create increasingly complex and detailed computer simulations. In astrophysics, simulations are extensively used to create a virtual cosmos from scratch, which we can control and study in ways that we cannot do with the Universe we live in. Numerical simulations play a key role in my study of the nature of gravity, and in this chapter, I will delve deeper into the specifics of my implementations of modified gravity. Specifically, I will discuss how to simulate the time evolution of a scalar field out of the quasi-static approximation, and how to implement the extra fifth force in N-body simulations.

3.1 History and Linear Theory

By assuming that small scales do not affect the large scales significantly, it is possible to apply perturbation theory to the different components of the Universe (dark matter, baryons, and radiation), and infer the growth of structures on different scales. Working in Fourier space, computer simulations that evolve the linear Einstein–Boltzmann equations (see Appendix C) can track the linear evolution of many different scales independently, resulting in a linear power spectrum. This method can be used to estimate the power spectrum of the temperature fluctuations of the CMB, or the large scales of the matter power spectrum at redshift zero. These Einstein–Boltzmann solvers can be combined with a Monte Carlo Markov chain (MCMC) code for efficient parameter estimation, which has been done by for instance the Planck collaboration when predicting ΛCDM parameters from CMB data [Pla+18].

Linear perturbation theory and ΛCDM successfully reproduce CMB measurements of the early universe, as well as the large scales structures of the observed universe today. However, linear theory breaks down at high densities, meaning that the power spectrum on the smallest scales, where the density perturbations have grown beyond the validity of the linear regime, cannot be trusted [Sch06]. The approximate terminology for length scales I use in my work is: linear scales are larger than 100 Mpc, quasi-linear scales are between a few and 100 Mpc, and non-linear scales are smaller than a few Mpc. In the quasi-linear regime, it is still possible to get good results with linear theory, given some tweaking [Ber96].

On smaller, non-linear scales, other methods must be used to calculate the evolution of matter. One commonly used method is *N-body simulations*, where lumps of matter with the mass of millions, or even billions, of solar masses are

considered individual particles. This corresponds to reducing a galaxy to a few point particles. The motions of the underlying matter distribution is traced through computing the motion of the particles in what is called a gravitational N-body system. By allowing these point masses to interact individually, one can expect a precision limited by the resolution of your simulation. Such simulations are used to reach non-linear resolutions below a Mpc, even down to kiloparsecs, at which scale baryon physics starts to become important for the evolution of structures, like galaxies. In this work, I will focus on N-body simulations without baryonic physics.

The gravitational two-body problem can be solved exactly by using calculus. However, the three-body problem is shown to not have a general solution on closed form, except for in special configurations of the three masses [MQ14]. The general N-body problem with $N \gg 2$ must be solved numerically, which in practice means using computer simulations. A numerical solution is always an approximation to the motion that the bodies would have in reality, but through higher resolution and improved numerical methods, it is possible to come arbitrarily close to the real solution, given that the problem is numerically stable.

Light intensity goes as $1/r^2$, just like gravity. Therefore, gravitational forces could be modelled in a laboratory using light sources as "point masses". Using light bulbs and photocell measurements, the gravitational motions of a galaxy were integrated forward in time numerically using an analogue version of an N-body solver before advanced computers were available [Hol41].

The first computer implementation employed *direct summation*; For every time step, the gravitational acceleration of each individual particle is calculated by summing up the forces from each of the other particles. This kind of calculation has a complexity of $\mathcal{O}\left(n^2\right)$. This means that having ten times more particles will increase the computation time a hundredfold. With this implementation, we cannot have very many particles before being limited by the processing power of our computers.

3.2 Cosmological N-body Simulations

There are many different implementations of cosmological N-body simulations that allows better performance than direct summation of the forces. Some of the most commonly used codes are `Ramses` [Tey02], `Gadget` [Spr05], and `Pkdgrav` [Sta01]. These codes are designed to run in parallel on modern supercomputers with thousands of CPU cores. The mentioned codes have the capability to include a hydrodynamic component to simulate baryonic physics as well as the dark matter N-body component. The dark matter N-body part of the currently used methods now agree to a sub-percent level in the power spectrum ([Sch+16] show less than a percent difference in power for $k < 1\,h/\mathrm{Mpc}$).

In modern N-body simulations, millions or billions of point particles are used to trace the underlying continuous matter distribution. The particles are distributed in a simulation box with side lengths of megaparsecs to gigaparsecs.

A larger box size means including more cosmic volume and therefore more total mass; each cubic megaparsec of space contains on average 45 billion solar masses of matter[1].

A smaller volume box allows finer resolution for the mass particles, as well as resolving smaller structures like galaxies and satellite galaxies. However, a small volume box does not allow any structures larger than the box size to form. This is a problem because the environment inside of enormous under-dense *supervoids* and over-dense *superclusters* provides different conditions for structure formation on small scales than a box with the average density of the Universe. To get a realistic sample of environments similar to the ones found in the observed universe, the box size should ideally be bigger than the biggest expected structures; The biggest observed structure is a cosmic wall several Gpc wide [HHB13].

The expansion of space is calculated from Friedmann equations (1.4) and (1.5). This is included in the N-body simulation by using a *comoving* coordinate system, where the simulation box and the coordinate grid are continuously expanding according to the calculated scale factor. In this prescription, only the *peculiar motions* of the particles relative to the expanding grid are tracked.

In the simplest cases, the particles only interact through gravity. Pure gravitational N-body is well suited for tracing the evolution of pressureless matter. The main matter content of the Universe is consistent with collisionless and pressureless dark matter, and even stars and galaxies are usually far enough from each other for gravity to dominate. On scales larger than galaxies, where baryon physics are negligible, the collisionless N-body prescription is sufficient. See [KVA12] for a comprehensive review of dark matter-only simulations.

In cosmology, we are mostly interested in the larger picture, but in other areas of astrophysics, one might want to precisely simulate scales of galaxies and smaller. In this case, the effects of the electromagnetic force on baryons must be included. This can be done through hydrodynamic simulations, where a baryonic gas component—separate from the dark matter N-body component—is simulated with effects like temperature, pressure and friction. More advanced simulations include radiation/neutrino components, stellar- and supernova feedback, magneto-hydro-dynamics, and processes for radiative transfer. In addition to baryon physics that are available in N-body codes like `Ramses` and `Gadget`, there are other astrophysical codes developed specifically for hydrodynamical simulations, like `Arepo` [Vog+12] and `Gasoline` [WKQ17]. Simulating baryons properly is significantly more computationally expensive than dark matter, meaning that it is preferred to run dark matter-only simulations if the relevant scales are not affected by gas physics. Hence, none of these baryonic effects are included in the simulations done in this thesis.

An alternative to hydrodynamical simulations that still allows us to see structures on galaxy scales is to "paint on" the gas and the galaxies after a pure dark matter N-body simulation is finished. This method uses some statistical

[1]Calculated by assuming $\Omega_m \approx 0.3$ and using the value of the critical density of the Universe given in [McG].

prescription to populate dark matter haloes with galaxies. The tuning of the parameters in this method is not exact, because different sources (including both simulations and observations) do not agree perfectly. Furthermore, care must be taken when applying such a prescription to theories beyond ΛCDM because the modifications may change the halo masses, rates of occupation, and gas fraction [Dev+19].

3.3 Implementation for GR

Numerical solutions involve the discretisation of mass, space and time. Particle motions are integrated forward in time using a time-stepping algorithm. For each time step, the acceleration of each particle is calculated from the gravitational force, while the position and velocity are found from a discrete time integration scheme (like Euler or Runge-Kutta). The biggest bottleneck in this method is the calculation of the gravitational on each particle. There are several different ways to improve the force calculation from $\mathcal{O}\left(n^2\right)$ to $\mathcal{O}\left(n \log n\right)$ or better. The general idea is that particles that are far away do not need to be summed over individually, but rather averaged in some way.

`Pkdgrav` splits the particles into a binary k-d tree structure by bisecting the simulation volume until each leaf of the tree contains at most 8 particles. Particles that are close to each other in the tree structure are on average close to each other physically. When calculating gravity, far away particles are grouped according to the nodes of the tree structure, while nearby particles are summed over directly.

`Gadget` also splits the particles into a tree structure, but they follow the approach of Barnes & Hut [BH86] to repeatedly subdivide the cells in the volume into eight sub-cells, each with half the side lengths of the parent cell. This generates an *oct-tree*, which groups the particles in a hierarchical structure depending on their distance. The oct-tree is traversed to determine if a node of the tree is far enough away to count as a group, or if the node has to be opened and the eight sub-nodes considered individually.

`Ramses` is a particle-mesh code. The acceleration of particles are not calculated through gravitational force calculations between each particle, but rather through calculating the gravitational potential from the density distribution on the simulation grid. The code adaptively and recursively splits the grid cells into oct-trees to increase the resolution of structures where particles are clustered. The modified gravity N-body code `Isis` [LMW14], which I am most familiar with, is based on `Ramses`. Hence, specific details in the rest of this section reflects this particle-mesh N-body solver.

3.3.1 Initial Conditions

It is not necessary to run a full N-body solver from the initial perturbations at the time of inflation, because the density perturbations in the early universe are small enough for linear theory to hold for all scales. It is typical to evolve the

perturbations linearly first, then make a *particle realisation* of the density field and start the N-body simulation at around redshift $z = 50$. It has been found that the power spectrum and mass functions do not change significantly even when starting at a redshift of $z = 25$ in GR [Kne+09].

3.3.2 Interactions over Short and Long Distances

To avoid that the $1/r^2$ force grows unbounded when two particles are close to each other, a softening of the force is often introduced. The point particles represent smooth blobs of matter, meaning that in a real situation they would not have a hard 2-body interaction when their centres of mass pass close to each other. A typical form of the amplitude of the softened force is

$$F = \frac{Gm_1m_2}{r^2 + \epsilon^2}, \tag{3.1}$$

for some smoothing length ϵ. At large distances, $r \gg \epsilon$ and the force behaves as $1/r^2$, but for shorter distances, the force asymptotically approaches an upper limit set by $1/\epsilon^2$.

`Ramses` finds the Newtonian force F_N on the particles from the gradient of the gravitational potential,

$$\mathbf{F}_N = -\nabla\Psi. \tag{3.2}$$

To calculate the gravitational potential Ψ, a gravitational *Poisson's equation* is solved numerically. The equation is

$$\nabla^2\Psi = 4\pi G\delta\rho, \tag{3.3}$$

where $\delta\rho$ is the matter over-density. The equation in itself is solved with numerical methods described in detail in [Tey02]. To find the density field on the mesh grid, a cloud-in-cell interpolation scheme is used to assign particles to the grid cells. With this scheme, the point particles don't just contribute to the density in the cell where they reside, but their mass is distributed over neighbouring grid cells as well according to the distance from the centre of the cells. This ensures that there is a smooth change in the density field as a particle crosses a boundary between two grid cells.

Structures that form near the edge of the simulation box should in principle interact with structures that have formed outside of the simulation edges. To emulate an infinite Universe with a finite box size, it's common to apply periodic boundary conditions. In this way, we ensure that particles are affected by a gravitational force from far away structures in all directions. The force of gravity goes down with distance as $1/r^2$, so there are usually no issues with a structure interacting with itself through the other side of the box, given a large enough box size.

3.3.3 Adaptive Mesh Refinements

The initial matter distribution at the start of the N-body run is very smooth. The grid of `Ramses` typically starts with the same amount of grid cells as there

are particles in the initial realisation. For instance, a run with $1024^3 \approx 10^9$ particles starts with a *domain grid* of $1024 \times 1024 \times 1024$ grid cells, typically with one particle in each cell. When matter clusters under gravity, many particles concentrate in small areas of the grid, leaving other grid cells empty. Because the force is calculated on the grid, the force interactions between particles within one grid cell are not precise. To solve this, the *Adaptive Mesh Refinement* (AMR) method is introduced. This method involves that a cell is split on-the-fly if certain refinement criteria are met. A typical refinement criterion for pure N-body simulations is to split a cell in eight equal sub-cells if there are more than eight particles in it[2].

The AMR refinements can be applied recursively on already refined cells if they meet the refinement criteria, resulting in a spatial grid with arbitrary precision in regions of high matter density. Each new refined level has effectively a higher spatial resolution. This also implies that to track the particle motions correctly, the code needs a higher temporal resolution as well. This can be seen from the Courant–Friedrichs–Lewy condition, which requires $\Delta t \lesssim C\Delta x$ for some constant C to guarantee convergence of a numerical solution. As Δx is halved in the AMR process, each refined cell needs twice the amount of time steps compared to the parent cell. The higher spatial and temporal resolution increases the computation time and memory requirements for highly refined regions drastically. For this reason, it is common to specify an upper level of refinements, which limits the final resolution.

3.3.4 Weak Field Limit and Newtonian Gravity

Even if we allow densities to grow to non-linear values ($\rho/\rho_0 \gg 1$), the gravitational potential is still approximately uniform on scales larger than our solar system. The metric perturbation Ψ is $\mathcal{O}\left(10^{-6}\right)$ close to the Sun, and much smaller on relevant cosmological scales. Taking Ψ to first order (often called the weak field limit) is considered safe and is equivalent to the Newtonian limit of GR. Relativistic effects of compact objects and high energies are not considered in a cosmological context, which allows us to make many simplifications to the equations and reduce the computation time. N-body simulations applying the weak field simplification will not be able to simulate forces close to neutron stars, or the precession of Mercury correctly. Furthermore, the simulations do not include black holes or gravitational waves, and the speed of gravity is considered infinite. It is assumed that gravitational waves do not affect the matter distribution significantly and can be neglected. The massive N-body particles trace a large volume of cold dark matter, which changes very slowly. The slow movement indicates that the matter distribution does not change measurably during the travelling time of gravity; This means that instantaneous forces give the same acceleration as the true forces, which should propagate

[2]The number 8 appears here because we split the (cubical) cell in two along all 3 dimensions; the first split bisects the cell in two cells along one axis, the split along the second axis gives a total of four cells, and finally each of them are split in two along the third axis, resulting in $2 \times 2 \times 2 = 8$ cubes.

with the speed of light. All relevant relativistic effects on the largest scales are included through the background expansion of the grid from the Friedmann equations.

For scales larger than a few kiloparsecs, the weak field (Newtonian) implementation of gravity is expected to work well. On kpc to Mpc scales, correctly including baryonic effects are much more important than higher-order relativistic corrections to gravity. The N-body code `Gevolution` includes higher-order relativistic effects, which in theory allows Mercury precession, as well as other corrections that can be visible on kpc to Mpc scales [Ada+16]. The field of numerical relativity is dedicated to studying extreme astrophysical phenomena on smaller scales, including black holes, binary neutron stars, and gravitational waves. Numerical relativity is beyond the scope of this thesis.

3.4 Review on Modified Gravity Simulations

A lot of effort has already been done in the field of numerical simulations of modified gravity. This section lists a few of the contributions and ideas that have been developed. In addition to `Isis`, which is developed at the University of Oslo, other research groups worldwide have developed codes for modified gravity simulations; Some of the available codes are `Ecosmog` [Li+12], `MG-Gadget` [PBS13], and `Dgpm` [Sch09]. The implementations of these codes have been compared, and the results agree within 1 % in the power spectrum for the compared models [Win+15].

By using these codes, and spending significant computing resources, it is possible to generate suites of simulations for extracting observables like the matter power spectrum. One example of a suite of high-resolution simulations with $f(R)$-gravity is the lightcone simulation project [Arn+19].

Because simulations of modified gravity are generally orders of magnitude more computationally expensive than GR-simulations, there have been considerable efforts in ways to simulate the models more efficiently. One prescription, which also works for speeding up simulations of GR, is to use perturbation theory for large scales and allow significantly longer time steps for the particles [Win+17]. Another prescription is to only run a GR simulation, and modify the observables after the simulation has finished, for instance by applying a transformation to the power spectrum [Win+19].

In an nDGP model, the Vainshtein screening mechanism hides small scale modifications to GR effectively. It has been discovered that the scalar field does not need to be solved on the refined levels of the particle-mesh grid, but only on the domain grid. This technique speeds up the simulations by more than a factor of 10, while the impact on the matter power spectrum is less than 1 % [BBL15]. For quasi-static $f(R)$ simulations, the same group has also discovered a possibility for significant speed-up; The Newton–Gauss–Seidel iterative method, which is commonly employed to solve Poisson's equation, has a very poor convergence rate. They propose alternative solver for the scalar field which, even when allowing AMR, gives a speed-up of a factor of at least 5 [Bos+17].

The clustering effects of modified gravity can in some cases be degenerate with other astrophysical effects, like warm dark matter and massive neutrinos. Some numerical studies that investigate how to break these degeneracies are [BV16] and [Mer+19].

There have been some studies on implementing baryonic effects in modified gravity simulations, and on the possible degeneracies between baryonic physics and modified gravity [EFM18; Ham+15b]. More recently, hydrodynamical simulations with realistic baryon physics have uncovered new possible probes for modified gravity, including expected changes in the neutral hydrogen power spectrum and in the amount of galaxies forming discs [ALL19].

3.5 Simulating a Scalar Field

In the Einstein frame, scalar–tensor theories result in a fifth force acting on matter, in addition to the gravitational force of GR. In a modified gravity N-body code like `Isis`, the particle motions are calculated by applying fifth forces in addition to the Newtonian forces [LMW14]. For each time step of the particles, the fifth forces can be found from equation (2.4) or equivalent depending on theory. The fifth force calculation in conformal theories typically involve the scalar field gradient and possibly the scalar field value; For instance, in the conformal symmetron model, the fifth force is $F_\phi \propto \phi\nabla\phi$. These quantities are needed at each point in space and for each time step of the force calculation in the N-body scheme. For more complex theories than the simple conformal scalar field, higher order derivatives (in space and time) of the field are needed for calculating the force.

To find the scalar field ϕ and its derivatives needed for the force calculation, the starting point is the EOM (2.5). The full equation of motion of the scalar field is a computationally expensive equation to solve numerically (it is a non-linear and hyperbolic differential equation which is second order in time). I will present a method for solving the full equation in section 3.5.2, but a faster method is to apply the quasi-static approximation.

3.5.1 The Quasi-Static Approximation

The realisation that leads to the *quasi-static* approximation is analogous to the justification for not including the speed of gravity in GR simulations; Because the density field evolves slowly, the effective potential—and the expectation value of the scalar field—is expected to evolve slowly as well. This approximation implies ignoring time derivatives of the scalar field in the EOM (2.5). This reduces the EOM to a Poisson's equation,

$$\nabla^2\phi = f\left(\phi, \rho\right). \tag{3.4}$$

The field value can be found at each time step from solving the simplified equation, similarly to how the gravitational potential is found in a Newtonian N-body code (see section 3.3).

The quasi-static approximation is found to be valid for predicting some observables (including the power spectrum) in cosmological simulations of the $f(R)$ model [BHL15] and the symmetron model [Win+15]. It is reasonable to assume it works well for most conformal theories. Nevertheless, it is important to test the assumption for any given model by comparing the results with simulations performed out of the quasi-static assumption.

3.5.2 Naive Non-Static Implementation in the N-body Code

Out of the quasi-static approximation, the field has memory of previous time steps—a certain momentum—and should be integrated forward in time instead of solved independently for each time step. The method described here was first implemented in [LM14].

The quasi-static assumption has not been tested thoroughly for disformally coupled fields. The fifth force for a pure disformal coupling, given by equation (2.12), depends on the local value of the first and second time derivatives of the scalar field. These quantities can be found more precisely out of the quasi-static approximation. Furthermore, both in the conformal and the disformal case, solving the full EOM allows for wave propagation in the scalar field. In Paper I, we conclude that such waves can have a significant impact on the PPN parameter γ_{PPN}.

The full EOM is an initial value problem. Because each calculation of the field needs some information about the past of the field, we need to set up the initial conditions of the field at the start of our simulation. Optimally the initial perturbations of the field should be decided from linear theory, like the initial perturbations of the density field. However, we find in the tested disformal models that the resulting field evolution and density distribution at redshift zero are not very sensitive to the initial conditions of the field. This is also the case for the disformally coupled symmetron [HLM16], but although we expect it to be the case for many models, the assumption should be verified for every new branch of models.

The non-static method solves the full EOM with a *leapfrog scheme*, similar to the work explained in my master thesis [Hag15] and in [LM14]. The principle of the leapfrog scheme is similar to the simple forward Euler method, except that the field velocity $\dot{\phi}$ is calculated at points in time that are shifted by half a time step $\Delta t/2$ relative to the integer time steps of the field value ϕ.

Oscillations in the scalar field are typically significantly faster than the motions of the N-body particles. To track the field evolution precisely, we find that there should be thousands of time steps for the scalar field for each time step of the particles. Due to this, the non-static implementation is computationally expensive and requires at least a factor of 100 more CPU time than a quasi-static simulation with the same resolution.

Another disadvantage of the current implementation of the non-static solver is that it does not allow for AMR in the simulation grid. This can be implemented in the future, but the task is not trivial; When a grid cell is refined, the field in the refined cells must be interpolated with higher-order methods designed to avoid

artificial waves. A sloppy interpolation method can introduce perturbations in the scalar field which are not of a physical origin.

Performing a full N-body simulation of modified gravity to study a specific phenomena is not only computationally expensive but also impractical because the scalar field dynamics are very complex in a cosmological simulation. I have developed a simple stand-alone solver of the non-static EOM to understand how scalar fields behave on smaller scales than the domain grid of the cosmological N-body simulations.

3.5.3 Higher Resolution in Spherical Symmetry

To understand how the scalar field behaves in the presence of a matter overdensity, I implemented a one-dimensional, spherically symmetric solver. Just like the implementation in the N-body code, this solver uses the leapfrog integration scheme. However, due to the spherical symmetry, it only solves the EOM in one dimension. This allows me to increase the spatial and temporal resolution significantly without increasing the computation time too much. This code is customisable to allow many different EOMs for different theories, with full control of the profile of the central spherical density distribution as well as the boundary conditions for the scalar field—allowing for instance external incoming waves. The code can be used to look for phenomena in the scalar field, predict fifth forces, and check the importance of scalar field waves. Optionally, log-spaced radial coordinates allow higher resolution close to the centre of the simulation. This is useful when simulating waves of short wavelength arriving from many Mpc distance, and still allows us to resolve the scalar field dynamics inside of the Milky Way galaxy.

The code does not include an evolution of the background matter density nor the cosmic expansion. The currently implemented density distribution is a static Navarro–Frenk–White (NFW) matter overdensity. I used this code during my work on Paper I to estimate how external waves in the scalar field affect the screened regions of the symmetron model. In this paper, it is described how external waves entering the Milky Way halo can disrupt the value of γ_{PPN} sufficiently to be measured by the Cassini experiment.

3.6 Disformal Phenomenology

In the following section, I describe the numerical implementation of a disformally coupled scalar field, without assuming the quasi-static approximation. I also describe and discuss phenomena that appear when including the disformal coupling. This section is in essence a supplement to Paper II.

3.6.1 Previous Discoveries and Motivation

Disformally coupled fields have been investigated analytically and in the linear regime, [Bek93; BM18; Koi08; Sak14; vM15; Zum+10], but at the time of writing, results from these studies have not been confirmed in the non-linear regime. The

non-static version of `ISIS` has been used to study the symmetron model with and without a disformal term [HLM16; LM14], and includes all the necessary routines to implement the pure disformal EOM and the associated fifth force. Part of my work related to Paper II was to extend `ISIS` for a pure disformal model, which is a step forward in the study of disformally coupled fields in the non-linear regime.

For my master thesis, I studied a conformal symmetron model with an additional disformal coupling. In this way, it was possible to study the added disformal effects, while the conformal part of the model ensured that the scalar field remained stable. See [HLM16] for a paper describing the main results from the work during my master.

A pure conformal symmetron model is known to increase power with respect to ΛCDM. Adding a disformal coupling on top of the conformal model results in a reduction of power, but not below the original ΛCDM value. The suppression of the conformal contribution by the disformal factor has also been found in linear theory [vM15].

In the symmetron, the effective potential has a deep minimum at $\phi = 0$ in regions of very high density. An unexpected result found in [HLM16] is that the addition of an intermediate strength disformal coupling increases the amplitude of scalar wave oscillations in centre of haloes. Due to the deep potential in these regions, a significant amount of energy is needed to perturb the field by the amount found in the simulations.

3.6.2 Possible Explanations

By evolving the disformal scalar field evolution in spherical symmetry (see section 3.5.3), I was able to study the disformal scalar field in a controlled setting.

The *disformal effect*, which can explain many of the observations, is the phenomenon that a disformally coupled scalar field slows down in high densities. The field reacts slower to the potential and the Laplacean because the acceleration $\ddot{\phi}$ is suppressed by a factor $1/\left(1+\gamma^2\rho\right)$ in the EOM[3].

In a mixed conformal and disformal model, the disformal effect reduces the growth of field perturbations in the early universe; the conformal effects will take longer time to work, and the conformal fifth force is suppressed while the perturbations are small. This effect is related to the disformal screening mechanism [KMZ12]. The reduction of power could also be due to repulsive fifth forces, which we study further in Paper II.

The disformal effect also leads to clustering of waves inside of haloes. The waves in the scalar field move with approximately the speed of light in vacuum, but if a scalar field wave enters a high-density region, it slows down significantly. See figure 3.1, which shows how a long-wavelength wave packet can become trapped inside a galaxy and get increased gradients. If a galaxy is immersed in a background of scalar field waves, wave energy will build up over time.

[3] In the limit of low kinetic energy, $X \approx 0$, the fraction $\gamma^2 \equiv B/(1-2BX)$ simplifies to B.

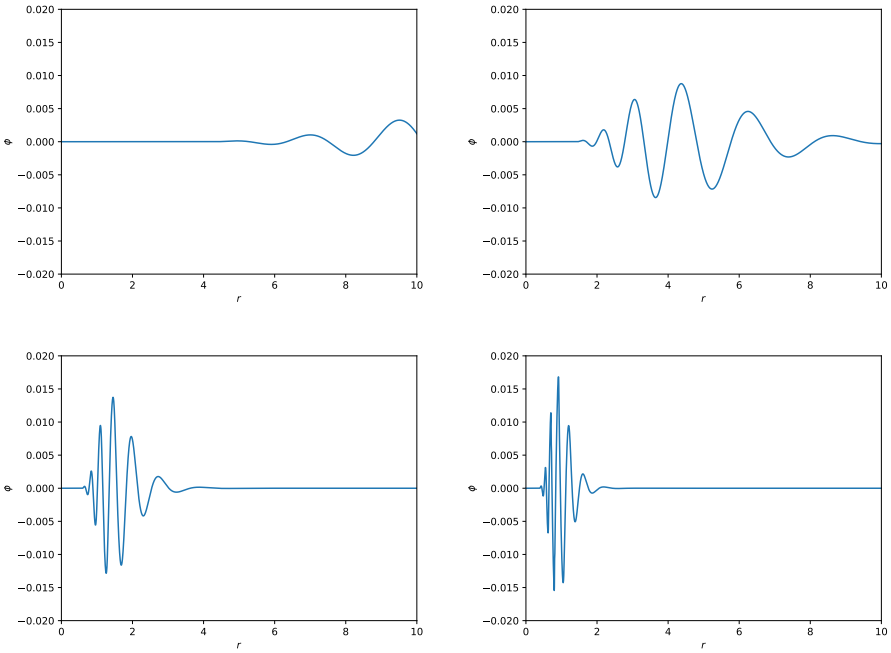

Figure 3.1: Sketch of a wave packet entering a massive galaxy from the right. The four panels are four different snapshots, increasing in time in reading order (top left, top right, bottom left, bottom right). The horizontal axis is the distance from the centre of the galaxy (normalised to 1 Mpc) and the vertical axis is the perturbation of the scalar field (normalised to 1 $M_{\rm Pl}$).

3.6.3 N-body Simulations with Disformally Coupled Quintessence

One of the goals of this doctorate thesis was to build upon the modified gravity N-body code `Isis` ([LMW14]) to simulate and study a scalar field coupled disformally to matter. The main results of this effort are presented in Paper II. In this section, I explain the code and discuss some of the results beyond the description in the paper.

3.6.3.1 Numerical Set-up

The EOM (2.9) is a second order differential equation which must be split into two first order equations to be integrated numerically. Furthermore, to avoid units, the scalar field has to be normalised with respect to a mass scale. We chose the renormalisation $\chi = \phi/M_{\rm Pl}$ and an auxillary velocity field $q = \chi'/a$,

where a prime denotes a derivative with respect to super-comoving time[4]. The numerical leapfrog integration evolves the variables q and χ as a set of coupled differential equations, specifically

$$q_{i+1/2} = q_{i-1/2} + q'_i \times \Delta t, \tag{3.5}$$

$$\chi_{i+1} = \chi_i + a q_{i+1/2} \times \Delta t. \tag{3.6}$$

The derivative of q is $q' = a'\chi' + a\chi''$, where χ'' can be derived from the EOM by transforming cosmic time derivatives to supercomoving time derivatives. I will not do this derivation here, but rather re-state the implemented equations in their normal form.

After isolating $\ddot{\phi}$ on the left-hand side, the disformal EOM is given by

$$\ddot{\phi} = \frac{1}{(1+\gamma^2\rho)}\left[\frac{1}{a^2}\nabla^2\phi - 3H\dot{\phi} - \gamma^2\rho\left(\frac{B_{,\phi}}{2B}\dot{\phi}^2\right) - V_{,\phi}\right], \tag{3.7}$$

where

$$\gamma^2 = \frac{B}{1-2BX}. \tag{3.8}$$

The fifth force for a non-relativistic particle ($v \ll c$) in an expanding FLRW metric in the pure disformal case is given by

$$\mathbf{F}_\phi = -\frac{1}{a^2}\frac{\left(B\ddot{\phi} + \frac{1}{2}B_{,\phi}\dot{\phi}^2\right)}{1-2BX}\nabla\phi = -\frac{\gamma^2}{a^2}\left(\ddot{\phi} + \frac{B_{,\phi}}{2B}\dot{\phi}^2\right)\nabla\phi. \tag{3.9}$$

See Appendix A for the derivation of both of these equations. I implemented these disformal equations into the non-static version of `Isis` (albeit on a slightly transformed form with different variables).

For the potential V, we chose a decreasing exponential given by

$$V(\phi) = V_0 e^{-\nu\frac{\phi}{M_{\rm Pl}}}, \tag{3.10}$$

for positively valued constants V_0 and ν. For the disformal term B, we chose an increasing exponential

$$B(\phi) = B_0 e^{\beta\frac{\phi}{M_{\rm Pl}}}, \tag{3.11}$$

where B_0 is required to be positive (to avoid superluminal wave propagation in the EOM), and β is a dimensionless constant specifying the disformal slope. The special case $\beta = 0$ gives a constant disformal coupling $B(\phi) = B_0$, which is sufficient to understand the basic disformal effects; I will assume $\beta = 0$ in this thesis, even though we describe some effects of $\beta \neq 0$ in Paper II.

The name *disformal quintessence* comes from the sloped shape of the potential, which allows the field to roll and give rise to quintessence dark energy. The exponential forms of B and V are widely employed when studying disformal quintessence in the background and in the linear regime [BM18; Koi08; vM15;

[4]Super-comoving time coordinates are used in `Ramses`. The supercomoving time τ is defined as $a^2 \mathrm{d}\tau = \mathrm{d}t$.

Zum+10]. One of the advantages of exponentials is that they allow us to write the derivatives in a compact form where

$$V_{,\phi} = -\frac{\nu}{M_{\rm Pl}} V(\phi), \tag{3.12}$$

$$B_{,\phi} = \frac{\beta}{M_{\rm Pl}} B(\phi). \tag{3.13}$$

We chose a flat $\phi = 0$ initial condition for the disformally coupled scalar field. The global initial value of the field is not an independent parameter when studying this model; Thanks to the exponential forms of B and V, a shift in the initial background value can be absorbed in a redefinition of the constants B_0 and V_0. The initial perturbations of the field can in theory have an effect, which we neglect when setting $\phi = 0$. Our choice of a uniform initial field value does not correspond to the value that could be calculated from linear perturbation theory. In Paper II we argue that the matter distribution is not significantly affected by this choice, because the fifth force is small compared to the Newtonian force before the field perturbations reach the equilibrium value. In figure 7 of Paper II, the relative error between the simulated scalar field and the theoretical equilibrium scalar field (see equation 3.16) drops below 1 % before redshift $z = 4$. We expect primordial gradients in the scalar field to be washed out during inflation, and we expect the scalar field acceleration $\ddot{\phi}$ to be suppressed in the early universe due to the high matter density. This suppresses the fifth force ($F_\phi \propto \ddot{\phi}\nabla\phi$), as well as $\dot{\phi}$ at redshifts before the start of the N-body simulation, at least for the parameters studied here. A hypothetical mechanism that leads to significant field gradients and time derivatives at early times was not studied, but such an injection of kinetic energy can have a lingering effect both on the field evolution and the particle evolution at later times.

3.6.3.2 On the $1 - 2BX$ Singularity

There is a possibility for a singularity in the γ^2 term of equation (2.9). The singularity appears when the denominator of

$$\gamma^2 = \frac{B}{1 - 2BX} \tag{3.14}$$

is exactly zero, or when $2BX = 1$. In the early universe, we assume $2BX$ to be negligible because the field is frozen and the perturbations are small. To avoid the instability, we require $2BX < 1$ at later times. As the field rolls along the potential, the kinetic energy,

$$X \propto \left(\dot{\phi}\right)^2 - (\nabla\phi)^2, \tag{3.15}$$

is expected to increase. However, in a physical setting, the apparent instability is avoided because the field will gradually freeze as it approaches the singularity [ZKM13]. The finite time step of numerical methods means that the field jumps large steps at once, ignoring the progressive freezing that could have happened

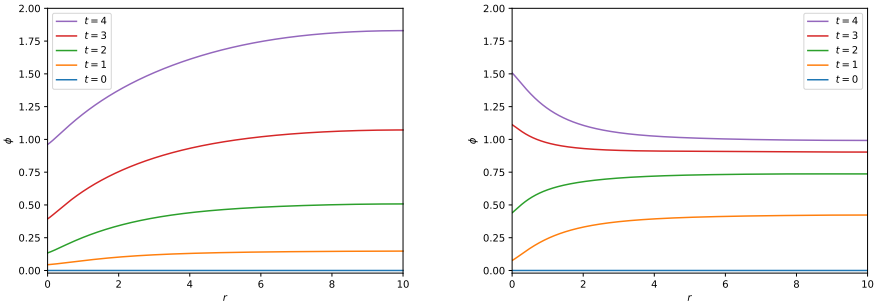

Figure 3.2: Time evolution of disformal field profile around an NFW halo. The left panel shows a scenario where the field acceleration $\ddot{\phi}$ is always positive, while the right panel shows a scenario where the field acceleration is first positive, then becomes negative. The unit along the x-axis is Mpc, while the field value along the y-axis is normalised to $M_{\rm Pl}$.

between each time step. This numerical method is usually fine in continuous regions of the effective potential, but close to singularities, this can lead to numerical errors. For some sets of parameters, the term $2BX$ can evolve fast, and special care should be taken to increase the amount of time steps accordingly. Disformal dark energy, with parameters constrained to fit the CMB ([BM18]) is allowed without numerical instabilities in the N-body case we explored.

3.6.3.3 Field Profile

The background field is expected to accelerate to higher values as it rolls down the quintessence-like potential. As the field rolls, it acquires depressions around over-dense haloes. This effect can also be explained by the suppression of the field acceleration. The left-hand panel of figure 3.2 shows how the field grows faster in low densities than in the centre of the halo ($r = 0$). The plot is created from a simulation of the disformal EOM in the high-resolution spherical code.

In Paper II we find that the scalar field perturbation evolves to become approximately proportional to the gravitational potential,

$$\phi \approx \xi_0 \Psi + \phi_0. \tag{3.16}$$

Here, ξ_0 is a factor that can be calculated from background quantities, and ϕ_0 is the background value of the scalar field. I will call equation (3.16) the *proportionality assumption*. The proportionality factor ξ_0 is an approximation of ξ, which is given by

$$\xi \equiv 2M_{\rm Pl}^2 \left(B\ddot{\phi} + \frac{1}{2} B_{,\phi} \dot{\phi}^2 \right). \tag{3.17}$$

Then, ξ_0 is calculated by using background quantities for ϕ and its derivatives. The proportionality assumption requires that the quantities used to calculate ξ_0

(i.e. B, $\dot{\phi}$, and $\ddot{\phi}$) do not deviate far from their background values. This assumption holds for most parts of the tested parameter space; The time derivatives $\dot{\phi}$ and $\ddot{\phi}$ are nearly uniform after the field velocity has reached an equilibrium roll. The full derivation of the proportionality assumption is explained in Paper II.

The factor ξ can be negative. For the case $\beta = 0$, this happens if $\ddot{\phi} < 0$, which means that the field is in a decelerating phase. A negative ξ means that the field flips from having depressions in over-dense regions to having spikes in over-dense regions. The gradient of the field changes from pointing out of over-densities to pointing into over-densities. The process of *field flipping* around a halo is seen in the right-hand panel of figure 3.2. The existence of a phase of negative field acceleration depends on the shape of the potential V, and on the model parameters. In the case of the quintessence potential, the field has a high acceleration early on, and when the slope of the potential flattens out, the field acceleration drops. Then, the Hubble friction term ($H\dot{\phi}$) is allowed to dominate and provides a negative acceleration.

3.6.3.4 Repulsive Fifth Forces and Reduced Power

The fifth force given in equation (3.9) can be written as

$$\mathbf{F}_\phi \propto -\xi \nabla \phi. \tag{3.18}$$

Under the proportionality assumption for the scalar field, the fifth force is approximated as

$$\mathbf{F}_\phi \propto -\xi_0^2 \nabla \Psi. \tag{3.19}$$

In Paper II we find that under these assumptions, the field profile flips at the same time as the fifth force pre-factor changes sign, and the fifth force always points in the same direction as the Newtonian force.

In the full N-body simulation, ξ is calculated locally without the proportionality assumption. In this case, the pre-factor ξ in the equation for the fifth force (3.18) is allowed to change sign first, while the field spends some time flipping. This results in a short period of time when the fifth force points in the opposite direction of Newtonian gravity. For the sets of parameters studied, just one of the simulations exhibited a field flip with transient repulsive fifth forces. In this simulation, the repulsive forces lasted for a short period of time and were weak compared to gravity, which leads us to believe that they do not have a big impact on cosmological structures.

A few of the simulations exhibited a small reduction of power on small scales with respect to ΛCDM, but we conclude that this is not due to prolonged repulsive fifth forces. The reason for this reduction is not yet known, but one possibility is that when the attractive fifth forces increase, they tighten the binding energy of virialised structures, but when the fifth forces decrease, energy conservation leads to a subsequent expansion of the structures. This possibility has to be studied further.

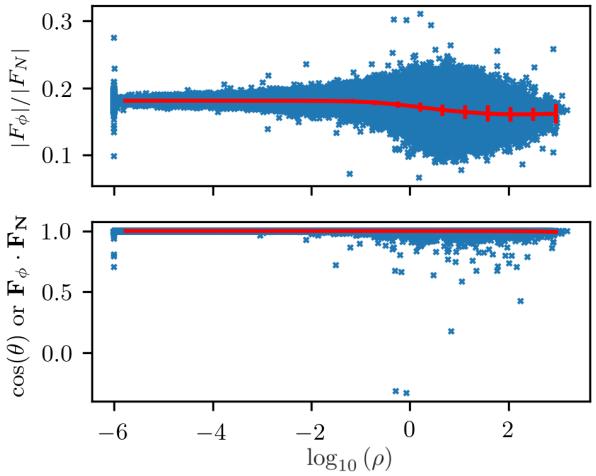

Figure 3.3: The disformal fifth force compared to the Newtonian force, as a function of the local density. The top panel compares the absolute value (amplitude), while the bottom panel compares the dot product. A dot product of 1 means that the forces are parallel, while -1 means that the forces are anti-parallel. Each cross is one grid cell in the simulation of 256^3 grid cells. The red line is the binned average, with error bars indicating the standard deviation in that bin.

3.6.4 Speeding up Modified Gravity Simulations by Assuming G_{eff} Globally

In Paper II we find that we can apply a time-varying effective gravitational constant $G \to G_{\text{eff}}(t)$ to achieve a decent approximation to the disformal fifth force on large scales. A plot of the fifth forces from one snapshot of one of the simulations is shown in figure 3.3. From this plot we can see that the average of the ratio of $|F_\phi| / |F_N|$ is fairly flat around 0.2, which indicates that in this snapshot we could apply $G_{\text{eff}} \approx G \times 1.2$ instead of calculating the fifth force explicitly.

Applying a global G_{eff} is a lot faster than typical simulations for modified gravity because there is no need to simulate the scalar field; a Newtonian simulation with a formula for $G_{\text{eff}}(t)$ is sufficient. This implementation is a work in progress, and is expected to work for the disformal quintessence, and several non-screened conformal models. This kind of simulations can be especially important for exploring models which hides their modifications to gravity through a coupling in the dark sector instead of a strong screening mechanism.

This method implies losing some phenomenology, which can be understood from the spread in figure 3.3, where the fifth forces in the individual grid cells

are not arranged in a line, but have values ranging from 0.1 to 0.3 times the Newtonian force. This spread is not achieved with the approximation of a global G_{eff}. Furthermore, a flat value $|F_\phi| / |F_N| = 0.2$ does not account for the reduced fifth force due to the disformal screening, an effect which we see evidence of in the high-density end on the right-hand side of the plot.

Papers

Paper I

Cosmic Tsunamis in Modified Gravity: Scalar waves disrupting screening mechanisms

Robert Hagala, Claudio Llinares, David F. Mota

Published in *Physical Review Letters*, March 2017, volume 118, issue 10, 101301. DOI: 10.1103/PhysRevLett.118.101301. arXiv: 1607.02600.

Cosmic Tsunamis in Modified Gravity: Disruption of Screening Mechanisms from Scalar Waves

R. Hagala,[1,*] C. Llinares,[2] and D. F. Mota[1]
[1]Institute of Theoretical Astrophysics, University of Oslo, PO Box 1029 Blindern, 0315 Oslo, Norway
[2]Institute for Computational Cosmology, Department of Physics, Durham University, Durham DH1 3LE, United Kingdom
(Received 18 July 2016; revised manuscript received 24 November 2016; published 10 March 2017)

Extending general relativity by adding extra degrees of freedom is a popular approach for explaining the accelerated expansion of the Universe and to build high energy completions of the theory of gravity. The presence of such new degrees of freedom is, however, tightly constrained from several observations and experiments that aim to test general relativity in a wide range of scales. The viability of a given modified theory of gravity, therefore, strongly depends on the existence of a screening mechanism that suppresses the extra degrees of freedom. We perform simulations, and find that waves propagating in the new degrees of freedom can significantly impact the efficiency of some screening mechanisms, thereby threatening the viability of these modified gravity theories. Specifically, we show that the waves produced in the symmetron model can increase the amplitude of the fifth force and the parametrized post Newtonian parameters by several orders of magnitude.

DOI: 10.1103/PhysRevLett.118.101301

Since 1998, it has been known that the Universe expands at an accelerating rate that is consistent with the existence of a cosmological constant [1]. Attempts to interpret the cosmological constant as the vacuum energy from particle physics yields a mismatch of several orders of magnitude. This is known as the cosmological constant problem [2]. A possible solution to this problem may lie on an extension of general relativity in such a way that a new gravity degree of freedom drives the accelerated expansion on large scales [3].

General relativity is, however, one of the most successfully tested theories in a wide range of scales, including table top experiments on Earth, laser ranging and radio wave bending in the Solar System, the rotation of black hole binaries, and the timing of pulsars [4]. Therefore, any modification to Einstein's gravity must include a screening mechanism to hide the new extra degree of freedom and reduce the theory to general relativity in those well tested regimes [5].

The common feature to all the screening mechanisms proposed in the literature is that they are built, and their efficiency tested, assuming the so called quasistatic approximation for the field equations. For instance, in scalar-tensor theories, a scalar degree of freedom is introduced into the standard Einstein-Hilbert action. This field follows the Klein-Gordon equation of motion, which determines both its time and spatial variations. When constructing screening mechanisms to hide the scalar field within the accurately tested regimes, the quasistatic approximation is invariably applied to the equations of motion for the field. This simplifies the calculations by implying that the scalar field is at rest in the minimum of the local effective potential at all points in space and time. This reduces the equation of motion to a Poisson-like equation, which is readily solved to find the approximated scalar field value at any point.

Notice, however, that the full equation of motion for the scalar field is, in fact, a second order differential equation in time, more similar to a wave equation. Therefore, ignoring the time evolution of the field, via the quasistatic approximation, is to shortfall effects that are only possible to realize when considering the full equation of motion [6,7].

In this Letter, we find that, when relaxing the quasistatic approximation, the presence of waves may result in striking consequences for the efficiency and viability of the screening mechanism. In particular, we show that energetic waves in the extra degree of freedom strongly weaken the screening process for a theory with a standard kinetic term. Therefore, modified gravity theories previously considered viable may, in fact, be ruled out by the present days gravity experiments and observational data. To understand the implications of these waves in greater detail, we simulate a scalar degree of freedom with externally generated waves. The waves propagate radially in towards a spherically symmetric matter distribution, modeled after the Milky Way halo.

The Model.—As a working example, we implement a specific form of modified gravity called the symmetron [8]. This is a scalar-tensor theory with a screening mechanism, constructed to hide modifications to general relativity in

high density regions. In spite of this specificity, the results presented in this Letter should be considered for any modified gravity theories that have extra degrees of freedom with wave-type equations of motion. Examples of such screening mechanisms include the chameleon [9], disformal [10], Dirac-Born-Infeld fields [11], or K-mouflage [12].

We consider the following general scalar-tensor action for canonical scalar fields:

$$S = \int \left[\sqrt{-g} \left(\frac{R}{16\pi G} - \frac{1}{2}\phi^{,\mu}\phi_{,\mu} - V(\phi) \right) + \sqrt{-\tilde{g}}\tilde{\mathcal{L}}_m \right] d^4x, \tag{1}$$

where g is the Einstein frame (geometric) metric, and $\tilde{g}$ is the Jordan frame metric—the metric dictating the geodesics of particles. R is the Ricci scalar, and $\tilde{\mathcal{L}}_m$ is the Lagrangian density of matter (computed using the Jordan frame metric $\tilde{g}$). The field potential $V(\phi)$ is the quartic symmetron potential with the three free parameters μ, λ, and V_0

$$V(\phi) = -\frac{1}{2}\mu^2\phi^2 + \frac{1}{4}\lambda\phi^4 + V_0. \tag{2}$$

The Jordan frame metric $\tilde{g}$ is related to the Einstein frame metric according to the conformal transformation $\tilde{g}_{\mu\nu} = C(\phi)g_{\mu\nu}$. The specific form of C for the symmetron is $C(\phi) = 1 + (\phi/M)^2$. The mass scale M is a free parameter that gives the strength of the interaction with the matter fields.

The equation of motion for the scalar field is

$$\ddot{\phi} + 3H\dot{\phi} - \frac{1}{a^2}\nabla^2\phi = -\rho\frac{C_{,\phi}(\phi)}{2C(\phi)} - V_{,\phi}(\phi), \tag{3}$$

where a dot represents a partial derivative with respect to cosmic time, $H = (\dot{a}/a)$ is the Hubble parameter, and a is the scale factor. The Einstein frame metric is assumed to be a flat Friedmann-Lemaître-Robertson-Walker metric with a single scalar perturbation Ψ_E, specifically

$$ds^2 = -(1 + 2\Psi_E)dt^2 + a^2(t)(1 - 2\Psi_E)dr^2. \tag{4}$$

For convenience, we normalize the field to the vacuum expectation value of the symmetron field, $\phi_0 \equiv (\mu/\sqrt{\lambda})$. As such, the new dimensionless field $\chi = \phi/\phi_0$ should behave in a controlled way, with $|\chi| \lesssim 1$. Also, for numerical convenience, we introduce the parameter $a_{\rm SSB}$, which defines the expansion factor at the time of spontaneous symmetry breaking. We also introduce a dimensionless symmetron coupling constant $\beta \equiv [(\phi_0 M_{\rm Pl})/M^2]$, and the range of the symmetron field in vacuum, $\lambda_0 \equiv [1/(\sqrt{2}\mu)]$. By taking into account these definitions, we can rewrite Eq. (3) as

$$\ddot{\chi} + 3H\dot{\chi} - \frac{\nabla^2\chi}{a^2} = -\frac{1}{2\lambda_0^2}\left[\left(\frac{a_{\rm SSB}^3}{C}\frac{\rho}{\rho_0} - 1 \right)\chi + \chi^3 \right], \tag{5}$$

where ρ is the total matter density, and ρ_0 the background density of the Universe.

As a working example, we fix the symmetron parameters such that $\beta = 1$, $a_{\rm SSB} = 0.5$, and $\lambda_0 = 0.25$ Mpc$/h$. This is equivalent to a symmetron mass $M = 3.4 \times 10^{-4} M_{\rm pl} = 4.2 \times 10^{15}$ GeV$/c^2$. These parameters are being widely assumed to represent a viable model that evades all the bounds from both Solar System and astrophysical data. With this choice of parameters, we aim to prove that even such a model may, in fact, be ruled out when one fully integrates the equations of motion of the field without the quasistatic assumption and, thereby, allow for the effects of the scalar waves.

Solar System constraints.—In order to test how screening mechanisms work in the Solar System, the community generally chooses a static, spherically symmetric matter distribution to mimic the Galaxy. We follow this approach and choose the Navarro-Frenk-White (NFW) density profile with the characteristics to represent the Milky Way galaxy, specifically with a virial radius of $r_{\rm vir} = 137$ kpc$/h$ and concentration $c = 28$, resulting in a halo mass of $1.0 \times 10^{12}\ M_\odot$ and a circular velocity of 220 km/s at 8 kpc. The reason for the high value of the concentration is simply that we are modeling not only dark matter, but the total matter of the Milky Way, which is more concentrated than the pure dark matter halo. We also did the calculations with an Einasto profile with identical virial mass, and found that the results presented in this Letter are not very sensitive to the choice of distribution. Because of limitations of spherical symmetry, we did not model a galactic disc.

One of the most precisely measured gravity parameters to probe deviations from general relativity is the parametrized post-Newtonian (PPN) parameter γ. It can be expressed as the ratio of the metric perturbations in the Jordan frame, Ψ_J and Φ_J. We find the expression for $\gamma - 1$ to be

$$\gamma - 1 = -\frac{\phi^2}{M^2}\frac{2}{\frac{\phi^2}{M^2} - 2\Psi_E - 2\Psi_E\frac{\phi^2}{M^2}}. \tag{6}$$

In general relativity, $\gamma = 1$ exactly. The strongest constraint to date, measured by the Cassini spacecraft [13], is $\gamma - 1 = (2.1 \pm 2.3) \times 10^{-5}$.

The screening mechanism of the symmetron model works by modifying the effective potential such that the field value is pushed towards zero in high density regions—like the inner regions of the Galaxy. This results in $\gamma - 1 \to 0$, such that the deviations from general relativity in the proximity of the Solar System are small. The same occurs for the fifth force F_ϕ associated to the scalar field.

We calculate the γ parameter arising from the smoothed matter distribution of the Milky Way. Note that, by using this method, we find an upper bound on the actual value of $|\gamma - 1|$ in the inner Solar System. This is because we do not include the presence of massive bodies like the Sun, which will increase the screening to some degree. Nevertheless, most of the screening is believed to come from the matter distribution of the Galaxy because, in the symmetron model, the Solar System cannot screen itself in vacuum, and therefore, the theory depends on a working screening from the Galaxy.

Simulations.—Since the equation of motion is a hyperbolic partial differential equation, it can be solved as an initial value and boundary condition problem. The initial condition at $t = 0$ is chosen to be the static solution of the nonlinear Klein-Gordon equation of motion. With a constant boundary condition, this would imply that the field will stay at rest forever. The boundary condition at the edge of the simulation at $r_{\max}$ is chosen to emulate incoming sinusoidal waves in the scalar field, specifically $\chi(r_{\max}, t) = \chi_0(r_{\max}) + A \sin(\omega t)$. Possible sources of such waves will be discussed later.

We set up a radial grid, divided into linearly spaced steps Δr up to $r_{\max} = 4$ Mpc$/h$. On each of the grid points, we specify the matter density according to the NFW halo. Starting from the initial value and with the inclusion of incoming waves, we evolve Eq. (5) forward in time steps of size Δt, using the leapfrog algorithm for time integration in each grid point. Tests of this technique applied to the symmetron are presented in [6,14]. We are only interested in events that happen during the last few megayears of cosmic time, meaning that we take the approximations $z \approx 0$ and $a \approx 1$ in all computations. Spatial derivatives are found using a finite difference method in spherical coordinates, assuming all derivatives in the tangential directions vanish. The code outputs the evolution of the scalar field and, more importantly, the value of $|\gamma - 1|$ at 8 kpc from the center—corresponding to the position of the Solar System in the Milky Way.

We confirm that the values used for technical parameters of our solver give a stable solution by running convergence tests. These are performed by increasing the resolution in factors of two (both temporal and spatial resolution separately) until the resulting scalar field at some later time $t_{\max}$ does not change significantly with resolution.

Results.—Figure 1 shows an example of how the PPN parameter γ changes when a wave enters the inner 100 kpc of the Milky Way. The vertical line shows the position of the Solar System, which we assume to be 8 kpc from the Galactic center. The modifications to gravity are initially screened very well in the regions around this position, with $|\gamma - 1| < 10^{-8}$ (blue dashed line). However, after the wave has arrived (black solid line), the scalar field is perturbed enough to breach the Solar System constraints, $|\gamma - 1| > 2 \times 10^{-5}$. In other words, the screening mechanism breaks down under these circumstances. The wave in this particular simulation has an amplitude $A = 0.01$ and a frequency $\omega = 40$ Myr^{-1}. The cusps are regions where the scalar field is zero, which exist since the wave oscillates both above and below $\chi = 0$.

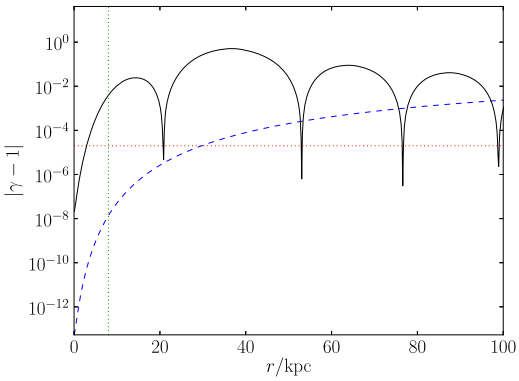

FIG. 1. The PPN parameter $|\gamma - 1|$, plotted against distance from the center of the Galaxy. The curves show $|\gamma - 1|$ in the quasistatic case (blue dashed line), as well as after a scalar wave has entered the halo (black solid line). The vertical (green dotted) line indicates the position of the Solar System, and the horizontal (red dotted) line indicates the highest allowed value of $\gamma - 1$ in the Solar System from the Cassini experiment. When the wave enters the Milky Way, it increases the value of $|\gamma - 1|$ by several orders of magnitude.

When measuring γ arising from a single sinusoidal wave with low frequency, there is a possibility that the local wave is between two extrema at the time of measurement. This could render this kind of detection difficult for several thousand years. Nevertheless, given that various astrophysical events—such as supernovae—can generate waves, the probability that one of the wavefronts would bring us away from the minima at the present time is not negligible.

In order to investigate how our result depends on the frequency ω and amplitude A of the waves, we simulate incoming waves with several values of these two parameters. Figure 2 shows the maximum growth of $|\gamma - 1|$ that we found at 8 kpc from the Galactic center. Brighter colors mean a larger increase of $|\gamma - 1|$ compared to the quasistatic approximation. The values of the frequency and amplitude that lie in the black region of the plot, give waves that do not significantly impact γ compared to the quasistatic solution. Therefore, in this region of parameter space, the screening mechanism is efficient and hides the extra degree of freedom from gravity experiments.

From Figure 2, it is possible to conclude that higher frequencies and amplitudes for the incoming scalar waves give larger deviations from the general relativity result (i.e., $\gamma = 1$). The limit where amplitude and frequency go to zero is equivalent to the quasistatic limit, where no waves are produced and their energy is zero. As one goes into the high

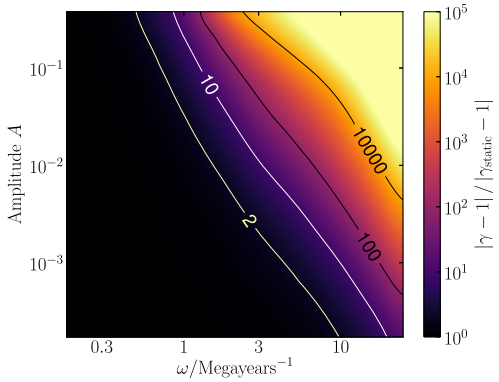

FIG. 2. Maximum increase in the PPN parameter $|\gamma - 1|$ due to incoming scalar field waves at the position of the Sun in the Galaxy (8 kpc from the center) as a function of amplitude and frequency of the incoming waves. The color indicates by which factor $|\gamma - 1|$ is increased when compared to the quasistatic case with no waves.

frequency and amplitude regime, the waves carry more energy, and therefore, the PPN parameter γ starts deviating significantly from the quasistatic limit. Note that, since in the symmetron model, the fifth force is $F_\phi \propto \nabla\phi^2/M^2$, these values can be immediately extrapolated to the impact of the waves on this quantity [8].

The dependence of the γ PPN parameter on the wave amplitude is straightforward to understand: When a wave propagates through the screened regions of the halo, a larger amplitude wave will lead to larger displacements of the field from the screening value $\phi \approx 0$. Therefore, $|\gamma - 1| \propto \phi^2$ will increase accordingly.

The frequency dependence of the γ parameter is a consequence of the following: The effective potential of the symmetron grows steeper and narrower in high density areas. In other words, the mass of the field increases towards the center of the halo. Therefore, it becomes more difficult to perturb the field away from the minimum, and a higher wave energy is needed to displace it. Specifically, if the energy of the external waves is small compared to the mass of the field, the field will not be perturbed and the γ parameter will not be affected.

The results obtained in this Letter imply that if waves with sufficient amplitude or frequency can somehow be generated in a given model for modified gravity, they will have to be taken into account when constraining the model parameters. Cosmic tsunamis, resulting from extreme events, could even completely ruin the screening mechanisms in modified gravity by increasing the deviations from general relativity by several orders of magnitude compared to the quasistatic case. A subject that must be discussed now is the generation of such waves. Extreme events on small scales, such as collision of neutron stars, stellar, or super-massive black holes are obvious examples. Generation of waves by pulsating stars are another possibility [15].

In the specific case of the symmetron model, it is possible to obtain waves from events that occur on cosmological scales. First, the symmetron model undergoes a phase transition when the density falls below a specific threshold. This transition first occurs in voids when the expansion factor is close to $a_{\rm SSB}$ [6,14]. When this happens, the scalar field receives a kick, which produces waves traveling from the center of the voids towards the dark matter halos. By doing postprocessing of simulations presented in [16], we find that, in a symmetron model with slightly different parameters, the amplitude of cosmological waves is typically smaller that 0.1 and the associated frequencies are of the order of 1/Myr. Note that these values depend on the model parameters and, hence, must be taken only as indicative. Scalar waves can also be created through the collapse of topological defects, which are known to exist in any model in which such phase transition occurs. The energies associated with these kinds of waves are studied in [17].

Conclusions.—Modifications to general relativity have long been studied, both when searching for the source of the accelerated expansion of the Universe, and to construct a UV complete theory of gravity. However, there are strong Solar System constraints on the deviation from Einstein's gravity when extending the theory by adding new degrees of freedom. Thus, the viability of modified theories of gravity is strongly dependent on the existence of a screening mechanism that suppresses any extra degrees of freedom at these scales. In this Letter, we show that waves propagating in an additional gravity degree of freedom, may significantly spoil the screening mechanism and, hence, jeopardize the viability of the given modified gravity theory. Specifically, we show that waves in a given model can increase the amplitude of the fifth force and the post-Newtonian parameter $|\gamma - 1|$ by several orders of magnitude, rendering theories previously assumed to be viable unfeasible.

We reach our conclusions by performing numerical simulations of the propagation of waves through a Milky Way sized dark matter halo. For a particular set of model parameters, we determine the importance of the amplitude and frequency of the incoming waves. Increased amplitudes and frequencies (i.e., higher energy waves) lead to a greater impact on observables associated to the Solar System.

Our results were obtained in the context of a specific model of modified gravity, the symmetron model. We expect that they can be generalized to other models as well. For instance, including an extra disformal term in the coupling of the symmetron field can increase the amplitude of the oscillations of the scalar field in the center of the halos [16], thus, weakening the efficiency of the screening mechanism even further. Waves were also studied in a particular version of $f(R)$ theories [18]. While the impact of these waves was

found to be negligible in a cosmological context (i.e., structure formation), their effect in Solar System tests may still be detectable and help in further constraining the model. To demonstrate that similar effects can be expected in other theories, we propose a simple calculation regarding a viable chameleon model [19] ($n = 1, M = 10^{-3} M_{\rm Pl}, \Lambda = 2$ meV). When a white dwarf explodes as a type Ia supernova, waves in the chameleon field will be measurable at several Mpc distance. Full details on this calculation can be found in the Supplemental Material [20].

The applicability of the quasistatic approximation should be carefully analyzed when obtaining constraints for modified gravity theories from Solar System experiments. Our results show that, in modified gravity, the Solar System—and indeed, the Galaxy—can not be studied in isolation; events that occur on cosmological scales might actually impact events that happen in the inner Solar System. While our conclusions make it more difficult to build viable modified gravity theories based on screening mechanisms, the existence of nonstatic effects opens a completely new window for developing new tests of gravity.

We thank Chung-Chi Lee for useful discussion. R. H. and D. F. M. acknowledge support from the Research Council of Norway, and the NOTUR facilities. C. L. L. acknowledges support from the STFC consolidated Grant No. ST/L00075X/1.

*robert.hagala@astro.uio.no

[1] A. G. Riess *et al.*, Astrophys. J. **116**, 1009 (1998).
[2] S. Weinberg, Rev. Mod. Phys. **61**, 1 (1989).
[3] T. Clifton, P. G. Ferreira, A. Padilla, and C. Skordis, Phys. Rep. **513**, 1 (2012).
[4] S. Reynaud and M.-T. Jaekel, in *Atom Optics and Space Physics: Proceedings of the International School of Physics "Enrico Fermi," Course CLXVIII, Varenna on Lake Como, Villa Monastero, 2007*, edited by E. Arimondo, W. Ertmer, W. P. Schleich, and E. M. Rasel (IOS Press, Amsterdam, 2009), p. 203.
[5] A. Joyce, B. Jain, J. Khoury, and M. Trodden, Phys. Rep. **568**, 1 (2015).
[6] C. Llinares and D. F. Mota, Phys. Rev. Lett. **110**, 161101 (2013).
[7] J. Ø. Lindroos, C. Llinares, and D. F. Mota, Phys. Rev. D **93**, 044050 (2016).
[8] K. Hinterbichler and J. Khoury, Phys. Rev. Lett. **104**, 231301 (2010).
[9] J. Khoury and A. Weltman, Phys. Rev. Lett. **93**, 171104 (2004).
[10] T. S. Koivisto, D. F. Mota, and M. Zumalacárregui, Phys. Rev. Lett. **109**, 241102 (2012).
[11] C. Burrage and J. Khoury, Phys. Rev. D **90**, 024001 (2014).
[12] E. Babichev, C. Deffayet, and R. Ziour, Int. J. Mod. Phys. D **18**, 2147 (2009).
[13] B. Bertotti, L. Iess, and P. Tortora, Nature (London) **425**, 374 (2003).
[14] C. Llinares and D. F. Mota, Phys. Rev. D **89**, 084023 (2014).
[15] A. Silvestri, Phys. Rev. Lett. **106**, 251101 (2011).
[16] R. Hagala, C. Llinares, and D. F. Mota, Astron. Astrophys. **585**, A37 (2016).
[17] C. Llinares and L. Pogosian, Phys. Rev. D **90**, 124041 (2014).
[18] S. Bose, W. A. Hellwing, and B. Li, J. Cosmol. Astropart. Phys. 02 (2015) 034.
[19] C. Burrage and J. Sakstein, J. Cosmol. Astropart. Phys. 11 (2016) 045.
[20] See Supplemental Material at http://link.aps.org/supplemental/10.1103/PhysRevLett.118.101301 for detailed calculations estimating the impact of waves produced in a Supernova type Ia explosion, by considering the energy difference in the chameleon effective potential.

Supplementary Material, Cosmic Tsunamis in Modified Gravity

R. Hagala, C. Llinares, D. F. Mota

Chameleon Waves from Supernova Type Ia

In this supplementary material we do an order-of-magnitude estimate of the effects of Chameleon scalar field waves generated by a type Ia supernova. We will first find the energy that can be released into scalar field waves in such an event, and then consider the amplitude of scalar waves with this energy. Finally, we will predict the measurable impact on $|\gamma - 1|$ from waves with this amplitude. All calculations are initially performed with natural units $\hbar = c = 1$, with preferred units of mass. These will then be translated to lengths or times as needed.

Let us regard a simple $n = 1$ Chameleon field with effective potential

$$V_{\rm eff} = \rho\left(1 + \frac{\beta}{M_{\rm Pl}}\phi\right) + \frac{M^5}{\phi}. \tag{1}$$

For such a model, the scalar field value at the minimum of the potential and the effective mass will be given by

$$\phi_{\rm min} = \left(\frac{M^5 M_{\rm Pl}}{\rho\beta}\right)^{1/2}, \tag{2}$$

$$m_{\rm eff} = \left(\frac{4\rho^3\beta^3}{M_{\rm Pl}^3 M^5}\right)^{1/4}. \tag{3}$$

To be specific, we set

$$M = 0.2\,{\rm meV} \approx 10^{-31} M_{\rm Pl},$$
$$\beta = 10^3,$$

in agreement with all current observational and experimental constraints [1][2]. This choice corresponds to a Chameleon range in the background density of the universe of $\lambda_c = 1/m_{\rm eff} = 0.04$ parsec.

For the supernova, we will assume the simplest possible model: a white dwarf – located in or close to our Milky Way – with radius $2 \cdot 10^6$ m, and mass $1.4 M_\odot$; it has a density of about $\rho_{\rm WD} = 10^{37}\rho_0$. This white dwarf is completely destroyed over some short time, spreading the matter evenly over several parsec such that $\rho_{\rm end} \ll \rho_{\rm WD}$. Inside the white dwarf, the Chameleon field range will be sub-micrometre scale, so we can safely assume $\phi = \phi_{\rm min}$ throughout the white dwarf.

The proposal is that there is a significant energy difference for the scalar field when the effective potential goes from a density of $\rho_{\rm WD}$ to $\rho_{\rm end}$. This energy difference will be released (at least partially) in the form of scalar field waves. Assuming the field follows the minimum of $V_{\rm eff}$ as the density changes, one can insert the expression for the field value (2) into the effective potential equation (1).

$$V_{\rm eff} = \rho + 2\left(\frac{M^5\beta\rho}{M_{\rm Pl}}\right)^{1/2}. \tag{4}$$

The change in the effective potential when the density goes from $\rho_{\rm WD}$ to $\rho_{\rm end}$ can then be found from

$$\Delta V_{\rm eff} = \rho_{\rm WD} - \rho_{\rm end} + 2\left(\frac{M^5\beta}{M_{\rm Pl}}\right)^{1/2}\left(\rho_{\rm WD}^{1/2} - \rho_{\rm end}^{1/2}\right). \tag{5}$$

Using the conversion factors

$$\rho_0 = 3\Omega_0 H_0^2 M_{\rm Pl}^2 \approx H_0^2 M_{\rm Pl}^2,$$
$$H_0 = 2 \cdot 10^{-4}\,{\rm Mpc}^{-1} \approx 6 \cdot 10^{-61} M_{\rm Pl},$$

one finds the energy density expected at the source of the supernova,

$$\Delta V_{\rm eff} \approx \rho_{\rm WD} \approx 3.6 \cdot 10^{-84} M_{\rm Pl}^4. \tag{6}$$

The other terms of equation (5) are many orders of magnitude smaller and can be safely neglected for this purpose. Assuming no Hubble friction, this energy will be diluted with $1/r^2$ as the waves travel radially outward, until they reach the solar system.

Now we need to estimate the amplitude of oscillations of the field resulting from this release. Close to the sun – where Cassini measured γ [3] – the average density is around $\rho_\odot \approx 10^{29}\rho_0$. If the field is at rest at the bottom of the effective potential, it will have a field value dictated by equation (2). For small ϕ, the Chameleon will have a γ parameter following $|\gamma - 1| \propto \phi$. Inserting numbers, we find

$$\phi_{{\rm min},\odot} = \left(2.7 \cdot 10^{-67} M_{\rm Pl}^2\right)^{1/2}$$
$$= 5.2 \cdot 10^{-34} M_{\rm Pl}.$$

To increase $|\gamma - 1|$ by a factor of 10, we would need oscillations within the potential with enough energy to lift ϕ from $\phi_{{\rm min},\odot}$ to $10 \cdot \phi_{{\rm min},\odot}$ given a constant density $\rho_\odot$. To find numbers for the energy density needed, we

can calculate the difference in the value of the effective potential V_{eff} when going from from $\phi_{\text{min},\odot}$ to $10 \cdot \phi_{\text{min},\odot}$.

$$\begin{aligned}\Delta V_{\text{eff}} &= V_{\text{eff}}\left(\phi = 10\phi_{\text{min},\odot}\right) - V_{\text{eff}}\left(\phi = \phi_{\text{min},\odot}\right) \quad (7)\\ &= 9\rho_\odot \frac{\beta}{M_{\text{Pl}}}\phi_{\text{min},\odot} - \frac{9M^5}{10\phi_{\text{min},\odot}},\\ &= \frac{81}{10}\left(\frac{\rho_\odot \beta M^5}{M_{\text{Pl}}}\right)^{1/2},\\ &\approx 1.5 \cdot 10^{-121} M_{\text{Pl}}^4. \quad (8)\end{aligned}$$

When comparing this to the scalar field energy released in the supernova (equation 5), one can find that even if less than 1% of the energy is released into waves (the rest can be transferred to the nearby matter through the fifth force), one should be able to measure a 10-fold increase in $|\gamma - 1|$ as far as 10 Mpc away from the supernova – a distance within which there are several hundreds of galaxies. This serves as proof that there exists phenomena that can release measurable scalar field waves in viable Chameleon models as well as the Symmetron model presented in the Letter.

On a final note: if we are at a minimum and not at a maximum of a wave, it could significantly lower the value of $|\gamma - 1|$. How long time will it take for the measurable maximum to arrive? To find the frequency of the waves, let us model the effective potential around ϕ_{min} to second order in $\delta\phi$, we find

$$V_{\text{eff}} \approx V_{\text{min}} + M^5\left(\frac{\rho\beta}{M^5 M_{\text{Pl}}}\right)^{3/2}(\delta\phi)^2, \quad (9)$$

a simple harmonic oscillator with natural frequency

$$\omega_0 = \sqrt{2M^5}\left(\frac{\rho\beta}{M^5 M_{\text{Pl}}}\right)^{3/4}. \quad (10)$$

Considering the energy scales we have been using in the Letter and in this reply, $\delta\phi$ is not small enough for this approximation to hold perfectly, but the order of magnitude should nevertheless give us a useful estimate. Inserting the average density of the universe ρ_0, and the chosen Chameleon parameters, we find

$$\begin{aligned}\omega_0 &= \sqrt{2 \cdot 10^{-155} M_{\text{Pl}}^5}\left(3.6 \cdot 10^{37} M_{\text{Pl}}^{-2}\right)^{3/4},\\ \omega_0 &= 6.6 \cdot 10^{-50} M_{\text{Pl}} \approx 2 \cdot 10^{-7}\,\text{Hz},\end{aligned}$$

in the order of a couple oscillations per year. Such a frequency is viable to observe in e.g. the rate of change of γ over time.

[1] C. Burrage and J. Sakstein, Journal of Cosmology and Astroparticle Physics **2016**, 045 (2016), arXiv:1609.01192.

[2] From the top left panel of Figure 3 in [1], one can check that $M_c/M_{\text{pl}} = 10^{-3}$ and $\Lambda = 2 \times 10^{-4}\,\text{eV}$ is outside of the excluded regions. In our notation, $\beta = M_{\text{pl}}/M_c = 10^3$ and $M = \Lambda = 0.2\,\text{meV}$.

[3] B. Bertotti, L. Iess, and P. Tortora, Nature **425**, 374 (2003).

Paper II

Non-linear Phenomenology of Disformally Coupled Quintessence

Claudio Llinares, Robert Hagala, David F. Mota

Accepted for publication in *Monthly Notices of the Royal Astronomical Society*, arXiv: 1902.02125.

II

MNRAS 000, 1–20 (2019) Preprint 30 September 2019 Compiled using MNRAS LATEX style file v3.0

Non-linear Phenomenology of Disformally Coupled Quintessence

Claudio Llinares,[1,2]* Robert Hagala[3], and David F. Mota[3]
[1]Institute of Cosmology and Gravitation, University of Portsmouth, Dennis Sciama Building, Portsmouth PO1 3FX, United Kingdom
[2]Institute for Computational Cosmology, Department of Physics, Durham University, Durham DH1 3LE, U.K.
[3]Institute of Theoretical Astrophysics, University of Oslo, PO Box 1029 Blindern, 0315 Oslo, Norway

Accepted XXX. Received YYY; in original form ZZZ

ABSTRACT
The Quintessence model is one of the simplest and better known alternatives to Einstein's theory for gravity. The properties of the solutions have been studied in great detail in the background, linear and non-linear contexts in cosmology. Here we discuss new phenomenology that is induced by adding disformal terms to the interactions. Among other results, we show analytically and using cosmological simulations ran with the code `Isis` that the model posses a mechanism through which is it possible to obtain repulsive fifth forces, which are opposite to gravity. Although the equations are very complex, we also find that most of the new phenomenology can be explained by studying background quantities. We used our simulation data to test approximate relations that exist between the metric and scalar field perturbations as well as between the fifth force and gravity. Excellent agreement was found between exact and approximated solutions, which opens the way for running disformal gravity cosmological simulations using simply a Newtonian solver. These results could not only help us to find new ways of testing gravity, but also provide new motivations for building alternative models.

Key words: gravitation – cosmology:theory – cosmology:dark energy – cosmology:dark matter – cosmology:large-scale structure of Universe – methods: numerical

1 INTRODUCTION

Observations of distant supernovae, quasars, and of the Cosmic Microwave Background are consistent with a universe with late time accelerated expansion (Riess & et al. (1998); Astier et al. (2006); Risaliti & Lusso (2015); Planck Collaboration et al. (2016a)). Although this effect can be mimicked by introducing a cosmological constant to Einstein's equations, the true nature of the expansion is still unknown. Moreover, the apparent value of the cosmological constant does not correspond to the vacuum energy predicted by particle physics (e.g. Weinberg 1989). Among the several solutions to these inconsistencies, there is the idea of modifying Einstein's theory for gravity. A comprehensive description of many of these theories and their cosmological implications can be found in reviews by Clifton et al. (2012), Amendola et al. (2018), Copeland et al. (2006), Silvestri & Trodden (2009), Weinberg et al. (2013), Joyce et al. (2015), Lue et al. (2004), Koyama (2016), Nojiri et al. (2017) or Li et al. (2018).

Many of these modified gravity (MG) theories can be interpreted as having two geometries for space-time. One of these two geometries characterizes the curvature of space-time, while the other describes the impact that this curvature has on the dynamics of matter. The simplest way of relating these two metrics is through a conformal transformation (i.e. one metric is obtained from the other with a rescaling). This rescaling factor is equal in all dimensions and hence conserves shapes. The next step in complexity consists in adding a dependence with the direction to this relation. This can be done through so called disformal transformations, which in the case of scalar-tensor theories depend on the derivatives of a scalar field (Bekenstein 1993). These kind of transformations have been studied in several contexts in cosmology such as inflation (Kaloper 2004), dark matter (Skordis et al. 2006; Arroja et al. 2015), dark energy (Koivisto 2008; Koivisto & Mota 2008; van de Bruck et al. 2017; Sakstein 2015), screening of modified gravity (Koivisto et al. 2012; Ip et al. 2015), non-linear structure formation (Hagala et al. 2016) and others (Barrow & Mota 2003; Brax et al. 2013; Bettoni & Liberati 2013; Deruelle & Rua 2014; Ben Achour et al. 2016; van de Bruck et al. 2016; Sakstein 2014; Sakstein & Verner 2015).

In this work, we will study the impact that the addition

* E-mail: claudio.llinares@port.ac.uk

of a disformal coupling has on the solutions of field equations and the non-linear matter distribution. We give a concrete example which we obtained by perturbing with a disformal coupling the quintessence model, which is one of the best known extended models of gravity. Contrary to other works in which the emphasis is put on parameter estimation, here we are interested in finding novel phenomenology associated to this coupling, independently of the validity of the model from an observational perspective. Doing this is important because knowing what effects are associated to this particular coupling could help to construct models with similar phenomenology, but that are compatible with specific data sets. This in turn may enable us to construct novel tests of gravity based on this new phenomenology.

Among other characteristics of the solutions of the Klein-Gordon equation for the quintessence field, we will discuss a very simple relation that the disformal coupling induces between this field and the gravitational potential, which can be translated into a similar relation between the fifth force associated to the scalar field and gravity. We will first analyse this and other effects analytically. We will confirm these estimations a posteriori in a realistic set up given by fully non-linear cosmological simulations. These simulations track the scalar field by means of a non-linear hyperbolic solver which takes into account time derivatives in the background as well as in the perturbations and thus, provides the most accurate solution can that be obtained, without assuming specific symmetries or neglecting terms in the equations.

We present details of the model in section 2. In section 3 we describe analytical properties of the evolution of the background and perturbed scalar field as well as of the fifth force that arises from it. Section 4 describes the cosmological simulation suit in which we base our non-linear analysis. We present results from these simulations on the scalar field and matter distributions in Sections 5 and 6 respectively. We summarize our results and conclude in section 7.

2 DISFORMALLY COUPLED QUINTESSENCE

The model that we consider in this work can be defined with the following action

$$S=\int\left[\sqrt{-g}\left(\frac{R}{16\pi G}+X-V(\phi)\right)+\sqrt{-g}\mathscr{L}_B+\sqrt{-\tilde{g}}\tilde{\mathscr{L}}_{DM}\right]\mathrm{d}^4x, \tag{1}$$

where X is the kinetic energy density of the field, defined by

$$X\equiv-\frac{1}{2}\phi^{,a}\phi_{,a} \tag{2}$$

and $\mathscr{L}_B$ and $\tilde{\mathscr{L}}_{DM}$ are the Lagrangians of the baryonic and dark matter fields respectively. We assume that the coupling is non-universal and that these two fields are coupled to the Einstein and Jordan frames metrics g_{ab} and $\tilde{g}_{ab}$ respectively, which are related through the following disformal transformation:

$$\tilde{g}_{ab}=g_{ab}+B(\phi)\,\phi_{,a}\phi_{,b}. \tag{3}$$

The reason for adopting a non-universal coupling is that the model does not include a screening mechanism. With this assumption, we ensure that only the dark matter component of the Universe will be affected by the modification to gravity and that Solar System constraints will be fulfilled. Furthermore, the choice of a non-universal coupling also ensures that the model is compatible with recent constraints on the speed of gravity waves that were obtained through the detection of an optical counterpart of a black-hole collision (Abbott et al. 2017). Note that a similar approach was followed by several authors already (Xia 2013; Li & Barrow 2011; Skordis et al. 2015; Brevik et al. 2015; van de Bruck & Morrice 2015). Screening mechanisms may be added by making appropriate choices of the conformal part of the transformation, which we assume is equal to one. An example of such a procedure was presented by Hagala et al. (2016), who studied the effects of a disformal coupling included on top of the symmetron model, which is defined by a conformal coupling $1+\phi^2$.

We choose the following form for the disformal coupling B and the potential V

$$B(\phi)=B_0\exp\left(\beta\phi/M_{\rm pl}\right), \tag{4}$$

$$V(\phi)=V_0\exp\left(-\nu\phi/M_{\rm pl}\right), \tag{5}$$

which were already studied on several occasions by Koivisto (2008), Koivisto et al. (2012), Zumalacárregui et al. (2013), van de Bruck & Morrice (2015), van de Bruck et al. (2016), Zumalacárregui et al. (2010) and Sakstein (2015). This choice was made not only because it provides simple equations from which several analytical properties can be studied, but also because a change of the initial value of the scalar field, $\phi\rightarrow\phi_{\rm init}+\tilde{\phi}$, can be collected into a change of the parameters B_0 and V_0. Taking this into account releases us from treating the initial value of the field as a free parameter, allowing us to fix $\phi_{\rm init}=0$ without loss of generality.

We will restrict our analysis to positive values of B_0, V_0, and ν. The potential $V(\phi)$ is thus a decreasing function of ϕ, which will result in a background field rolling down the potential towards infinity. Negative values of ν would simply make the field roll towards negative values instead, and the analysis in this paper would be identical after the transformation $\phi\rightarrow-\phi$ and $\beta\rightarrow-\beta$. A positive choice of B_0 is needed to ensure $B(\phi)>0$. As mentioned by Bekenstein (1993), a negative coupling $B(\phi)$ breaks causality by allowing information in the scalar field to propagate faster than the speed of light. We will look at three different general cases for β: negative, positive, and zero. These correspond to a disformal coupling $B(\phi)$ which is respectively decreasing with ϕ, increasing with ϕ, or constant.

Variation of the action (1) with respect to the field ϕ yields the following equation of motion for the scalar field:

$$\ddot{\phi}=\frac{1}{(1+\gamma^2\rho)}\left[\frac{c^2}{a^2}\nabla^2\phi-3H\dot{\phi}-\frac{B_{,\phi}\gamma^2}{2B}\rho\dot{\phi}^2-V_{,\phi}\right], \tag{6}$$

where

$$\gamma^2=\frac{B}{1+B\phi^{,a}\phi_{,a}}, \tag{7}$$

we assumed that matter is a pressureless perfect fluid and that the Einstein frame metric takes the following form:

$$\mathrm{d}s^2=-(1+2\Psi)\mathrm{d}t^2+a^2(t)(1-2\Psi)\left(\mathrm{d}x^2+\mathrm{d}y^2+\mathrm{d}z^2\right), \tag{8}$$

where the Newtonian frame scalar perturbation Ψ is the

Type of transition	Without damping	With damping
Quintessence linear → Quintessence non-linear	$T_a^{\rm nd} \equiv 2\sqrt{2}$	$T_a \equiv 5.7$ (numerical)
Disformal linear → Quintessence linear	$T_b^{\rm nd} \equiv \sqrt{6D}$	$T_b \equiv \sqrt{2D}$
Disformal linear → disformal non-linear	$T_c^{\rm nd} \equiv 3^{7/12}\Gamma^{1/3}(3/4)\sqrt{2}D^{1/4}$	$T_c \equiv T_c^{\rm nd}$

Table 1. Characteristic time scales that arise in the background solutions of the Klein-Gordon equation for Einstein-de Sitter cosmology. Note that the non-linear regimes mentioned here are associated with the moment in which the background equation for the scalar field becomes non-linear (and not to the non-linear regime usually studied in cosmology). The superscript nd makes reference to "non-damped" solutions.

usual Newtonian potential. Here and throughout this paper, a dot corresponds to a partial derivative with respect to cosmic time t. Note that the only differences that the equation of motion (6) has with respect to the usual quintessence model are:

- A factor $\left(1+\gamma^2\rho\right)^{-1}$ which changes both the speed at which the scalar field evolves in the background and the speed of scalar waves.
- The addition of a term $(B_{,\phi}\gamma^2)/(2B)\rho\dot{\phi}^2$ (i.e. an additional force acting on the field).

These two additional terms are not exclusive to the base model we choose (in this case the quintessence model), but are characteristic of the disformal coupling. The aim of this paper is to understand the consequences that these terms have in both the solutions of the Klein-Gordon equation and the non-linear distribution of matter in the Universe.

3 ANALYTICAL PROPERTIES OF THE MODEL

This section describes analytical solutions of the Klein-Gordon equation for the scalar field. We will study separately the time evolution of the scalar field in the background (for an Einstein-de Sitter universe) and its perturbations. Furthermore, we will discuss properties of the fifth force that arise from it.

3.1 Disformal field dynamics: background evolution in an Einstein-de Sitter universe

Before studying properties of the solutions, it is convenient to write the Klein-Gordon equation (6) with dimensionless variables. In the limit $\gamma^2 \to B$, the equation takes the following form:

$$\partial_{\tilde{t}}^2\tilde{\chi} = -2\frac{\tilde{t}}{\tilde{t}^2+D\exp(F\tilde{\chi})}\partial_{\tilde{t}}\tilde{\chi} - \frac{1}{2}\frac{FD}{\tilde{t}^2+D\exp(F\tilde{\chi})}(\partial_{\tilde{t}}\tilde{\chi})^2 + \frac{\tilde{t}^2}{\tilde{t}^2+D\exp(F\tilde{\chi})}\exp(-\tilde{\chi}), \quad (9)$$

where we used the following dimensionless variables:

$$\tilde{\chi} \equiv \nu\frac{\phi}{M_{\rm P}}, \quad (10)$$

$$\tilde{t} \equiv \sqrt{v_0}\nu H_0 t \quad (11)$$

and the following dimensionless parameters:

$$b_0 \equiv H_0^2M_{\rm pl}^2B_0, \qquad D \equiv \frac{4}{3}b_0v_0\nu^2, \quad (12)$$

$$v_0 \equiv \frac{V_0}{H_0^2M_{\rm pl}^2}, \qquad F \equiv \frac{\beta}{\nu}. \quad (13)$$

Cosmological energy scales are of the order of $H_0^2M_{\rm pl}^2$, meaning that these rescalings will give cosmological consequences for model parameters b_0 and v_0 close to unity. Since details of the background evolution of the metric are not expected to change the phenomenology provided by the disformal terms, we will study the simplest case: a flat universe with no cosmological constant. Thus, we derived Eq. 9 by assuming the following relations between time and expansion factor

$$a(t) = \left(\frac{3H_0t}{2}\right)^{2/3} \quad (14)$$

and the following evolution of the background density

$$\rho(a) = \frac{\rho(a=1)}{a^3} = \frac{3H_0^2M_P^2}{a^3}. \quad (15)$$

Note that this solution is not strictly valid in disformal gravity. However, taking into account corrections associated with the disformal coupling will add a new layer of complexity which is beyond the scope of this paper. We briefly discuss these solutions in Appendix B.

These definitions show that the four original free parameters V_0, ν, B_0 and β are degenerate and that the shape of the background solutions depends only on two free parameters D and F. The limit $(D,F) \to 0$ corresponds to the usual quintessence model which does not depend on any free parameter (all the information provided by the two original parameters V_0 and ν can be condensed in the rescaling of the time and the scalar field). The limit $F \to 0$ is associated with a constant disformal coupling, where $\beta = 0$. We will study these two limits first separately and then the most general case with $\beta \neq 0$.

3.1.1 Quintessence

The quintessence limit is defined by assuming $(D,F) \to 0$ and gives rise to the following Klein-Gordon equation for the evolution of the background field:

$$\partial_{\tilde{t}}^2\tilde{\chi} = -\frac{2}{\tilde{t}}\partial_{\tilde{t}}\tilde{\chi} + \exp(-\tilde{\chi}). \quad (16)$$

The solution is shaped by the presence of a damping term and of a non-linear regime which is triggered when the field is large enough to reach the non-linear part of the exponential function. In order to understand consequences of two effects, we study four different cases that correspond to equations that are and are not linearized with respect to the field and with and without the addition of the damping term. Table A1 in Appendix A summarizes properties of these four solutions. The definition of the time scales that appear in these results is given in Table 1 in this section. The left panel of Fig. 1 shows the evolution of the field in these four special cases.

The complete solution of the quintessence equation of

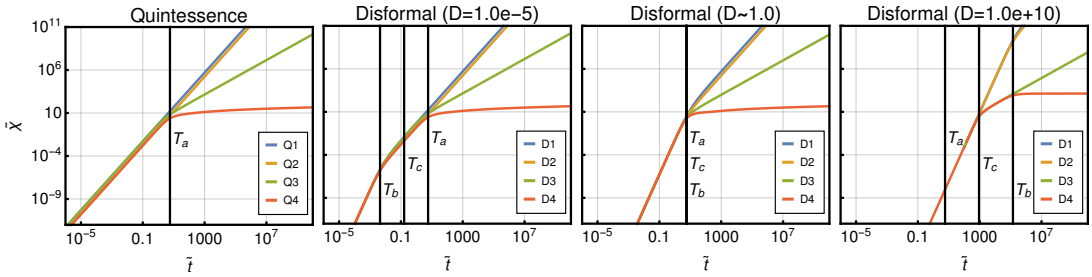

Figure 1. Background evolution of the field for quintessence model (left panel) and disformal model with constant coupling (for three different values of the free parameter D and $F = 0$). Each panel contains four curves that correspond to the four models described in Tables A1 and A2 in Appendix A. The vertical lines correspond to the different time scales defined in Table 1 for the case that includes damping. The numerical values of these time scales are very close to the values that do not include damping.

motion (Eq. 16; red curve in Fig. 1) has a characteristic time scale that divides the linear regime at early times from the non-linear regime at late times. At early times, the damping term interacts with the force that induces the field to roll down the potential in such a way that only the normalization of the solution is changed with respect to the undamped solution. This regime is characterized by a logarithmic slope ($\frac{d\log\tilde{\chi}}{d\log\tilde{t}} = \frac{\tilde{t}}{\tilde{\chi}}\partial_{\tilde{t}}\tilde{\chi}$) equal to two. During the transition to the non-linear regime, the force that accelerates the field becomes negligible and thus, the evolution of the field is damped and approaches a solution with a logarithmic slope equal to zero.

3.1.2 *Disformal gravity with constant disformal coupling*

We now study solutions of the Klein-Gordon equation in the limit $F \to 0$ and $D \neq 0$:

$$\partial^2_{\tilde{t}}\tilde{\chi} = -2\frac{\tilde{t}}{\tilde{t}^2+D}\partial_{\tilde{t}}\tilde{\chi} + \frac{\tilde{t}^2}{\tilde{t}^2+D}\exp(-\tilde{\chi}). \quad (17)$$

Properties of the solutions for the same four special cases discussed in the previous section are summarized in Table A2 in Appendix A. These solutions are shown in the three right panels of Fig. 1 for three different values of the only free parameter D. The red curve in these panels corresponds to the solution of the complete equation (Eq. 17).

These results can be summarized as follows. The evolution of the field at early times can be described analytically by linearizing the equation with respect to time and the field itself. Since the coefficient that appears in front of the time derivative in the damping term approaches zero at early times, it is possible to neglect it in this regime (note that this cannot be done in the quintessence model, for which this coefficient diverges at $\tilde{t} = 0$). The solution for the early universe is then a power law with a logarithmic slope equal to four, which is higher than in the quintessence case and thus, implies a slower evolution at early times. Once this early stage is finalized, three different processes dictate the further evolution:

(i) The two explicit functions of time that exist in the two terms in the right hand side of Eq. 17 approach the quintessence value ($1/\tilde{t}$ and 1 respectively).

(ii) The damping term increases with time.

(iii) The term that forces the field to roll down the potential (second term on the right hand side of the equation) drops (i.e. the non-linear regime is reached).

Three possible solutions exist depending on which of these processes is activated first, which in turn depends on the amplitude of D. For small values of D (red curve in the second panel from left to right of Fig. 1), the transition towards the quintessence limit occurs first (i.e. $T_b < T_a$ and $T_b < T_c$). In this case the equation is transformed into the same equation that defines the quintessence model and thus the evolution continues following the solutions described in the previous section and in Table A1 in Appendix A.

For intermediate values of D (red curve in the third panel from left to right of Fig. 1), the damping term dominates before the occurence of the transition to the quintessence regime. In this case the acceleration of the field becomes negative and the field loses kinetic energy. The solution becomes flat with a logarithmic slope equal to zero.

Finally, for very large values of D (red curve in the fourth panel from left to right of Fig. 1), the evolution of the field stays in the disformal regime until the exponential function in the potential starts decaying. The equation of motion becomes the equation of a free particle, whose solution has a logarithmic slope equal to one. Once this happened, the field continues evolving unperturbed until the damping term dominates. At this moment, the field decelerates and the slope becomes equal to zero.

These apparently complex solutions can be summarized in a simple way by plotting their logarithmic slope as a function of D and $\tilde{t}$, which we calculated numerically and show in Fig. 2. The transition between different regimes is given by the characteristic time scales defined in Table 1.

3.1.3 *Disformal gravity with exponential disformal coupling*

Assuming β (which is equivalent to F in the parametrization studied here) is different than zero has two effects in the equation of motion (Eq. 9). Firstly, it gives an additional dependence with the field $\tilde{\chi}$ to the coefficients that control the transition between the disformal and quintessence

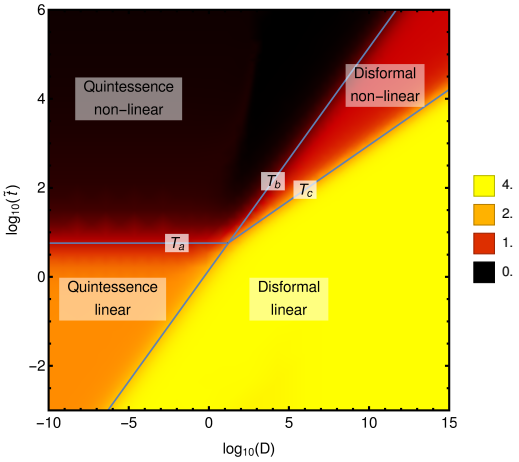

Figure 2. Colour coded is the logarithmic slope of the solution of the background Klein-Gordon equation for the disformal model with $\beta = 0$ and an Einstein-de Sitter universe. The three lines correspond to the three time scales defined in Table 1 (for the case that includes damping).

regimes. This new dependence converts the parameter D into an effective parameter $\tilde{D} = D\exp(F\tilde{\chi})$. Positive or negative values of F will result in $\tilde{D}$ increasing or decreasing with time, which in turn, will delay or accelerate the transition to the quintessence regime (defined by T_b). Secondly, assuming $F \neq 0$ will add a new term to the equation of motion which will act as an additional damping term or external force on the field depending on the sign of F.

In the case $F > 0$, the parameter $\tilde{D}$ will grow exponentially with the value of the field. This will decrease the time required to reach the transition to the non-linear regime as well as decrease the importance of the damping terms. Since the new damping term decreases faster with time than the usual one, it will not have any impact on the overall shape of the solutions. Figure 3 shows the logarithmic slope of the solution in the plane $(D,\tilde{\tau})$ for different values of F. For small values of D and intermediate values of F (second panel from the left), the damping term kicks in before the transition to the non-linear regime is reached and thus, the solution gets flat, with a logarithmic slope equal to zero. However, the dependence of $\tilde{D}$ with $\tilde{\chi}$ will force the damping to decrease faster that the usual case, thus giving the chance to the potential term to resurge and change the logarithmic slope of the solution back to one. Afterwards, all the terms on the right hand side will dissapear, which let the field evolve as a free particle, with a slope equal to one. For large values of F, the transition to the non-linear disformal regime is faster than the transition to the linear quintessence regime, and so the slope of the solution has a direct transition from four to one.

To analyse the case $F < 0$, it is convenient to re-write the equation of motion (Eq. 9) as follows:

$$\partial^2_{\tilde{\tau}}\tilde{\chi} = -\frac{1}{4}\left[\frac{4\tilde{\tau}+FD\partial_{\tilde{\tau}}\tilde{\chi}}{\tilde{\tau}^2+D\exp(F\tilde{\chi})}\right]\partial_{\tilde{\tau}}\tilde{\chi} + \frac{\tilde{\tau}^2}{\tilde{\tau}^2+D\exp(F\tilde{\chi})}\exp(-\tilde{\chi}). \tag{18}$$

Here, it becomes evident that the condition for the first term of the right hand size to be negative (and thus, to act as a damping term instead of an external force) is

$$4\tilde{\tau}+FD\partial_{\tilde{\tau}}\tilde{\chi} > 0. \tag{19}$$

By substituting the possible asymptotic limits discussed in Table A2 (i.e. $\tilde{\tau}^4$, $\tilde{\tau}^2$, $\tilde{\tau}$ and $\log(\tilde{\tau})$), we can see that the equation of motion will eventually become unstable for negative values of F. In the particular regime in which $\tilde{\chi} \propto \tilde{\tau}^2$, the solution is unstable for all $\tilde{\tau}$.

3.2 Disformal field dynamics: perturbations

The model we are dealing with does not include conformal or explicit couplings. However, the disformal coupling that we allowed for can generate perturbations in the field by itself. The mechanism by which these perturbations originate is based on the fact that, thanks to the term $(1+\gamma^2\rho)^{-1}$ in the Klein-Gordon equation (Eq. 6), the field rolls down the potential V at different rates in regions that have different densities (slower rate in higher density regions). The shape of these perturbations can be summarized in a simple relation between the metric perturbation Ψ and the scalar field ϕ, which can be translated (after appropriate approximations) into a similar relation between the fifth force associated with the scalar field and gravity.

We can determine the exact form of field perturbations by re-writing the Klein-Gordon equation (Eq. 6) as follows:

$$\nabla^2\phi = \frac{a^2}{c^2}\frac{\gamma^2}{B}\left[B\ddot{\phi}+\frac{1}{2}B_{,\phi}\dot{\phi}^2\right]\delta\rho+\varepsilon, \tag{20}$$

where we decomposed the density in a background value plus a (not necessarily small) perturbation

$$\rho(\mathbf{x},t) = \rho_0(t)+\delta\rho(\mathbf{x},t) \tag{21}$$

and we defined

$$\varepsilon \equiv \left[(1+\gamma^2\rho_0)\ddot{\phi}+3H\dot{\phi}+\frac{B_{,\phi}\gamma^2}{2B}\rho_0\dot{\phi}^2+V_{,\phi}\right]\frac{a^2}{c^2}, \tag{22}$$

which is equal to zero in the background. By substituting the factor $\delta\rho$ that appears in Eq. 20 with the corresponding value that can be obtained from the Poisson's equation for the metric perturbation

$$\nabla^2\Psi = \frac{a^2}{2M_P^2}\delta\rho, \tag{23}$$

we can relate the Laplacian of the scalar field and the metric perturbation:

$$\nabla^2\phi = \xi\nabla^2\Psi+\varepsilon, \tag{24}$$

where we have defined

$$\xi \equiv \frac{2M_P^2}{c^2}\frac{\gamma^2}{B}\left(B\ddot{\phi}+\frac{1}{2}B_{,\phi}\dot{\phi}^2\right). \tag{25}$$

We now substitute all the dependences with the scalar field and its time derivatives with background values. The term ε will disappear and we will end up with an equation that can be integrated and whose solution is

$$\phi = \xi_0\Psi+\phi_0+\upsilon, \tag{26}$$

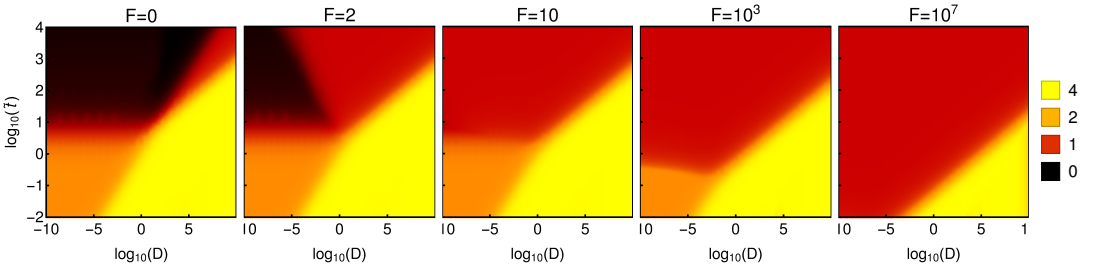

Figure 3. Color coded is the logarithmic slope of the solution of the background Klein-Gordon equation for the disformal model for different values of F in an Einstein-de Sitter universe.

where υ is a solution of the Laplace equation, which, together with the background value of the field ϕ_0, acts as an integration constant. We will test this relation in the following sections by comparing results obtained from non-linear simulations which do not rely on approximations. Since it will be used a posteriori, we show here the explicit form that the coefficient ξ acquires when assuming an exponential potential as in Eqs. 4 and 12:

$$\xi_0 = \frac{2b_0}{H_0^2 c^2}\left(\ddot{\phi}_0 + \beta\frac{\dot{\phi}_0^2}{2M_p}\right)\frac{\exp(\beta\phi_0/M_p)}{1-\frac{b_0}{H_0^2 M_P^2}\dot{\phi}^2}. \tag{27}$$

The sub-index zero in these expressions highlights the fact that these are background quantities. The relation between the fields given by Eq. 26 depends on the model parameter b_0 and β and thus, breaks the degeneracy between parameters that enabled us to define D and F (Eqs. 12 and 13). In the following section, we will study the consequences of breaking this degeneracy by simulating models that have the same background parameters D and F, but different b_0.

An important characteristic of Eq. 26 is that the sign of the coefficient ξ_0 depends in part on the sign of the second derivative of the field. This means that at the moment in which the background field transitions towards the non-linear regime described in previous section (i.e. the moment in which its second derivative becomes negative), the scalar field perturbations will be able to flip; their usual distribution will thus be inverted and local minima of the field will correspond to local minima in the density distribution. The physical mechanism responsible for this phenomenon is related to the fact that the term $(1+\gamma^2\rho)^{-1}$ in the Klein-Gordon equation (Eq. 6) increases the efficiency of the damping term in low density regions. Thus, at the moment in which the damping term grows to the point in which it can affect the evolution of the field, the values in the halos overshoot that of the voids and inverts the sign of the perturbations. Since the fifth force has an explicit dependence on the potential V (and thus, on the scalar field itself), the flip in the perturbations will have a direct impact on the distribution of forces and the evolution of matter that is defined by it.

3.3 The fifth force

The acceleration of a test particle in scalar-tensor theories can be found by studying the Jordan frame geodesics equations (Zumalacárregui et al. 2013; Hagala et al. 2016). In the weak field limit of a general theory with a purely disformal coupling, the geodesic equation for a non-relativistic test particle is given by

$$\ddot{\mathbf{x}} + 2H\dot{\mathbf{x}} + (\boldsymbol{\zeta}\cdot\dot{\mathbf{x}})\nabla\phi + \frac{\nabla\Psi}{a^2} + \frac{c^4}{2M_P^2}\frac{\xi}{g_\phi}\frac{\nabla\phi}{a^2} = 0, \tag{28}$$

where we have defined

$$g_\phi \equiv 1 - 2BX \tag{29}$$

to simplify the notation and the 3-vector $\boldsymbol{\zeta}$ is a function of derivatives of ϕ. Eq. 28 is equivalent to Newton's second law, where the acceleration of a body is proportional to the sum of forces acting on it. The second term on the left hand side of the equation corresponds to a damping force induced by the expansion of the Universe; the third term is second order and the last two correspond to the Newtonian and fifth forces, which we define as:

$$\mathbf{F}_\Psi \equiv -\frac{\nabla\Psi}{a^2}, \tag{30}$$

$$\mathbf{F}_\phi \equiv -\frac{c^4}{2M_P^2}\frac{\xi}{g_\phi}\frac{\nabla\phi}{a^2}. \tag{31}$$

These two force fields can be related to each other by taking into account the connection that exists between the scalar field and the metric perturbation discussed in the previous section. As the version of that relation that does not rely on approximations applies to the Laplacian of the fields (Eq. 24), it is convenient to study the divergence of these force fields. Thus, by taking into account definitions 30 and 31 and Eq. 24, we can write

$$\nabla\cdot\mathbf{F}_\phi = (1-\delta d)\,\eta^2\nabla\cdot\mathbf{F}_\Psi, \tag{32}$$

where the quantity

$$\delta d \equiv \frac{g_\phi}{\xi^2\nabla\cdot\mathbf{F}_\Psi}\left[\nabla\left(\frac{\xi}{g_\phi}\right)\cdot\nabla\phi + \frac{\xi}{g_\phi}\varepsilon\right] \tag{33}$$

is exactly zero in the background and we defined

$$\eta^2 \equiv \frac{c^2}{2M_P^2}\frac{\xi^2}{g_\phi}. \tag{34}$$

The sign of η^2 depends exclusively on the sign of g_ϕ, which must be positive for the theory to be stable. This is because the disformal transformation (Eq. 3) becomes singular when $g_\phi = 0$ (i.e $\tilde{g}^\mu_\mu = 0$ and thus, the metric becomes not invertible), so this crossing must be avoided. Futhermore, Koivisto

et al. (2012) showed that the evolution of the field will naturally avoid this singularity by progressively freezing the field before $2BX$ reaches unity. We can therefore assume $g_\phi > 0$, which results in η^2 being positive.

Eq. 32 can be integrated after evaluating the coefficient $(1-d\delta)\eta^2$ in the background, which is the same as we did in the previous section when integrating Eq. 24 to connect the field with the metric perturbations. The end result is:

$$\mathbf{F}_\phi = \eta_0^2 \mathbf{F}_\Psi + \nabla \times \mathbf{k}, \tag{35}$$

where the curl field $\mathbf{k}$ is an integration constant (in the sense that its divergence is zero) and we took into account that δd is equal to zero in the background. The properties of $\nabla \times \mathbf{k}$ are very well known in the context of Modified Newtonian Dynamics (MOND). In particular, it has been shown that it is exactly zero for particular symmetries and that behaves at least as r^{-3} for non-symmetric configurations (Bekenstein & Milgrom 1984). Its effects in structure formation (in the context of MOND, which deals with a universe without dark matter) were studied in detail by Llinares et al. (2008) (additional results associated with this paper can be found in Llinares (2011)).

The results described in this section and the previous one can be used to define two different simulation methods which will depend on two different approximations. First, it is possible to neglect the effects induced by the term υ in Eq. 26. Assuming also that ξ_0 is independent of the position (which we actually did to derive that equation), we can discretise the space and time derivatives that appear in the definition of the fifth force (Eq. 31). Thus, the fifth force can be calculated as a linear combination of values of ϕ in space and time. We will discuss in the following section the impact that making these approximations has in the estimation of the scalar field by comparing with exact results obtained from cosmological simulations. A companion paper will also contain a detailed estimation of how the error associated with these approximations translates into the predictions of observable quantities.

A different simulation approach that can be defined from these results consists in neglecting the curl term in Eq. 35 to find a relation between the Newtonian and fifth force fields. This second case is equivalent to assume that all the gravitational effects can be condensed in an effective gravitational constant $G_{\rm eff} = G(1+\eta_0^2)$, which is assumed to be independent of the position. Note that similar approximations were discussed in Sakstein (2014) in the context of Solar System tests.

3.4 Achieving a repulsive fifth force

The presence of non-canonical kinetic terms in the definition of a scalar tensor theory, can give rise to repulsive forces (Amendola 2004). Since disformal gravity fulfils this condition when written in the Jordan frame, it may be worth investigating how repulsive forces can be achieved in this model. The possibility of obtaining repulsive fifth forces is not only interesting from a theoretical perspective, but becomes relevant in the context of the discrepancy found by the Planck collaboration between the normalization of density perturbations σ_8 that can be inferred from the CMB and from lensing (Planck Collaboration et al. 2016b). Although the measured discordance could be due to unknown biases or even statistical fluctuations (Addison et al. 2016; Couchot et al. 2017; Kitching et al. 2016), these results could also be a signal of new physics. A repulsive MG force will delay clustering with respect to GR and thus could help in reducing the tension.

The necessary condition for the fifth force to be opposite to gravity can be obtained from the relation between these two force fields provided by Eq. 35. However, since approximations where made when deriving this equation, a more appropriate starting point for this analysis is the divergence of this relation, for which we present an exact expression in Eq. 32. This equation tells us that the only way in which the divergence of the two force fields can have different sign is by having

$$\delta d > 1. \tag{36}$$

Since this quantity is equal to zero in the background, the disformal fifth force is parallel to gravity at order zero. At first order in perturbations of the field, δd takes the following form:

$$\delta d \sim \frac{\left(1+\gamma^2\rho_0\right)\ddot{\delta\phi} + 3H\dot{\delta\phi} + V_0 \nu^2/M_P^2 \delta\phi}{\xi^2 \nabla\cdot\mathbf{F}_\Psi}, \tag{37}$$

where we assumed $\beta = 0$ for simplicity. Since the sign of δd depends on the sign of the perturbations, this quantity can certainly be positive. It will also become larger than one at least in the specific redshifts in which ξ changes sign and in regions where $\nabla\cdot\mathbf{F}_\Psi$ changes sign (i.e. in the transition between voids and over-dense regions). So we can be certain that repulsive forces do exist in this model at least as a transient and in specific regions of space. This result show that the approximations that we made to obtain Eq. 35 from Eq. 32 may be important in specific situations and thus cannot be taken by granted in general. This may be important in particular because voids and their outer limits, where $\nabla\cdot\mathbf{F}_\Psi$ approaches zero, were discussed in several opportunities as relevant probes of modified gravity (Llinares 2011; Cai et al. 2015; Barreira et al. 2015; Voivodic et al. 2017; Falck et al. 2018).

An additional result that comes from Eq. 37 is that the fifth force has an explicit dependence with the potential V, and thus with the absolute value and sign of the perturbations. This may be important since we showed in Section 3.2 that the scalar field perturbations are proportional to the metric perturbations (Eq. 26) and that they can flip following the sign of the coefficient ξ_0. So the moment in which the field perturbations flip, will be associated with a change in the amplitude of the fifth force.

4 *N*-BODY SIMULATIONS

We summarize in this section technical aspects of the 3D cosmological simulations that we run to both confirm the results presented above in a realistic set up and quantify the impact that the fifth force has in the matter distribution in the non-linear regime. This section also describes in detail our motivation for choosing the particular set of model parameters that we simulated.

[t!]

Model	v_0	ν	b_0	β	D	F	$v_0\nu$	Notes
GR	—	—	—	—	—	—	—	ΛCDM with Planck 2015 parameters
DDE	3.055	0.4	1	(-10,0,10)	0.65	$(-25,0,25)$	1.22	Correct amount of Disformal Dark Energy
Fiducial	1	1	1	0	1.3	0	1	—
VF	10	1	0.1	0	1.3	0	10	Velocity flips in less than a Hubble time.
Steep	10^{-3}	10^3	0.01	0	1.3×10^1	0	1	V is steep ⇒ fast transition to non-linear phase.
FF	0.1	100	1	(-10,0,10)	1.3×10^3	$(-0.1,0,0.1)$	10	Field flips in less than a Hubble time.

Table 2. Model parameters used for the N-body runs. See Section 4 for explanation.

4.1 Set up of the simulations

The simulations were run with the modified gravity N-body cosmological code `Isis` (Llinares et al. 2014), which is based of the particle mesh code `Ramses` by Teyssier (2002). The code includes a solver for the non-linear MG elliptic equations that can be obtained after assuming the quasi-static approximation. However, since in disformal gravity the time derivatives play a central role in both the Klein-Gordon and geodesics equations (Eqs. 6 and 28), the validity of this approximation is not guaranteed. Thus, we made use of the non-static solver of `Isis` (Llinares & Mota 2014; Hagala et al. 2016), which relies on a non-linear hyperbolic solver that can take into consideration time derivatives of the background and perturbed fields.

To be consistent with the simulation code `Isis/Ramses`, we will use the supercomoving time τ, which relates to cosmic time t through $d\tau = dt/a^2$ (Martel & Shapiro 1998). We will denote derivatives with respect to this new time with a prime. We will also work with the following normalized scalar field

$$\chi \equiv \frac{\phi}{M_{\rm pl}}. \tag{38}$$

The code variables associated to the time derivatives $\dot{\phi}$ and $\ddot{\phi}$ are

$$q \equiv a\chi', \tag{39}$$
$$q' = a'\chi' + a\chi''. \tag{40}$$

We performed N-body simulations with 256^3 particles in a cubic box with a comoving side length of 256 Mpc/h. The background cosmology is assumed to be the same for all the runs and given by Planck 2015 best fit ΛCDM parameters (Planck Collaboration et al. 2016a): $(H_0, \Omega_\Lambda, \Omega_m, \sigma_8) = (67.74$ km/s/Mpc, $0.6911, 0.3089, 0.8159)$. The assumption behind this selection for the background expansion is that the energy of the scalar field is compatible with a cosmological constant with the value required by observations. Thus, from the numerical point of view, taking into account the energy of the scalar field is equivalent to adding a cosmological constant. We note that not all the models that we simulated possess this property. However, in this paper, rather that finding the best fit disformal parameters, we are interested in looking for new phenomenology which may provide us with novel ways of looking at the data. This may potentially lead to a detection of deviations from GR in the data, which does not necessarily correspond exactly to the model studied here, but that share observable signatures with it. Taking into account the energy of the scalar field will complicate the analysis, but will not provide additional information on the disformal effects associated with the perturbations.

The initial conditions for the N-body particles were generated assuming that the impact of the scalar field at high redshift is negligible. Thus, all the simulations use the same initial conditions, which were generated with the Zeldovich approximation with the code `Grafic2` (Bertschinger 2001). These sets of initial conditions share not only the power spectrum, but also the phases. By doing this, we ensure that differences found between the various simulated models are induced by the presence of a fifth force and not the initial particle distribution.

The codes `Ramses` and quasi-static `Isis` include adaptive mesh refinements (AMR), which means that they can increase the resolution locally as required by the complexity of the solutions. However, the non-static version of `Isis` does not include this technique. Thus, our analysis will only be valid up to the Nyquist frequency of the domain grid which covers the whole simulation box and has 256 nodes per dimension. The three-dimensional particle data was output at nine different snapshots, at $z = 2.33$, 1.00, 0.43, 0.25, 0.11, 0.081, 0.053, 0.026, and 0. In addition, the code outputs all the available fields (density, metric perturbation, scalar field and its derivatives) in a two-dimensional slice that crosses the center of the box at 200 different points in time, ranging from $z = 16$ to $z = 0$.

4.2 Simulated models

Table 2 lists the model parameters that we chose for the simulations. We also included the derived background parameters D and F defined in Section 3.1 and the product $v_0\nu$ which will be useful to interpret results in the following sections. Note that the background parameters D and F were original defined for an Einstein-de Sitter universe, so they must be taken only as indicative. The slope of the disformal coupling β is set to zero for all the runs except the models DDE and FF, for which we made two additional runs with $\beta = \pm 10$. A brief explanation of the motivation for each set of parameters follows.

In the Fiducial run, all three free parameters of the model are set to one. These values give a background evolution that is very close to that of the ΛCDM model. To confirm this, we also run the Disformal Dark Energy (DDE) simulation with parameters that were specifically tuned to recover the ΛCDM expansion rate. The parameters of this simulation are such that the potential $V(\phi)$ gives the observed amount of Dark Energy at redshift zero and at the same time stays within constraints obtained in the linear regime by van de Bruck & Mifsud (2018). We find that their upper limit for the coupling, $B_0 = (0.2\,\mathrm{meV})^4$, is equivalent to $B_0 \approx 1/\left(H_0^2 M_{\rm pl}^2\right)$ in the units used in this work. Consequently, using a dimensionless coupling $b_0 = \mathcal{O}(1)$ will give a model that is within the constraints given in that study.

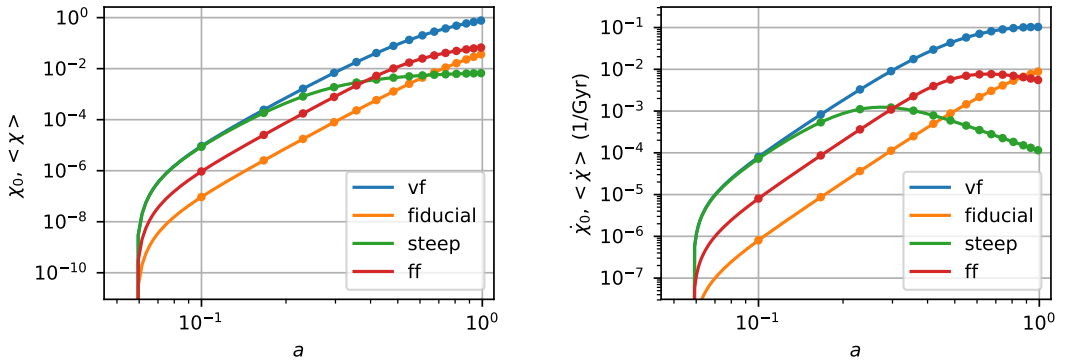

Figure 4. Background evolution of the scalar field (left) and its time derivative (right) for the simulated models as a function of the expansion factor a. The continuous curves are Runge-Kutta solutions of the order zero Klein-Gordon equation and the points are the mean values obtained from the non-linear simulations in slices that pass through the centre of the box. Results of the DDE run are very similar to those of the Fiducial run, so we exclude them to avoid overcrowding the plots.

The initial potential, $v_0 = 3.055$, was found with a shooting algorithm, following van de Bruck & Mifsud (2018). Combining this with a small value for ν (i.e. a flat potential) results in $V \sim 3H_0^2 M_{\rm pl}^2$ today, and hence gives rise to a dark energy component similar to a cosmological constant. Most of the results that come out of these two simulations (Fiducial and DDE) are similar. Thus, we will show only results of the Fiducial run and point out differences when needed.

The parameters of the Field Flipping (FF) and Velocity Flipping (VF) models were chosen to present a broad spectrum of phenomenology. The FF simulation enters the non-linear background phase discussed in Section 3.1.2 before redshift zero. The analysis presented in Section 3.2 shows that this will induce a flip in the scalar field perturbations. Once this happens, the distribution of the field perturbations will contradict the usual profile for a coupled scalar field and will associate high density regions with local maxima in the field. In the VF case, a Hubble time is enough to get the flip in the time derivative of the field, but not in the field itself. The parameters of this model were chosen to study how the degeneracy that exists between background parameters D and F can be broken by looking at the perturbations in the fields. Thus, the simulation shares the values of D and F with the Fiducial simulation, however, it has a different value of b_0.

The Steep model was run using parameters that correspond to a steep potential V, and thus undergoes an early transition towards the non-linear regime (i.e. corresponds to a small value T_c). The aim of this simulation is to analyse the consequences of a field that is active only at high redshift and is damped afterwards.

5 SIMULATION RESULTS: PROPERTIES OF THE FIELDS

We discuss in this section several aspects of the distribution of the simulated fields as well as a comparison with the analytic estimations presented in Section 3.

5.1 Background evolution of scalar field

Given that the simulations track the scalar field χ rather than its perturbations $\delta\chi$ on a background χ_0, it is worth asking if the mean value of the simulated scalar field agrees with the background value that can be calculated, for instance, with a Runge-Kutta solver. We show such a comparison in Figure 4. The lines in the left and right panels are Runge-Kutta solutions for the background scalar field and its time derivative respectively. The points are the mean values obtained from the N-body simulations in slices that pass through the centre of the box. The abrupt decline towards zero at high redshift is related to the fact that the initial conditions are not given at $a = 0$, but at the starting redshift of the simulations, when we assumed that the field is equal to zero. Both solutions agree very well, which is a confirmation of a reliability of the code.

5.2 Qualitative behaviour of scalar field perturbations

Figure 5 shows the time evolution of scalar field perturbations as found in 2D slices that pass through the center of the 3D box. Different rows correspond to different redshifts (shown to the left of the color bar). The first column shows the density distribution, while the other four correspond to the perturbation in the scalar field. In this section we are only interested in a qualitative description of the effects associated to the disformal coupling, thus we normalized the perturbations with the maximum value reached in each model separatelly. When using this normalization, the perturbations lie always between minus one and one. A quantitative description will be presented in following sections. Since the Fiducial and DDE models have almost identical evolution, we show only one of these two models.

The panels show that scalar field perturbations can do more that simply grow with time as happens in other scalar tensor theories. The only model that has a monotonic growth of perturbations is the Fiducial one. In the VF model, the perturbations grow until redshift of about $z = 0.82$ and then wash out until being completely absent at redshift $z = 0$.

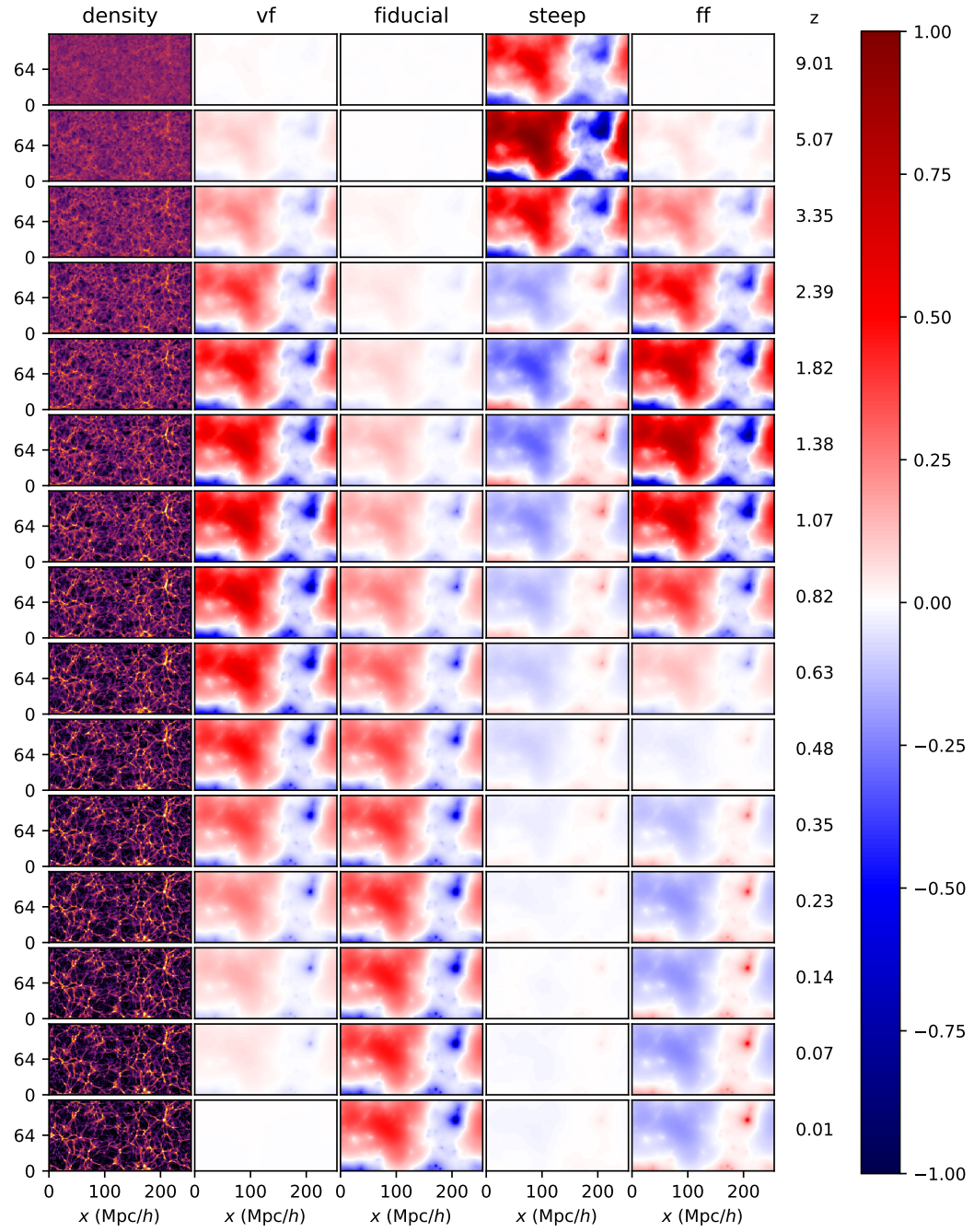

Figure 5. The first column shows the evolution of the density distribution. The rest of the columns show the time evolution of scalar field perturbations for different models. The colours correspond to the scalar field perturbations normalized to the maximum reached in each model, which means that the values go from -1 (dark blue) to +1 (dark red). The scaling of the colours is symmetric-log. The numbers next to the color bar correspond to the redshift of each row. For reasons of space, we show only the bottom half of each slide.

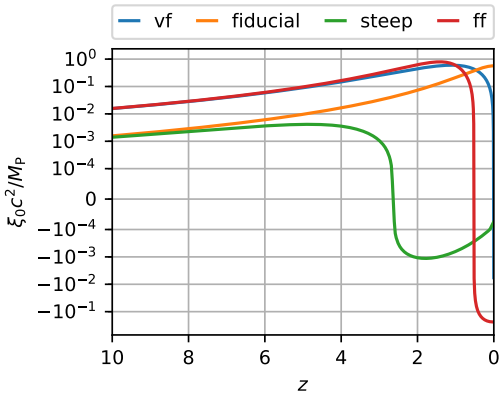

Figure 6. Time evolution of the coefficient ξ_0 that relates metric perturbations Ψ with the scalar field χ (Eq. 26) for the simulated models. The DDE model is similar to the Fiducial one, and thus not shown to avoid overcrowding the plot. The sharp transitions between positive and negative values are produced by the symlog scaling that we used for the vertical axis. See section 5.2 for explanation.

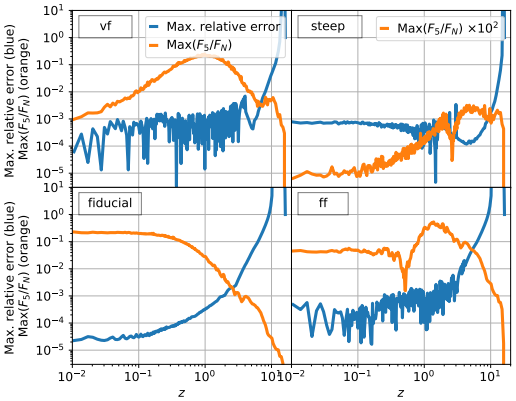

Figure 7. The blue curves correspond to the maximum relative difference between the scalar field values obtained from the N-body simulations and the ones we obtained from the gravitational potential by assuming υ is zero in Eq. 26. The gravitational potential was obtained by solving Poisson's equation with the same solver that was used to run the simulations. The orange curves are the maximum ratio between the fifth force $\mathbf{F}_\Psi$ and gravity $\mathbf{F}_\phi$. By comparing blue and orange curves, we can confirm that the times where the relative error associated to the approximation is large, the force is small and thus, no measurable effect should appear in the density distribution. We show results from 2D slices that pass through the center of the 3D box. See Section 5.3 for explanation.

In the Steep model, the perturbations grow very rapidly at early times, reaching their maximum at $z \sim 5$. Then the field flips, developing maxima in the position of the halos and minima in the voids. After the flip occurs, the perturbations washed out as happened in the VF model. Finally, the FF model has a behaviour which is similar to the Steep model: a maximum of the perturbations at $z \sim 1.38$, followed by a flip at $z \sim 0.48$. In this particular case, the perturbations continue being almost constant until $z = 0$.

The solutions shown in these panels seem very complex, but can be easily explained with the relation between the scalar field ϕ and the gravitational potential Ψ that we discussed in Section 3.2 (Eq. 26). Assuming that the integration constant υ in that equation is zero, we find that both fields are related through the parameter ξ_0, whose time dependence is shown in Figure 6 for the same models presented in Figure 5. Two pairs of models have identical behaviour at high redshift. This has the consequence that the early evolution of ξ_0[1]:

$$\xi_0(t \ll 1) = \frac{3M_P H_0^2}{c^2} t^2 \left[\frac{v_0 \nu}{4} + \frac{M_P H_0^4}{85} \frac{v_0^2 \nu^2 \beta}{b_0} t^4 \right] \exp(\beta \phi_0 / M_p) \quad (41)$$

depends on the product $v_0\nu$, which is the same for the two pairs of models (Fiducial, Steep) and (VF, FF) (see specific values in Table 2). This degeneracy is broken at later times, and thus models that agreed at high redshift depart from each other later on. The reason for this degeneracy to be absent in different columns of Figure 5 is that the normalization chosen for these panels is different for different models. Finally, figure 6 also shows that ξ_0 becomes larger for smaller values of b_0. This may seem to contradict the fact that the solutions provided in Section 3, which depend only on D, are independent of b_0. However, one must take into account that there is an additional factor b_0 in the definition of $\bar{t}$ used in that section.

Comparison of Figures 5 and 6 unveils the close relation that exists between the evolution of the perturbations and ξ_0. The maxima in the perturbations agree with the maxima in ξ_0. Also the moment in which the flips occur in the field agree with the change in the sign of ξ_0.

The fact that the scalar field perturbations shown in Figure 5 go back and forth in the FF simulation may open the question of the possibility of obtaining sustained oscillations in the field perturbations. However, these changes in the perturbations are associated with transitions between different regimes in the background evolution of the field, which are condensed in the evolution of ξ_0. The analysis presented in Section 3.1 shows that after the second oscillation occurred, the perturbations cannot do more than to approach zero.

5.3 Testing analytic predictions for field perturbations

A more quantitative comparison between the the scalar field that we extracted from the self-consistent N-body simulations and the predictions that we can obtain by assuming that $\upsilon = 0$ in Eq. 26 is shown in Figure 7. The blue curves are the maximum relative difference between these two fields

[1] We derived this special case by taking into account the early redshift solution (Eq.A5) together with the definitions provided in Section 3.1 and the definition of ξ_0.

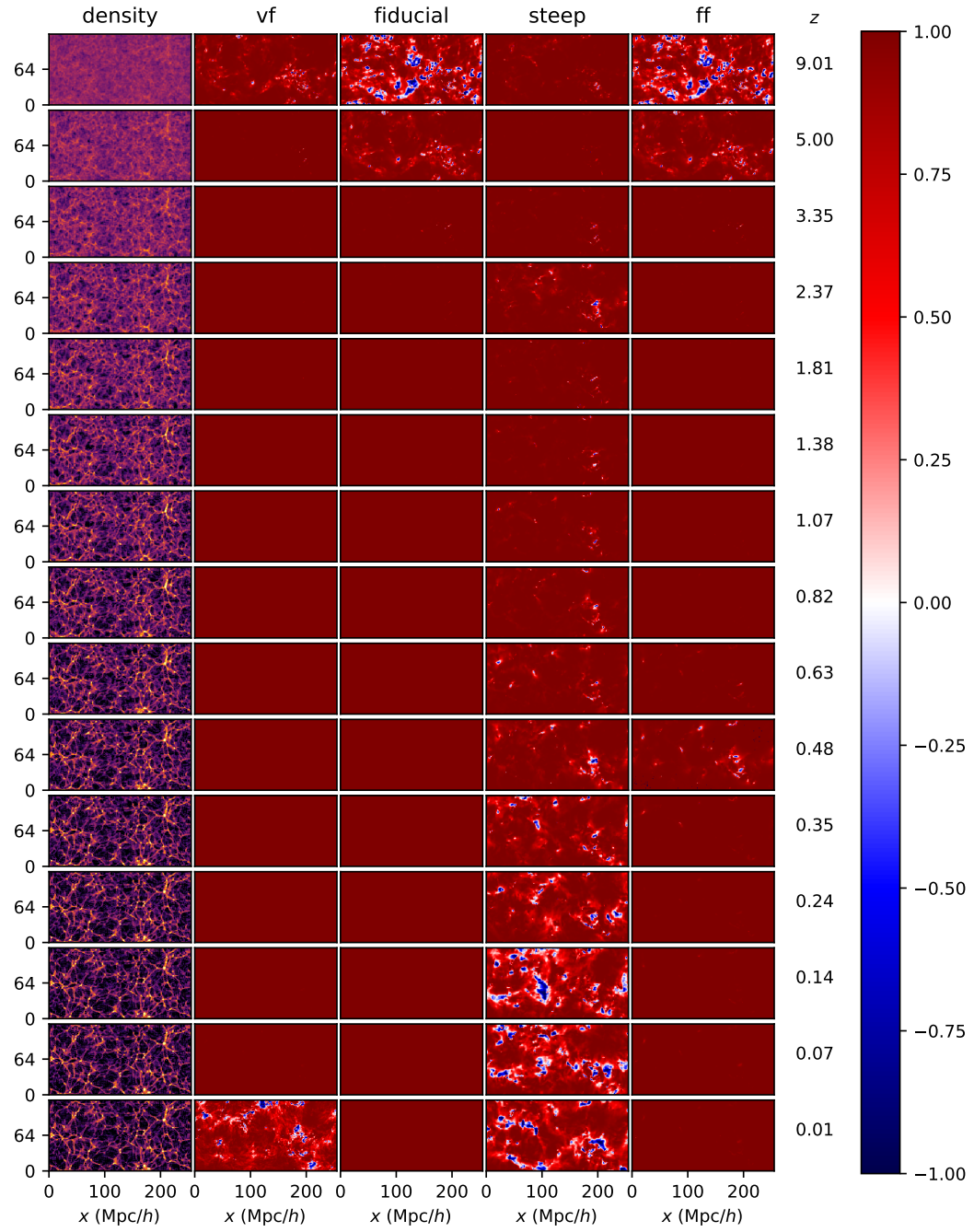

Figure 8. Cosine of the angle between Newtonian and fifth force as a function of time and simulated model. Dark red and blue correspond to force fields that are parallel or antiparallel respectively. The numbers to the left of the colour bar correspond to the redshift of each row.

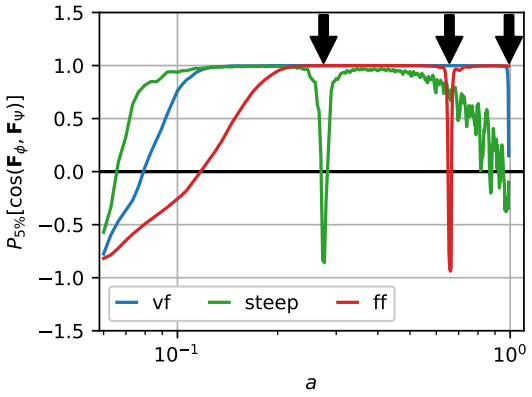

Figure 9. Percentile five of the distribution of the cosine of the angle between the Newtonian and fifth force as found in the 2D slides of our 3D simulations. We show only the models for which we expect repulsive forces associated to the zeros of ξ_0: VF, FF and Steep. The vertical arrows show the zeros of ξ_0 for these models.

as found in 2D slices that pass through the centre of the box and as a function of redshift. Different panels correspond to different simulations. The fields that we used for this comparison are the fully non-linear scalar field ϕ and the solution of the Poisson's equation Ψ that are used to calculate the forces while the simulations run. In other words, these are the most accurate fields (ϕ and Ψ) that we have at hand. The plots show that there is a very good agreement between the exact field provided by the simulations and our prediction: differences are below 0.1% at all times after $z = 1$. The larger differences that occur at high redshift are related to the fact that we did not take into account perturbations of the scalar field in the initial conditions for the simulations (instead, we approximated them by zero). Thus, there is a transient in which the field evolves from zero to a field that has a power spectrum compatible with Eq. 26.

These high redshift differences can be reduced by choosing more accurate initial conditions (for instance, generated as a realization of a linear power spectrum). However, given that they occur at a moment in the history of the Universe when the fifth force is negligible, is it likely that they will not affect the matter distribution. We confirmed this by plotting the maximum ratio between the fifth force $\mathbf{F}_\phi$ and gravity $\mathbf{F}_\Psi$ on the 2D slices as a function of time (orange curves in Figure 7). As expected, the fifth force is sub-dominant at high redshift. By the moment in which the fifth force goes above 1% of the Newtonian force, the error in our prediction of the scalar field is already below 0.1% and continues decreasing from there.

The good agreement that we found between exact and approximate solutions shows that it does make sense to run disformal gravity cosmological simulations by using Eq. 26 instead of a hyperbolic solver (as described at the end of Section 3.2). This will largely reduce the overhead associated with the modified gravity solver and will make disformal simulations competitive in terms of speed. The impact of this approximation in the predicted power spectrum of density perturbations will be presented in a companion paper.

5.4 Direction of the fifth force

In section 3.4, we discussed a sufficient condition for the presence of repulsive fifth forces (i.e. opposite to gravity), which is condensed in Eqs. 36 and 37. Given that our simulations track the evolution of the scalar field without making any approximations or simplifications in the equations, it is possible to use the simulated force field to confirm if repulsive forces do exist in a realistic set up. Figure 8 shows the cosine of the angle between the Newtonian and fifth forces in the same slices and for the same redshifts and simulations we presented in Figure 5. Dark red and blue correspond to parallel and antiparallel forces and the numbers to the left of the colour bar make reference to the redshift of each slice.

The panels show that all the simulations produce repulsive forces at high redshift, however these occur during the warm up phase of the simulation in which the scalar field transitions from the initial condition ($\phi = 0$) to a distribution that is consistent with the density field (see discussion in the previous section). Moving forward in time, we see that repulsive forces appear only at specific redshifts. These redshift values are consistent with the discussion presented in Section 3.4, where we found that repulsive forces will occur in the zeros of the function ξ_0. This is confirmed in Figure 9, where we show the fifth percentile of the distribution of the angle between the forces as a function of scale factor for the 2D slices. The vertical arrows are the zeros of ξ_0, which are consistent with the moments in which the forces become antiparallel.

6 SIMULATION RESULTS: IMPACT OF THE FIFTH FORCE ON THE MATTER DISTRIBUTION

We describe now the effects that the presence of the fifth force has on the distribution of matter. We do this by studying differences between the power spectrum of dark matter density perturbations of the GR and MG simulations. We do firstly the analysis for the models that have $\beta = 0$ and discuss a posteriori the differences induced by adding a dependence of the coupling with the scalar field through β.

6.1 Power spectrum of models with $\beta = 0$

Figure 10 shows the time evolution of the relative difference between the MG and GR power spectra for the models that have a constant disformal coupling (i.e. with $\beta = 0$). Different panels correspond to the different models that we simulated and different lines within each panel to different redshifts. In the Steep run, the evolution is very close to GR, and thus we multiplied these curves by 10^4. As the curves have positive and negative values, we show their absolute values and highlight the negative parts with dotted lines.

The models can be divided in two different categories: those in which the fifth force produces a monotonic increase of power with respect to GR (models DDE and Fiducial) and those that have a monotonic increase until some specific redshift and then continue increasing at large scales, but

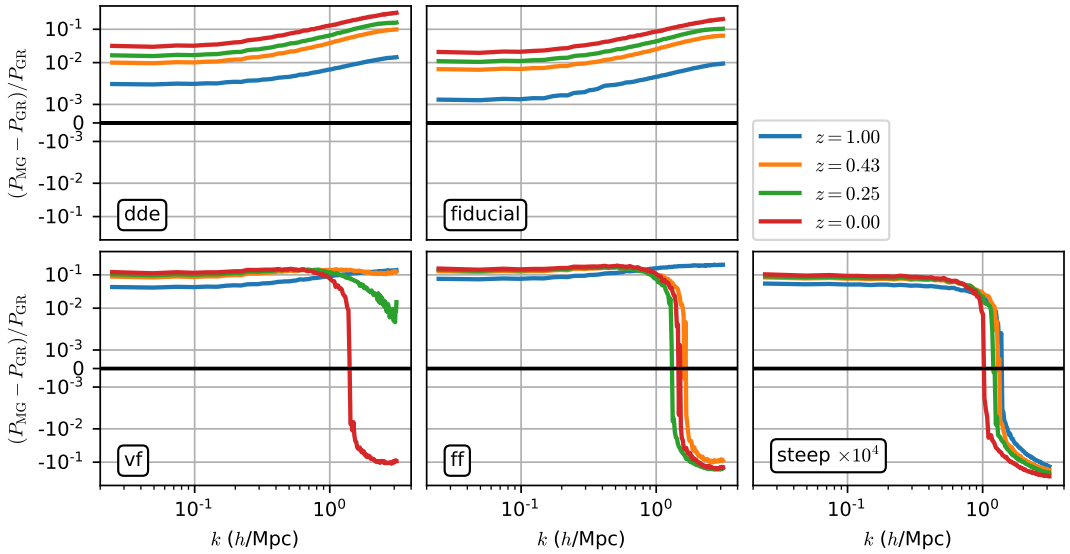

Figure 10. Relative difference between MG and GR dark matter power spectrum from all the simulations. The values obtained from the Steep simulation are much smaller than the scale used for the other models, and thus we multiplied them by 10^4 for presentation purposes only.

have a slower evolution than GR at small scales (models FF, VF and Steep).

Some insight on the phenomenology associated to these curves can be gained by comparing the amplitude of the fifth force with the gravitational force. By assuming that δd is second order in Eq. 32, we can obtain Eq. 35. If we further assume $\nabla \times \mathbf{k} \ll 1$, we find that the amplitude of the fifth force for a particular set of parameters depends exclusively on the background quantity η_0^2, which we show in Figure 11 for all the simulated models as a function of the expansion factor a. Since the values of the DDE run are very close to those of the Fiducial run, we excluded them from this plot. The discontinuities in the derivatives of these curves are not real, but related to the log scaling of the vertical axis. However, these discontinuities do have a physical meaning, since they occur at moments when the parameter ξ_0 changes sign (see Figure 6).

From these curves, we can see that the pairs of models M_1 = (Fiducial, Steep) and M_2 = (VF, FF) have identical forces at high redshift and so it is expected that their early time evolution will be identical. The fact that η_0^2 of the models M_2 is more than two orders of magnitude larger than that of the modes M_1 is responsible for the large differences found in Figure 10: models M_2 have a much faster evolution, reaching differences with respect to GR of more than 10% at large scales. Note that the model FF has a smaller coupling constant than the Fiducial model. Naively, one will expect that a smaller coupling constant will be associated to a slower evolution, however, the particulars of the definition of η_0^2 (in particular, the functions ξ and g_ϕ) give stronger forces in the FF case.

Comparison between the Steep and Fiducial values of η_0^2 show that even if both models share the same force fields at high redshift, they depart from each other later on. In the Steep simulation, the forces stay always close to zero and thus differences in the power spectrum with respect to GR are minimal.

Figure 11 can also help us understand why the power spectrum of the MG simulations goes below the GR values at low redshifts. In particular, it is possible to see that the moment in which $(P_{\rm MG} - P_{\rm GR})/P_{\rm GR}$ starts moving back to zero corresponds to the moment in which η_0^2 starts decreasing and approaches zero. Also, this change in the behaviour of the power spectrum occurs at small scales, where the structure of the halos dominates the signal. These facts are consistent with a decrease of power in MG simulations induced by an expansion of the halos when the fifth force disappears and the kinetic energy of the dark matter particles dominates.

Finally, we would like to point out that late evolution of the models DDE and Fiducial is almost scale independent. After an initial shape is given to the difference between MG and GR, that shape is almost conserved later on. Departure from scale invariance evolution of these curves occurs close to the Nyquist frequency of the simulations, and thus higher resolution simulations should be run in order to confirm this result.

Note that our analysis based on η_0^2 does not take into account the back-reaction that the presence of the fifth force has on the metric perturbations (through changes in the density distribution). However, this effect was taken into account in the simulations, which are fully self-consistent.

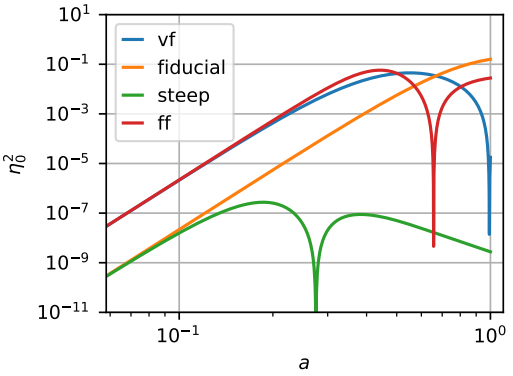

Figure 11. Time evolution of the dimensionless coefficient η^2 that relates Newtonian and fifth force fields when calculated with background quantities for the simulated models. The DDE model is similar to the Fiducial one and thus, is not shown to avoid overcrowding the plot. The discontinuities in the derivatives are not real, but produced by the log scaling.

6.2 Response of the power spectrum to changes in β

In this section, we discuss the impact that the parameter β, which determines the slope of the disformal coupling, has on the power spectrum of density perturbations. Figure 12 shows a comparison between simulations that were run with $\beta = 0$ and $\beta = \pm 10$. The left and right panels correspond to the base models DDE and FF respectively. Continuous and dotted lines correspond to positive and negative values of β.

The left panel shows that allowing β to be different than zero in the DDE model has a monotonic effect with frequency. Positive values of β force the coupling to go up with the value of the field (see Eq. 4), which in turn increases the power with respect to the base model defined by $\beta = 0$. As in this model, the power increases with respect to GR, the net effect is a faster evolution with respect to GR. The opposite happens when β is negative: the coupling decreases as the field rolls down the potential, and thus reduces the impact of modified gravity in the power spectrum. This decrease in power is relevant when it comes to use perturbations to further constrain the parameter space of this model. In the previous section, we showed that even if the DDE model is compatible with CMB observations (van de Bruck & Mifsud 2018) it gives an increase in the power spectrum of about 10% at $k \sim 3\ h/\mathrm{Mpc}$, which might be too large for it to be compatible with galaxy surveys. This being a problem or not will naturally depend on the galaxy formation model used to connect these predictions with the actual distribution of galaxies. In case this is indeed a problem, we show here that it can be alleviated by choosing negative values for β. In fact, the relative difference between the simulation that was run with $\beta = -10$ and $\beta = 0$ at the Nyquist frequency is of the same order than the effect that the base model with $\beta = 0$ has with respect to GR and thus can reduce the modified gravity effects by a factor of about two.

The effects of β in the FF model are more complex. A positive coupling constant β has the same effect in the power spectrum as in the DDE model at large scales (i.e. it induces an increase in power). However, at small scales, the impact of modified gravity in the power spectrum decreases with respect to the base model with $\beta = 0$. Note that the same happens when comparing the base model with GR, however the transition between positive and negative MG effects occurs at different frequency k. The net effect of assuming positive β is to increase even more the power with respect to GR at large scales and reduce it at small scales. The opposite occurs when β is assumed to be negative: there is a reduction of power at large scales and an increase at small scales. As in the DDE case, allowing β to move away from zero may help in reducing the problem that we found in previous section with excessive increase in power at large scales. However, in this case, the effects of β are one order of magnitude below the effect produced by the base model with $\beta = 0$ and thus, including β cannot save the model (at least not with the parameter we choose, which is equal to -10).

7 CONCLUSIONS

We studied new phenomenology that arises when adding a disformal coupling to a very simple and well known extension to General Relativity (GR) such as the quintessence model. The paper is divided in two main parts. We first discuss analytical properties of the solutions of the field equation for the background as well as the perturbations. In the second part, we present cosmological non-linear simulations that we run with the code `Isis` (Llinares et al. 2014), which is based of the particle mesh code `Ramses` (Teyssier 2002). We use the simulated data to show how our analytic predictions perform in realistic situations associated with the non-linear regime of cosmological evolution.

We start by describing background solutions of the Klein-Gordon equation for an Einstein-de Sitter cosmology. We found that the shape of the solution depends on only two parameters D and F (see Eq. 12 and 13), which are combinations of the original four free parameters (V_0, ν, B_0 and β). In the case $F = 0$, we identified three different characteristic time scales (shown in Table 1 and Figure 2), which determine the structure of the solution. These scales consist in a transition between a disformal regime and a quintessence regime and a transition between these two regimes and a non-linear regime that occurs when the fields grow to the point that it is not possible to linearise the potential V. Assuming $F \neq 0$ changes the definition of these time scales for $F > 0$ and induces an instability in the case $F < 0$, for which we provide a condition on its associated time scale.

The first part of the paper also deals with analytic properties of the perturbed Klein-Gordon equation. In particular, we show that there is an approximate proportionality relation between the perturbed scalar field and the scalar perturbations of the metric. The relation can be simplified by substituting the fields that constitute the proportionality factor with background quantities. By analysing the modified geodesics equation, we also show that a similar relation exists between the Newtonian force and the fifth force that arises from the scalar field. We close the analytic section by discussing the conditions under which the fifth force can be repulsive. This is relevant in the context of the tension that

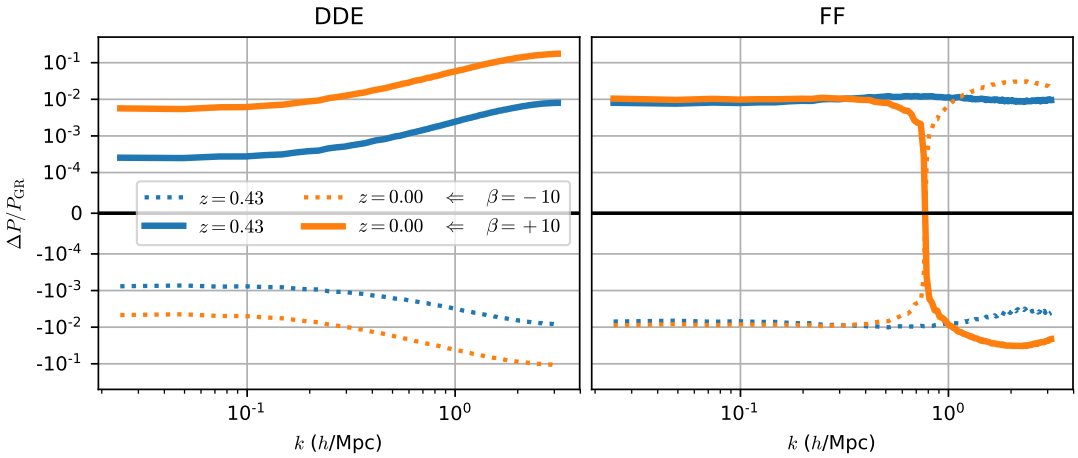

Figure 12. Relative difference between dark matter power spectra of simulations with β equal and different than zero. The left and right panels correspond to the DDE and FF models respectively. Different colours are different redshifts and different line styles correspond to simulations run with $\beta=-10$ and $\beta=10$. The sharp transition between positive and negative values in the right panel is generated by the symlog scaling that we use to be able to plot positive and negative values.

is known to exist between measurements of the normalization of density perturbations in the universe using high and low redshift data sets (Planck Collaboration et al. 2016b; Addison et al. 2016; Couchot et al. 2017; Kitching et al. 2016).

In the second part of the paper, we first used our N-body simulations to study properties of the field distribution. Very good agreement was found between the exact solution obtained by the non-linear hyperbolic solver of the cosmological code (which can solve the equation without relying on any assumptions or approximations) and the prediction obtained following the proportionality relation with the metric perturbations. This shows that, although the model is very complex, it can be simulated with a very simple algorithm based on the solution of the Poisson's equation, which exists in any standard gravity cosmological code. We will present in a companion paper a detailed analysis of the accuracy with which the method can predict the evolution of matter.

An additional result associated with the simulated fields is that the perturbations do not grow monotonically with time, but can undergo oscillations. Combining these results with our analytic results, we show that these oscillations cannot be sustained, but that field perturbations can have at most one maximum and one minimum and that ultimately will decrease towards zero. The time scale for these oscillations naturally depends on the model parameters.

Our simulations also show that the repulsive forces that we predicted analytically do emerge in realistic situations. We found that depending on the model parameters, repulsive forces can appear as transients that occur only at specific redshifts or be sustained in time. In both cases, the existence of forces is related with the zeros of the function ξ_0, which connects metric and scalar field perturbations.

It is worth mentioning that repulsive forces may arise in laboratory experiments aimed to the detection of fifth forces (e.g. Burrage et al. 2015; Burrage & Copeland 2016; Burrage et al. 2016a,b; Jaffe et al. 2017; Brax & Davis 2016; Llinares & Brax 2019). Since these effects are encoded in the term $\nabla\times\mathbf{k}$ defined in Eq. 35 and this term is exactly zero in spherical symmetry, a spherically symmetric experiment will not give rise to repulsive forces. More complex matter distributions are needed to give the desired effect. In other words, the presence of repulsive forces (which are opposite to gravity independently of the force that is associated to the walls of the experiment) can be tested by comparing results obtained with different distributions of matter (e.g. spherical vs. cubic). Note that this reasoning can be done only after evaluating the coefficient $(1-\delta d)\eta^2$ in the background (see derivation of Eq. 32). Relaxing this assumption may give additional mechanisms for the realization of repulsive forces.

We complete the analysis of our simulations by studying how the fifth force that arises from the scalar field affects the matter distribution. In particular, we focus on the power spectrum of density perturbations. For the models that have $\beta=0$ (i.e. a constant disformal coupling), we show that models with weak coupling produce an increase of power at small scales, which is almost scale invariant at late times. Models with larger coupling have an early increase in power which is followed with a decrease. In these cases, the fifth force is such that it reduces the clustering with respect to GR. We also studied the impact of β in the density perturbations. We found that positive or negative β, increase or decrease the effects of the fifth force at all scales.

Only one of all the simulated models (the DDE model) provides a background cosmology that is consistent with CMB data. However, the aim of this work is not to provide best parameters, but to highlight new phenomenology. The effects that we describe here may also appear in similar models which may be consistent with background data for different sets of parameters. In other words, it may be pos-

sible to build models with effects similar to those discussed here and that at the same time provide a background that is consistent with data.

ACKNOWLEDGEMENTS

Many thanks to Jack Morrice for helpful discussions and David Bacon and Kazuya Koyama for carefully reading the manuscript. We also thank the Research Council of Norway for their support. CLL acknowledges support from STFC consolidated grant ST/L00075X/1 & ST/P000541/1 and ERC grant ERC-StG-716532-PUNCA. The simulations used in this paper were performed on the NOTUR cluster FRAM. This paper is based upon work from COST action CA15117 (CANTATA), supported by COST (European Cooperation in Science and Technology).

REFERENCES

Abbott B. P., et al., 2017, ApJ, 848, L13
Addison G. E., Huang Y., Watts D. J., Bennett C. L., Halpern M., Hinshaw G., Weiland J. L., 2016, ApJ, 818, 132
Amendola L., 2004, Physical Review Letters, 93, 181102
Amendola L., et al., 2018, Living Reviews in Relativity, 21, 2
Arroja F., Bartolo N., Karmakar P., Matarrese S., 2015, J. Cosmology Astropart. Phys., 9, 051
Astier P., et al., 2006, A&A, 447, 31
Barreira A., Cautun M., Li B., Baugh C. M., Pascoli S., 2015, J. Cosmology Astropart. Phys., 8, 028
Barrow J. D., Mota D. F., 2003, Class. Quant. Grav., 20, 2045
Bekenstein J. D., 1993, Phys. Rev. D, 48, 3641
Bekenstein J., Milgrom M., 1984, ApJ, 286, 7
Ben Achour J., Langlois D., Noui K., 2016, Phys. Rev., D93, 124005
Bertschinger E., 2001, ApJS, 137, 1
Bettoni D., Liberati S., 2013, Phys. Rev., D88, 084020
Brax P., Davis A.-C., 2016, Phys. Rev., D94, 104069
Brax P., Burrage C., Davis A.-C., Gubitosi G., 2013, JCAP, 1311, 001
Brevik I., Obukhov V. V., Timoshkin A. V., 2015, Ap&SS, 359, 11
Burrage C., Copeland E. J., 2016, Contemporary Physics, 57, 164
Burrage C., Copeland E. J., Hinds E. A., 2015, J. Cosmology Astropart. Phys., 3, 042
Burrage C., Copeland E. J., Stevenson J. A., 2016a, J. Cosmology Astropart. Phys., 8, 070
Burrage C., Kuribayashi-Coleman A., Stevenson J., Thrussell B., 2016b, J. Cosmology Astropart. Phys., 12, 041
Cai Y.-C., Padilla N., Li B., 2015, MNRAS, 451, 1036
Clifton T., Ferreira P. G., Padilla A., Skordis C., 2012, Phys. Rep., 513, 1
Copeland E. J., Sami M., Tsujikawa S., 2006, International Journal of Modern Physics D, 15, 1753
Couchot F., Henrot-Versillé S., Perdereau O., Plaszczynski S., Rouillé d'Orfeuil B., Spinelli M., Tristram M., 2017, A&A, 597, A126
Deruelle N., Rua J., 2014, JCAP, 1409, 002
Falck B., Koyama K., Zhao G.-B., Cautun M., 2018, MNRAS, 475, 3262
Hagala R., Llinares C., Mota D. F., 2016, A&A, 585, A37
Ip H. Y., Sakstein J., Schmidt F., 2015, J. Cosmology Astropart. Phys., 10, 051
Jaffe M., Haslinger P., Xu V., Hamilton P., Upadhye A., Elder B., Khoury J., MÃijller H., 2017, Nature Phys., 13, 938
Joyce A., Jain B., Khoury J., Trodden M., 2015, Phys. Rep., 568, 1
Kaloper N., 2004, Physics Letters B, 583, 1
Kitching T. D., Verde L., Heavens A. F., Jimenez R., 2016, MNRAS, 459, 971
Koivisto T. S., 2008, preprint, (arXiv:0811.1957)
Koivisto T., Mota D. F., 2008, JCAP, 0808, 021
Koivisto T. S., Mota D. F., Zumalacárregui M., 2012, Physical Review Letters, 109, 241102
Koyama K., 2016, Reports on Progress in Physics, 79, 046902
Li B., Barrow J. D., 2011, Phys. Rev. D, 83, 024007
Li B., Koyama K., et al., 2018, International Journal of Modern Physics D, 27, 1802009
Llinares C., 2011, PhD thesis, Univ. Groningen, ISBN: 978-90-367-4760-8
Llinares C., Brax P., 2019, Phys. Rev. Lett., 122, 091102
Llinares C., Mota D. F., 2014, Phys. Rev. D, 89, 084023
Llinares C., Knebe A., Zhao H., 2008, MNRAS, 391, 1778
Llinares C., Mota D. F., Winther H. A., 2014, A&A, 562, A78
Lue A., Scoccimarro R., Starkman G., 2004, Phys. Rev. D, 69, 044005
Martel H., Shapiro P. R., 1998, MNRAS, 297, 467
Nojiri S., Odintsov S. D., Oikonomou V. K., 2017, Phys. Rep., 692, 1
Planck Collaboration et al., 2016a, A&A, 594, A13
Planck Collaboration et al., 2016b, A&A, 594, A15
Riess A. G., et al. 1998, AJ, 116, 1009
Risaliti G., Lusso E., 2015, ApJ, 815, 33
Sakstein J., 2014, J. Cosmology Astropart. Phys., 12, 012
Sakstein J., 2015, Phys. Rev. D, 91, 024036
Sakstein J., Verner S., 2015, Phys. Rev. D, 92, 123005
Silvestri A., Trodden M., 2009, Reports on Progress in Physics, 72, 096901
Skordis C., Mota D. F., Ferreira P. G., Boehm C., 2006, Phys. Rev. Lett., 96, 011301
Skordis C., Pourtsidou A., Copeland E. J., 2015, Phys. Rev. D, 91, 083537
Teyssier R., 2002, A&A, 385, 337
Voivodic R., Lima M., Llinares C., Mota D. F., 2017, Phys. Rev. D, 95, 024018
Weinberg S., 1989, Reviews of Modern Physics, 61, 1
Weinberg D. H., Mortonson M. J., Eisenstein D. J., Hirata C., Riess A. G., Rozo E., 2013, Phys. Rep., 530, 87
Xia J.-Q., 2013, Journal of Cosmology and Astro-Particle Physics, 2013, 022
Zumalacárregui M., Koivisto T. S., Mota D. F., Ruiz-Lapuente P., 2010, Journal of Cosmology and Astro-Particle Physics, 2010, 038
Zumalacárregui M., Koivisto T. S., Mota D. F., 2013, Phys. Rev. D, 87, 083010
van de Bruck C., Mifsud J., 2018, Phys. Rev. D, 97, 023506
van de Bruck C., Morrice J., 2015, J. Cosmology Astropart. Phys., 4, 036
van de Bruck C., Mifsud J., Mimoso J. P., Nunes N. J., 2016, J. Cosmology Astropart. Phys., 11, 031
van de Bruck C., Mifsud J., Morrice J., 2017, Phys. Rev. D, 95, 043513

APPENDIX A: ASYMPTOTIC SOLUTIONS FOR BACKGROUND FIELDS FOR AN EINSTEIN-DE SITTER UNIVERSE

Tables A1 and A2 summarize solutions of the Klein-Gordon equation described in Sections 3.1.1 and 3.1.2. These are solutions for the limits $(D,F) \to 0$ (Table A1) and $F \to 0$

Q1. Quintessence, linear ($\tilde{\chi} << 1$), without damping:

$$\partial_{\tilde{t}}^2 \tilde{\chi} = 1 \qquad \Rightarrow \qquad \tilde{\chi} = \frac{\tilde{t}^2}{2} \tag{A1}$$

The equation of motion is linear; its solution is a power law.

Q2. Quintessence, linear ($\tilde{\chi} << 1$), with damping:

$$\partial_{\tilde{t}}^2 \tilde{\chi} = -\frac{2}{\tilde{t}} \partial_{\tilde{t}} \tilde{\chi} + 1 \qquad \Rightarrow \qquad \tilde{\chi} = \frac{\tilde{t}^2}{6} \tag{A2}$$

The equation of motion is still linear. The damping term is present at all times and changes only the normalization of the solution (not the slope).

Q3. Quintessence, non-linear ($\tilde{\chi} \sim 1$), without damping:

$$\partial_{\tilde{t}}^2 \tilde{\chi} = \exp(-\tilde{\chi}) \qquad \Rightarrow \qquad \tilde{\chi} = \log\left[\cosh^2\left(\frac{\tilde{t}}{\sqrt{2}}\right)\right] \sim \begin{cases} \tilde{t}^2/2 & \text{if } \tilde{t} \lesssim T_a^{\rm nd}, \\ \sqrt{2}\tilde{t} & \text{if } \tilde{t} \gtrsim T_a^{\rm nd} \end{cases} \tag{A3}$$

Taking into account the exponential definition of the potential gives a non-linearity to the equation which is active only for large enough values of $\tilde{\chi}$. This non-linearity is negligible at early times and thus, the solutions behave as the linear solutions Q1 and Q2. At late times, the force responsible for the evolution of the field decreases with time, giving a different slope to the solution. The transition time $T_a^{\rm nd}$ between the linear and non-linear regimes can be calculated as the moment in which the two asymptotes of the solution cross each other.

Q4. Quintessence, non-linear ($\tilde{\chi} \sim 1$), with damping:

$$\partial_{\tilde{t}}^2 \tilde{\chi} = -\frac{2}{\tilde{t}} \partial_{\tilde{t}} \tilde{\chi} + \exp(-\tilde{\chi}) \qquad \Rightarrow \qquad \tilde{\chi} \sim \begin{cases} \tilde{t}^2/6 & \text{if } \tilde{t} \lesssim T_a, \\ \log(\tilde{t}^2/2) & \text{if } \tilde{t} \gtrsim T_a \text{ (this is an exact solution)} \end{cases} \tag{A4}$$

A combination of the presence of the damping term and the reduction of the potential with time changes the slope of the solution in the non-linear regime, which becomes logarithmic at large times. This changes slightly the transition time T_a, which we estimated numerically as the moment in which the logarithmic slope of the solution is the mean of the two asymptotes. Note that the transition between linear and non-linear regimes and undamped and damped regimes occurs approximately at the same time.

Table A1. General properties of background solutions of the quintessence model. See section 3.1.1 for explanation.

(Table A2) for small and large values of the field and with and without including the damping term in the equation.

APPENDIX B: NON-EDS BACKGROUND SOLUTIONS

We discussed in Section 3.1 solutions of the Klein-Gordon for an Einstein-de Sitter universe (i.e. a flat Universe with $\Omega_m = 1$). This simplification in the energy content of the Universe, enabled us to obtain analytic solutions for several models from which general properties can be understood. In the more realistic case, in which the energy of the scalar field is taken into account, the solutions are far more complex. An example of these solutions is presented in Figure B1, were we show colour coded the logaritmic slope of the scalar field

$$\frac{d\log\tilde{\chi}}{d\log a} = \frac{a}{\tilde{\chi} da/d\tilde{t}} \frac{d\tilde{\chi}}{d\tilde{t}} \tag{B1}$$

as a function of expansion factor and the free parameter D for three different models.

The model presented in the left panel assumes the background metric is EDS. The solutions are the same that we presented in Figure 2; although here we show derivatives with respect to $\log(a)$ intead of time and thus, the exact numbers of the slope in different regimes are different. The central panel shows the result of assuming a ΛCDM background. The presence of a dark energy component changes the behaviour of the model for large values of D: instead of a transition to the disformal non-linear regime (see Figure 2 for nomenclature), we have a transition to the quintessence linear regime, which occurs at values of a that are independent of D. The right panel shows an example of the complete solution, in which the energy of the scalar field is included in the Friedmann equations (which results in additional terms in the equation for the density parameter Ω_m). Here, the new transition that occurred at large values of D in the previous case is not only delayed, but also has a complex dependence with D. Different solutions occur for different values of ν.

A complete analysis of the fully self-consistent background evolution is beyond the scope of this paper. In order to simplify the work of those who want to move forward in the understanding of these solutions, we provide the complete set of equations that need to be solved in convenient

D1. Disformal, $\beta = 0$, linear ($\chi << 1$), without damping:

$$\partial_{\tilde{t}}^2\tilde{\chi} = \frac{\tilde{t}^2}{\tilde{t}^2+D} \quad \Rightarrow \quad \tilde{\chi} = \frac{\tilde{t}^2}{2}\left[1 - \frac{2\sqrt{D}}{\tilde{t}}\tan^{-1}\left(\frac{\tilde{t}}{\sqrt{D}}\right) + \frac{D}{\tilde{t}^2}\log\left(\frac{\tilde{t}^2+D}{D}\right)\right] \sim \begin{cases} \tilde{t}^4/(12D) & \text{if } \tilde{t} \lesssim T_b^{\rm nd}, \\ \tilde{t}^2/2 & \text{if } \tilde{t} \gtrsim T_b^{\rm nd} \end{cases} \tag{A5}$$

The disformal coupling gives a time dependence to the term associated to the external force, which is such that it approaches zero at early times. This changes the logarithmic slope of the solution with respect to the equivalent solution of the quintessence model (model Q1 in Table A1) at early times. At late times, the time dependence approaches a constant and thus, the evolution of the field is as in the quintessence model Q1. The transition time $T_b^{\rm nd}$ can be estimated as the moment where the two assymptotes cross each other.

D2. Disformal, $\beta = 0$, linear ($\chi << 1$), with damping:

$$\partial_{\tilde{t}}^2\tilde{\chi} = -2\frac{\tilde{t}}{\tilde{t}^2+D}\partial_{\tilde{t}}\tilde{\chi} + \frac{\tilde{t}^2}{\tilde{t}^2+D} \quad \Rightarrow \quad \tilde{\chi} = \frac{\tilde{t}^2}{6}\left[1 - \frac{D}{\tilde{t}^2}\log\left(\frac{\tilde{t}^2+D}{D}\right)\right] \sim \begin{cases} \tilde{t}^4/(12D) & \text{if } \tilde{t} \lesssim T_b, \\ \tilde{t}^2/6 & \text{if } \tilde{t} \gtrsim T_b \end{cases} \tag{A6}$$

The damping term of the disformal equation differs with respect to the one we find in the quintessence case (model Q2 in Table A1) in that it approaches zero at early times. Thus, the early time solution is not affected by the presence of this term (i.e. it is a power law with a logarithmic slope equal to four as in D1). At late times, the solution switches to the solution for the quintessence model that includes damping (model Q2). The transition occurs at a slightly earlier time T_b.

D3. Disformal, $\beta = 0$, non-linear ($\chi \sim 1$), without damping:

$$\partial_{\tilde{t}}^2\tilde{\chi} = \frac{\tilde{t}^2}{\tilde{t}^2+D}\exp(-\tilde{\chi}) \quad \Rightarrow \quad \begin{cases} \dfrac{D \ll 1}{(T_c^{\rm nd} \lesssim T_b^{\rm nd})} & \Rightarrow \quad \chi \sim \begin{cases} \tilde{t}^4/(12D) & \text{if } \tilde{t} \lesssim T_b^{\rm nd} \\ \tilde{t}^2/2 & \text{if } T_b^{\rm nd} \lesssim \tilde{t} \lesssim T_a^{\rm nd} \\ \sqrt{2}\tilde{t} & \text{if } \tilde{t} \gtrsim T_a^{\rm nd} \end{cases} \\ \dfrac{D \gg 1}{(T_c^{\rm nd} \gtrsim T_b^{\rm nd})} & \Rightarrow \quad \chi \sim 3\left[e^{-\tilde{t}^4/(12D)} - 1\right] - \dfrac{3^{3/4}}{\sqrt{2}D^{1/4}}\Gamma\left[3/4, \dfrac{\tilde{t}^4}{12D}, 0\right]\tilde{t} \sim \begin{cases} \tilde{t}^4/(12D) & \text{if } \tilde{t} \lesssim T_c^{\rm nd} \\ \frac{3^{3/4}\Gamma(3/4)}{\sqrt{2}D^{1/4}}\tilde{t} & \text{if } \tilde{t} \gtrsim T_c^{\rm nd} \end{cases} \end{cases} \tag{A7}$$

For $D \ll 1$, the equation can be linearised with respect to D and becomes a perturbed quintessence equation: $\partial_{\tilde{t}}^2\tilde{\chi} = (1 - D/\tilde{t}^2)\exp(-\chi)$. Since the disformal effects are a perturbation, the transition to the quintessence regime occurs before anything else happens. Thus, the solution transitions first from the linear disformal to the linear quintessence regimes at $T_b^{\rm nd}$ (as in solution $D1$) and then towards the non-linear quintessence regime at $T_a^{\rm nd}$ (as in solution Q3).

For $D \gg 1$, the transition towards the non-linear regime occurs before the transition to the quintessence regime. We can obtain a good approximation of the solution by linearizing the equation with respect to time and substituting the early time solution in the exponential function (i.e. by solving $\partial_{\tilde{t}}^2\tilde{\chi} = \tilde{t}^2\exp\left(-\tilde{t}^4/(12D)\right)$). After the transition to the non-linear regime occured, the field behaves as a free particle and thus, no more transitions occur.

D4. Disformal, $\beta = 0$, non-linear ($\chi \sim 1$), with damping:

$$\partial_{\tilde{t}}^2\tilde{\chi} = \frac{\tilde{t}^2}{\tilde{t}^2+D}\exp(-\tilde{\chi}) \quad \Rightarrow \quad \begin{cases} \dfrac{D \ll 1}{(T_c \lesssim T_b)} & \Rightarrow \quad \chi \sim \begin{cases} \tilde{t}^4/(12D) & \text{if } \tilde{t} \lesssim T_b \\ \tilde{t}^2/6 & \text{if } T_b \lesssim \tilde{t} \lesssim T_a \\ \log\left(\tilde{t}^2/2\right) & \text{if } \tilde{t} \gtrsim T_a \end{cases} \\ \dfrac{D \gg 1}{(T_c \gtrsim T_b)} & \Rightarrow \quad \chi \sim \begin{cases} \tilde{t}^4/(12D) & \text{if } \tilde{t} \lesssim T_c \\ \frac{3^{3/4}\Gamma(3/4)}{\sqrt{2}D^{1/4}}\tilde{t} & \text{if } T_c \lesssim \tilde{t} \lesssim T_b \\ \log\left(\tilde{t}^2/2\right) + 3^{5/4}\Gamma(3/4)D^{1/4} & \text{if } \tilde{t} \gtrsim T_b \end{cases} \end{cases} \tag{A8}$$

For $D \ll 1$, the solution has a quick transition towards the linear quintessence regime as in D3. Since damping was taken into account in these solutions, the transition is towards Q4 instead of Q3).

For $D \gg 1$, we have again (as in D3) that the transition towards the non-linear regime occurs before the transition to the quintessence regime. The transition can be obtained by patching solutions of the different regimes, but taking into account that damping affects the quintessence regime at large $\tilde{t}$ and adding an appropiate constant to ensure continuity at T_c.

Table A2. General properties of background solutions of models with conformal coupling.

variables for the case $\beta = 0$:

$$\partial_{\tilde{t}}^2\tilde{\chi} = \frac{1}{1 + \frac{3}{4}D\tilde{\Omega}_m}\left[-3\tilde{H}\partial_{\tilde{t}}\tilde{\chi} + \exp(-\tilde{\chi})\right] \tag{B2}$$

$$\partial_{\tilde{t}}\tilde{\Omega}_m = -3\tilde{H}\tilde{\Omega}_m - \frac{D}{\nu^2}\frac{\partial_{\tilde{t}}\tilde{\chi}}{1 + \frac{3}{4}D\tilde{\Omega}_m}\left[3\tilde{H}\partial_{\tilde{t}}\tilde{\chi} - \exp(-\tilde{\chi})\right]\tilde{\Omega}_m \tag{B3}$$

$$\tilde{H}^2 = \tilde{\Omega}_m + \frac{1}{3\nu^2}\left[\frac{\partial_{\tilde{t}}\tilde{\chi}}{2} + \exp(-\tilde{\chi})\right], \tag{B4}$$

where we used a renormalized density parameter:

$$\tilde{\Omega}_m \equiv \frac{\Omega_m}{v_0\nu^2}. \tag{B5}$$

The equation of motion for this quantity (Eq. B3) can be obtained by combining Eq. B4 (i.e. the component 00 of the

background Einstein's equations) and the *ii* equation:

$$H^2 - \frac{\ddot{a}}{a} = -\frac{1}{M_P^2}\left[\frac{\dot{\phi}^2}{2} - V(\phi)\right]. \tag{B6}$$

The equations can be further simplified by defining $q \equiv \partial_{\tilde{t}}\tilde{\chi}$ and using $u = \ln a$ intead of $\tilde{t}$ as integration variable:

$$\partial_u \tilde{\chi} = \frac{q}{\tilde{H}} \tag{B7}$$

$$\partial_u q = \frac{1}{1+\frac{3}{4}D\tilde{\Omega}_m}\left[-3q + \frac{\exp(-\tilde{\chi})}{\tilde{H}}\right] \tag{B8}$$

$$\partial_u \tilde{\Omega}_m = -3\tilde{\Omega}_m - \frac{D}{v^2}\frac{q\tilde{\Omega}_m}{1+\frac{3}{4}D\tilde{\Omega}_m}\left[3q - \frac{\exp(-\tilde{\chi})}{\tilde{H}}\right] \tag{B9}$$

$$\tilde{H}^2 = \tilde{\Omega}_m + \frac{1}{3v^2}\left[\frac{q^2}{2} + \exp(-\tilde{\chi})\right]. \tag{B10}$$

The initial conditions for the scalar field and its derivative are defined as equal to zero at very high redshift. To define the initial condition for $\tilde{\Omega}_m$, it is possible to use a shooting method, and force the solution to be equal to 0.3 (aproximatelly the ΛCDM value) at $a = 1$.

This paper has been typeset from a TEX/LATEX file prepared by the author.

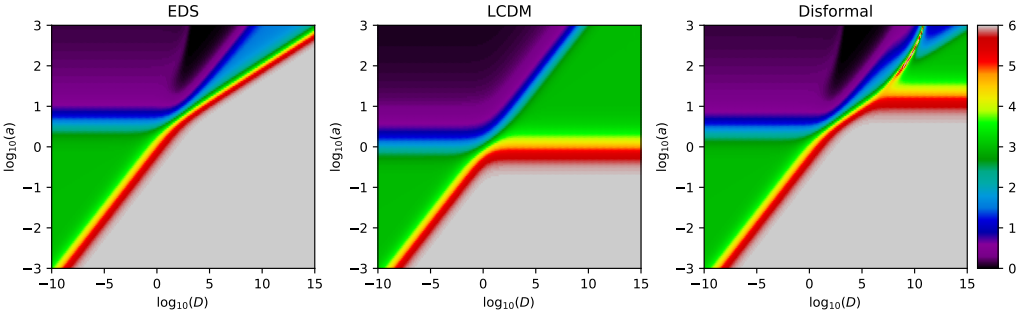

Figure B1. Colour coded is the logarithmic slope of the solution of the background Klein-Gordon equation for the disformal model with $\beta = 0$ and three different models for the background expansion: Einstein-de Sitter, ΛCDM (with a cosmological constant) and disformal model with $\nu = 100$. The EDS model is the same as shown in Figure 2, with the difference that here we used expansion factor as independent variable and thus, the exact values of the slopes are different.

Paper III

The Slingshot Effect as a Probe of Transverse Motions of Galaxies

Robert Hagala, Claudio Llinares, David F. Mota

Published in *Astronomy & Astrophysics*, August 2019, volume 628, A30. DOI: 10.1051/0004-6361/201935261. arXiv: 1907.01429.

Astronomy & Astrophysics manuscript no. output
July 10, 2019

The slingshot effect as a probe of transverse motions of galaxies

R. Hagala[1], C. Llinares[2], and D. F. Mota[1]

[1] Institute of Theoretical Astrophysics, University of Oslo, PO Box 1029 Blindern, 0315 Oslo, Norway
e-mail: robert.hagala@astro.uio.no
[2] Institute of Cosmology and Gravitation, University of Portsmouth, Dennis Sciama Building, Portsmouth PO1 3FX, United Kingdom

ABSTRACT

Context. There are currently no reliable methods to measure the transverse velocities of galaxies. This is an important piece of information that is lacking in galaxy catalogues, and it could allow us to probe the physics of structure formation and to test the underlying theory of gravity. The slingshot effect—a special case of the integrated Sachs–Wolfe effect—is expected to create dipole signals in the temperature fluctuations of the cosmic microwave background (CMB) radiation. This effect creates a hot spot behind and a cold spot in front of moving massive objects. The dipole signal created by the slingshot effect can be used to measure transverse velocities, but because the signal is expected to be weak, the effect has not been measured yet.
Aims. Our aim is to show that the slingshot effect can be measured by stacking the signals of galaxies falling into a collapsing cluster. Furthermore, we evaluate whether the effect can probe modified gravity.
Methods. We used data from a simulated galaxy catalogue (MultiDark Planck 2) to mimic observations. We identified a $10^{15} M_{\odot}$ cluster, and made maps of the slingshot effect for photons passing near 8438 infalling galaxies. To emulate instrument noise, we added uncorrelated Gaussian noise to each map. We assumed that the average velocity is directed towards the centre of the cluster. The maps were rotated according to the expected direction of motion. This assures that the dipole signal adds up constructively when stacking the maps. We compared the stacked maps to a dipole stencil to determine the quality of the signal. We also evaluated the probability of fitting the stencil in the absence of the slingshot signal.
Results. Each galaxy gives a signal of around $\Delta T/T \approx 10^{-9}$, while the current precision of CMB experiments is $\Delta T/T \approx 4 \times 10^{-6}$. By stacking around 10 000 galaxies and performing a stencil fit, the slingshot signal can be over the detectable threshold with today's experiments. However, due to the difficulty of distinguishing an actual signal from false positives, future CMB experiments must be used to be certain of the strength of the observed signal.

1. Introduction

By precisely measuring the positions and velocities of galaxies, we can use them as tracers for mapping the underlying matter distribution of the large-scale structure of the Universe. Furthermore, in systems where the matter distribution is known from other methods, for instance from gravitational lensing, precise catalogues of the positions and velocities of galaxies can be used as a consistency check to test our models of gravity and structure formation. While the radial velocity with respect to the Earth is measurable through the Doppler effect, transverse velocities of galaxies are more challenging to measure. The only reliable method of estimating transverse velocities of an object directly is through detecting a change in position relative to the background between two observations, which is known as the proper motion of the object. The recent data release of Gaia (Gaia Collaboration et al. 2018) presented the proper motions of over a billion stars in our galaxy, where the velocities were found using this method. However, this option becomes unfeasible at scales larger than our galaxy because many years must pass before distant galaxies will move far enough for the motion to be resolved.

When a galaxy is affected by an external force like gravity, the resulting acceleration first changes the velocity of the galaxy before the position of the galaxy changes significantly. Better knowledge of the peculiar velocities of observed galaxies will help us compare our models of gravity on large scales with the forces acting on those galaxies. This can be particularly useful when studying theories of modified gravity, but can also be used to measure the amount and distribution of dark matter in the context of ΛCDM. Velocities can be used as a consistency check for our models of structure formation. The best models predict the matter distribution very well, but the velocity fields of the same models are not usually compared to observations (Stebbins 2006). Furthermore, measurements of tangential velocities can break the degeneracy between expansion velocity and peculiar velocity, which is a problem when using only the redshift to measure velocities.

The slingshot effect was first mentioned by Birkinshaw & Gull (1983), and is a promising probe for measuring transverse motions. It is a special case of the integrated Sachs–Wolfe (ISW) effect (Sachs & Wolfe 1967). The ISW contribution to the cosmic microwave background (CMB) is due to the evolution of a gravitational potential while photons are passing through it. The most relevant result of the late-time ISW is what is known as the Rees–Sciama effect (Rees & Sciama 1968). As structure collapses under gravity—or expands with the Hubble flow—while a photon passes through, the change in the gravitational potential of the structure will affect the photon energy. The Rees–Sciama effect results in an overall increase or decrease in the measured CMB temperature centred around clusters and voids. The Rees–Sciama effect can be estimated from galaxy surveys, and is expected to be important at the largest angular scales (Maturi et al. 2007a). In the literature, the slingshot effect is also called the Birkinshaw–Gull effect or the moving lens effect. Sometimes the name of the Rees–Sciama effect is used interchangeably with the slingshot effect, even though it describes a related but slightly different phenomenon.

The slingshot effect is related to the Rees–Sciama effect, but instead of a single hot spot centred on the halo, it creates a dipole

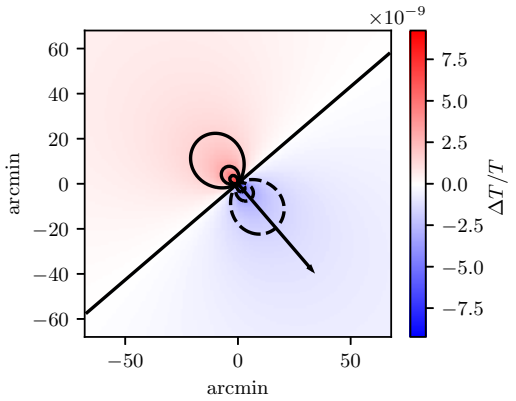

Fig. 1. Contour plot of the temperature dipole created by the slingshot effect. The arrow indicates the direction of motion of the galaxy. An increase in photon temperature is indicated in red; a decrease in temperature is illustrated in blue and with dashed contours. This example is a galaxy of virial mass $1.2 \times 10^{12}\, M_\odot$, moving with a transverse velocity component of 880 km/s, viewed at a distance of 100 Mpc

pattern with a cold spot in front of a moving halo and a hot spot behind it. Stebbins (2006) states that transverse motions of galaxies can be measured on the small scales of the CMB by statistically analysing these dipole patterns. The intention of this paper is to propose a method for measuring this effect. Sufficiently precise measurements of the effect can be used as a self-consistency check of our models of structure formation, and as a more direct measure of the gravitational forces acting on large scales.

The mechanism behind the dipole pattern of the slingshot effect can be understood as follows. If a CMB photon enters in front of the moving halo, the gravitational potential becomes deeper while the photon is passing through the potential well, meaning that the photon has to spend more energy getting out and becomes redshifted. Likewise, if a CMB photon enters behind the moving halo, the gravitational potential along the photon trajectory becomes shallower while the photon passes, allowing the photon to gain some energy. The result is a dipole signal. An example of the signal is represented visually in figure 1. The increase or decrease in photon energy can be compared to the gravity assist manoeuvre: a spacecraft can gain velocity relative to the heliocentric reference frame by passing in the trail of a moving planet. An effect related to the slingshot effect was proposed by Molnar et al. (2013), where a difference in redshift between two lensed images from the same source can be used to infer the tangential velocity of the lens. Other attempts at indirectly inferring transverse velocities include analysing microlensing parallaxes in very specific set-ups, where a quasar can be found behind the galaxy whose velocity is to be found (see e.g. Gould 1994).

The slingshot signal grows stronger with more massive and faster moving structures. Birkinshaw & Gull (1983) predicted that a massive and rapidly moving galaxy cluster should produce a measurable signal, but to our knowledge the effect has not been measured yet. As indicated by Stebbins (2006), the difficulty in measuring the effect could be due to similar dipole patterns being produced by the kinematic Sunyaev–Zel'dovich effect and by the lensing of the CMB anisotropies. With the current CMB experiments it is therefore impossible to measure the slingshot effect of a single galaxy. Recently, Hotinli et al. (2018) investigated the detectability of the slingshot effect by estimating the corrections to the CMB power spectrum. Furthermore, Yasini et al. (2018) proposed an estimator for the pairwise peculiar velocities of clusters using the slingshot effect. Both of these recent studies found that the combined effects of transversely moving objects should be measurable with CMB surveys in the near future.

The process of image stacking has the ability to isolate the slingshot effect from that of the kinematic Sunyaev–Zel'dovich effect and the lensed CMB. These two confounding effects are not correlated with position and velocity in the same way as the slingshot effect, meaning that their contribution is expected to average to zero when stacking enough images. Maturi et al. (2007b) propose that the slingshot effect can be measured by stacking the CMB maps of 1000 cluster mergers. In the current work we present a method for detecting the average peculiar infall velocity of galaxies around a single cluster. By aligning and stacking the signal from galaxies in a mock catalogue, and then fitting the stacked image to a template, we show that the effect will be detectable with CMB experiments in the near future, such as CMB-S4 (Abazajian et al. 2016).

2. Methods

The ISW effect changes the temperature of the CMB photons during the time t they spend in an evolving gravitational potential Φ. Specifically,

$$\frac{\Delta T}{T} = 2 \int \dot{\Phi}\, \mathrm{d}t, \tag{1}$$

where the dot indicates a time derivative. We adopt units such that $c = 1$.
The slingshot effect is the change in photon temperature due to the transverse motion of an unevolving gravitational well. Following a flow of photons travelling through a moving halo, this effect can be expressed as

$$\frac{\Delta T_{\mathrm{slingshot}}}{T} = 2 \int \mathbf{v}_\perp \cdot \nabla \Phi\, \mathrm{d}t. \tag{2}$$

We chose a coordinate system where light moves in the positive z-direction, along the line of sight. The projected motion $\mathbf{v}_\perp$ of the halo is taken to be constant and along the x-axis. In this frame, we define v_x as the velocity component perpendicular to the line of sight. Since the photons move with the speed of light and we chose units where $c = 1$, the time integral can be changed into an integral along z:

$$\frac{\Delta T_{\mathrm{slingshot}}}{T} = 2 v_x \int \frac{\partial \Phi}{\partial x}\, \mathrm{d}z. \tag{3}$$

The coordinates x, y, and z represent physical distances (measured in non-comoving megaparsecs). To estimate the magnitude of the slingshot effect, we assume a simple yet realistic model for the gravitational potential Φ derived from the halo model set-up.

2.1. Halo model set-up

For the purpose of calculating the signal from a single halo, we modelled the halo as a spherically symmetric matter distribution, centred at $x = y = z = 0$. We assumed that all of the dark matter halo mass is in a Navarro–Frenk–White (NFW) profile with

concentration $c_{\rm NFW} = 15$ (Navarro et al. 1995). We populated the halo with baryons, consisting of an additional 10% of the dark matter mass. We used a Hernquist profile for the baryons (Hernquist 1990), applying a Hernquist scale length a that relates to the virial radius $r_{\rm vir}$ of the dark matter halo according to

$$a = \frac{0.015\, r_{\rm vir}}{1 + \sqrt{2}} \tag{4}$$

(see the Appendix for the detailed calculations of the slingshot effect from the NFW and the Hernquist component). The resulting expression we implemented to calculate the slingshot effect from a single halo is

$$\frac{\Delta T_{\rm slingshot}}{T} = \frac{2Gm_{DM}v_x}{r_{\rm vir}}\left(Q_{\rm NFW} + \frac{1}{10}Q_{\rm Hernq}\right), \tag{5}$$

where

$$Q_{\rm NFW} \equiv \frac{g x_r}{x_r^2 + y_r^2}\left[\ln\left(\frac{c_{\rm NFW}^2\left(x_r^2 + y_r^2\right)}{4}\right) - S\,(2\arctan(S) - \pi)\right], \tag{6}$$

and

$$Q_{\rm Hernq} \equiv \left(\frac{1+\sqrt{2}}{0.015}\right)\frac{x_a}{x_a^2 + y_a^2 - 1}\left[2 + U\,(2\arctan(U) - \pi)\right]. \tag{7}$$

Here, m_{DM} is the virial mass of the dark matter halo. The constant g depends on the concentration $c_{\rm NFW}$ according to equation (16) in the Appendix. We use the following notation for dimensionless coordinates: $x_r \equiv x/r_{\rm vir}$ and $x_a \equiv x/a$. Furthermore,

$$S \equiv \frac{1}{\sqrt{c^2\left(x_r^2 + y_r^2\right) - 1}} \tag{8}$$

and

$$U \equiv \frac{1}{\sqrt{x_a^2 + y_a^2 - 1}}. \tag{9}$$

We note that the Q-expressions here are independent of halo parameters for the chosen model. This means that we only needed to calculate a template of the slingshot effect once, using units of the virial radius, we then re-scaled the template to galaxies of any size. The deciding factor for the amplitude of the slingshot effect is the combination $mv_x/r_{\rm vir}$.

2.2. Realistic observational set-up

The slingshot effect, described by equation (5), increases with the mass of the halo, and with the transverse velocity v_x relative to the CMB. We find that the slingshot signal from a single large galaxy with mass $10^{13} M_\odot$, moving at 1000 km/s, is around $\Delta T/T \sim 10^{-8}$, equivalent to $0.03\,\mu$K. Most galaxies would be less massive and move more slowly, giving an average signal of $\Delta T/T \approx 3\times10^{-9}$ (see section 2.3). Figure 1 shows the raw slingshot signal from an example galaxy, with a cold spot in front of the moving galaxy and a hot spot behind. This example galaxy is slightly heavier and moves slightly faster than the average, resulting in a stronger signal than $\Delta T/T \approx 3\times10^{-9}$.

The Atacama Cosmology Telescope (ACT) has instrument noise down to $6\,\mu{\rm K}\cdot{\rm arcmin}$, or a per-pixel noise of $\sigma_{\Delta T/T} \sim 4\times10^{-6}$ when assuming 0.5 arcmin pixels[1] (see Hincks et al. 2010 for details on the expected sensitivity and beam profile point spread function of ACT). The given noise level indicates that measuring the signal from a single massive galaxy is impossible since the signal of $\Delta T/T \sim 10^{-8}$ would be drowned out by noise. To get a signal-to-noise ratio (S/N) of the order of one, we would need to increase the signal, or reduce the noise, by a factor of 400. The signal increases with the square root of the number of stacked images, which means that we would have to stack the signal of over 160 000 fast and massive galaxies, or closer to 10^7 average galaxies. Furthermore, these galaxies must be close enough to us for the dipole to be resolved in the CMB map. The ACT has 1.3 arcmin full width at half maximum (FWHM) beam resolution. A typical galaxy with virial radius of 100 kpc must be within about 250 Mpc to be resolved with two or more pixels.

An important consideration when stacking these dipole images is that they need to be oriented correctly, such that the galaxy velocity directions point along approximately the same axis. Because there are no good ways to measure the transverse velocity of a single galaxy yet, it is necessary to stack observable galaxies only where the approximate direction of motion can be inferred from other means. While other papers suggest using the relative velocity of pairs of galaxy clusters (e.g. Yasini et al. 2018), in this work we study the infall velocity of galaxies in the large-scale structure of the cosmos. To estimate a direction of peculiar motion, we assumed that galaxies will fall towards not yet virialised cluster structures in their vicinity. This is not true for absolutely all galaxies, but when stacking images it is sufficient for the sample to have an average velocity in the radial direction. Another option not covered in this paper is stacking galaxies near the edges of voids. We expect void galaxies to have an average velocity directed out of the underdense region.

We suggest using the Coma Cluster to align the velocities of nearby galaxies in a realistic observational set-up. At a distance of about 100 Mpc (Liu & Graham 2002), the Coma Cluster is within the 250 Mpc needed to resolve a slingshot dipole. It is well studied, and not obscured by the Milky Way disc. The Coma Cluster is located approximately at a RA of 195 degrees and Dec of +28 degrees. Several current surveys cover this region, for instance the BOSS spectrographic survey of the SDSS (Sloan Digital Sky Survey). The Coma Cluster has a mass of about $1.9\times10^{15} M_\odot$ (found through weak lensing by Kubo et al. 2007). Together with the Leo Cluster, it is part of the rich Coma Supercluster, which is large enough to have not yet completely virialised. The total number of galaxies falling towards the supercluster could be sufficient to achieve a S/N of the order of unity through stacking [2]. Reaching a S/N of one requires that all of the infalling galaxies should be catalogued with position and redshift, and that on average they are falling in as fast as expected from simulations. Furthermore, the presence of foreground sources in our own galaxy can interfere with the precise measurement of the CMB around some of these galaxies.

To identify the signal even when the total stacked S/N is less than one, we propose fitting the expected dipole signal to the stacked image. Furthermore, we propose to estimate the probability of having false positives by fitting a template of the expected signal to several stacks of uncorrelated noise maps. If it

[1] It is common to construct maps using 2-3 pixels per FWHM of the instrument beam. The FWHM of ACT is 1.3 arcmin.

[2] Assuming that there are, on average, a few galaxies per cubic megaparsec of space, there should be approximately 10^6 galaxies within a 50 Mpc sphere.

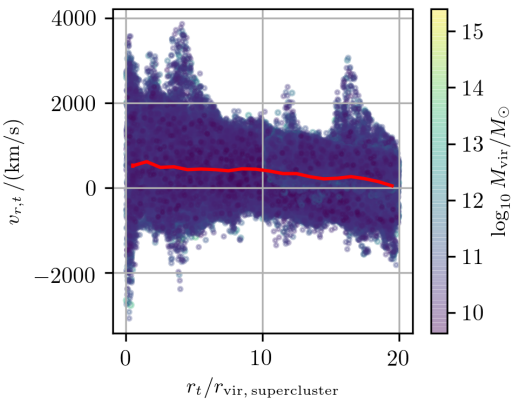

Fig. 2. Scatter plot of the projected radial motion of halos close to the massive supercluster. The horizontal axis shows the projected distance from the centre of the structure (in units of the virial radius of the supercluster). The vertical axis shows the projected radial velocity of the halo in question; positive values indicate infalling motion. The red line shows the binned mean. The error of the mean is consistent with the width of the line. The colour of a point indicates the virial mass of that halo.

is sufficiently improbable to achieve the best fit dipole randomly with just noise, we can say that the dipole is detectable, even if it is not visible by eye in the stacked image.

2.3. Stacking images from a simulated halo catalogue

To emulate realistic halos, we used the halo catalogue from the MultiDark Planck 2 survey described by Prada et al. (2012). The data set contains dark matter halos identified with the Rockstar halo finder (Behroozi et al. 2013). In this $(1\mathrm{Gpc}/h)^3$-box simulation, we identified one of the largest halos. It has a virial mass of the order of $M_{\mathrm{vir,\,supercluster}} \approx 10^{15}\,M_\odot$ and a virial radius $r_{\mathrm{vir,\,supercluster}} \approx 4$ Mpc, which is similar to values for the Coma Cluster. We find that this is the centre of a massive supercluster that has not yet virialised, meaning that nearby smaller halos are falling towards the supercluster. The virial mass and virial radius estimated by the halo finder at redshift zero is significantly lower than the actual mass affected gravitationally.

When studying subhalos close to the identified supercluster, we find that they indeed have a velocity component directed towards the centre of the structure (see figure 2 for a scatter plot of the velocities of halos surrounding the supercluster). The net inward flow of matter is apparent from closer than $1\,r_{\mathrm{vir,\,supercluster}}$, up to distances of about $20\,r_{\mathrm{vir,\,supercluster}}$.

We picked out nearby halos with virial mass above $10^{11} M_\odot$ within $10\,r_{\mathrm{vir,\,supercluster}}$ (approximately 40 Mpc) of the central supercluster. The mass cut-off was chosen to exclude halos hosting dwarf galaxies because they are more difficult to observe and they add a weak signal to the stack. The distance cut-off was chosen by hand; repeating the analysis with a $15\,r_{\mathrm{vir,\,supercluster}}$ distance cut-off instead did not significantly improve the results compared to $10\,r_{\mathrm{vir,\,supercluster}}$. We draw the conclusion that the halos that are further away add more noise than signal, for instance because their velocities are misaligned due to other nearby structure. The chosen cut of $10\,r_{\mathrm{vir,\,supercluster}}$ and $M > 10^{11} M_\odot$ leaves 8438 halos in our final sample. These halos mostly consist of galaxies, but also some galaxy groups and galaxy clusters. The selected halos have an average mass of $1.79 \times 10^{12}\,M_\odot$. We chose the z-axis of the 3D simulation as the line of sight, and projected the velocity of each halo down to the plane perpendicular to this axis (the x-y plane).

To simulate the signal observed with ACT, we created a 2D map of $\Delta T_{\mathrm{slingshot}}/T$ for each galaxy halo. The map size was chosen to fit two times the virial radius of that galaxy, with 0.5 arcmin pixel size. We smoothed the map with Gaussian blur with 2.6 pixels FWHM to emulate the 1.3 arcmin beam of ACT (Hincks et al. 2010). We assumed that each pixel of each image has an independent noise, drawn from a normal distribution with standard deviation $\sigma_{\Delta T/T}$. We performed the full analysis with three different values for the noise standard deviation: 4×10^{-6}, 1×10^{-6}, and 1×10^{-7}. We did not vary the other parameters, such as the angular resolution.

We neglected perturbations in the CMB background because we assumed the background can be modelled well enough, and subtracted on the relevant scales (corresponding to $l > 500$). We also neglected non-dipole contributions like foreground sources. All of these are either expected to average out when stacked (if they are not correlated with the galaxy position and direction of motion) or have a monopole signal that will not contribute to the dipole stencil fit. Furthermore, we also neglected galaxy lensing of large-scale CMB gradients, which will introduce dipoles on scales similar to the slingshot effect. The large-scale gradients of the CMB are not expected to be correlated with the velocity of low redshift galaxies falling into a massive cluster, so the amplitude of lensing of the CMB will be negligible with large enough data sets, as outlined by Stebbins (2006). To further help remove this confounding signal, a delensing algorithm can be applied to the map around each galaxy before stacking (see e.g. Manzotti 2018; a process of delensing for the purpose of isolating the slingshot signal is suggested in Maturi et al. 2007b). Similarly, we also neglected the signals from nearby galaxies or galaxies located behind the observed ones; if another galaxy is within $2r_{\mathrm{vir}}$ of the imaged galaxy, it will introduce an additional dipole which is not positioned at the centre of the map. The chance of such an overlap is not negligible, but since the relative positions are not considered correlated with the direction of infall velocity, the stacking and fitting process is not expected to be sensitive to this signal.

The combined maps of each nearby halo were, after applying the instrumental point spread function and adding noise, aligned according to the expected infall direction (i.e. radially towards the centre of the supercluster) to simulate real observations where we have no a priori knowledge of the individual peculiar velocities. Since we used realistic simulations, our mock data sets take into account the fact that the individual galaxy motion is not necessarily aligned with the radial direction. Before stacking, the maps were re-scaled with respect to the virial radius of each galaxy, using linear interpolation. This ensures that the stacked image will not be radially smeared due to size inconsistencies. In the main analysis we assumed that we have perfect knowledge of the virial radius, but we also did a smaller analysis consisting of fewer individual stacks than the main analysis, where we included the uncertainties on the virial mass and radius to show that our results are robust to this uncertainty.

The signal from each individual halo was summed up, and divided by the number of halos to achieve an average (or effective) signal. Example realisations of this average signal after stacking 8438 halos are shown in the top row of figure 3. The three columns are for three different noise levels: current ACT

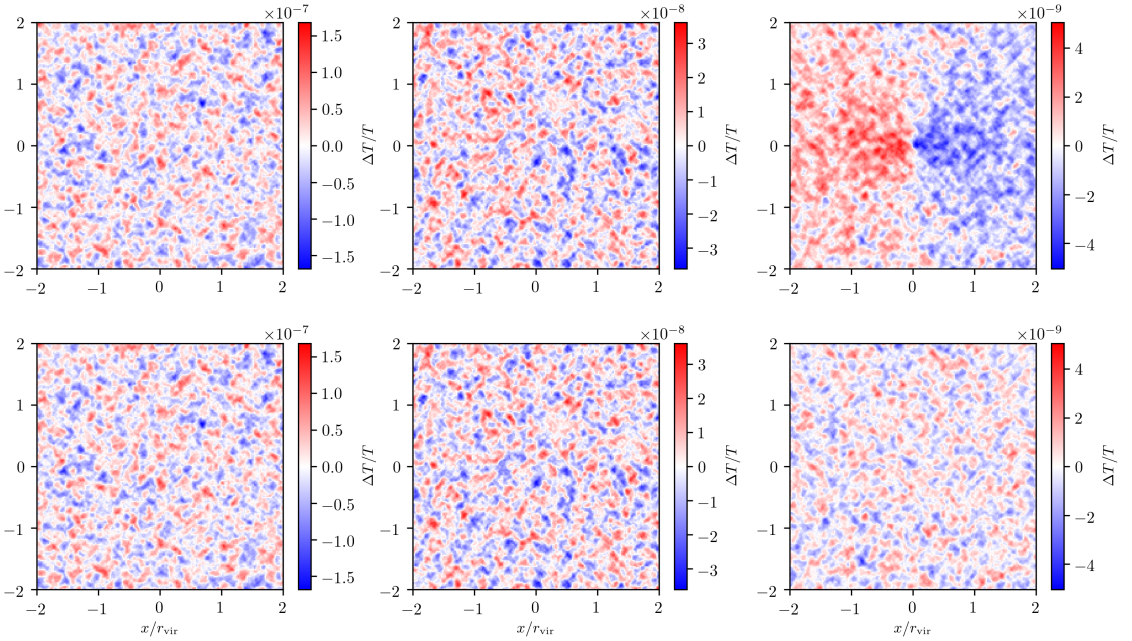

Fig. 3. Example realisations of the stacks (top row), and the residuals (bottom row) after stacking the slingshot signal of 8438 halos and subtracting the best fit. The left panels are for a noise per pixel of $\sigma_{\Delta T/T} = 4 \times 10^{-6}$, resembling current surveys. The central panels have 'near-future' noise levels of $\sigma_{\Delta T/T} = 1 \times 10^{-6}$, and the rightmost panels are for a very low noise per pixel ($\sigma_{\Delta T/T} = 1 \times 10^{-7}$) to visually see the emergence of an image. The individual images are scaled with respect to the virial radius of the halo before stacking. The x- and y-axes are in units of the virial radius of the halo.

noise ($\sigma_{\Delta T/T} = 4{\times}10^{-6}$), a CMB-S4 noise level in the near future ($\sigma_{\Delta T/T} = 1{\times}10^{-6}$), and a futuristic survey ($\sigma_{\Delta T/T} = 1{\times}10^{-7}$). We do not vary the resolution between these experiments, because CMB-S4 is expected to have a similar spatial resolution to ACT (1 and a few arcminutes; see Abazajian et al. 2016). The ACT noise level is equivalent to $6\,\mu\mathrm{K} \cdot \mathrm{arcmin}$ (Hincks et al. 2010), while the CMB-S4 noise level is equivalent to $1.5\,\mu\mathrm{K} \cdot \mathrm{arcmin}$, consistent with the $\sim 1\,\mu\mathrm{K} \cdot \mathrm{arcmin}$ (Abazajian et al. 2016). The futuristic noise level in the rightmost column is shown to emphasise the expected visual signal if we had sufficiently good statistics, and is not considered realistic in the foreseeable future. The best fit stencil to the low noise stack suggests a signal amplitude of $\Delta T/T \approx 3{\times}10^{-9}$. We are stacking almost 10 000 halos, which is expected to increase the S/N by a factor of 100. The best fit and the residuals are of similar amplitude when the noise per pixel is 10^{-7}, indicating a S/N $\sim$ 1 after stacking. The stacked signal is expected to be 100 times stronger than the average signal from a single halo, which confirms that an average halo has a signal of the order of $\Delta T/T \sim 10^{-9}$. The realisation with the 'near-future' noise level, shown in the middle column of figure 3, also recovers the expected signal with amplitude $\Delta T/T \approx 3 \times 10^{-9}$, but the ACT noise level of $4{\times}10^{-6}$ results in a S/N that is too low for the fitting algorithm to find a statistically significant dipole pattern in the shown example.

In the main analysis we used a uniform weighting when averaging the stacks. However, the S/N can possibly be improved by choosing a different weighting for the galaxy maps. Specifically the weighting can be chosen in such a way that bigger and faster galaxies contribute more to the stack than smaller and slower galaxies, which add mostly noise. As seen in figure 2, the average radial velocity is expected to be greatest around 1 virial radius from the central region of the supercluster, and then to reduce with distance. This suggests the possibility of weighting the galaxies according to distance. Another possibility is to weight them according to their estimated mass. In addition to the main analysis, we performed a small analysis with three weighting schemes. The first weights galaxies according to projected distance from the centre of the supercluster, $r_\perp$ (normalised to the virial radius of the supercluster), with weight $w_d = \sqrt{r_\perp} e^{-0.3 r_\perp}$. The second weights galaxies according to the logarithm of the galaxy mass (including a random spread in the halo mass) as $w_m = \log_{10}(M_{\mathrm{vir}}/10^{10} M_\odot)$. The third weighting scheme combines the distance and mass weighting, $w_c = w_d \times w_m$.

2.4. Observational challenges

The analysis assumes that we can identify $O(10^4)$ galaxies near the Coma cluster. The area of the sky where these galaxies can be found is a 40 Mpc radius circle at a distance of 100 Mpc, corresponding to 1400-1500 square degrees. There is a possibility that the least massive galaxies will not be visible in the galaxy surveys. The faintest galaxies we studied have a halo mass of $10^{11} M_\odot$. To estimate if the observed magnitude of these galaxies can be seen with optical surveys, we assume 1/10 mass in baryons and a mass-to-light ratio of 10 (in Faber & Gallagher 1979 all of the measured galaxies have a mass-to-light ratio lower than 12). This results in a luminosity of 10^9, and a bolometric magnitude of approximately 19 at the largest distances of

up to 200 Mpc. This is within the scope of contemporary surveys like the SDSS. The slingshot signal contribution will be strongest from the most massive galaxies, so missing a few of the faintest galaxies is not expected to change the stack significantly.

To rescale the galaxy maps correctly, we suggest inferring the virial radius from the galaxy virial mass. In many cases when a lensing analysis has not been performed, the total halo mass is not known and must be estimated from the galaxy luminosity. A possibility is to go via the mass of neutral hydrogen (HI), which can be measured from the HI line or estimated from visible light. To distinguish galaxies in the vicinity of the cluster from distant background galaxies, it is important to know the redshift of each galaxy fairly well, within an error of approximately 50%. At a distance of 100 Mpc (corresponding to about $z = 0.02$), the uncertainty of a measurement of the photometric redshift is $\sigma_z \gtrsim 0.03$ (Bolzonella et al. 2000). This implies that we need spectroscopic data for all the galaxies used in the stacking process.

Several of the above problems can be partially solved if we consider data from the upcoming Square Kilometre Array (SKA) phase 2, expected to be online in 2030 (Bull 2016). SKA is a planned full-sky spectroscopic survey, and Norris et al. (2014) suggest that it is expected to identify the position and redshift of all galaxies of the relevant magnitudes up to $z = 0.05$. We expect SKA to find the HI mass of all viable slingshot galaxies with fair certainty.

Whether using data from SKA or the SDSS, the biggest source of error when estimating the virial radius is the conversion from HI mass to halo mass. Villaescusa-Navarro et al. (2018) and Padmanabhan & Kulkarni (2017) both indicate a spread of about one order of magnitude in the halo mass for a given HI mass. We did not include this error when rescaling the individual maps in the main analysis, but we performed a separate smaller analysis where we included the corresponding error in virial radius. We find that the error in rescaling of the virial radius does not induce a bias, and does not significantly increase the uncertainty of the results. We expand upon this in the results section (section 4).

In this analysis, we assumed that the CMB behind the galaxies is known and can be subtracted. If there are no other significant contributions between the surface of last scattering and the observed galaxy, the CMB is a Gaussian random field with a standard deviation in $\Delta T/T$ of $\sigma_{\Delta T/T} = 10^{-4}$. By masking out the signal surrounding the galaxy, the CMB signal from the external area can be interpolated it into the masked region (see e.g. Bucher & Louis 2012 for an example prescription to fill in masked regions of the CMB map). Subtracting the expected interpolated CMB from the actual observed signal will leave signal and noise, without the CMB perturbations. Likewise, the galaxy itself, lensing of gradients in the CMB, and foreground sources can outshine the dipole signal from the slingshot effect. None of these effects are expected to give a dipole correlated with the infall velocity, so the process of stacking in itself should suppress any apparent signals from other sources.

3. Statistical analysis

For realistic noise levels of 10^{-6} and above, it is impossible to see the dipole fit by eye. We compared the stacked image to the model in equation (5), using a least-squares method with two free parameters. The two free parameters used in the fit are the combination $mv_x/r_{\rm vir}$, which gives the amplitude of the signal, and an image-smoothing radius $r_{\rm smooth}$, which is related to the instrument beam. When stacking images that are re-scaled with respect to their radius, the stack will consist of images with different effective beam widths. The resulting merged image is not exactly equivalent to a dipole signal with a single-Gaussian smoothing like the one we apply in our least-squares procedure. We find that fitting the stencil with a single effective smoothing radius consistently overestimates the signal by 3–4 %. This can be avoided by choosing a different stencil, for instance pregenerating a stencil from a stack of noiseless smoothed maps.

In the following sections we introduce measurements of the quality of the fit and amplitude of the signal. We also show that these two quantities can be combined into a single estimator that can be used to distinguish a true detection from a false positive.

3.1. Lower bound on the dipole amplitude

If the best fit of a stack corresponds to a very low amplitude $mv_x/r_{\rm vir}$, it is indistinguishable from zero amplitude. A detection limit for this number should be estimated based on the error bars of the data, and on the expected masses and velocities of the stacked galaxies. This limit will therefore depend on the mass and structure of the central supercluster and on the precision of data in the galaxy catalogue in the real-world scenario. The least-squares method we applied has discrete values for the combination $mv_x/r_{\rm vir}$. This means that below some threshold value, the amplitude will be rounded down to zero in our implementation. We chose this value conservatively in a way that does not significantly impact the results.

In our case, the average expected velocity is $O(100)$ km/s (as seen in figure 2), and the average galaxy mass is $1.8 \times 10^{12}\ M_\odot$. To be conservative, we set the threshold for a zero amplitude detection corresponding to a $10^{12}\ M_\odot$ galaxy, moving at less than 10 km/s. This choice is arbitrary and different values can be chosen when handling actual observations. The chosen threshold is equivalent to a factor of about 0.05 of the expected value for $mv_x/r_{\rm vir}$. This does not mean that we ignore individual images of galaxies that are smaller or slower than this threshold. We stacked all galaxies, and considered the stacked signal to have zero amplitude if the best fit indicates that the average value for $mv_x/r_{\rm vir}$ is less than ~ 5 % of the expected average.

3.2. Quality of fit

For each stack d we found the best fit template t with a least-squares method. The template t is a smoothed image of the pure slingshot signal (equation 5). Both d and t are column vectors containing each pixel of the stacked image and the best fit template. To gauge the quality of the fit, we calculated the normal equations

$$q = \frac{t^T d}{t^T t}, \tag{10}$$

where t^T is a row vector equivalent to the transpose of t. This statistic is related to the χ^2-statistic. If you imagine the t and d vectors of dimension $n = n_x \times n_y$ (with n_x and n_y being the amount of pixels in the x- and y-direction of the map, respectively), the q statistic is equivalent to the Euclidean dot product between the data and the template, normalised to the length of the expected template vector. The result is equal to 1 if the two vectors are of equal length and parallel to each other, and 0 if they are orthogonal. Calculating q is equivalent to summing up the pixel-by-pixel product of stack and template (vector dot product), and normalising to the squared norm of the template.

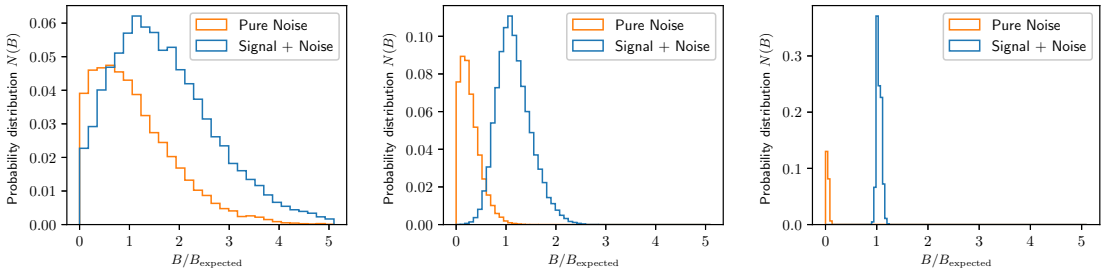

Fig. 4. Histogram of the B statistic from stacks of pure noise (orange) and of signal plus noise (blue). The three panels correspond to 4×10^{-6}, 1×10^{-6}, and 1×10^{-7} noise levels (from left to right). Values of B below 0 are not plotted.

A true fit of a stack with a slingshot signal, like the ones shown in figure 3, gives $q \approx 1$ if the noise is low. Fitting a template when no signal is present gives $q \approx 0$. The probability distribution of the best fit q has a spread, which widens with higher noise levels. In practice it is possible to get $q > 1$ if the stack data d is parallel and has a bigger amplitude than the template t. It is also possible to get $q < 0$ if the dot product is negative (i.e. when the vectors are anti-parallel). Both of these options are worse quality fits than $q = 1$.

3.3. Combined statistic to identify false positives

In addition to the possibility of a low quality fit when the signal is present, there is also a chance for the algorithm to detect a signal in pure noise with no actual signal present. We call such a detection a false positive. We consider a signal to be a proper detection if two conditions are met simultaneously: the quality of fit q is close to 1, and the fitted amplitude of the combination mv_x/r_{vir} is close to the expected amplitude. We consider a signal to be a bad detection if the best fit amplitude is low or if the quality of fit q is small (or negative). To take into account both of these measures of the detection level, we define a combined statistic,

$$B \equiv q \times \frac{mv_x}{r_{\mathrm{vir}}}. \tag{11}$$

The B statistic combines both qualities we are interested in when looking for a good detection: a significant amplitude for the fitted dipole, and a decent quality of the fit. We made a probability distribution of the outcome for measurements of B given a specific noise level by creating several real stacks and several false stacks (with no dipole signal). We created several realisations of the real stack, by repeating the pipeline described in section 2.3, but using a different random seed for the noise for each realisation. We also created several false stacks, where each of the stacks consists of images of the 8438 halos in our selection. The individual images pass through the same pipeline as the real stacks, but without the addition of the slingshot dipole. Each image consists purely of the per-pixel noise, and is later smoothed and re-scaled with respect to the expected virial radius of the halo.

For each realisation we calculated B, and combined the data from all samples to find a probability distribution for B. If there is significant overlap between the probability distributions from the stacks with a signal and without a signal, it is impossible to distinguish whether an observed stack contains a signal or not. If the distributions are sufficiently separated along B, the probability of a strong observed signal being a false positive is small, hence we can distinguish a true signal from a false positive.

4. Results

In this section, we first discuss the probability of a statistically significant detection, with current and future surveys. Then we present results from our smaller sets of test analyses, where we estimate the bias from having an uncertainty in the assumed virial radius of a galaxy, and evaluate the effectivity of our weighting schemes. Finally we consider how the results apply to modified gravity.

4.1. Detection probability

Histograms of B/B_{expected} are shown in figure 4. The three panels correspond to the distributions found from stacks with 4×10^{-6}, 1×10^{-6}, and 1×10^{-7} noise, respectively. The histograms emerging from multiple realisations of the stack can be interpreted as an estimate of the probability distribution of measuring a certain value of B, given a known noise level. The orange histograms are for stacks of pure noise, while the blue histograms are for stacks of signal and noise. The values are binned in evenly spaced bins from $B = 0$ to $B/B_{\mathrm{expected}} = 5$. The expected value, B_{expected}, is found by assuming $q = 1$ and taking the average mv_x/r_{vir} in the sample. The average mass of the halos in our sample is $1.79 \times 10^{12}\, M_\odot$, the average radial infall velocity is 675 km/s, and the average virial radius is 196 kpc. For the galaxies around the simulated supercluster we study, we find the value

$$B_{\mathrm{expected}} = 7.29 \times 10^9\, M_\odot/\mathrm{Mpc} = 2.08 \times 10^{-10}/G. \tag{12}$$

In the realisations with 4×10^{-6} noise, the histograms of the stacks with signal and with pure noise overlap significantly, and the probability of observing a value we can distinguish from noise is low. For near-future noise levels of 1×10^{-6}, the situation is better. The mean value for B when no signal is present is about three standard deviations lower than the mean value for B with signal. This suggests a very good probability of measuring a value of B high enough to be reasonably sure it is not from noise. In the futuristic noise realisations, the histograms do not overlap at all, meaning that in this theoretical scenario we can always distinguish the existence of a signal from a case with no signal.

We present data for the different runs in Table 1. $P(\mathrm{ND})$ is the probability of a non-detection. The chance of a non-detection is calculated as the probability for a given stack to be indistinguishable from $B = 0$ within one standard deviation. For noise levels

Table 1. Details of the analysis of the simulated stacks

Noise	Signal	# stacks	P(ND)	mean q	mean B	$(mv/r_{\rm vir})$	95 OSCI $\left(B/B_{\rm expected}\right)$	P(FP)
4×10^{-6}	No	45 000	72.7 %	0.413	0.514	0.68 ± 0.89		51.44 %
1×10^{-6}	No	65 000	72.9 %	0.399	0.130	0.176 ± 0.220		2.89 %
1×10^{-7}	No	45 000	81.0 %	0.1696	0.0089	0.023 ± 0.018		0.00 %
4×10^{-6}	Yes	20 000	45.0 %	0.898	1.433	1.59 ± 1.23	0	
1×10^{-6}	Yes	20 000	0.22 %	0.986	1.165	1.200 ± 0.374	0.661	
1×10^{-7}	Yes	20 000	0 %	0.9961	1.046	1.050 ± 0.052	0.9709	

Notes. P(ND) is the probability of a non-detection (i.e. how many of the stacks are indistinguishable from $B = 0$ within 1σ). The mean measured B and the mean amplitude $mv/r_{\rm vir}$ are normalised with respect to the expected value of the average sample. The amplitude column shows the average value and also the standard deviation among all the realisations. 95 OSCI is the lower 95 % one-sided confidence interval, or the 5th percentile of $B/B_{\rm expected}$. P(FP) is the probability of a false positive among the stacks of pure noise.

of 4×10^{-6}, we find a 45 % probability for non-detections among the stacks that include a signal. This means that, even with current experiments, there is a better than 50-50 chance of achieving a fit that is distinguishable from zero. For the near-future noise levels, we get very few non-detections in the stacks that include an actual signal. However, because pure noise can also lead to a detection, we must also consider the chance of a false positive before labelling any detection above the threshold a true detection.

The mean B shown in the table is normalised with respect to the expected value of B for the galaxies in the sample (i.e. the shown B is divided by $B_{\rm expected}$ from equation (12)). Specifically, unbiased measurements of the normalised B have an expected mean of $B = 1$ when the dipole signal is present, and 0 when there is only noise. The amplitude $mv/r_{\rm vir}$ of the signal is also normalised with respect to the expected amplitude, $(mv/r_{\rm vir})_{\rm expected}$, which has the same value as $B_{\rm expected}$. The column labelled 95 OSCI contains the lower 95 % one-sided confidence interval, or the 5th percentile of $B/B_{\rm expected}$; 95 % of all stacks in this set of stacks has a B above this level. The probability of a false positive, P(FP), is shown in the last column of Table 1. This probability is found by computing what percentage of the stacks with pure noise, no signal, and that give a value of B that falls above the 5th percentile we would expect if there were a signal. Specifically, $P(\mathrm{FP}) = P(B_{\rm no-signal} > B_{95\,\rm OSCI})$, where $B_{\rm no-signal}$ is B in a stack with pure noise, and $B_{95\,\rm OSCI}$ is the lower 95 % OSCI for B in the stacks with signal.

A conservative estimate for the chances of measuring a false positive can be found in the rightmost column of Table 1. We focus on the results for the near future experiments with 1×10^{-6} noise. A true stack with this noise level has $B/B_{\rm expected} > 0.661$ with 95 % confidence. If there is no signal in the stacks, the chance of getting $B/B_{\rm expected} > 0.661$ is just 2.89 %. This means that with CMB-S4 we can distinguish the slingshot signal from pure noise with $P < 0.05$ certainty. Furthermore, if the signal is present in near-future observations, we should also be able to put error bars on the measurement of the combination $mv/r_{\rm vir}$ because the expected value for this combination is approximately three standard deviations away from zero.

4.2. Testing assumptions and weighting schemes

We repeated four sets of a smaller analysis, where each set includes 5000 realisations of the stack instead of the 20 000 realisations used in the main analysis. One of the sets includes a random error in the assumed virial masses, which induces an error in the virial radius when assuming $m_{\rm vir} \propto r_{\rm vir}^3$. The result of including this error is that the stack is slightly smeared, but the dipole stencil still clearly detects the signal. For the 10^{-6} noise level simulations, the chance of detecting a false positive increases from 2.89 % to 4.06 %, and the standard deviation of the recovered $mv/r_{\rm vir}$ increases slightly. The detection is still greater than two sigma significance, indicating that the analysis is robust to the possible error in estimated virial radius.

The other three sets of analyses include the three non-uniform weighting schemes described in section 2.3. The distance-based weighting scheme, $w_d = \sqrt{r_\perp}e^{-0.3r_\perp}$, has a maximum weight at 1.67 virial radius of the cluster. This weighting increases the signal by 5 %, but also increases the averaged noise level similarly. The averaged noise increases when using a weighted average instead of uniform weights because the galaxies that are suppressed contribute less to the cancellation of noise. Other weighting schemes for distance are not considered, but the studied one does not improve the S/N according to our analysis. Even if the S/N does not improve, a benefit of this method is that we do not need to put in a sharp distance cut-off by hand, but rather we can tune the slope of the weighting function.

We also used a mass-based weighting scheme, with $w_m = \log_{10}(M_{\rm vir}/10^{10}M_\odot)$. This weighting increases the S/N significantly by weighting massive galaxies more than light galaxies. The expected detection of the slingshot signal with 10^{-6} noise level increases from 3 σ to 5 σ, and the chance of a false positive decreases from 2.89 % to 0.02 %. This suggests that a mass-based weighting scheme should be considered when using real observations. The final weighting scheme we tested is a combination of the distance- and mass-based weighting scheme, but it does not improve the results over the pure mass-based weighting scheme. A possible method for defining a more optimal weighting scheme in a future analysis is via matched filtering. For the noise levels of current surveys (4×10^{-6}), the mass weighting does not increase the S/N sufficiently to avoid the confusion with false positives.

4.3. Applications to modified gravity

When using the method discussed in this paper, we estimate an average $mv_x/r_{\rm vir}$ of infalling galaxies around a cluster. This can be combined with other observables, like the velocity along the line of sight and the inferred halo mass from lensing. Compared with such additional data, the slingshot effect can be used as an independent probe of modified gravity. Many scalar–tensor theories will increase the clustering on scales of kiloparsecs to megaparsecs. For instance, the Chameleon model studied by Brax et al. (2013) shows increased clustering. If the modifications apply on galaxy scales, each galaxy can be more massive and more

dense. If the modifications apply on megaparsec scales, galaxies will fall faster due to the fifth forces on large scales (Ivarsen et al. 2016). Both of these effects would increase the expected slingshot signal with respect to a similar scenario in ΛCDM, making it a possible probe for enhanced gravity over several different scales. Because the method described in this paper only measures the combination $mv_x/r_{\rm vir}$, the separate effects of higher infall velocity and higher galaxy density are degenerate.

From the halo mass function of the pure Symmetron case in Hagala et al. (2016), we find that in a typical Symmetron scenario, the individual galaxies will have a 20 % increase in mass. Assuming a 10% increase in infall velocity[3], we estimate that the average $mv_x/r_{\rm vir}$ at redshift zero can increase by about 30 % relative to GR. In the case of uniform weighting of the galaxy maps and 10^{-6} noise level, this increase is equivalent to the one standard deviation measurement error on the slingshot signal.

We find that the average $mv_x/r_{\rm vir}$ amongst the 4700 most massive clusters in the simulated catalogue has a standard deviation similar to the average of $mv_x/r_{\rm vir}$. This means that, even in the context of ΛCDM, the amplitude of the slingshot signal around a single cluster is not decided by the mass of the cluster alone, but also by a combination of the surrounding large-scale structure and the merger history of the cluster. Unless we know such specifics about the studied cluster, we would need to observe 36 clusters to reduce the error of the mean for the 'universal' $mv_x/r_{\rm vir}$ with a factor $1/\sqrt{36} \approx 1/6$. If we can do this, the uncertainty of our measurements can be low enough for us to begin distinguishing gravitational models like the Symmetron from pure ΛCDM, with two sigma significance. Better knowledge of the mass distribution of the surroundings of the cluster and a better weighting scheme for the stacking of galaxy maps can both reduce the number of clusters needed to distinguish between different gravitational models.

5. Conclusion

In this paper, we present a method for detecting transverse motions of galaxies by stacking the dipole signal of the slingshot effect. For this method to work we need to be able to identify a preferential direction to align the galaxies along their expected direction of motion. This can be done by taking into account galaxies that either fall into clusters or move away from the centre of the voids. We show a detection strategy for galaxies falling into a nearby cluster, like the Coma Cluster. A similar analysis can be performed for galaxies around voids.

The possibility of detecting the signal with certainty with CMB-S4 experiments is very high. There are some simplifications in this paper that should be considered more thoroughly when analysing real data. The most important considerations relate to the choice of cut-off in halo mass, and the cut-off in distance from the central cluster. We use a mass cut-off of $M > 10^{11} M_\odot$ when considering a halo for stacking. A cut-off that is too low means adding mostly noise for each image, while a mass cut-off that is too high gives fewer halos to stack. Furthermore, we do not include an upper mass limit. This means that in practice we are stacking the dark matter halos of some smaller galaxy clusters as well as individual galaxies. Choosing the halo mass cut-offs in a more sophisticated way (e.g. using a weighting scheme) could improve the signal. Increasing the distance within which to consider infalling galaxies will allow us to include more galaxies and could result in better statistics. An inner radius cut-off can also be considered, since galaxies within approximately one virial radius of the cluster do not appear to have a preferred radial direction. When excluding these galaxies, a better signal can be expected. Another option is to use a distance-based weighting scheme instead of a hard cut-off. We tested a simple distance-based weighting scheme, which does not impact the S/N significantly. We also tested a mass-based weighting scheme, which we find to increase the S/N by weighting massive galaxies more than light galaxies. When used on real data, this weighting scheme can be more or less efficient depending on the confidence of the mass estimates in the galaxy catalogue.

In this paper, we stacked the CMB maps centred on $O\left(10^4\right)$ simulated galaxies, and oriented them according to their expected infall direction towards a nearby massive cluster. By fitting a dipole template to the stacked signal, we show that the slingshot effect is statistically distinguishable from noise when using the next generation of CMB experiments. By measuring the slingshot signal around 36 clusters, we can constrain the signal sufficiently to test alternative theories for gravity.

[3] For all Symmetron models except the one with the weakest coupling, Ivarsen et al. (2016) found a > 10% increase in pairwise velocities

Acknowledgements

We would like to thank several people at the Institute of Theoretical Astrophysics in Oslo for their ideas and comments, especially: Håkon Dahle, Hans Kristian Eriksen, Marta Bruno Silva, Håvard Tveit Ihle, Øyvind Christiansen, and Daniel Heinesen. A great thanks to Sigurd Kirkevold Næss for helping with technical details. Many thanks for detailed and helpful comments and questions from the referee, which helped strengthen the paper significantly. We thank the Research Council of Norway for their support. This paper is based upon work from the COST action CA15117 (CANTATA), supported by COST (European Cooperation in Science and Technology). The CosmoSim database used in this paper is a service by the Leibniz-Institute for Astrophysics Potsdam (AIP). The MultiDark database was developed in cooperation with the Spanish MultiDark Consolider Project CSD2009-00064.

References

Abazajian, K. N., Adshead, P., Ahmed, Z., et al. 2016
Behroozi, P. S., Wechsler, R. H., & Wu, H. Y. 2013, Astrophysical Journal
Birkinshaw, M. & Gull, S. F. 1983, Nature
Bolzonella, M., Miralles, J.-M., & Pello', R. 2000
Brax, P., Davis, A. C., Li, B., Winther, H. A., & Zhao, G. B. 2013, Journal of Cosmology and Astroparticle Physics
Bucher, M. & Louis, T. 2012, Monthly Notices of the Royal Astronomical Society
Bull, P. 2016, The Astrophysical Journal, 817, 26
Faber, S. M. & Gallagher, J. S. 1979, Annual Review of Astronomy and Astrophysics, 17, 135
Gaia Collaboration, Brown, A. G. A., Vallenari, A., et al. 2018
Gould, A. 1994
Hagala, R., Llinares, C., & Mota, D. 2016, Astronomy and Astrophysics, 585
Hernquist, L. 1990, The AN ANALYTICAL MODEL FOR SPHERICAL GALAXIES AND BULGES, Tech. rep.
Hincks, A. D., Acquaviva, V., R Ade, P. A., et al. 2010, THE ATACAMA COSMOLOGY TELESCOPE (ACT): BEAM PROFILES AND FIRST SZ CLUSTER MAPS, Tech. rep.
Hotinli, S. C., Meyers, J., Dalal, N., et al. 2018
Ivarsen, M. F., Bull, P., Llinares, C., & Mota, D. F. 2016
Kravtsov, A. V. 2013, Astrophysical Journal Letters
Kubo, J. M., Stebbins, A., Annis, J., et al. 2007
Liu, M. C. & Graham, J. R. 2002, The Astrophysical Journal, 557, L31
Łokas, E. L. & Mamon, G. A. 2001, Monthly Notices of the Royal Astronomical Society
Manzotti, A. 2018, Physical Review D, 97

Maturi, M., Dolag, K., Waelkens, A., Springel, V., & Ensslin, T. 2007a, Astronomy & Astrophysics, 476, 83
Maturi, M., Enßlin, T., Hernández-Monteagudo, C., & Rubiño-Martín, J. A. 2007b, A&A, 467, 411
Molnar, S. M., Broadhurst, T., Umetsu, K., et al. 2013, Astrophysical Journal
Navarro, J. F., Frenk, C. S., White, S. D. M., & Fellow, B. J. B. 1995, The Structure of Cold Dark Matter Halos, Tech. rep.
Norris, R. P., Basu, K., Brown, M., et al. 2014, in Proceedings of Science, Vol. 9-13-June-2014 (Proceedings of Science (PoS))
Padmanabhan, H. & Kulkarni, G. 2017, Monthly Notices of the Royal Astronomical Society, 470, 340
Prada, F., Klypin, A. A., Cuesta, A. J., Betancort-Rijo, J. E., & Primack, J. 2012, Monthly Notices of the Royal Astronomical Society
Rees, M. J. & Sciama, D. W. 1968, Nature
Sachs, R. K. & Wolfe, A. M. 1967, General Relativity and Gravitation [arXiv:0605122v1]
Stebbins, A. 2006, Measuring velocities using the CMB and LSS
Villaescusa-Navarro, F., Genel, S., Castorina, E., et al. 2018
Yasini, S., Mirzatuny, N., & Pierpaoli, E. 2018, Pairwise Transverse Velocity Measurement with the Rees-Sciama Effect, Tech. rep.

Appendix: Calculation of slingshot effect from a spherical halo model

We have that

$$\frac{\Delta T_{\rm slingshot}}{T} = 2v_x \int \frac{\partial \Phi}{\partial x}\,{\rm d}z. \tag{13}$$

Since gravitational potentials are additive, we will have a contribution from the NFW dark matter profile and from the Hernquist profile:

$$\frac{\Delta T_{\rm slingshot}}{T} = 2v_x \int \frac{\partial \Phi_{\rm NFW}}{\partial x} + \frac{\partial \Phi_{\rm Hernq}}{\partial x}\,{\rm d}z. \tag{14}$$

We now calculate these integrals separately. In principle the integral limits is from the surface of last scattering and until today, but as long as the kernel we are integrating peaks around $z = 0$, we can safely integrate from $z = -\infty$ to $z = \infty$ instead.

NFW

From Łokas & Mamon (2001), the gravitational potential of the NFW halo is given by

$$\Phi_{\rm NFW} = -Gmg \times \frac{\ln\left(1 + \frac{c_{\rm NFW} r}{r_{\rm vir}}\right)}{r}, \tag{15}$$

where $c_{\rm NFW}$ is the concentration (we assume $c_{\rm NFW} = 15$) and

$$g \equiv \frac{1}{\ln(c_{\rm NFW} + 1) - \frac{c_{\rm NFW}}{c_{\rm NFW}+1}}. \tag{16}$$

Substituting $r = \sqrt{x^2 + y^2 + z^2}$, we can do the derivative with respect to x,

$$\frac{\partial \Phi_{\rm NFW}}{\partial x} = \frac{Gmgx}{r^2}\left(\frac{\ln\left(1 + \frac{c_{\rm NFW} r}{r_{\rm vir}}\right)}{r} - \frac{c_{\rm NFW}/r_{\rm vir}}{1 + \frac{c_{\rm NFW} r}{r_{\rm vir}}}\right). \tag{17}$$

We can find the indefinite integral

$$\int \frac{\partial \Phi_{\rm NFW}}{\partial x}{\rm d}z = \frac{Gmgx\left(\frac{r_{\rm vir}\arctan\left(\frac{c_{\rm NFW} z}{\sqrt{c_{\rm NFW}^2\left(x^2+y^2\right) - r_{\rm vir}^2}}\right)}{\sqrt{c_{\rm NFW}^2\left(x^2+y^2\right) - r_{\rm vir}^2}} - \frac{r_{\rm vir}\arctan\left(\frac{r_{\rm vir} z}{r\sqrt{c_{\rm NFW}^2\left(x^2+y^2\right) - r_{\rm vir}^2}}\right)}{\sqrt{c_{\rm NFW}^2\left(x^2+y^2\right) - r_{\rm vir}^2}} + \frac{z\ln\left(\frac{c_{\rm NFW} r}{r_{\rm vir}}+1\right)}{r} - \ln(r+z)\right)}{x^2+y^2} \tag{18}$$

$$\tag{19}$$

We are interested in evaluating this integral with limits $z = -\infty$ and $z = \infty$. We start by finding the limits of the arctangent expressions. We use that $\lim_{x\to\pm\infty} arctan\,(x) = \pm\pi/2$, and find that the first arctangent has the limit

$$\arctan\left(\frac{c_{\rm NFW} z}{\sqrt{c_{\rm NFW}^2\left(x^2+y^2\right) - r_{\rm vir}^2}}\right)\Bigg|_{z\to\infty} = \lim_{Z\to\infty}\arctan(Z) = \frac{\pi}{2}, \tag{20}$$

and similarly

$$\arctan\left(\frac{c_{\rm NFW} z}{\sqrt{c_{\rm NFW}^2\left(x^2+y^2\right) - r_{\rm vir}^2}}\right)\Bigg|_{z\to-\infty} = -\frac{\pi}{2}. \tag{21}$$

To evaluate the limits of the second arctangent, we note that

$$\lim_{z\to\pm\infty}\frac{z}{r} = \pm 1. \tag{22}$$

This leaves us with the following arguments for the second arctangent:

$$\left.\frac{r_{\rm vir}z}{r\sqrt{c_{\rm NFW}^2\left(x^2+y^2\right)-r_{\rm vir}^2}}\right|_{z\to\infty} = \frac{r_{\rm vir}}{\sqrt{c_{\rm NFW}^2\left(x^2+y^2\right)-r_{\rm vir}^2}}, \tag{23}$$

$$\left.\frac{r_{\rm vir}z}{r\sqrt{c_{\rm NFW}^2\left(x^2+y^2\right)-r_{\rm vir}^2}}\right|_{z\to-\infty} = -\frac{r_{\rm vir}}{\sqrt{c_{\rm NFW}^2\left(x^2+y^2\right)-r_{\rm vir}^2}}. \tag{24}$$

Regarding the logarithmic expressions, the limit at $z \to \infty$ is

$$\lim_{z\to\infty}\frac{z\ln\left(\frac{c_{\rm NFW}r}{r_{\rm vir}}+1\right)}{r}-\ln\left(r+z\right)=\lim_{z\to\infty}\ln\left(\frac{c_{\rm NFW}r}{r_{\rm vir}}+1\right)-\ln\left(z+z\right)=\lim_{z\to\infty}\ln\left(\frac{c_{\rm NFW}z/r_{\rm vir}}{2z}\right)=\ln\left(\frac{c_{\rm NFW}}{2r_{\rm vir}}\right). \tag{25}$$

The limit of the logarithmic terms when $z \to -\infty$ is

$$\lim_{z\to-\infty}\frac{z\ln\left(\frac{c_{\rm NFW}r}{r_{\rm vir}}+1\right)}{r}-\ln\left(r+z\right)=\lim_{z\to-\infty}-\ln\left(\frac{c_{\rm NFW}z}{r_{\rm vir}}\right)-\ln\left(z\sqrt{1+\frac{x^2+y^2}{z^2}}-z\right)=\lim_{z\to-\infty}-\ln\left(\frac{c_{\rm NFW}z}{r_{\rm vir}}\right)-\ln\left(\frac{x^2+y^2}{2z}\right) \tag{26}$$

$$=-\ln\left(\frac{c_{\rm NFW}\left(x^2+y^2\right)}{2r_{\rm vir}}\right), \tag{27}$$

where we use that $\sqrt{1+x} \approx 1 + x/2$ for small x.

Combining all of these, we are left with

$$\int_{-\infty}^{\infty}\frac{\partial\Phi_{\rm NFW}}{\partial x}{\rm d}z=\frac{Gmgx}{x^2+y^2}\left[S\left(\pi-2\arctan\left(S\right)\right)+\ln\left(\frac{c_{\rm NFW}^2\left(x^2+y^2\right)}{4r_{\rm vir}^2}\right)\right]. \tag{28}$$

Here, we have defined

$$S\equiv\frac{r_{\rm vir}}{\sqrt{c_{\rm NFW}^2\left(x^2+y^2\right)-r_{\rm vir}^2}}. \tag{29}$$

Hernquist

The gravitational potential of a Hernquist halo with mass m is simply given by

$$\Phi_{\rm Hernq}=-\frac{Gm}{r+a}, \tag{30}$$

where a is a scale length, which is related to the half-mass radius as $a = \frac{r_{1/2}}{1+\sqrt{2}}$. We chose $r_{1/2} = 0.015 r_{\rm vir}$ based on figure 1 from Kravtsov (2013), where the data indicates $r_{1/2} \approx 0.015 r_{200c}$.

The derivative with respect to the x coordinate is

$$\frac{\partial\Phi_{\rm Hernq}}{\partial x}=\frac{Gmx}{r\left(a+r\right)^2}, \tag{31}$$

which results in the following indefinite integral along z:

$$\int\frac{\partial\Phi_{\rm Hernq}}{\partial x}{\rm d}z=\frac{Gmx}{a^2}\left(\frac{a^2z}{\left(x^2+y^2-a^2\right)\left(r+a\right)}+\frac{a^3\arctan\left(\frac{az}{r\sqrt{x^2+y^2-a^2}}\right)}{\left(x^2+y^2-a^2\right)^{3/2}}-\frac{a^3\arctan\left(\frac{z}{\sqrt{x^2+y^2-a^2}}\right)}{\left(x^2+y^2-a^2\right)^{3/2}}\right). \tag{32}$$

We chose to define

$$U\equiv\frac{a}{\sqrt{x^2+y^2-a^2}}, \tag{33}$$

which does not depend on z.

The limits of the first term when $z \to \pm\infty$ are

$$\lim_{z\to\infty} \frac{U^2 z}{(r+a)} = U^2 \tag{34}$$

and

$$\lim_{z\to-\infty} \frac{U^2 z}{(r+a)} = -U^2. \tag{35}$$

The limits of the second term are

$$\lim_{z\to\infty} U^3 \arctan\left(U\frac{z}{r}\right) = U^3 \arctan(U) \tag{36}$$

and

$$\lim_{z\to-\infty} U^3 \arctan\left(U\frac{z}{r}\right) = -U^3 \arctan(U). \tag{37}$$

The last arctangent converges to $\pm\pi/2$, giving

$$\lim_{z\to\infty} -U^3 \arctan\left(U\frac{z}{a}\right) = -\frac{\pi U^3}{2} \tag{38}$$

and

$$\lim_{z\to-\infty} -U^3 \arctan\left(U\frac{z}{a}\right) = \frac{\pi U^3}{2}. \tag{39}$$

Finally, the slingshot integral for the Hernquist distribution can be written

$$\int_{-\infty}^{\infty} \frac{\partial \Phi_{\rm Hernq}}{\partial x} \mathrm{d}z = Gmx\frac{U^2}{a^2}\left(2 + U\left[2\arctan(U) - \pi\right]\right). \tag{40}$$

Sum

Because we are assuming that the total mass m_{DM} of the dark matter halo is in the NFW component, with an additional $m_{DM}/10$ in baryons, we write the combined effect as

$$\frac{\Delta T_{\rm slingshot}}{T} = 2v_x \int \frac{\partial}{\partial x}\Phi_{\rm NFW}(m = m_{DM}) + \frac{\partial}{\partial x}\Phi_{\rm Hernq}\left(m = \frac{m_{DM}}{10}\right)\mathrm{d}z = \frac{2Gm_{DM}v_x}{r_{\rm vir}}\left(Q_{\rm NFW} + \frac{1}{10}Q_{\rm Hernq}\right). \tag{41}$$

Here, we use the following notation for dimensionless coordinates: $x_r \equiv x/r_{\rm vir}$ and $x_a \equiv x/a$. Furthermore,

$$Q_{\rm NFW} \equiv \frac{g x_r}{x_r^2 + y_r^2}\left[\ln\left(\frac{c_{\rm NFW}^2\left(x_r^2 + y_r^2\right)}{4}\right) - S\left(2\arctan(S) - \pi\right)\right], \tag{42}$$

and

$$Q_{\rm Hernq} \equiv \left(\frac{1+\sqrt{2}}{0.015}\right)\frac{x_a}{x_a^2 + y_a^2 - 1}\left[2 + U\left(2\arctan(U) - \pi\right)\right]. \tag{43}$$

The factor of $\left(1+\sqrt{2}\right)/0.015$ is to convert from the Hernquist scale a to $r_{\rm vir}$. We repeat the definitions

$$S \equiv \frac{1}{\sqrt{c_{\rm NFW}^2\left(x_r^2 + y_r^2\right) - 1}}, \tag{44}$$

$$U \equiv \frac{1}{\sqrt{x_a^2 + y_a^2 - 1}}. \tag{45}$$

We note that S and U can become imaginary for light passing close to the centre of the halo. Specifically, both U and S are $\in [-i, -\infty i)$. However, $z\left(2 \times \arctan(z) - \pi\right)$ always has one real value, even for imaginary z.

Proof: For a real $x > 1$, it follows that $z = -ix$ is negative imaginary with the same domain as U and S. Using the logarithm definition of the complex arctangent, we have

$$(-ix)\,(2 \times \arctan(-ix) - \pi) = (-ix)\left(2 \times \frac{i}{2} \ln\left(\frac{1-x}{1+x}\right) - \pi\right) \tag{46}$$

$$= x\left(\ln\left(\frac{1-x}{1+x}\right) + \pi i\right) = x\left(\ln\left(\frac{x-1}{1+x}\right) + 2\pi i\right) \tag{47}$$

$$\underset{\text{choice}}{=} x \ln\left(\frac{x-1}{1+x}\right). \tag{48}$$

In the last line, we used the fact that for complex logarithms, $\ln(z) = \ln(-z) + \pi i$. Furthermore, any addition of $2\pi i$ can be cancelled by the corresponding free choice of $2k\pi i$ in the multi-valued complex logarithm. With $x > 1$, this result proves that there is always a real branch of the expression $z\,(2 \times \arctan(z) - \pi)$. This expression is also continuous for values of $r^2 = x^2 + y^2$ crossing through the singularity in U or S.

Chapter 4

Conclusions

The ΛCDM concordance model describes the observed properties of the universe well on large scales, but it has several problems. A key question in the quest to solve some of these problems is to explain the nature of dark energy, for which modified gravity is a possible candidate.

The focus of this thesis has been to better understand scalar–tensor theories for gravity in the non-linear regime. Specifically, I have investigated phenomena appearing out of the quasi-static approximation, when allowing time derivatives of the scalar field. During my PhD, I have developed a fast, spherically symmetric code to test and understand properties of the equation of motion of a scalar field. Furthermore, I have implemented the disformal quintessence model in the modified gravity N-body code `Ramses`. I have also proposed a new probe for measuring peculiar transverse velocities, which can be used to distinguish theories of modified gravity from GR. These are examples of specialised analyses which can be used for improving the prediction power of old probes, as well as for suggesting new signatures of modifications to gravity. In this chapter, I summarise and discuss the three papers of my doctorate, before concluding and placing my work in a greater perspective.

4.1 Scalar Field Waves

In Paper I we used the spherically symmetric code to test the quasi-static approximation, which is commonly assumed when studying conformal models. We found that the symmetron and the chameleon screening mechanisms in general work well under the influence of waves. The exceptions are very special set-ups, for instance where incoming spherically concentrated waves in the scalar field can disrupt the scalar field enough to break the Cassini bounds on the PPN quantity $|\gamma_{\rm PPN} - 1|$. Specifically, in the symmetron model, we suggest that the collapse of domain walls in a void surrounding a galaxy can lead to waves with a significant amplitude entering the galaxy. In this scenario, the wave energy is sufficiently concentrated to excite the field even in the regions where the effective potential well is steep and narrow. Furthermore, we found that in the chameleon model, a very energetic event which moves a lot of matter—like a nearby supernova explosion—can generate waves in the scalar field that have a large enough amplitude to temporarily break the chameleon screening.

My main contribution to Paper I was to implement and test the spherical scalar field EOM solver, as well as to run the code and interpret the output. This included selection of model parameters, set-up of the density profile, analysis of previous N-body output to determine a suitable range of external wave parameters (in amplitude and frequency), and creation of figures. Significant

parts of the analytical calculations and interpretations of the results were also done by me, including the supplementary material following Paper I, wherein I proposed and calculated how a type Ia supernova can generate waves in the chameleon scalar field.

We did not study the effect of waves on other scalar–tensor theories than the symmetron and chameleon; a similar analysis has yet to be done for instance for theories relying on screening through the Vainshtein mechanism. In Paper I we only studied the impact of waves on one specific probe, the Cassini experiment for measuring $\gamma_{\rm PPN}$ in the Solar System. Other probes, especially ones sensitive to time variations of the scalar field, can be better indicators of scalar field waves. This calls attention to the study of new non-linear probes, as well as for estimating the effect of waves in other regions, like in un-screened dwarf galaxies. We do not expect scalar waves to have a significant impact on structure formation through the fifth force. This is because the extra force from a sinusoidal wave changes direction as the wave passes, leading to a cancellation over time. However, the extra energy in the stochastic scalar waves can affect the overall background evolution. Furthermore, in theories where the speed of waves is reduced in regions with high matter–energy density, waves are allowed to cluster and form structures. This is the case in for instance disformally coupled theories, which I studied in Paper II. The effects and possibilities of the clustering of scalar field waves in the context of modified gravity has yet to be studied.

A follow-up study of the effect of scalar field waves on the Solar System was performed by Ip and Schmidt [IS18]. Their main finding is that our conclusion on the significance of waves in violating the bounds on $|\gamma_{\rm PPN}-1|$ is to a large extent due to the spherical geometry we applied; The wave energy is concentrated on the inner part of the Milky Way galaxy when allowing a spherical wave to propagate inwards. According to their linear analysis, when allowing a plane wave of amplitude $\delta\phi/\phi_{\rm QS}=0.01$ to enter the Milky Way[1], the amplitude of $|\gamma_{\rm PPN}-1|$ is only enhanced by a factor of 16 over the quasi-static value, compared to our prediction of a factor larger than 10^2-10^4. In the case of the chameleon model, they agree that a supernova can generate large amplitude waves in the scalar field due to the release of scalar charge, but they argue that only waves with wavenumbers higher than the effective mass of the scalar field will propagate into the Solar System, $k\gtrsim m_{\rm SS}$. Under this assumption, waves of sufficient frequency to propagate in the Solar System are expected to have a shorter wavelength than the extent of the Cassini experiment described in [BIT03]. The effect of such high-frequency waves are effectively cancelled over the time it takes light to travel in the experiment, and hence will not give a measurable signal. Although the chameleon screening can act as a high pass filter and reduce the propagation of long-wavelength waves, a full scalar field simulation has yet to be done for a supernova wave entering the solar system.

[1]Where $\phi_{\rm QS}$ is the quasi-static value of the scalar field, and $\delta\phi/\phi_{\rm QS}=0.01$ is the higher end expected deviation from the quasi-static value due to the stochastic scalar field wave background found in [LM14].

4.2 Disformal Phenomenology

In Paper II we studied a pure disformal model through N-body simulations. We found a mechanism for the evolution of the field profile; The field moves freely in voids, but in areas of high density, the disformal effect will slow down the field acceleration with the suppressing factor $1/\left(1+\gamma^2\rho\right)$. The disformal effect plays an important role for the scalar field evolution, in setting up the field profiles around overdensities, and for the deformation and clustering of scalar field waves. We found that the scalar field profile in the quasi-static limit[2] achieves a shape proportional to the Newtonian gravitational potential $\delta\phi \propto \Psi$. This proportionality assumption is valid for a quintessence-like potential, where the potential slope drives the scalar field towards higher values. We identified one scenario where the proportionality assumption does not hold, which is during a short amount of time when the proportionality constant changes sign. During this period, we found indications of a transient repulsive fifth force.

My main contribution to Paper II was to extend `Ramses/Isis` to simulate a pure disformally coupled scalar field, building upon earlier work of Claudio Llinares. I implemented several auxillary tools for data post-processing, analysis, and visualisation. I was responsible for the N-body related part of the paper, including convergence testing and exploration of the parameter space of this choice of disformal coupling and potential functions. The analysis of the repulsive fifth forces associated with the field flip was to a large extent carried out by me.

Under the proportionality assumption, we derived a global formula for the relation between the fifth force and the Newtonian force. This opens for the possibility to do simulations of disformal quintessence faster, through applying $G \to G_{\text{eff}}(t)$ directly to a Newtonian simulation. This simplification ignores non-linear screening effects as well as non-static effects like scalar field waves. Nevertheless, this method can prove to be a valuable tool to assess the effects of modified gravity on quasi-linear scales or to test the parameter space of the model more efficiently. Similar simple simulations with G_{eff} have been done for conformally coupled theories. For instance, [LMB11] study extended quintessence models, where the modification to gravity is seen in the Jordan frame as the scalar field being coupled to the curvature[3]. For the case of the extended quintessence models they studied, they find that the large scale properties of the simulation are very well approximated by the assumption $G \to G_{\text{eff}}(t)$ and a modified background equation.

The N-body simulations we performed in Paper II do not modify the background evolution compared to ΛCDM. This simplification is based on the assumption that we expect the background evolution for viable theories to follow ΛCDM closely. Furthermore, when keeping the background evolution fixed, the differences between the particle distributions are only attributed to the fifth forces. In this way, we avoid possible degeneracies between the effects coming from the background evolution and effects of the fifth forces on the

[2] i.e. when neglecting time derivatives of the field perturbations $\delta\phi$.

[3] Which is identical to a conformal theory with a fifth force after a conformal transformation.

particle distribution.

There have been proposed many methods to distinguish disformally coupled scalar fields from other theories of gravity or GR. Many of the methods are on astrophysical small scales or in relativistic environments and require non-linear treatments, or even quantum field theory calculations. On the background level, the work of [vMM17] suggests that a disformal coupling is slightly favoured over ΛCDM. Furthermore, they find that a disformal coupling on top of a conformal coupling relaxes the constraints on the conformal parameters because the disformal coupling suppresses the scalar field evolution in the early universe. This suggests that adding a disformal coupling on top of a conformal model can be used to build models with measurable small scale phenomenology, without altering the background evolution significantly. On the level of cosmological perturbations, there has been suggested a degeneracy between disformal and conformal couplings [vM15]. This emphasises the need to go to non-linear simulations and probes—like the ones presented in this thesis—to distinguish disformal from conformal theories. A comprehensive study of disformal couplings is done by [Sak14]. Although the author ignores the term $\ddot{\phi}$ in the fifth force, the results are nevertheless useful for the probes discussed, which include the Cassini probe for γ_{PPN}, lunar laser ranging, laboratory tests, and the background evolution. In [BBE15] the authors put bounds on the disformal coupling B using data from the LHC particle collider. These bounds assume that the scalar field couples disformally to the known Standard Model particles, and hence the bounds do not apply to disformal couplings in the dark sector. Gravitational waves, especially the recent binary neutron star merger with an electromagnetic counterpart, enforce stringent constraints on many theories of modified gravity, including theories with a disformal coupling [EZ18]. A disformal tuning is allowed to save some sets of theories by forcing the speed of light to be equal to the propagation speed of gravitational waves. Furthermore, a disformal coupling only in the dark sector allows the Standard Model particles (including photons) to travel on the same geodesics as the gravitational waves.

4.3 Transverse Velocities

The study of peculiar motions of galaxies is important for understanding the underlying gravitational force. In combination with data on positions and densities, velocities can be used as an independent consistency check of the model of gravity. In Paper III we proposed a method to use the slingshot effect for detecting the mean transverse velocity of galaxies falling into a cluster. The method requires a massive galaxy cluster located no more than 200 Mpc away, a galaxy catalogue with the positions and redshifts of the surrounding galaxies, and a high-resolution map of the CMB around these galaxies. The method consists of subtracting the expected CMB signal close to each infalling galaxy and delensing the maps, then orienting the residue map from each galaxy along the radial direction, and stacking the maps centred on the infalling galaxies. This procedure ensures that instrument noise and confounding effects are kept

to a minimum. After fitting a dipole stencil to the stacked maps, the amplitude of the stencil yields an average value for the quantity $m_{\rm g} v_r / r_{\rm vir,g}$ for the stacked galaxies, where $m_{\rm g}$ and $r_{\rm vir,g}$ are the virial mass and the virial radius of a given galaxy, and v_r is the projected infall velocity of the galaxy. With this method, the slingshot effect should be measurable with the next generation of observations, and given measurements of the average infall velocity around enough clusters, we expect that this method can be used for distinguishing theories of modified gravity from general relativity[4]. Other recent papers have suggested detecting signals of the slingshot effect in the CMB power spectrum [Hot+18], or using the effect to estimate the mean pairwise velocities of galaxy clusters [YMP18]. Both of these also conclude that next-generation CMB experiments (CMB stage 4) have good enough noise levels for the slingshot effect to be measurable.

Almost all of the work on paper Paper III, as well as most of the writing and editing of the manuscript, was done by me. The general idea—that a moving galaxy should have an effect on the measured CMB sky—and a sketch of the slingshot equations presented in Appendix B along with a preliminary plot, were provided by Claudio Llinares as a starting point for my work on this paper. The idea of stacking the signal to battle instrument noise, as well as the choice to orient the dipoles according to infall velocity around a cluster, was suggested by me. I implemented the software for using a (publicly available) halo catalogue for estimating the effect, as well as wrapper software to visualise and run statistics on the output.

4.4 Outcome and Future Prospects

N-body simulations and other non-linear methods are useful tools to test and investigate the small-scale effects of GR and modified theories of gravity. However, due to the limitations of box size, as well as the large computational cost of high-resolution simulations, these methods cannot be used as efficiently as linear perturbation simulations to test the parameter space of cosmological models. Especially on large scales where the linear approximation is expected to hold, running N-body simulations for the purpose of parameter fitting is a waste of resources. The quasi-linear and non-linear regimes of theories of modified gravity can be explored more efficiently through the use of semi-analytic methods [KTB16] and emulators [Win+19]. Machine learning has already been used in the context of ΛCDM to predict structure formation with cosmological parameters significantly beyond what was included in the original training data [He+19]. In the future, machine learning and deep learning provides promising possibilities to extract astrophysical data about certain models of modified gravity, without having to run a separate N-body simulation for each set of parameters.

The CMB power spectrum and redshift zero matter power spectrum are still the most used probes when comparing GR with alternative theories. Linear theory and N-body simulations can be used as complementary tools to investigate

[4]For a typical symmetron scenario, we estimate that we need data from approximately 36 galaxy clusters to distinguish the modified gravity model from GR.

alternative probes of modifications to GR. For instance, when studying a new model for modified gravity, linear simulations can be used to effectively constrain the parameter space when comparing the model to CMB or the background evolution. The constrained parameter space can then be used to choose a few sets of interesting parameters to explore in the non-linear regime through N-body simulations. The final positions and velocities of the particles can then be used to infer the non-linear power spectrum, as well as extract estimates for other probes. In section 2.7, I briefly discussed several possible probes and their applications to modified gravity theories. A recent comprehensive work on alternative probes reviews new ways to test gravity [Bak+19]. In the non-linear regime accessible by N-body simulations, some important tests the authors propose are based on velocity statistics and peculiar velocities of galaxies, cluster abundance and density profiles, as well as void statistics. To test and constrain a wider range of theories at once, parametrisations like the PPN formalism and effective field theory can be utilised instead of testing the theories one by one. Several relevant frameworks and their application to observations are described in [Lom18]. Machine learning is also a promising area for the investigation of non-linear probes; The algorithms can effectively distinguish otherwise similar cosmological models [Mer+19].

The quasi-static approximation has been tested in cosmological contexts in the case of the $f(R)$ model with chameleon screening ([BHL15]), the symmetron model ([Win+15]), and for several models with Vainshtein screening ([WF15]). All of these studies conclude that the fifth forces and the matter distribution in high densities are not significantly impacted by assuming the quasi-static approximation. In low-density regions, and for probes that are more sensitive to modifications of gravity than the power spectrum is, the importance of scalar field waves and other non-static effects is still not clear. Energetic events like supernova explosions can create scalar waves of significant amplitude in the chameleon model, but even though the authors of [IS18] argue that only waves with a too high frequency to be measured can enter the Milky Way, this claim has yet to be tested with high-resolution non-static simulations.

My overall conclusion from all my work is to always question and justify the assumptions applied when studying a given theory of gravity. The novelty of my research consists of studying phenomena and probes associated with scalar fields, as well as specifically studying the disformal quintessence model in the non-linear and non-static regime. My work paves the way for using simulations to find new signatures of gravity, and to test the validity of assumptions in the non-linear regime. In the future, mankind can use cosmological simulations—perhaps based on the work presented here—to better understand gravity and how the Universe works.

Bibliography

[ACD08] Ananda, K. N., Carloni, S., and Dunsby, P. K. S. "Evolution of cosmological gravitational waves in f(R) gravity". In: Phys. Rev. D vol. 77, no. 2, 024033 (Jan. 2008), p. 024033. DOI: 10.1103/PhysRevD.77.024033. arXiv: 0708.2258 [gr-qc].

[Ada+16] Adamek, J. et al. "gevolution: a cosmological N-body code based on General Relativity". In: J. Cosmology Astropart. Phys. Vol. 2016, no. 7, 053 (July 2016), p. 053. DOI: 10.1088/1475-7516/2016/07/053. arXiv: 1604.06065 [astro-ph.CO].

[Ada46] Adams, J. C. *An explanation of the observed irregularities in the motion of Uranus*. Printed by W. Clowes and Sons, 1846. DOI: 10.5479/sil.163941.39088015628639.

[Afo+19] Afonso, V. I. et al. "Correspondence between modified gravity and general relativity with scalar fields". In: *Phys. Rev. D* vol. 99 (4 Feb. 2019), p. 044040. DOI: 10.1103/PhysRevD.99.044040.

[ALL19] Arnold, C., Leo, M., and Li, B. "Realistic simulations of galaxy formation in f(R) modified gravity". In: *Nature Astronomy* (July 2019), p. 386. DOI: 10.1038/s41550-019-0823-y. arXiv: 1907.02977 [astro-ph.CO].

[Arn+19] Arnold, C. et al. "The modified gravity light-cone simulation project - I. Statistics of matter and halo distributions". In: MNRAS vol. 483, no. 1 (Feb. 2019), pp. 790–805. DOI: 10.1093/mnras/sty3044. arXiv: 1805.09824 [astro-ph.CO].

[AT10] Amendola, L. and Tsujikawa, S. *Dark Energy: Theory and Observations*. Dark Energy: Theory and Observations. Cambridge University Press, 2010.

[Bak+19] Baker, T. et al. "The Novel Probes Project – Tests of Gravity on Astrophysical Scales". In: *arXiv e-prints*, arXiv:1908.03430 (Aug. 2019), arXiv:1908.03430. arXiv: 1908.03430 [astro-ph.CO].

[Bas15] Bass, S. D. "Vacuum energy and the cosmological constant". In: *Modern Physics Letters A* vol. 30, no. 22, 1540033-321 (June 2015), pp. 1540033–321. DOI: 10.1142/S0217732315400337. arXiv: 1503.05483 [hep-ph].

[BBE15] Brax, P., Burrage, C., and Englert, C. "Disformal dark energy at colliders". In: *Physical Review D* vol. 92, no. 4, 044036 (Aug. 2015), p. 044036. DOI: 10.1103/PhysRevD.92.044036. arXiv: 1506.04057 [hep-ph].

[BBL15] Barreira, A., Bose, S., and Li, B. "Speeding up N-body simulations of modified gravity: Vainshtein screening models". In: *JCAP* vol. 1512, no. 12 (2015), p. 059. DOI: 10.1088/1475-7516/2015/12/059. arXiv: 1511.08200 [astro-ph.CO].

[BCH15] Burrage, C., Copeland, E. J., and Hinds, E. "Probing dark energy with atom interferometry". In: *Journal of Cosmology and Astroparticle Physics* vol. 2015, no. 03 (Mar. 2015), pp. 042–042. DOI: 10.1088/1475-7516/2015/03/042.

[BD13] Babichev, E. and Deffayet, C. "An introduction to the Vainshtein mechanism". In: *Classical and Quantum Gravity* vol. 30, no. 18, 184001 (Sept. 2013), p. 184001. DOI: 10.1088/0264-9381/30/18/184001. arXiv: 1304.7240 [gr-qc].

[BDZ09] Babichev, E., Deffayet, C., and Ziour, R. "k-MOUFLAGE Gravity". In: *International Journal of Modern Physics D* vol. 18, no. 14 (Jan. 2009), pp. 2147–2154. DOI: 10.1142/S0218271809016107. arXiv: 0905.2943 [hep-th].

[Bek93] Bekenstein, J. D. "Relation between physical and gravitational geometry". In: Phys. Rev. D vol. 48, no. 8 (Oct. 1993), pp. 3641–3647. DOI: 10.1103/PhysRevD.48.3641. arXiv: gr-qc/9211017 [gr-qc].

[Ber96] Bernardeau, F. "Large-Scale Structure Formation in the Quasi-Linear Regime." In: *Dark Matter in Cosmology Quantam Measurements Experimental Gravitation.* Ed. by Ansari, R., Giraud-Heraud, Y., and Tran Thanh Van, J. Jan. 1996, p. 187. arXiv: astro-ph/9607004 [astro-ph].

[BH86] Barnes, J. and Hut, P. "A hierarchical O(N log N) force-calculation algorithm". In: Nature vol. 324, no. 6096 (Dec. 1986), pp. 446–449. DOI: 10.1038/324446a0.

[BHL15] Bose, S., Hellwing, W. A., and Li, B. "Testing the quasi-static approximation in f(R) gravity simulations." In: *Journal of cosmology and astroparticle physics.* Astronomy Group vol. 2015, no. 02 (Feb. 2015), p. 034.

[BIT03] Bertotti, B., Iess, L., and Tortora, P. "A test of general relativity using radio links with the Cassini spacecraft". In: Nature vol. 425 (Sept. 2003), pp. 374–376. DOI: 10.1038/nature01997.

[BM18] Bruck, C. van de and Mifsud, J. "Searching for dark matter-dark energy interactions: Going beyond the conformal case". In: *Phys. Rev. D* vol. 97 (2 Jan. 2018), p. 023506. DOI: 10.1103/PhysRevD.97.023506.

[Bol+13] Bolotin, Y. et al. "Cosmological Evolution With Interaction Between Dark Energy And Dark Matter". In: *International Journal of Modern Physics D* vol. 24 (Sept. 2013). DOI: 10.1142/S0218271815300074.

[Bos+17] Bose, S. et al. “Speeding up N-body simulations of modified gravity: chameleon screening models”. In: J. Cosmology Astropart. Phys. Vol. 2017, no. 2, 050 (Feb. 2017), p. 050. DOI: 10.1088/1475-7516/2017/02/050. arXiv: 1611.09375 [astro-ph.CO].

[Bou+17] Bourgoin, A. et al. “Constraints on Lorentz symmetry violations with Lunar Laser Ranging”. In: *arXiv e-prints*, arXiv:1706.01243 (June 2017), arXiv:1706.01243. arXiv: 1706.01243 [gr-qc].

[Bra+16] Brax, P. et al. “LHC signatures of scalar dark energy”. In: *Phys. Rev. D* vol. 94 (8 Oct. 2016), p. 084054. DOI: 10.1103/PhysRevD.94.084054.

[Bra12] Brax, P. “Lectures on Screened Modified Gravity”. In: *arXiv e-prints*, arXiv:1211.5237 (Nov. 2012), arXiv:1211.5237. arXiv: 1211.5237 [hep-th].

[Bro+06] Brookfield, A. W. et al. “Cosmology with Massive Neutrinos Coupled to Dark Energy”. In: Phys. Rev. Lett. Vol. 96, no. 6, 061301 (Feb. 2006), p. 061301. DOI: 10.1103/PhysRevLett.96.061301. arXiv: astro-ph/0503349 [astro-ph].

[Buc+15] Buchert, T. et al. “Is there proof that backreaction of inhomogeneities is irrelevant in cosmology?” In: *Classical and Quantum Gravity* vol. 32, no. 21 (Oct. 2015), p. 215021. DOI: 10.1088/0264-9381/32/21/215021.

[Bur+19] Burrage, C. et al. “Symmetron scalar fields: Modified gravity, dark matter, or both?” In: *Phys. Rev. D* vol. 99 (4 Feb. 2019), p. 043539. DOI: 10.1103/PhysRevD.99.043539.

[BV16] Baldi, M. and Villaescusa-Navarro, F. “Cosmic Degeneracies II: Structure formation in joint simulations of Warm Dark Matter and $f(R)$ gravity”. In: *arXiv e-prints*, arXiv:1608.08057 (Aug. 2016), arXiv:1608.08057. arXiv: 1608.08057 [astro-ph.CO].

[CJ91] Coles, P. and Jones, B. “A lognormal model for the cosmological mass distribution”. In: MNRAS vol. 248 (Jan. 1991), pp. 1–13. DOI: 10.1093/mnras/248.1.1.

[Cli+12] Clifton, T. et al. “Modified gravity and cosmology”. In: *Physics Reports* vol. 513, no. 1 (2012). Modified Gravity and Cosmology, pp. 1–189. DOI: https://doi.org/10.1016/j.physrep.2012.01.001.

[Coo04] Cooray, A. “Non-linear galaxy power spectrum and cosmological parameters”. In: *Monthly Notices of the Royal Astronomical Society* vol. 348, no. 1 (Feb. 2004), pp. 250–260. DOI: 10.1111/j.1365-2966.2004.07358.x. eprint: http://oup.prod.sis.lan/mnras/article-pdf/348/1/250/4216096/348-1-250.pdf.

[Dev+19] Devi, N. C. et al. “The Galaxy Halo Connection in Modified Gravity Cosmologies: Environment Dependence of Galaxy Luminosity function”. In: (2019). DOI: 10.1093/mnras/stz1664. arXiv: 1901.02121 [astro-ph.CO].

[DJS18] Desjacques, V., Jeong, D., and Schmidt, F. "Large-scale galaxy bias". In: Phys. Rep. Vol. 733 (Feb. 2018), pp. 1–193. DOI: 10.1016/j.physrep.2017.12.002. arXiv: 1611.09787 [astro-ph.CO].

[DL17] Del Popolo, A. and Le Delliou, M. "Small Scale Problems of the ΛCDM Model: A Short Review". In: *Galaxies* vol. 5, no. 1 (Feb. 2017), p. 17. DOI: 10.3390/galaxies5010017. arXiv: 1606.07790 [astro-ph.CO].

[DNS15] Domènech, G., Naruko, A., and Sasaki, M. "Cosmological disformal invariance". In: J. Cosmology Astropart. Phys. Vol. 2015, no. 10, 067 (Oct. 2015), p. 067. DOI: 10.1088/1475-7516/2015/10/067. arXiv: 1505.00174 [gr-qc].

[Dod03] Dodelson, S. *Modern Cosmology*. Academic Press, Elsevier Science, 2003.

[Dom+15] Domènech, G. et al. "Derivative-dependent metric transformation and physical degrees of freedom". In: Phys. Rev. D vol. 92, no. 8, 084027 (Oct. 2015), p. 084027. DOI: 10.1103/PhysRevD.92.084027. arXiv: 1507.05390 [hep-th].

[DSA19] Douspis, M., Salvati, L., and Aghanim, N. "On the tension between Large Scale Structures and Cosmic Microwave Background". In: *arXiv e-prints*, arXiv:1901.05289 (Jan. 2019), arXiv:1901.05289. arXiv: 1901.05289 [astro-ph.CO].

[EFM18] Ellewsen, T. A. S., Falck, B., and Mota, D. F. "Degeneracies between modified gravity and baryonic physics". In: A&A vol. 615, A134 (July 2018), A134. DOI: 10.1051/0004-6361/201731938. arXiv: 1803.04197 [astro-ph.CO].

[EZ18] Ezquiaga, J. M. and Zumalacárregui, M. "Dark Energy in Light of Multi-Messenger Gravitational-Wave Astronomy". In: *Frontiers in Astronomy and Space Sciences* vol. 5 (2018), p. 44. DOI: 10.3389/fspas.2018.00044.

[Fal+18] Falck, B. et al. "Using voids to unscreen modified gravity". In: MNRAS vol. 475, no. 3 (Apr. 2018), pp. 3262–3272. DOI: 10.1093/mnras/stx3288. arXiv: 1704.08942 [astro-ph.CO].

[Fer19] Ferreira, P. G. "Cosmological Tests of Gravity". In: *arXiv e-prints*, arXiv:1902.10503 (Feb. 2019), arXiv:1902.10503. arXiv: 1902.10503 [astro-ph.CO].

[FJ97] Ferreira, P. G. and Joyce, M. "Structure Formation with a Self-Tuning Scalar Field". In: Phys. Rev. Lett. Vol. 79, no. 24 (Dec. 1997), pp. 4740–4743. DOI: 10.1103/PhysRevLett.79.4740. arXiv: astro-ph/9707286 [astro-ph].

[Fra82] Frautschi, S. "Entropy in an Expanding Universe". In: *Science* vol. 217, no. 4560 (1982), pp. 593–599.

[Fre17] Freedman, W. L. “Correction: Cosmology at a crossroads”. In: *Nature Astronomy* vol. 1, 0169 (June 2017), p. 0169. DOI: 10.1038/s41550-017-0169. arXiv: 1706.02739 [astro-ph.CO].

[Gar17] Garcia-Bellido, J. “Massive Primordial Black Holes as Dark Matter and their detection with Gravitational Waves”. In: *Journal of Physics: Conference Series* vol. 840 (May 2017), p. 012032. DOI: 10.1088/1742-6596/840/1/012032.

[GE15] Greiner, M. and Enßlin, T. A. “Log-transforming the matter power spectrum”. In: A&A vol. 574, A86 (Feb. 2015), A86. DOI: 10.1051/0004-6361/201323181. arXiv: 1312.1354 [astro-ph.CO].

[Gle+15] Gleyzes, J. et al. “New Class of Consistent Scalar-Tensor Theories”. In: Phys. Rev. Lett. Vol. 114, no. 21, 211101 (May 2015), p. 211101. DOI: 10.1103/PhysRevLett.114.211101. arXiv: 1404.6495 [hep-th].

[GSO16] Gerosa, D., Sperhake, U., and Ott, C. D. “Numerical simulations of stellar collapse in scalar-tensor theories of gravity”. In: *Classical and Quantum Gravity* vol. 33, no. 13 (May 2016), p. 135002. DOI: 10.1088/0264-9381/33/13/135002.

[Hag15] Hagala, R. “Cosmological simulations with disformally coupled symmetron fields”. MA thesis. 2015.

[Ham+15a] Hamilton, P. et al. “Atom-interferometry constraints on dark energy”. In: *Science* vol. 349, no. 6250 (2015), pp. 849–851. DOI: 10.1126/science.aaa8883. eprint: https://science.sciencemag.org/content/349/6250/849.full.pdf.

[Ham+15b] Hammami, A. et al. “Hydrodynamic effects in the symmetron and f(R)-gravity models”. In: MNRAS vol. 449, no. 4 (June 2015), pp. 3635–3644. DOI: 10.1093/mnras/stv529. arXiv: 1503.02004 [astro-ph.CO].

[Har+15] Harris, P. et al. “Constraining dark sectors at colliders: Beyond the effective theory approach”. In: *Physical Review D* vol. 91, no. 5, 055009 (Mar. 2015), p. 055009. DOI: 10.1103/PhysRevD.91.055009. arXiv: 1411.0535 [hep-ph].

[He+19] He, S. et al. “Learning to predict the cosmological structure formation”. In: *Proceedings of the National Academy of Sciences* vol. 116, no. 28 (2019), pp. 13825–13832. DOI: 10.1073/pnas.1821458116. eprint: https://www.pnas.org/content/116/28/13825.full.pdf.

[HHB13] Horvath, I., Hakkila, J., and Bagoly, Z. “The largest structure of the Universe, defined by Gamma-Ray Bursts”. In: *arXiv e-prints*, arXiv:1311.1104 (Nov. 2013), arXiv:1311.1104. arXiv: 1311.1104 [astro-ph.CO].

[Hir+13] Hirt, C. et al. “New ultrahigh-resolution picture of Earth’s gravity field”. In: Geophys. Res. Lett. Vol. 40 (Aug. 2013), pp. 4279–4283. DOI: 10.1002/grl.50838.

[HK10] Hinterbichler, K. and Khoury, J. “Screening Long-Range Forces through Local Symmetry Restoration”. In: Phys. Rev. Lett. Vol. 104, no. 23, 231301 (June 2010), p. 231301. DOI: 10.1103/PhysRevLett.104.231301. arXiv: 1001.4525 [hep-th].

[HLM16] Hagala, R., Llinares, C., and Mota, D. F. “Cosmological simulations with disformally coupled symmetron fields”. In: A&A vol. 585, A37 (Jan. 2016), A37. DOI: 10.1051/0004-6361/201526439. arXiv: 1504.07142 [astro-ph.CO].

[Ho 09] Ho řava, “Quantum gravity at a Lifshitz point”. In: *Phys. Rev. D* vol. 79 (8 Apr. 2009), p. 084008. DOI: 10.1103/PhysRevD.79.084008.

[Hol41] Holmberg, E. “On the Clustering Tendencies among the Nebulae. II. a Study of Encounters Between Laboratory Models of Stellar Systems by a New Integration Procedure.” In: ApJ vol. 94 (Nov. 1941), p. 385. DOI: 10.1086/144344.

[Hor74] Horndeski, G. W. “Second-Order Scalar-Tensor Field Equations in a Four-Dimensional Space”. In: *International Journal of Theoretical Physics* vol. 10 (Sept. 1974), pp. 363–384. DOI: 10.1007/BF01807638.

[Hot+18] Hotinli, S. C. et al. “Transverse Velocities with the Moving Lens Effect”. In: (2018).

[How+17] Howlett, C. et al. “2MTF - VI. Measuring the velocity power spectrum”. In: MNRAS vol. 471, no. 3 (Nov. 2017), pp. 3135–3151. DOI: 10.1093/mnras/stx1521. arXiv: 1706.05130 [astro-ph.CO].

[IS18] Ip, H. Y. S. and Schmidt, F. “Tsunamis and ripples: effects of scalar waves on screening in the Milky Way”. In: J. Cosmology Astropart. Phys. Vol. 2018, no. 6, 035 (June 2018), p. 035. DOI: 10.1088/1475-7516/2018/06/035. arXiv: 1801.07453 [gr-qc].

[Iva+16] Ivarsen, M. F. et al. “Distinguishing screening mechanisms with environment-dependent velocity statistics”. In: A&A vol. 595, A40 (Oct. 2016), A40. DOI: 10.1051/0004-6361/201628604. arXiv: 1603.03072 [astro-ph.CO].

[Joy+15] Joyce, A. et al. “Beyond the cosmological standard model”. In: Phys. Rep. Vol. 568 (Mar. 2015), pp. 1–98. DOI: 10.1016/j.physrep.2014.12.002. arXiv: 1407.0059 [astro-ph.CO].

[Ken19] Kennefick, D. *No Shadow of a Doubt: The 1919 Eclipse That Confirmed Einstein’s Theory of Relativity*. Princeton University Press, 2019.

[Kie+17] Kierdorf, M. et al. “Relics in galaxy clusters at high radio frequencies”. In: A&A vol. 600, A18 (Apr. 2017), A18. DOI: 10.1051/0004-6361/201629570. arXiv: 1612.01764 [astro-ph.GA].

[KMZ12] Koivisto, T. S., Mota, D. F., and Zumalacárregui, M. “Screening Modifications of Gravity Through Disformally Coupled Fields”. In: Phys. Rev. Lett. Vol. 109, no. 24, 241102 (Dec. 2012), p. 241102. DOI: 10.1103/PhysRevLett.109.241102. arXiv: 1205.3167 [astro-ph.CO].

[Kne+09] Knebe, A. et al. “ON THE STARTING REDSHIFT COSMOLOGICAL SIMULATIONS: FOCUSING ON HALO PROPERTIES”. In: *The Astrophysical Journal* vol. 698, no. 1 (May 2009), pp. 266–274. DOI: 10.1088/0004-637x/698/1/266.

[Koi08] Koivisto, T. S. “Disformal quintessence”. In: *arXiv e-prints*, arXiv:0811.1957 (Nov. 2008), arXiv:0811.1957. arXiv: 0811.1957 [astro-ph].

[KTB16] Kamdar, H. M., Turk, M. J., and Brunner, R. J. “Machine learning and cosmological simulations - I. Semi-analytical models”. In: MNRAS vol. 455, no. 1 (Jan. 2016), pp. 642–658. DOI: 10.1093/mnras/stv2310. arXiv: 1510.06402 [astro-ph.GA].

[KVA12] Kuhlen, M., Vogelsberger, M., and Angulo, R. “Numerical simulations of the dark universe: State of the art and the next decade”. In: *Physics of the Dark Universe* vol. 1, no. 1 (2012). Next Decade in Dark Matter and Dark Energy, pp. 50–93. DOI: https://doi.org/10.1016/j.dark.2012.10.002.

[KW04] Khoury, J. and Weltman, A. “Chameleon Fields: Awaiting Surprises for Tests of Gravity in Space”. In: Phys. Rev. Lett. Vol. 93, no. 17, 171104 (Oct. 2004), p. 171104. DOI: 10.1103/PhysRevLett.93.171104. arXiv: astro-ph/0309300 [astro-ph].

[Lev11] Leveillee, N. P. “Inquiries Journal/Student Pulse”. In: vol. 3. 05. 2011. Chap. Copernicus, Galileo, and the Church: Science in a Religious World.

[Li+12] Li, B. et al. “ECOSMOG: an Efficient COde for Simulating MOdified Gravity”. In: J. Cosmology Astropart. Phys. Vol. 2012, no. 1, 051 (Jan. 2012), p. 051. DOI: 10.1088/1475-7516/2012/01/051. arXiv: 1110.1379 [astro-ph.CO].

[LM14] Llinares, C. and Mota, D. F. “Cosmological simulations of screened modified gravity out of the static approximation: Effects on matter distribution”. In: Phys. Rev. D vol. 89, no. 8, 084023 (Apr. 2014), p. 084023. DOI: 10.1103/PhysRevD.89.084023. arXiv: 1312.6016 [astro-ph.CO].

[LM17] Llinares, C. and McCullagh, N. “Weighted density fields as improved probes of modified gravity models”. In: MNRAS vol. 472, no. 1 (Nov. 2017), pp. L80–L84. DOI: 10.1093/mnrasl/slx137. arXiv: 1704.02960 [astro-ph.CO].

[LMB11] Li, B., Mota, D. F., and Barrow, J. D. “N-BODY SIMULATIONS FOR EXTENDED QUINTESSENCE MODELS”. In: *The Astrophysical Journal* vol. 728, no. 2 (Jan. 2011), p. 109. DOI: 10.1088/0004-637x/728/2/109.

[LMW14] Llinares, C., Mota, D. F., and Winther, H. A. “ISIS: a new N-body cosmological code with scalar fields based on RAMSES. Code presentation and application to the shapes of clusters”. In: A&A vol. 562, A78 (Feb. 2014), A78. DOI: 10.1051/0004-6361/201322412. arXiv: 1307.6748 [astro-ph.CO].

[Lom18] Lombriser, L. “Parametrizations for tests of gravity”. In: *International Journal of Modern Physics D* vol. 27, no. 15, 1848002 (Jan. 2018), p. 1848002. DOI: 10.1142/S0218271818480024. arXiv: 1908.07892 [astro-ph.CO].

[LS03] Lambiase, G. and Singh, P. “Matter-antimatter asymmetry generated by loop quantum gravity”. In: *Physics Letters B* vol. 565 (July 2003), pp. 27–32. DOI: 10.1016/S0370-2693(03)00761-5. eprint: gr-qc/0304051.

[Lum16] Luminet, J.-P. “Creation, Chaos, Time : from Myth to Modern Cosmology”. In: *arXiv e-prints*, arXiv:1604.03332 (Apr. 2016), arXiv:1604.03332. arXiv: 1604.03332 [physics.hist-ph].

[McG] McGaugh, S. “Some Useful Numbers in Astrophysics”. In: *http://astroweb.case.edu/ssm/astroconstants.html* ().

[Mer+19] Merten, J. et al. “On the dissection of degenerate cosmologies with machine learning”. In: MNRAS vol. 487, no. 1 (July 2019), pp. 104–122. DOI: 10.1093/mnras/stz972. arXiv: 1810.11027 [astro-ph.CO].

[MQ14] Musielak, Z. E. and Quarles, B. “The three-body problem”. In: *Reports on Progress in Physics* vol. 77, no. 6, 065901 (June 2014), p. 065901. DOI: 10.1088/0034-4885/77/6/065901. arXiv: 1508.02312 [astro-ph.EP].

[Mv17] Mifsud, J. and van de Bruck, C. “Probing the imprints of generalized interacting dark energy on the growth of perturbations”. In: J. Cosmology Astropart. Phys. Vol. 2017, no. 11, 001 (Nov. 2017), p. 001. DOI: 10.1088/1475-7516/2017/11/001. arXiv: 1707.07667 [astro-ph.CO].

[NJP15] Nemiroff, R. J., Joshi, R., and Patla, B. R. "An exposition on Friedmann cosmology with negative energy densities". In: J. Cosmology Astropart. Phys. Vol. 2015, no. 6, 006 (June 2015), p. 006. DOI: 10.1088/1475-7516/2015/06/006. arXiv: 1402.4522 [astro-ph.CO].

[NRT09] Nicolis, A., Rattazzi, R., and Trincherini, E. "Galileon as a local modification of gravity". In: Phys. Rev. D vol. 79, no. 6, 064036 (Mar. 2009), p. 064036. DOI: 10.1103/PhysRevD.79.064036. arXiv: 0811.2197 [hep-th].

[Nte+17] Ntelis, P. et al. "Exploring cosmic homogeneity with the BOSS DR12 galaxy sample". In: J. Cosmology Astropart. Phys. Vol. 2017, no. 6, 019 (June 2017), p. 019. DOI: 10.1088/1475-7516/2017/06/019. arXiv: 1702.02159 [astro-ph.CO].

[Pa99] Perlmutter, S. and al., et. "Measurements of Ω and Λ from 42 High-Redshift Supernovae". In: ApJ vol. 517 (June 1999), pp. 565–586. DOI: 10.1086/307221. eprint: astro-ph/9812133.

[Pad15] Padilla, A. "Lectures on the Cosmological Constant Problem". In: *arXiv e-prints*, arXiv:1502.05296 (Feb. 2015), arXiv:1502.05296. arXiv: 1502.05296 [hep-th].

[PBS13] Puchwein, E., Baldi, M., and Springel, V. "Modified-Gravity-GADGET: a new code for cosmological hydrodynamical simulations of modified gravity models". In: MNRAS vol. 436, no. 1 (Nov. 2013), pp. 348–360. DOI: 10.1093/mnras/stt1575. arXiv: 1305.2418 [astro-ph.CO].

[Pen91] Penrose, R. "What does the Big Bang tell us about quantum gravity ?" In: Mem. Soc. Astron. Italiana vol. 62 (Jan. 1991), p. 607.

[Per+19] Perico, E. L. D. et al. "Cosmic Voids in Modified Gravity Scenarios". In: *arXiv e-prints*, arXiv:1905.12450 (May 2019), arXiv:1905.12450. arXiv: 1905.12450 [astro-ph.CO].

[Pla+16] Planck Collaboration et al. "Planck 2015 results. XIV. Dark energy and modified gravity". In: A&A vol. 594, A14 (Sept. 2016), A14. DOI: 10.1051/0004-6361/201525814. arXiv: 1502.01590 [astro-ph.CO].

[Pla+18] Planck Collaboration et al. "Planck 2018 results. VI. Cosmological parameters". In: *arXiv e-prints*, arXiv:1807.06209 (July 2018), arXiv:1807.06209. arXiv: 1807.06209 [astro-ph.CO].

[PV14] Postma, M. and Volponi, M. "Equivalence of the Einstein and Jordan frames". In: Phys. Rev. D vol. 90, no. 10, 103516 (Nov. 2014), p. 103516. DOI: 10.1103/PhysRevD.90.103516. arXiv: 1407.6874 [astro-ph.CO].

[Ra98] Riess, A. G. and al., et. "Observational Evidence from Supernovae for an Accelerating Universe and a Cosmological Constant". In: AJ vol. 116 (Sept. 1998), pp. 1009–1038. DOI: 10.1086/300499. eprint: astro-ph/9805201.

[Ren19] Renevey, C. "Review on tests of General Relativity And Modified Gravity Using Pulsar Timing". In: *arXiv e-prints*, arXiv:1905.13720 (May 2019), arXiv:1905.13720. arXiv: 1905.13720 [gr-qc].

[Rie+16] Riess, A. G. et al. "A 2.4% Determination of the Local Value of the Hubble Constant". In: *The Astrophysical Journal* vol. 826, no. 1, 56 (July 2016), p. 56. DOI: 10.3847/0004-637X/826/1/56. arXiv: 1604.01424 [astro-ph.CO].

[Rio02] Riotto, A. "Inflation and the Theory of Cosmological Perturbations". In: *arXiv e-prints*, hep-ph/0210162 (Oct. 2002), hep–ph/0210162. arXiv: hep-ph/0210162 [hep-ph].

[Rov13] Rovelli, C. "Aristotle's Physics: a Physicist's Look". In: *arXiv e-prints*, arXiv:1312.4057 (Dec. 2013), arXiv:1312.4057. arXiv: 1312.4057 [physics.hist-ph].

[RP88] Ratra, B. and Peebles, P. J. E. "Cosmological consequences of a rolling homogeneous scalar field". In: Phys. Rev. D vol. 37 (June 1988), pp. 3406–3427. DOI: 10.1103/PhysRevD.37.3406.

[Sak14] Sakstein, J. "Disformal theories of gravity: from the solar system to cosmology". In: J. Cosmology Astropart. Phys. Vol. 2014, no. 12, 012 (Dec. 2014), p. 012. DOI: 10.1088/1475-7516/2014/12/012. arXiv: 1409.1734 [astro-ph.CO].

[Sch+16] Schneider, A. et al. "Matter power spectrum and the challenge of percent accuracy". In: J. Cosmology Astropart. Phys. Vol. 2016, no. 4, 047 (Apr. 2016), p. 047. DOI: 10.1088/1475-7516/2016/04/047. arXiv: 1503.05920 [astro-ph.CO].

[Sch06] Schneider, P. *Extragalactic Astronomy and Cosmology*. Berlin, Heidelberg: Springer Berlin Heidelberg, 2006. DOI: 10.1007/978-3-540-33175-9.

[Sch09] Schmidt, F. "Self-consistent cosmological simulations of DGP braneworld gravity". In: *Phys. Rev. D* vol. 80 (4 Aug. 2009), p. 043001. DOI: 10.1103/PhysRevD.80.043001.

[Sha90] Shapiro, I. I. "Solar system tests of general relativity: recent results and present plans". In: *General Relativity and Gravitation, 1989*. Ed. by Ashby, N., Bartlett, D. F., and Wyss, W. 1990, p. 313.

[Sho07] Shomer, A. "A pedagogical explanation for the non-renormalizability of gravity". In: *arXiv e-prints*, arXiv:0709.3555 (Sept. 2007), arXiv:0709.3555. arXiv: 0709.3555 [hep-th].

[SJV14] Sakstein, J., Jain, B., and Vikram, V. "Testing Gravity Theories Using Stars". In: *arXiv e-prints*, arXiv:1409.3708 (Sept. 2014), arXiv:1409.3708. arXiv: 1409.3708 [astro-ph.CO].

[Spr05] Springel, V. “The cosmological simulation code GADGET-2”. In: MNRAS vol. 364, no. 4 (Dec. 2005), pp. 1105–1134. DOI: 10.1111/j.1365-2966.2005.09655.x. arXiv: astro-ph/0505010 [astro-ph].

[Sta01] Stadel, J. G. “Cosmological N-body simulations and their analysis”. PhD thesis. UNIVERSITY OF WASHINGTON, Jan. 2001.

[Sta80] Starobinsky, A. “A new type of isotropic cosmological models without singularity”. In: *Physics Letters B* vol. 91, no. 1 (1980), pp. 99–102. DOI: https://doi.org/10.1016/0370-2693(80)90670-X.

[SV15] Sakstein, J. and Verner, S. “Disformal gravity theories: A Jordan frame analysis”. In: Phys. Rev. D vol. 92, no. 12, 123005 (Dec. 2015), p. 123005. DOI: 10.1103/PhysRevD.92.123005. arXiv: 1509.05679 [gr-qc].

[Tey02] Teyssier, R. “Cosmological hydrodynamics with adaptive mesh refinement. A new high resolution code called RAMSES”. In: A&A vol. 385 (Apr. 2002), pp. 337–364. DOI: 10.1051/0004-6361:20011817. arXiv: astro-ph/0111367 [astro-ph].

[Tsu15] Tsujikawa, S. “Cosmological disformal transformations to the Einstein frame and gravitational couplings with matter perturbations”. In: Phys. Rev. D vol. 92, no. 6, 064047 (Sept. 2015), p. 064047. DOI: 10.1103/PhysRevD.92.064047. arXiv: 1506.08561 [gr-qc].

[Upa13] Upadhye, A. “Symmetron Dark Energy in Laboratory Experiments”. In: *Phys. Rev. Lett.* Vol. 110 (3 Jan. 2013), p. 031301. DOI: 10.1103/PhysRevLett.110.031301.

[vM15] van de Bruck, C. and Morrice, J. “Disformal couplings and the dark sector of the universe”. In: J. Cosmology Astropart. Phys. Vol. 2015, no. 4, 036 (Apr. 2015), p. 036. DOI: 10.1088/1475-7516/2015/04/036. arXiv: 1501.03073 [gr-qc].

[vMM17] van de Bruck, C., Mifsud, J., and Morrice, J. “Testing coupled dark energy models with their cosmological background evolution”. In: Phys. Rev. D vol. 95, no. 4, 043513 (Feb. 2017), p. 043513. DOI: 10.1103/PhysRevD.95.043513. arXiv: 1609.09855.

[Vog+12] Vogelsberger, M. et al. “Moving mesh cosmology: numerical techniques and global statistics”. In: MNRAS vol. 425, no. 4 (Oct. 2012), pp. 3024–3057. DOI: 10.1111/j.1365-2966.2012.21590.x. arXiv: 1109.1281 [astro-ph.CO].

[Wat06] Waterhouse, T. P. “An Introduction to Chameleon Gravity”. In: *arXiv e-prints*, astro-ph/0611816 (Nov. 2006), astro–ph/0611816. arXiv: astro-ph/0611816 [astro-ph].

[WCW79] Walsh, D., Carswell, R. F., and Weymann, R. J. “0957 + 561 A, B - Twin quasistellar objects or gravitational lens”. In: Nature vol. 279 (May 1979), pp. 381–384. DOI: 10.1038/279381a0.

[WF15] Winther, H. A. and Ferreira, P. G. "Vainshtein mechanism beyond the quasistatic approximation". In: Phys. Rev. D vol. 92, no. 6, 064005 (Sept. 2015), p. 064005. DOI: 10.1103/PhysRevD.92.064005. arXiv: 1505.03539 [gr-qc].

[Wil06] Will, C. M. "The Confrontation between General Relativity and Experiment". In: *Living Reviews in Relativity* vol. 9, no. 1 (Mar. 2006), p. 3. DOI: 10.12942/lrr-2006-3.

[Win+15] Winther, H. A. et al. "Modified gravity N-body code comparison project". In: MNRAS vol. 454, no. 4 (Dec. 2015), pp. 4208–4234. DOI: 10.1093/mnras/stv2253. arXiv: 1506.06384 [astro-ph.CO].

[Win+17] Winther, H. A. et al. "COLA with scale-dependent growth: applications to screened modified gravity models". In: J. Cosmology Astropart. Phys. Vol. 2017, no. 8, 006 (Aug. 2017), p. 006. DOI: 10.1088/1475-7516/2017/08/006. arXiv: 1703.00879 [astro-ph.CO].

[Win+19] Winther, H. et al. "Emulators for the non-linear matter power spectrum beyond ΛCDM". In: *arXiv e-prints*, arXiv:1903.08798 (Mar. 2019), arXiv:1903.08798. arXiv: 1903.08798 [astro-ph.CO].

[WKQ17] Wadsley, J. W., Keller, B. W., and Quinn, T. R. "Gasoline2: A Modern SPH Code". In: *Mon. Not. Roy. Astron. Soc.* Vol. 471 (2017), p. 2357. DOI: 10.1093/mnras/stx1643. arXiv: 1707.03824 [astro-ph.IM].

[YMP18] Yasini, S., Mirzatuny, N., and Pierpaoli, E. *Pairwise Transverse Velocity Measurement with the Rees-Sciama Effect*. Tech. rep. 2018.

[Zha+16] Zhang, X. et al. "Post-Newtonian parameters and cosmological constant of screened modified gravity". In: Phys. Rev. D vol. 93, no. 12, 124003 (June 2016), p. 124003. DOI: 10.1103/PhysRevD.93.124003. arXiv: 1603.09450 [gr-qc].

[ZKM13] Zumalacárregui, M., Koivisto, T. S., and Mota, D. F. "DBI Galileons in the Einstein frame: Local gravity and cosmology". In: Phys. Rev. D vol. 87, no. 8, 083010 (Apr. 2013), p. 083010. DOI: 10.1103/PhysRevD.87.083010. arXiv: 1210.8016 [astro-ph.CO].

[ZNZ19] Zhang, X., Niu, R., and Zhao, W. "Constraining the scalar-tensor gravity theories with and without screening mechanisms by combined observations". In: Phys. Rev. D vol. 100, no. 2, 024038 (July 2019), p. 024038. DOI: 10.1103/PhysRevD.100.024038. arXiv: 1906.10791 [gr-qc].

[Zum+10] Zumalacárregui, M. et al. "Disformal scalar fields and the dark sector of the universe". In: J. Cosmology Astropart. Phys. Vol. 2010, no. 5, 038 (May 2010), p. 038. DOI: 10.1088/1475-7516/2010/05/038. arXiv: 1004.2684 [astro-ph.CO].

Appendices

Appendix A

Disformal Equations

The pure disformal model is defined by the Einstein–Hilbert action

$$S = \int \sqrt{-g}\left[\frac{R}{16\pi G} + \mathcal{L}_\phi\right] + \sqrt{-\tilde{g}}\tilde{\mathcal{L}}_M \mathrm{d}^4x, \tag{A.1}$$

where the pure disformal coupling is introduced through a disformal transformation in the matter sector, given by

$$\tilde{g}_{\mu\nu} = g_{\mu\nu} + B\left(\phi\right)\phi_{,\mu}\phi_{,\nu}. \tag{A.2}$$

A.1 Equation of Motion

From [KMZ12], the EOM for a disformal field is in general given by

$$\mathcal{M}^{\mu\nu}\nabla_\mu\nabla_\nu\phi + \frac{1}{1-2BX}\mathcal{Q}_{\mu\nu}T^{\mu\nu} + \mathcal{V} = 0, \tag{A.3}$$

where I have already inserted the conformal factor $A = 1$ throughout. Here we have defined

$$\begin{aligned}
\mathcal{M}^{\mu\nu} &= \mathcal{L}_{\phi,X}g^{\mu\nu} + \mathcal{L}_{\phi,XX}\phi^{,\mu}\phi^{,\nu} - \frac{B}{1-2BX}T_m^{\mu\nu},\\
\mathcal{Q}_{\mu\nu} &= \left(-\frac{B'}{2}\right)\phi_{,\mu}\phi_{,\nu},\\
X &\equiv -\frac{1}{2}\nabla^\mu\phi\nabla_\mu\phi = -\frac{1}{2}g^{\mu\nu}\phi_{,\mu}\phi_{,\nu} = -\frac{1}{2}\left(\partial\phi\right)^2,\\
\mathcal{V} &= \mathcal{L}_{\phi,\phi} + 2X\mathcal{L}_{\phi,X\phi}.
\end{aligned}$$

In this appendix, a prime denotes a derivative with respect to the scalar field ϕ.

When assuming a canonical scalar field,

$$\mathcal{L}_\phi = X - V\left(\phi\right), \tag{A.4}$$

we get

$$\begin{aligned}
\mathcal{L}_{\phi,X} &= 1,\\
\mathcal{L}_{\phi,XX} = \mathcal{L}_{\phi,X\phi} &= 0.
\end{aligned}$$

This simplifies the following symbols:

$$\begin{aligned}
\mathcal{M}^{\mu\nu} &= g^{\mu\nu} - \frac{B}{1-2BX}T_m^{\mu\nu}\\
\mathcal{V} &= -V'\left(\phi\right).
\end{aligned}$$

Furthermore, when assuming nonrelativistic, shearless, and pressureless matter with density ρ, the stress–energy tensor simplifies to

$$T_m^{\mu\nu} = \mathrm{diag}\left(\rho,\, 0,\, 0,\, 0\right). \tag{A.5}$$

This simplifies 15 components of $\mathcal{M}^{\mu\nu}$ (all except $\mu = \nu = 0$) to

$$\mathcal{M}^{\mu\nu} = g^{\mu\nu}, \tag{A.6}$$

while the 00-component is given by

$$\mathcal{M}^{00} = g^{00} - \frac{B}{1-2BX}\rho. \tag{A.7}$$

When inserting the above assumptions, it results in an equation of motion

$$g^{\mu\nu}\nabla_\mu\nabla_\nu\phi - \frac{B}{1-2BX}\rho\nabla_0\nabla_0\phi - \frac{1}{1-2BX}\frac{B'}{2}\phi_{,0}\phi_{,0}\rho - V'\left(\phi\right) = 0. \tag{A.8}$$

With the choice of Newtonian gauge, $g^{\mu\nu}$ is diagonal, and only the diagonal elements of $\nabla_\mu\nabla_\nu\phi$ will contribute in the first term. The inverse metric is given by

$$g^{\mu\nu} = \mathrm{diag}\left(-\left(1-2\Psi\right),\, \frac{1}{a^2\left(t\right)}\left(1+2\Psi\right),\, \frac{1}{a^2\left(t\right)}\left(1+2\Psi\right),\, \frac{1}{a^2\left(t\right)}\left(1+2\Psi\right)\right). \tag{A.9}$$

The first term of equation (A.8) can be written out as

$$g^{\mu\nu}\nabla_\mu\nabla_\nu\phi = -\left(1-2\Psi\right)\nabla_0\nabla_0\phi + \frac{1}{a^2}\left(1+2\Psi\right)\nabla_i\nabla_i\phi. \tag{A.10}$$

Where the covariant derivative applied twice on a scalar is given by

$$\nabla_\mu\nabla_\nu\phi = \nabla_\mu\left(\phi_{,\nu}\right) = \phi_{,\mu\nu} - \Gamma^\alpha_{\mu\nu}\phi_{,\alpha}. \tag{A.11}$$

The Einstein frame Christoffel symbols are defined as

$$\Gamma^\mu_{\alpha\beta} = \frac{1}{2}g^{\mu\nu}\left(g_{\nu\alpha,\beta} + g_{\nu\beta,\alpha} - g_{\alpha\beta,\nu}\right). \tag{A.12}$$

At this point, we make the choice of neglecting all terms where the Newtonian potential Ψ or its derivatives $\Psi_{,\mu}$ multiply the scalar field ϕ or its derivatives. These higher order terms are small on large scales in the non-relativistic and weak field limits, but their importance in non-static N-body simulations have not been assesed thoroughly. Nevertheless, this assumption (essentially equivalent to assuming the spatially flat FLRW metric when calculating the evolution of the scalar field) greatly simplifies the numerical calculations for $\ddot{\phi}$. The first term of equation (A.8) now approximates to

$$g^{\mu\nu}\nabla_\mu\nabla_\nu\phi = -\ddot{\phi} + \frac{1}{a^2}\phi_{,ii} - 3H\dot{\phi}, \tag{A.13}$$

where the term with $H = \dot{a}/a$ comes from the Christoffel symbol in the spatial part of $\nabla_\mu \nabla_\nu \phi$, each spatial component contributing with $H\dot{\phi}$ each to the sum. The final equation of motion for a pure disformally coupled scalar field, with disformal coupling function $B(\phi)$ and potential $V(\phi)$, in an expanding and spatially flat FLRW metric is

$$-\left(1+\gamma^2\rho\right)\ddot{\phi} + \frac{1}{a^2}\nabla^2\phi - 3H\dot{\phi} - \gamma^2\rho\left(\frac{B_{,\phi}}{2B}\dot{\phi}^2\right) - V_{,\phi} = 0, \tag{A.14}$$

where $\nabla^2\phi = \phi_{,ii}$ and we have introduced the definition

$$\gamma^2 \equiv \frac{B}{1-2BX}. \tag{A.15}$$

A.2 Geodesics and Fifth Force

The acceleration of a particle in scalar–tensor theories is in general given by the geodesics calculated in the Jordan frame metric, where the geodesic equation is

$$\ddot{x}^\mu + \bar{\Gamma}^\mu_{\alpha\beta}\dot{x}^\alpha\dot{x}^\beta = 0, \tag{A.16}$$

where $\bar{\Gamma}^\mu_{\alpha\beta}$ are the Christoffel symbols in the Jordan frame. These are given as [ZKM13]

$$\bar{\Gamma}^\mu_{\alpha\beta} = \Gamma^\mu_{\alpha\beta} + \frac{1}{2}\tilde{g}^{\mu\nu}\left[\nabla_\alpha\tilde{g}_{\beta\nu} + \nabla_\beta\tilde{g}_{\alpha\nu} - \nabla_\nu\tilde{g}_{\alpha\beta}\right]. \tag{A.17}$$

A non-relativistic particle with $v \ll 1$ has four-velocity

$$\dot{x}^\mu = \left(1,\, v^1,\, v^2,\, v^3\right). \tag{A.18}$$

In the assumption of non-relativistic particles, we only keep terms up to first order of the three-velocity v^i, which simplifies the geodesic equation to

$$\ddot{x}^i + \bar{\Gamma}^i_{00} + 2\bar{\Gamma}^i_{j0}\dot{x}^j = 0. \tag{A.19}$$

A particle completely at rest with respect to the expanding FLRW spacetime will not be affected by the $\bar{\Gamma}^i_{j0}$ term. Because we are studying particles of slowly moving cold dark matter, we chose to neglect all terms of $\bar{\Gamma}^i_{j0}$ except the Hubble friction term, $\Gamma^i_{j0} = H\delta^i_j$, which also appears in the GR case and is already implemented in `Ramses` through the choice of variables.

A.2.1 The Jordan Frame Metric and its Inverse

The Jordan frame metric is found from the definition of the disformal transformation, which in the pure disformal case is

$$\tilde{g}_{\mu\nu} = g_{\mu\nu} + B\phi_{,\mu}\phi_{,\nu}. \tag{A.20}$$

In [ZKM13] they state the general inverse of the disformal metric when allowing a conformal term A. In the pure disformal case with $A = 1$, the inverse metric is

$$\tilde{g}^{\mu\nu} = g^{\mu\nu} - \gamma^2\phi^{,\mu}\phi^{,\nu}. \tag{A.21}$$

A.2.2 The $i00$ Component

$$
\begin{aligned}
&\bar{\Gamma}^i_{00} \\
=&\Gamma^i_{00} + \frac{1}{2}\tilde{g}^{i\nu}\left[\nabla_0\tilde{g}_{0\nu} + \nabla_0\tilde{g}_{0\nu} - \nabla_\nu\tilde{g}_{00}\right] \\
=&\Gamma^i_{00} + \frac{1}{2}\tilde{g}^{i\nu}\left[2B\left(\nabla_0\phi_{,0}\phi_{,\nu}\right) + 2\phi_{,0}\phi_{,\nu}B_{,0} - B\left(\nabla_\nu\phi_{,0}\phi_{,0}\right) - \phi_{,0}\phi_{,0}B_{,\nu}\right] \\
=&\Gamma^i_{00} + \frac{1}{2}\tilde{g}^{i\nu}\left[2B\phi_{,\nu}\nabla_0\phi_{,0} + 2\phi_{,0}\phi_{,\nu}B_{,0} - \phi_{,0}\phi_{,0}B_{,\nu}\right]. \qquad \text{(A.22)}
\end{aligned}
$$

The first term gives the Newtonian force, it is given by

$$
\begin{aligned}
\Gamma^i_{00} &= \frac{1}{2}g^{i\nu}\left(g_{\nu 0,0} + g_{\nu 0,0} - g_{00,\nu}\right), \\
&= -\frac{1}{2}g^{ii}g_{00,i}, \\
&= \frac{\Psi_{,i}}{a^2}. \qquad \text{(A.23)}
\end{aligned}
$$

Here, only $\nu = i$ gives a nonzero contribution from $g^{i\nu}$, and therefore it follows that $g_{\nu 0,0} = g_{i0,0} = 0$.

The second term is

$$
\begin{aligned}
\frac{1}{2}\tilde{g}^{i\nu}2B\phi_{,\nu}\nabla_0\phi_{,0} =& B\left(g^{i\nu} - \gamma^2\phi^{,i}\phi^{,\nu}\right)\left(\phi_{,\nu}\nabla_0\phi_{,0}\right), \\
=& B\left(\frac{(1+2\Psi)}{a^2}\left(\phi_{,i}\nabla_0\phi_{,0}\right) - \gamma^2\phi^{,i}\phi^{,\nu}\phi_{,\nu}\nabla_0\phi_{,0}\right), \\
=& \frac{(1+2\Psi)}{a^2}\gamma^2\left(\phi_{,i}\nabla_0\phi_{,0}\right). \qquad \text{(A.24)}
\end{aligned}
$$

We neglect all higher order terms where Ψ multiplies the field or its derivatives. Under this assumption $\nabla_0\phi_{,0} = \ddot{\phi}$, which means that the second term can be written

$$
\frac{1}{a^2}\gamma^2\ddot{\phi}\phi_{,i}. \qquad \text{(A.25)}
$$

The third term is

$$
\begin{aligned}
\frac{1}{2}\tilde{g}^{i\nu}2\phi_{,0}\phi_{,\nu}B_{,0} &= \left(g^{i\nu} - \gamma^2\phi^{,i}\phi^{,\nu}\right)\phi_{,0}\phi_{,\nu}B_{,0} \\
&= \left(\frac{(1+2\Psi)}{a^2}\phi_{,0}\phi_{,i}B_{,0} + 2\gamma^2 g^{ii}\phi_{,i}\phi_{,0}XB_{,0}\right) \\
&= \frac{(1+2\Psi)}{a^2}\gamma^2\phi_{,0}\phi_{,i}\frac{B_{,0}}{B}. \qquad \text{(A.26)}
\end{aligned}
$$

Since B is a function of ϕ only, we can write $B_{,0} = B_{,\phi}\phi_{,0}$. When neglecting higher order terms where Ψ multiplies the field or its derivatives, the third term becomes

$$
\frac{1}{a^2}\gamma^2\frac{B_{,\phi}}{B}\dot{\phi}^2\phi_{,i} \qquad \text{(A.27)}
$$

Finally, the fourth term of $\bar{\Gamma}^i_{00}$ is given by

$$-\frac{1}{2}\tilde{g}^{i\nu}\phi_{,0}\phi_{,0}B_{,\nu} = -\frac{1}{2}\left(g^{i\nu} - \gamma^2\phi^{,i}\phi^{,\nu}\right)\phi_{,0}\phi_{,0}B_{,\nu}$$
$$= -\frac{1}{2}\frac{(1+2\Psi)\,\phi_{,0}\phi_{,0}B_{,i}}{a^2} + \frac{1}{2}\gamma^2\phi^{,i}\phi^{,\nu}\phi_{,0}\phi_{,0}B_{,\nu}. \tag{A.28}$$

After the usual neglections, rewriting $B_{,\nu} = B_{,\phi}\phi_{,\nu}$ and $\phi^{,i} = g^{ij}\phi_{,j} \approx \phi_{,i}/a^2$, and recognising that $\phi^{,\nu}\phi_{,\nu} = -2X$, the fourth term becomes

$$-\left(1 + 2X\gamma^2\right)\frac{B_{,\phi}}{2a^2}\dot{\phi}^2\phi_{,i}. \tag{A.29}$$

When writing out γ^2 and collecting the terms inside the parenthesis, this is equivalent to

$$-\frac{B_{,\phi}}{2Ba^2}\gamma^2\dot{\phi}^2\phi_{,i}. \tag{A.30}$$

A.2.3 The Acceleration of a Test Particle

When inserting all the terms as well as the Hubble friction into equation (A.19), and collecting terms, the resulting geodesic equation is

$$\ddot{x}^i + \frac{\Psi_{,i}}{a^2} + \frac{1}{a^2}\left(\ddot{\phi} + \frac{1}{2}\frac{B_{,\phi}}{B}\dot{\phi}^2\right)\gamma^2\phi_{,i} + 2H\dot{x}^i = 0. \tag{A.31}$$

The fifth force consists of the terms not found in GR; when removing the gradient of Ψ and the Hubble friction, the acceleration of a test particle due to the disformal fifth force is given by

$$\mathbf{F}_\phi = -\frac{1}{a^2}\left(\ddot{\phi} + \frac{1}{2}\frac{B_{,\phi}}{B}\dot{\phi}^2\right)\gamma^2\nabla\phi. \tag{A.32}$$

Appendix B

Slingshot Equations

The ISW effect changes the temperature of the CMB photons during the time t they spend in an evolving gravitational potential Ψ. Specifically,

$$\frac{\Delta T}{T} = 2 \int \dot{\Psi} \, \mathrm{d}t. \tag{B.1}$$

The slingshot effect is the change in photon temperature due to the transverse motion of an non-evolving potential well. Following a flow of photons travelling through a moving halo, this effect can be expressed as

$$\frac{\Delta T_{\mathrm{slingshot}}}{T} = 2 \int \mathbf{v}_{\perp} \cdot \nabla \Psi \, \mathrm{d}t. \tag{B.2}$$

We chose a coordinate system where light moves in the positive z-direction, along the line of sight. The projected motion $\mathbf{v}_{\perp}$ of the halo is taken to be constant and along the x-axis. In this frame, we define v_x as the velocity component perpendicular to the line of sight. The y and z components of the dot product are zero. The photons move with the speed of light, with $c = 1$, such that the time integral can be exchanged with an integral along z:

$$\frac{\Delta T_{\mathrm{slingshot}}}{T} = 2 v_x \int \frac{\partial \Psi}{\partial x} \, \mathrm{d}z. \tag{B.3}$$

This equation implies that the gradient of the gravitational potential Ψ close to the moving mass is the source of positive $\dot{\Psi}$ behind the mass and negative $\dot{\Psi}$ in front of the mass, even though the shape of the potential Ψ does not change relative to the moving mass.

See the appendix of Paper III for a concrete example of calculating $\frac{\Delta T}{T}$ for a specific functional form of $\Psi(r)$ around a galaxy assumed to consist of a NFW dark matter halo populated with baryons following a Hernquist density distribution.

Appendix C

Linear Perturbation Theory

In linear perturbation theory, we aim to solve the Einstein field equations in the case of a universe with small scalar perturbations in the metric and small perturbations around the background (average) quantities of the density and pressure for each fluid. Under the assumption that the perturbations are small, we neglect all terms of higher than first order in the perturbed quantities. For each component we add, we must close the system of equations by imposing energy–momentum conservation. The set of equations listed in this appendix are the perturbed Einstein equations; When combined with the Boltzmann equations they describe a system out of thermodynamic equilibrium (and allow for e.g. couplings between photons and baryons), and are often called the Einstein–Boltzmann equations.

I will use conformal time τ defined as $\mathrm{d}\tau = a^{-1}\mathrm{d}t$. The perturbed metric is now given by the line element

$$\mathrm{d}s^2 = a^2(\tau)\left[-(1+2\Psi)\,\mathrm{d}\tau^2 + (1-2\Phi)\,\mathrm{d}x^i\mathrm{d}x^i\right]. \tag{C.1}$$

Primes in this appendix are derivatives with respect to conformal time τ. Equations are adapted from the appendix of [Mv17].

C.1 In ΛCDM

In a universe with multiple fluids denoted by i (each with a density perturbation $\delta\rho_i = \rho_i - \bar{\rho}_i$, an overdensity $\delta_i = \delta\rho_i/\bar{\rho}_i$, a perturbed pressure $\delta p_i = p_i - \bar{p}_i$, an equation of state $w_i = p_i/\rho_i$, a velocity divergence $\theta_i = \nabla\cdot\mathbf{v}_i$, and an anisotropic stress scalar σ_i), the perturbed Einstein field equations are

$$k^2\Phi + 3\mathcal{H}(\Phi' + \mathcal{H}\Psi) = -4\pi G a^2 \sum_i \delta\rho_i, \tag{C.2}$$

$$k^2(\Phi' + \mathcal{H}\Psi) = 4\pi G a^2 \sum_i \rho_i(1+w_i)\,\theta_i, \tag{C.3}$$

$$\Phi'' + \mathcal{H}(\Psi' + 2\Phi') + \Psi\left(\mathcal{H}^2 + 2\mathcal{H}'\right) + \frac{k^2}{3}(\Phi - \Psi) = 4\pi G a^2 \sum_i \delta p_i, \tag{C.4}$$

$$k^2(\Phi - \Psi) = 12\pi G a^2 \sum_i \rho_i(1+w_i)\,\sigma_i, \tag{C.5}$$

where the last equation sets $\Phi = \Psi$ in the absence of anisotropic stress. Energy–momentum conservation, enforced by the condition $\nabla_\mu T^{\mu\nu} = 0$, leads to the

perturbed continuity and Euler equations

$$\delta_i' + 3\mathcal{H}\left(\frac{\delta p_i}{\delta\rho_i} - w_i\right)\delta_i = -\left(1+w_i\right)\left(\theta_i - 3\Phi'\right), \tag{C.6}$$

$$\theta_i' + \left[\mathcal{H}\left(1-3w_i\right) + \frac{w_i'}{1+w_i}\right]\theta_i = k^2\left[\Psi + \frac{\delta p_i}{\delta\rho_i}\frac{\delta_i}{1+w_i}\right] - k^2\sigma_i. \tag{C.7}$$

C.2 In Scalar–Tensor Theories

In a general scalar–tensor theory with coupling function Q, a single shear-free coupled fluid (denoted with subscript c) coupled to the scalar field ϕ will follow the modified continuity and Euler equations

$$\delta_c' + 3\mathcal{H}\left(\frac{\delta p_c}{\delta\rho_c} - w_c\right)\delta_c = -\left(1+w_c\right)\left(\theta_c - 3\Phi'\right) + \frac{Q}{\rho_c}\phi'\delta_c - \frac{Q}{\rho_c}\delta\phi' - \frac{\phi'}{\rho_c}\delta Q, \tag{C.8}$$

$$\theta_c' + \left[\mathcal{H}\left(1-3w_c\right) + \frac{w_c'}{1+w_c}\right]\theta_c = k^2\left[\Psi + \frac{\delta p_c}{\delta\rho_c}\frac{\delta_c}{1+w_c}\right] + \frac{Q}{\rho_c}\phi'\theta_c - \frac{Q}{\rho_c\left(1+w_c\right)}k^2\delta\phi, \tag{C.9}$$

which reduce to the uncoupled (GR) case when $Q \to 0$. In the Einstein frame, the modifications appear only in the motion of matter, and hence the Einstein equations (C.2 - C.5) are not modified. The extra scalar degree of freedom introduces an extra equation; Perturbations of the scalar field $\delta\phi$ are found from the perturbed scalar field equation of motion (Klein–Gordon equation)

$$\delta\phi'' + 2\mathcal{H}\delta\phi' + \left(k^2 + a^2V_{,\phi\phi}\right)\delta\phi = \left(\Psi' + 3\Phi'\right)\phi' - 2a^2V_{,\phi}\Psi + a^2\delta Q + 2a^2Q\Psi. \tag{C.10}$$

This full set of equations can be solved numerically for a given Q, which is what they did for a more general mixed conformal and disformal model in [Mv17].

C.2.1 A Conformally Coupled Fluid in the Quasi-Static Limit

In the case of a pure conformal coupling $A\left(\phi\right)$, and assuming that the coupled fluid is pressureless dark matter, the coupling function (and its perturbation) takes the form

$$Q_{\mathrm{conf}} = -\frac{1}{2}\frac{A_{,\phi}}{A}\rho_c = -\frac{1}{2}\frac{\partial\left(\ln A\right)}{\partial\phi}\rho_c, \tag{C.11}$$

$$\delta Q_{\mathrm{conf}} = -\frac{\rho_c}{A}\left(\frac{1}{2}A_{,\phi}\delta_c + \left[\frac{1}{2}A_{,\phi\phi} + \frac{QA_{,\phi}}{\rho_c}\right]\delta\phi\right). \tag{C.12}$$

In the case of only one fluid, namely the coupled pressureless dark matter, and no anisotropic stress, the perturbed Einstein and continuity equations simplify to

$$k^2\Psi + 3\mathcal{H}\left(\Psi' + \mathcal{H}\Psi\right) = -4\pi Ga^2\delta\rho_c, \tag{C.13}$$

$$k^2\left(\Psi' + \mathcal{H}\Psi\right) = 4\pi G a^2 \rho_c \theta_c, \tag{C.14}$$

$$\Psi'' + 3\mathcal{H}\Psi' + \Psi\left(\mathcal{H}^2 + 2\mathcal{H}'\right) = 0 \tag{C.15}$$

$$\delta_c' = -\left(\theta_c - 3\Psi'\right) + \frac{Q}{\rho_c}\phi'\delta_c - \frac{Q}{\rho_c}\delta\phi' - \frac{\phi'}{\rho_c}\delta Q, \tag{C.16}$$

$$\theta_c' + \mathcal{H}\theta_c = k^2\Psi + \frac{Q}{\rho_c}\phi'\theta_c - \frac{Q}{\rho_c}k^2\delta\phi. \tag{C.17}$$

In the quasi-static limit, where we neglect time derivatives of the scalar field and of the gravitational potential, the continuity equations (C.16 and C.17) and the EOM (C.10) can be written

$$\delta_c' = -\theta_c, \tag{C.18}$$

$$\theta_c' + \mathcal{H}\theta_c = k^2\left(\Psi + \frac{1}{2}\frac{A_{,\phi}}{A}\delta\phi\right), \tag{C.19}$$

$$\frac{k^2}{a^2}\delta\phi = -\frac{\rho_c}{2}\frac{A_{,\phi}}{A}\left(\delta_c - \left(\frac{1}{2}\frac{A_{,\phi}}{A}\right)\delta\phi + \Psi\right). \tag{C.20}$$

In over-dense regions where $\delta_c > |\Psi|, |\delta\phi|$, and on sub-horizon scales ($k \gg \mathcal{H}$), equations (C.13) and (C.20) lead to similar Poisson's equations for the Newtonian potential and for the scalar field, namely

$$\frac{k^2}{a^2}\Psi = -4\pi G\delta\rho_c, \tag{C.21}$$

$$\frac{k^2}{a^2}\delta\phi = -\frac{1}{2}\frac{A_{,\phi}}{A}\delta\rho_c. \tag{C.22}$$

In the case of a positively sloping conformal coupling, $A_{,\phi} > 0$, the field perturbation will always be negative, $\delta\phi < 0$, signifying that the scalar field—just like the gravitational potential—has a dip in over-dense regions[1]. It can be seen from the Euler equation (C.19) that the coupled matter gains a negative divergence because $\theta_c' < 0$ in over-dense regions, and specifically it gains a more negative divergence than in the GR case. This addition to the divergence is the reason for enhanced structure growth in many scalar–tensor theories.

[1] A special case is when $\frac{A_{,\phi}}{A}$ is a constant, then the quasi-static scalar field perturbation $\delta\phi$ is expected to evolve similarly to the Newtonian potential Ψ.